The analysis, modelling, and acoustic control of fluidic devices

Chris Nicholls
Lincoln College
University of Oxford

A thesis submitted for the degree of
Doctor of Philosophy

Michaelmas 2020

To Trevor
our feline companion

Acknowledgements

Pursing my DPhil has been a great adventure. The drama of the epic highs and crushing lows has made me significantly over-estimate the importance of my research at times. I am forever grateful to my supervisor, Dr Marko Bacic, for his steadying of the ship, like a great test match batsman after the top order has collapsed. His infectious excitement for engineering and science has been an inspiration to me, and made the last few years joyous as well as fruitful.

I am heavily indebted to Dr Brian Tang and Dr James Turner, whose combined knowledge of fluid mechanics continues to amaze me. Many times I have emerged from their office with my ideas mostly dismantled and obliterated; but what remains I know must be golden. I have thoroughly enjoyed working with them both, and hope to continue to learn from them.

I would like to thank Dr Michael Mair for the many hours of discussion we have shared. Without his ground-breaking work, none of my own would have been possible. His dedication to science and research is something I strive to emulate.

Thanks go to my thesis examiners, Prof. Aimee Morgans and Prof. David Gillespie, for their valued contributions and engaging discussion.

I have spent many great nights both out and in with my friends at Lincoln who have made my DPhil fun and special. The late-night monopoly games with Mat, Alice, & Megan are particularly fond memories. I am grateful to Mat for our bike rides together both in Oxford and abroad, and for initiating me into the world of cycling, which Emily no doubt regrets.

I also thank my HCBC friends, Callum, Simon, Chris, & Ben, for providing welcome distractions over the many years I have spent in Oxford. From the early mornings on the Isis and in the erg room to adventures on our bikes and walking Offa's Dyke path, I have discovered new limits and developed a life-long

affection for our countryside. Thanks also go to Alex, from whom I learned a great deal as we journeyed through our undergraduate studies together.

A special thanks must go to my parents who made this all possible with their strong commitment to my education, the greatest thing that anyone can inherit. It gives me pleasure to express formally the huge influence my father has been on my development as an engineer and a researcher. His patience and guidance has helped me more than he can know.

Finally, I thank Emily, my best friend and fiancée. She has heard a great deal about the 'Y-shaped tubes' over the years, and has lived through the highs and lows by my side. Her presence is a reminder of the important things in life when work is going badly.

A doctoral thesis brought to you by...

Abstract

Zero-carbon flight represents arguably the biggest challenge of the green revolution. A variety of novel flight concepts have been proposed in response to emissions targets set by the International Air Transport Association (IATA). The common theme to enabling these innovative technologies is efficient, reliable, low-weight solutions to the control of airflow: from controlling aircraft aerodynamics to heat transfer in gas turbines. Active flow control represents a family of such solutions, and is based on the idea of harnessing the natural amplification provided by nonlinearities in fluid mechanics to bring about large-scale system change with only a small energy input. Fluidic devices are a highly-reliable means of controlling high-speed flows and have a small response time.

A analytical, dynamic model of an attached jet, the canonical form of all fluidic devices, is developed from first principles. The jet is excited acoustically, which is modelled as a time-varying component of additional entrainment. The core component of the model is a novel, unsteady jet curvature equation, which finally removes the need for the quasi-steady jet assumption. An accompanying experimental validation is performed, and a strategy for inverting system nonlinearities is presented. The model is linearised so that magnitude and phase frequency responses can be compared with the validation data. Good agreement is found for one roll-off in the data, and explanations for a second, unmodelled roll-off are given.

A closed-loop controller is designed and implemented for an acoustically-driven fluidic amplifier in which the flow is continuously modulated. The attached-jet model provides good agreement with experimentally-identified frequency responses, and a black-box identification is used for control purposes. The performance of the resulting LQG controller is evaluated in several experiments, and is shown either to match or outperform its open-loop counterpart in every respect. However, closed-loop bandwidth is limited by turbulent noise in the

region of the system dynamics, and a means of overcoming this fundamental challenge is discussed.

The response of a jet shear layer to a modulated perturbation is explored from a signal processing perspective. The well-known shear layer demodulation property is identified specifically as an envelope detector because of its phase insensitivity. A novel input over-modulation technique is proposed that halves the required actuator bandwidth while suffering only a 2.7 dB reduction in response magnitude. It is further hypothesised that the shear layer response includes a sampler, and an analogy with the Nyquist sampling theorem is made. Early experiments appear to invalidate the analogy, although the experiments are somewhat inconclusive. If the Nyquist theorem does not hold, interesting implications are raised about the current paradigm of the response of shear layers to modulated perturbations.

Contents

Nomenclature

Miscellaneous

α	Wall incline angle (-)
α_{FF}	Feed-forward term gain (-)
β_1	Fraction of recirculated momentum exiting AS control volume at upstream boundary (-)
β_2	Fraction of recirculated momentum exiting US control volume at upstream boundary (-)
η	Nondimensional distance normal to jet centreline $\left(\eta = \frac{\sigma y}{s+s_0}\right)$ (-)
η_1	Value of η for SL 1 at AS attachment point ($s = R\theta$) (-)
η_2	Value of η for SL 2 at US attachment point ($s = x_{\text{US}}$) (-)
η_{DSL}	Value of η on DSL (-)
$\eta_{\text{DSL}_{\text{AS}}}$	Value of η_{DSL} on AS (-)
$\eta_{\text{DSL}_{\text{US}}}$	Value of η_{DSL} on US (-)
η_{pr}	Value of η at P_{out} probe position (-)
η_{SL}	Value of η for edge of shear layer (-)
η_{th}	Thermodynamic efficiency (-)
γ_{sh}	Ratio of specific heats (-)
γ_{ch}	Chirp sweep rate (Hzs^{-1})
γ	Coefficient of $\ddot{R}$ in JCE (-)
κ_1	Shape factor applied to value of v at y_{DSL} (-)
κ_2	Fitting parameter applied to γ, the coefficient of $\ddot{R}$ (-)
θ	Swept angle of jet centreline between orifice and wall (-)
ξ	Inflating factor for mass flow rate (-)
ξ_{ch}	Chirp initial frequency (Hz)
ϵ_{v}	Eddy viscosity (m^2s^{-1})
ϵ	Fraction of $\sigma_\sim$ included in AS bubble pressure dynamics (-)
ϵ_0	Critical value of ϵ where DC gain sign changes (-)
ϵ_1	Value of ϵ where system becomes NMP (-)
χ	Argument of inverse hyperbolic tangent functions in definition of ζ (-)
χ_1	Value of χ evaluated at $s = 0$ (-)
χ_2	Value of χ evaluated at $s = R\theta$ (-)
ζ	Coefficient of $\dot{R}$ term in JCE (-)
ρ	Air density (kgm^{-3})
σ	Jet spread factor (-)
σ_{AS}	σ on AS (-)
σ_{US}	σ on US (-)
$\Delta\sigma$	Difference between σ_{AS} & σ_{US} (-)
ϕ	Swept angle of point in jet velocity profile (-)
$\bar{\sigma}$	Mean of σ_{AS} & σ_{US} (-)
μ	Dynamic viscosity of air (Pa s)
$\sigma_\sim$	Time-varying spread factor (-)
τ_s	Nondimensional switching time (-)
$\Phi_{yu}(\omega)$	Output-input cross-spectral density (dB/Hz)
$\Phi_{uu}(\omega)$	Input power spectral density (dB/Hz)
$\hat{\delta\mathbf{x}}(t)$	State deviation estimate (-)
$\delta\mathbf{x}(t)$	State deviation from equilibrium (-)

$\delta y(t)$	Output deviations from reference (-)
$\delta y'(t)$	Noisy measurement of δy (-)
$\hat{\delta y}(t)$	Output deviation estimate (-)
$\delta u(t)$	Control input deviation from equilibrium (-)
$\psi_{f_c}(f_m)$	Quasi-steady jet response at f_c (-)
$\psi_D(f)$	$\psi(f)$ at design flow rate & carrier frequency (-)
σ_y^2	Sensor noise variance for $\delta y'(t)$ (-)
$\mathbf{A}$	State matrix (-)
$\mathbf{A}_{\text{aug}}$	Augmented state matrix (-)
b	Inlet nozzle width (mm)
B	Carrier offset tone amplitude (V)
$\mathbf{B}$	Input vector (-)
$\mathbf{B}_{\text{aug}}$	Augmented input vector (-)
$\mathbf{C}$	Output vector (-)
$\mathbf{C}_{\text{aug}}$	Augmented output matrix (-)
$C(z)$	Controller transfer function (-)
c_3	Constant ($c_3 = \frac{R_g T}{M_m}$) (Jkg^{-1})
C_{L}	Lift coefficient (-)
C_μ	Momentum coefficient (-)
d	Device depth (mm)
d_s	Splitter distance (mm)
D	Setback distance (mm)
D'	Alternative setback distance definition $\left(D' = D - b/2\right)$ (mm)
D_h	Hydraulic diameter (mm)
E	Entrainment rate (-)
$\mathbf{e}(t)$	State estimation error (-)
$\mathbf{e}_{\text{aug}}(t)$	Augmented state estimation error (-)
F^+	Nondimensional frequency (-)
$F(x)$	System amplitude nonlinearity (-)
$\mathbf{F}$	Disturbance input vector (-)
$\mathbf{F}_{\text{aug}}$	Augmented disturbance input vector (-)
$f(\theta)$	Volume of attached side bubble ($f(\theta) = V_{\text{B1}}$) ($\text{m}^3$)
f_0	Dynamic response initial frequency (Hz)
$f_1(t)$	Dynamic response step signal (Hz)
f_m	Modulating tone frequency (Hz)
$\bar{f_m}$	Upper limit of f_m tested experimentally (Hz)
f_c	Carrier tone frequency (Hz)
f_s	Sampling frequency (Hz)
$G(\omega)$	Jet dynamic system transfer function (-)
$\hat{G}(\omega)$	ETFE from measured data (-)
$G_{\text{delay}}(s)$	Transfer function model for transport delay (-)
$g(\theta)$	Radius of jet curvature ($g(\theta) = R$) (m)
$g_{\text{amp}}(t)$	Audio amplifier signal (V)
$g_{\text{ex}}(t)$	Excitation signal to drive audio amplifier (V)
$g_c(t)$	Carrier tone signal (-)
$g_m(t)$	Modulation signal / feedback term (-)
$g'_m(t)$	Control input (-)
g_{resp}	Nonlinear jet response (-)
$H(x)$	Limiting function (saturation limits) (-)
$H_{\text{plant}}(z)$	Transfer function fitted to plant (-)
J	Nominal jet inlet momentum (kgms^{-1})

$\bar{J}_{\mathrm{AS}}$	Jet momentum entering AS control volume (kgms^{-1})
$\bar{J}_{\mathrm{US}}$	Jet momentum entering US control volume (kgms^{-1})
$\bar{J}$	Inflated jet momentum integrated across nozzle exit (kgms^{-1})
J_1	AS forward momentum (kgms^{-1})
J_1'	US forward momentum (kgms^{-1})
J_2	AS recirculated momentum (kgms^{-1})
J_2'	US recirculated momentum (kgms^{-1})
J_{loss}	Momentum lost to wall through viscous shear in AS control volume (kgms^{-1})
J_{loss}'	Momentum lost to wall through viscous shear in US control volume (kgms^{-1})
K_{AW}	Anti wind-up gain (-)
K_{DC}	System DC gain (-)
K_f	Kalman filter gain matrix(-)
K_{L}	Total pressure loss coefficient (-)
K_{LQR}	LQR control gain matrix (-)
L_1	Side length of attached side control volume around attachment point (m)
L_2	Side length of unattached side control volume around attachment point (m)
L_{PC}	Potential core length (m)
L_{v}	Average distance between vortices (m)
L_{ve}	Length of region where vortices exist (m)
M	Blowing ratio (-)
M_n	Mach number (-)
$\dot{m}$	Inlet mass flow rate (kgs^{-1})
m_{B1}	Mass in attached side bubble (kg)
m_{B2}	Mass in unattached side bubble (kg)
$\dot{m}_c$	Control mass flow rate (kgs^{-1})
$\dot{m}_{\mathrm{e1}}$	AS entrainment flow rate (kgs^{-1})
$\dot{m}_{\mathrm{e2}}$	US entrainment flow rate (kgs^{-1})
$\dot{m}_f$	Time-varying mass flow filling channel (kgs^{-1})
$\dot{m}_{\mathrm{r1}}$	AS recirculation flow rate (kgs^{-1})
$\dot{m}_{\mathrm{r2}}$	US recirculation flow rate (kgs^{-1})
M_{m}	Molar mass of air (kgmol^{-1})
n	No. of standard volumes (b^2d) in control port channel (-)
n_{ts}	Number of time series (-)
N	Number of segments (-)
N_{MC}	Number of Monte Carlo analysis runs (-)
N_v	Average number of vortices present in shear layer (-)
ΔP	Pressure difference across jet (Pa)
P_∞	Pressure on downstream side of both AS & US control volumes (Pa)
P_{AS}	Pressure measured in AS bubble (Pa)
P_{B1}	AS bubble pressure (Pa)
P_{B2}	US bubble pressure (Pa)
P_c	Channel pressure in lumped model (Pa)
P_{f_m}	Power at f_m (dB)
P_{2f_m}	Power at $2f_m$ (dB)
P_{out}	Total pressure measurement used to indicate jet position (Pa)
P_{out_0}	Unexcited value of P_{out} (Pa)
P_{US}	Pressure measured in US bubble (Pa)

ΔP	Pressure difference across jet (Pa)
Q_c	Control flow rate (m^3s^{-1})
Q_{out}	Net flow exiting bubble (m^3s^{-1})
R	Radius of jet curvature (m)
R_g	Universal gas constant ($Jmol^{-1}K^{-1}$)
r	Radial distance from $(0, R)$ to point in velocity profile (m)
$r(t)$	Controller reference (-)
s	Distance along jet centreline downstream of inlet orifice (m)
$S(s)$	Sensitivity transfer function (-)
s_0	Distance along jet centreline between virtual origin and inlet orifice (m)
$s_{0_{AS}}$	Value of s_0 using σ_{AS} (m)
$s_{0_{US}}$	Value of s_0 using σ_{US} (m)
$s_{0_{AS}}$	Value of s_0 using σ_{AS} (m)
$s_{0_{mean}}$	Value of s_0 using $\bar{\sigma}$ (m)
s_{pr}	Value of s at P_{out} probe position (m)
St_x	Strouhal number with length scale x (-)
t_1	Hyperbolic tangent of η_1 ($t_1 = \tanh(\eta_1)$) (-)
t_2	Hyperbolic tangent of η_2 ($t_2 = \tanh(\eta_2)$) (-)
t_{SL}	Hyperbolic tangent of η_{SL} ($t_{SL} = \tanh(\eta_{SL})$) (-)
T	Temperature (K)
T_s	Sampling time (s)
T_d	Transport delay (s)
$T(s)$	Complimentary sensitivity transfer function (-)
u	Velocity in local streamwise direction (ms^{-1})
$u(t)$	Control input (-)
u_c	AM input for dynamic response identification (V)
$\bar{u}_{max}$	Max jet velocity along path from nozzle orifice to P_{out} probe (ms^{-1})
u_r	Radial velocity (ms^{-1})
u_{SL}	Input to shear layer (-)
u_ϕ	Tangential velocity (ms^{-1})
u_0	Control input equilibrium (-)
$u_{equil}(t)$	Steady carrier tone input to determine operating points (-)
$u_{FF}(t)$	Feed-forward term in control input (-)
v	Transverse velocity (ms^{-1})
$\bar{v}$	Normalised transverse velocity (-)
$\mathbf{v}(t)$	Sensor noise (-)
$\mathbf{V}$	Sensor noise covariance matrix (-)
V_{B1}	Volume of attached side bubble (m^3)
V_{B2}	Volume of unattached side bubble (m^3)
V_{const}	Device volume shared between bubbles (m^3)
v_{SL}	Vortex convection speed (ms^{-1})
W	Process noise variance (-)
$w(t)$	Process noise signal (-)
$\mathbf{x}(t)$	State vector (-)
$\mathbf{x}_{aug}(t)$	Augmented state vector (-)
$\mathbf{x_0}$	State vector equilibrium (-)
x_{co}	x-coordinate of control port/attachment wall corner (m)
x_R	Attachment length (m)
$X_{unforced}$	Unforced DC output (-)

x_{US}	Unattached side entrainment length (m)
y	Distance normal to jet centreline (m)
$y(t)$	System output (-)
$\bar{y}(t)$	Ensemble averaged output time series (-)
y_1	Distance from jet centreline to SL 1 at AS attachment point (m)
y_2	Distance from jet centreline to SL 2 at US attachment point (m)
y_{co}	y-coordinate of control port/attachment wall corner (m)
y_{DSL}	Value of y at DSL (m)
y_{SL}	Shear layer output (-)
$z(t)$	Integrator state (-)
$z'(t)$	Noisy measurement of z(t) (-)
$\hat{z}$	Integrator state estimate (-)

Abbreviations

ADC	Analogue-to-digital converter
AFC	Active flow control
AIAA	American Institute of Aeronautics and Astronautics
ALCR	Amplifier-loudspeaker-cavity response
AM	Amplitude modulation
AR	Aspect ratio
AS	Attached side
ATAG	Air Transport Action Group
BL	Boundary layer
BM	Burst modulation
CSL	Central streamline (jet centreline)
DAC	Digital-to-analogue converter
DSL	Dividing streamline
ETFE	Empirical transfer function estimate
EVR	Eddy viscosity ratio
FFT	Fast Fourier Transform
FPGA	Field programmable gate array
GM	Gain margin
HDL	Harry Diamond Laboratories
HP	High pressure
IATA	International Air Transport Association
IMC	Internal model control
JCE	Jet curvature equation
KF	Kalman filter
LEBU	Large eddy break-up
LP	Low pressure
LPA	Laminar proportional amplifier
LQR	Linear quadratic regulator
LQG	Linear quadratic gaussian
LTR	Loop transfer recovery
LUT	Look-up table
MIMO	Multi-input, multi-output
MC 1	Measurement connection 1
MC 2	Measurement connection 2
MLSM	Modified linear stochastic measurements
NACA	National Advisory Committee for Aeronautics
NMP	Non-minimum phase
OP	Operating point
PM	Phase margin
POD	Proper orthogonal decomposition
PT A	Pressure transducer A
PT A-x	$[x]$ mbar version of PT A
PT B	Pressure transducer B
RANS	Reynolds-averaged Navier Stokes
RMS	Root mean square
ROM	Reduced-order model
RSL	Reattaching streamline

SDBD	Single dielectric barrier discharge
SDC	Static deflection curve
SISO	Single-input, single-output
SL1	Streamline 1
SL2	Streamline 2
SPL	Sound pressure level
US	Unattached side
VG	Vortex generator
VGJ	Vortex generator jet
ZNMF	Zero-net mass flux

List of Figures

Chapter 1

Introduction

1.1 Motivation

In the past century, the aviation industry has evolved from serving an elite minority to become a mass transportation system. Global transport capacity has grown at around 5% per year over the last decade [88]. Prior to the COVID-19 global pandemic, similar growth was predicted until 2030 [88]. This would approximately equate to doubling the 2019 value. In December 2019, the International Air Transport Association (IATA) predicted a $16.5B profit for 2020 for the industry globally [53], which was revised to a $84B loss in late June 2020 [26] - the first loss since 2009. However, it seems likely that the industry will recover and global air traffic will increase from today's value. At the same time, various aerospace institutions and political bodies have set quantitative emissions goals to tackle the threat posed by climate change. The most cited are those from the IATA and the Air Transport Action Group (ATAG), which state that the overall CO_2 emissions of the global aviation fleet must be halved by 2050 relative to 2005 emission levels [88]. Another problem is the noise produced by aircraft, which is particularly problematic on take-off and landing; the negative effect on local residents has been well documented [20]. In 2011, the European Commission published their FlightPath 2050 target; a 65% reduction in perceived noise by 2050 relative to the levels in 2000 [42]. NASA's N + 3 targets, which are for 2030-2035, represent an even bigger challenge corresponding to a perceived noise level of ∼25% of the 2000 level [42].

If the passenger demand, emissions, and noise reduction targets are to be met, the aerospace industry must see drastic changes in the coming years.

Aside from new propulsion and energy storage technologies, flow control is a field with much potential to improve aircraft efficiency. Its uses include separation control, noise reduction, and tip leakage control [34]. One area for their application in aircraft is in gas turbines. The idealised cycle for a gas turbine is the Joule or Brayton Cycle. This is shown in the pressure-volume and temperature-entropy plots in Figures 1.1a and 1.1b, along with the schematic for a gas turbine in Figure 1.1c. With reference to Figure 1.1:

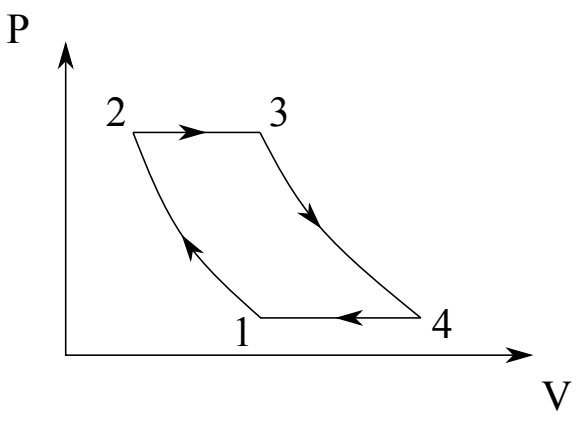

(a) Pressure against volume

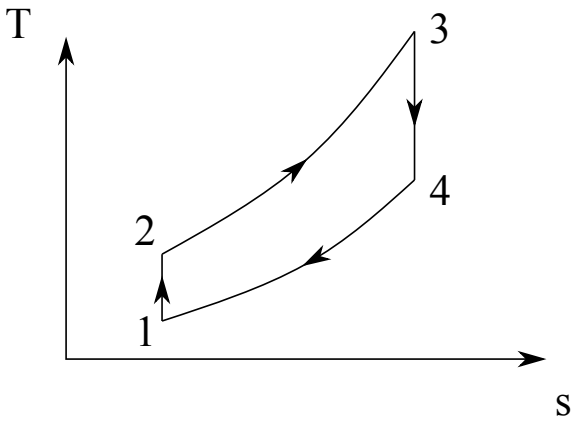

(b) Temperature against entropy

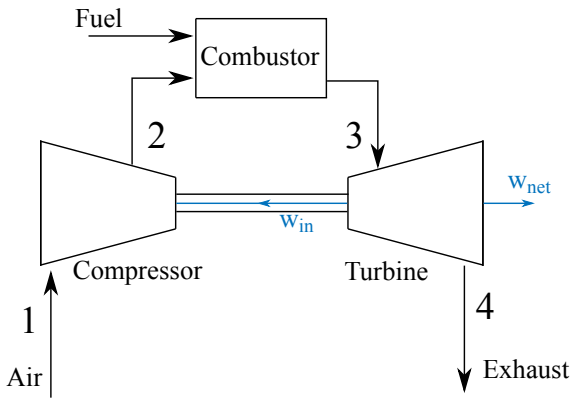

(c) Gas turbine schematic

Figure 1.1: The Joule or Brayton Cycle

- $1 \rightarrow 2$: air is drawn into the compressor where isentropic, adiabatic compression occurs, which increases the pressure and temperature;

- $2 \rightarrow 3$: fuel is burned to cause reversible, isobaric heating of the air in the combustor, such that the temperature increases but the pressure remains constant;
- $3 \rightarrow 4$: isentropic, adiabatic expansion occurs, where work is done by the fluid on the turbine, some of which is transferred through the shaft to drive the compressor, so that the temperature and pressure reduce;
- $4 \rightarrow 1$: the exhaust gases are ejected, representing reversible rejection of heat at constant pressure, reducing the temperature.

It is possible to derive the thermodynamic efficiency of the Joule Cycle in terms of the pressure ratio, which is given by

$$\eta_{\text{th}} = 1 - \frac{1}{\frac{p_{2,3}}{p_{1,4}}^{\frac{\gamma_{\text{sh}}-1}{\gamma_{\text{sh}}}}}, \tag{1.1}$$

where γ_{sh} is the ratio of the specific heats.

1.1.1 Unmodelled losses

There are losses in gas turbines which are unmodelled by the idealised Joule cycle. The most significant of these are discussed here. A Rolls Royce Trent 1000 gas turbine is shown in Fig. 1.2 for reference.

1. **Secondary air system** - Cooling flow is required in order to manage the temperature of the turbine, which is worked on by the hot gases issuing from the combustor. The cooling flow is supplied by the secondary air system, which also provides sealing flow that prevents hot gases from entering turbine disc cavities and bearings, as well as controlling the loads on the bearings, and pressurising the cabin [62]. The flow must be taken from the compressor, which reduces its effective pressure ratio and contributes to the losses.
2. **Tip leakage** - Tip leakage is a secondary flow where gas leaks through the gap between the blade tips and the casing in the rotor blades, driven by the pressure difference between the suction and pressure sides of the blades. This causes vortices

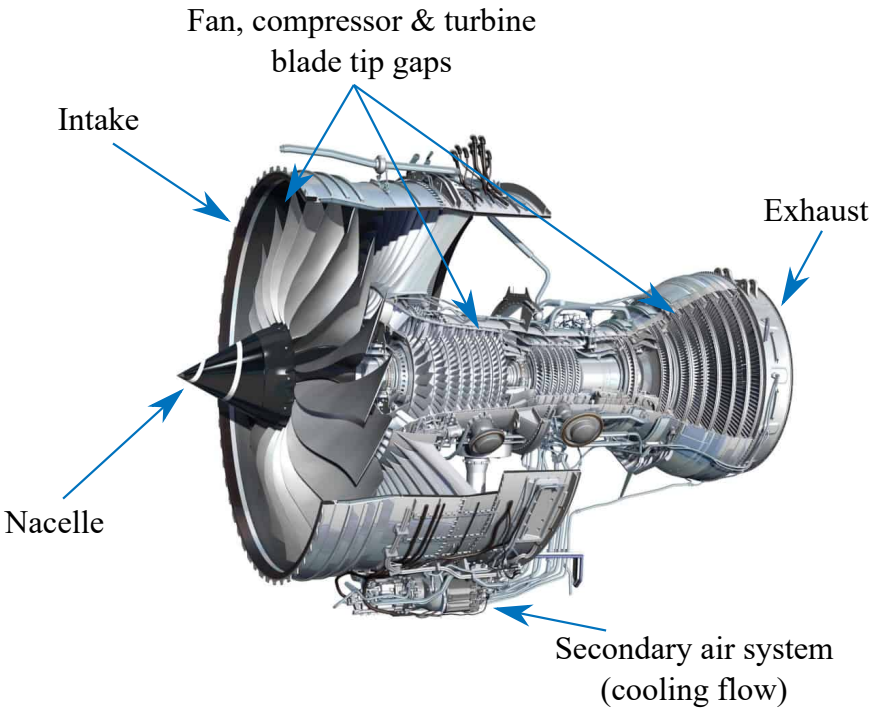

Figure 1.2: Rolls Royce Trent 1000 gas turbine

to roll-up and shed from the blade tips, as shown in Fig. 1.3 [109]. Tip leakage has been shown to make up at least one third of overall stage losses in turbines [10]. The tip gap has to be designed with some margin to avoid contact between the blade tips and the casing in the fan, compressor, and turbine due to vibrations, gust loads, and manoeuvering loads. Turbine blades expand dynamically under high thermal and centrifugal transients [63], increasing the required margin.

3. **Separation** - Separation from a surface (stalling) is where the flow becomes detached due to a lack of forward momentum close to the wall, and usually occurs when the flow is passing through an adverse pressure gradient. A stalled aerofoil has a smaller absolute pressure minimum near the leading edge of its suction surface, and a greatly reduced pressure recovery towards the trailing edge. These two effects result in a loss of lift and an increase in drag respectively [1]. Separation occurs when the angle of attack of an aerofoil becomes too large. Virtually every aerofoil on an aircraft, including the blades in a gas turbine, could be susceptible to separation at some point in a flight cycle.

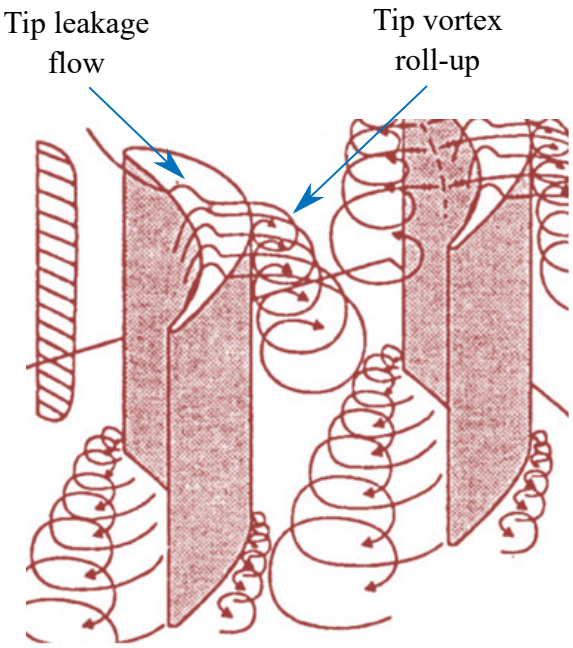

Figure 1.3: Blade tip vortices resulting from tip leakage, from Sjolander [109].

a **Compressor stall** - in the compressor, stage loading is limited due to the risk of separation [65]. If loading could be increased, the pressure ratio of the compressor would increase, which would improve gas turbine thermodynamic efficiency (see (1.1)). Tip leakage flow is the impetus for some kinds of compressor stall [66].

b **Intake separation** - The intake is made up of the engine casing that protrudes beyond the fan, called the cowling, and its leading edge is called the cowl lip [7]. Its purpose is to direct the flow at the fan, which is required because the free stream will not in general be aligned with the gas turbine axis, e.g. during manoeuvres or take-off. This must be achieved in a manner that maximises recovery of the free stream total pressure and minimises the distortion of the flow which enters the fan - a highly distorted flow causes local extrema in the velocity of flow entering the fan and necessitates a modest compressor stage loading to avoid compressor stall. Separation at the intake threatens both of these goals. The optimal design depends on the flight condition - at high angles of attack and low speeds, e.g. during take-off, a relatively thick cowl lip best avoids separation, whereas during cruise at comparatively low angles of attack and high speeds, a thinner cowl lip minimises drag [111]. Since separation at the

intake must be kept to a minimum to avoid compressor stall, a conservatively thick cowl lip is typically chosen on subsonic aircraft, resulting in relatively poor cruise performance [111].

1.1.2 Flow control solutions

Tip leakage control Several passive control methods to reduce turbine tip leakage have been applied, such as squealer tips [10], winglets, and shrouded aerofoils [22]. However, winglets and shrouds must be cooled and add weight [125]. Active control solutions have also been tested, such as blowing from rotor tips. Film cooling is often already used on high pressure (HP) turbine blade tips, which could be directed to reduce tip leakage losses. For example, Volino [125] injected flow from holes inclined towards the pressure side on HP turbine blades in a linear cascade. He found that on flat-tipped turbine blades, the total pressure drop could be reduced by around 20% with a blowing ratio of 1.5, using 0.4% of the main flow through the passage. The downside of active techniques that involve blowing is that the air must be taken from the compressor secondary air system, which comes at a fuel cost. In the case of Volino's 20% reduction in pressure loss, for example, the net improvement in fuel consumption is likely to be rather small, if positive at all.

Separation control A proven way to prevent separation is to inject air outwards from within the aerofoil to energise the flow [104, 89]. This works by promoting mixing between the high-momentum fluid in the free stream with the low-momentum fluid close to the wall when the direction of the injected fluid is normal to the aerofoil [85], and adds momentum directly when it is tangential [124]. Unsteady flow injection, injecting parcels of air at regular intervals, is more effective than steady blowing [103, 108] and uses less air. High injection frequencies are required, typically tens, hundreds, or thousands of times per second [106, 108]. Studies have shown that the timing of injection at many points on the aerofoil is key to maximising its effectiveness [119, 13].

1.2 Fluidics: the solution

The challenges described in section 1.1.1 limit the performance of gas turbines. Examples of how flow control could be used to tackle these problems were given above in section 1.1.2. The implementation of many of the flow control strategies outlined above requires a device to inject fluid into a flow to achieve the desired effect. The requirements on a flow control device can be summarised as the need to inject air with precise timing, at bandwidths on the order of kHz, with sufficient momentum to be effective, while satisfying the strict reliability criteria of such safety-critical applications. Fluidic devices are a family of flow control actuators that have the potential to fulfil these specifications, and are the subject of this thesis.

1.3 Thesis content

Chapter 2 reviews the available flow control actuators and focuses in on fluidic devices. Examples of their application are given, along with a review of the control theory concepts that have been employed in chapter 5. The chapter is concluded with a review of the use of feedback control in flow control applications. In chapter 3, an analytical model is developed for an acoustically-excited jet attached to an offset and inclined wall. The model is validated with experimental data in chapter 4, and its sensitivity to several parameters is investigated. Chapter 5 demonstrates an active means of controlling a fluidic device in the form a piezo-fluidic amplifier, whose geometry is similar to the attached jet modelled in chapter 3. Chapter 6 explores the response of jet shear layers to amplitude-modulated perturbations from a signal processing perspective. Finally, conclusions are drawn in chapter 7.

Chapter 5 has been published in the AIAA Journal [83], and was previously presented at the AIAA Flow Control Conference in 2018 [82]. Chapters 3 and 4 have been formed into a paper in preparation for submission to the Journal of Fluid Mechanics. A paper containing work on fluidic oscillators was presented at the AIAA Aviation Forum in 2019 [84], although the corresponding chapter of this thesis was removed for brevity. The fate of chapter 6 is yet to be decided.

Chapter 2

Flow control background & literature review

2.1 Introduction

This chapter provides a background on flow control strategies and the actuators required to implement them. The focus is placed on active control methods, described in section 2.3. Fluidic devices are missing from the actuator review in section 2.5 because they are sufficiently important to have a section (2.6) dedicated to them. An introduction to control theory is offered in section 2.7, and the chapter is concluded in section 2.8 with examples of closed-loop flow control from the literature.

2.2 Passive flow control

Experimental studies in flow control have largely been used to try to understand flow physics better. Passive techniques, such as the winglets, squealers, and vortex generators used in [101, 117], have the benefits of being simple, inexpensive, and reliable. On the other hand, since they cannot be 'switched off', they tend to result in a form drag penalty rather than a benefit when not in the operating regime where they are required. For instance, there are a great many drag reduction studies involving passive techniques that attempt to reduce the amount of skin friction drag more than the incurred increase in form drag [34]. Large eddy

Figure 2.1: Vortex generators

break-up devices (LEBUs) and riblets are common examples of passive technqiues. These have little in the way of a theoretical basis for their design, such that optimising their shape can be tedious, time-consuming, and often with a meagre (if positive at all) overall reduction in drag [34]. A more successful example of a passive technique is a vortex generator (VG). An array of VGs is shown in Fig. 2.1. VGs are used on aerofoils to encourage transition to a turbulent boundary layer in order to avoid laminar flow separation and its associated penalties on lift and drag. Turbulent boundary layers are less susceptible to separation because of the higher momentum close to the wall in the velocity profile [102, p. 46]. VGs, as with LEBUs and riblets, introduce a parasitic drag, motivating research into active flow control techniques.

2.3 Active flow control

Active flow control (AFC) is a methodology where energy is introduced to a system in order to bring about a desired change in flow conditions. A typical manifestation is the sucking or blowing of air into or from an aerofoil, which might require a slot or hole rather than a protrusion. This tends to avoid the parasitic form drag introduced by passive techniques. However, by definition an energy input is required, which may amount to or exceed the energy saved by adopting the method. Reviews of the subject have been provided by Brunton & Noack [12] and Gad-el-Hak [34]. The basic techniques are shown in Fig. 2.2.

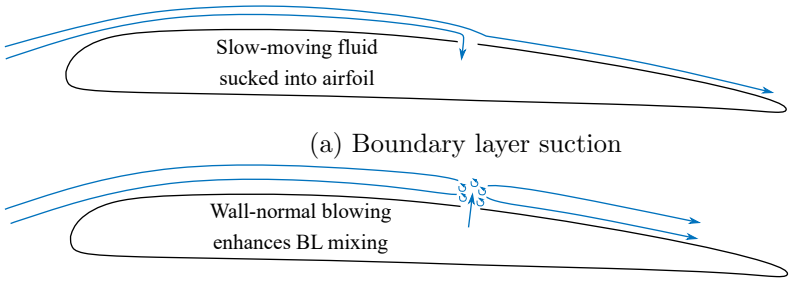

(a) Boundary layer suction

(b) Wall-normal injection

Figure 2.2: Illustration of boundary layer suction and injection techniques on aerofoil

Boundary layer suction The goal of boundary layer suction is to remove the laminar fluid from a boundary layer at or before the point of separation on the suction side of an aerofoil [36] (Fig. 2.2a). Its first mention in the literature dates back to 1943, when Stalker filed several patents [114, 115, 116] relating to suction slots on compressor stator & rotor blades as well as the casing, and the reuse of the air removed by re-injection to energise a boundary layer earlier in the compressor. The goal was to allow larger angles of attack on compressor blades and/or to improve the stall margin. Kerrebrock et al. [59] used boundary layer suction to control shock-boundary layer interactions in a transonic compressor, improving the stage pressure rise.

Boundary layer injection Injecting flow into a boundary layer in order to energise it and prevent separation is one of the most widely-researched classes of AFC. Injecting the flow tangentially, i.e. parallel to the flow, adds streamwise momentum directly, and has been demonstrated to be effective at reattaching a separated flow [124] and controlling shock-boundary layer interactions [28, 129]. Alternatively, wall-normal injection aims to enhance the mixing in the boundary layer, exchanging high-momentum fluid from the free stream with low-momentum fluid close to the wall [35] (Fig. 2.2b).

Vortex generator jets A vortex generator jet (VGJ) can be used to replace a passive vortex generator in order to prevent laminar separation. First introduced by Wallis [127], a VGJ is a jet that is injected into a boundary layer from an aerofoil. Streamwise vortices are created in the boundary that increase mixing in order to energise the boundary layer [57]. The holes are skewed relative to the flow and pitched relative to the aerofoil surface, which

is most effective for vortex production [55]. They are typically positioned, like a passive vortex generator, close to the leading edge where laminar separation is expected to occur at high angles of attack [127]. The advantage of a VGJ over passive VG is that the VGJ can be switched off when not required, while the form drag of the VG is experienced at all times. A VGJ is a variant of the more general class of boundary layer injection techniques and the mechanism to improve mixing is the production of an particular type of vortex.

2.4 Unsteady active flow control

In the above examples, if continuous blowing (or suction) is used, the energy input required for the flow control scheme either precludes its use or represents a significant cost. This has led researchers to consider the possibility of making more informed use of active methods by modulating the flow. In its simplest form, this could be switching the actuation on and off as required at different times in a flight cycle. For example, considerably less turbine cooling is required during cruise than for take-off, so that switching off some fraction of the cooling flow after take-off could make a significant improvement to specific fuel consumption. Another example is modulating the flow injected into a boundary layer. It is well known [103, 104, 85, 17] that pulsed flow injection greatly reduces the mass flow required to prevent separation or reattach a separated flow.

The nondimensional parameters commonly used to describe flow injection are listed here. First, nondimensional frequency, defined by

$$F^+ = \frac{fL}{U}, \tag{2.1}$$

where f is the frequency of the perturbation, L is the length of separated aerofoil ($\leq$ chord length), and U is the free stream velocity. This is the same as Strouhal number. Next, the blowing ratio is given by

$$M = \frac{\rho_i U_i}{\rho_m U_m}, \tag{2.2}$$

where i refers to injected flow conditions and m are the free stream conditions. Finally, the momentum ratio is given by

$$C_\mu = \frac{J_i}{\frac{1}{2}\rho U^2 c}, \tag{2.3}$$

where J_i is the momentum flux per unit length of the injected jet, ρ and U are the density and mean velocity of the free stream, and c is the chord length.

Bons et al. [9] investigated both steady and pulsed blowing into the boundary layer of a LP turbine blade in a linear cascade with VGJs and reported that a duty cycle of only 1% at $F^+ = 0.31$ had the same reduction in the wake loss coefficient as constant blowing. The maximum blowing ratio in each pulse was 2.

Seifert et al. [103] studied the effect of blowing on a trailing edge flap as a means of improving the lift coefficient, C_L. Constant blowing from a slot at the hinge between the flap and aerofoil increased the maximum C_L by around 60% and the lift-to-drag ratio was more than doubled in some ranges of angle of attack of the flap. However, this required a momentum coefficient of $C_\mu = 0.1$. An oscillatory (blowing and sucking) jet of $\langle c_\mu \rangle = 0.016$ was superimposed with a weaker constant blowing of $C_\mu = 0.001$, achieving very similar results to those of the strong constant jet with $C_\mu = 0.1$, but requiring only 14% of the momentum coefficient. The explanation for the improvement in performance was the complete reattachment of the flow to the flap.

Raman et al. [92] used flow injection at the leading and trailing edge of a cavity in order to suppress cavity tone resonances. Trailing edge injection was ineffective, and steady leading edge blowing produced only a 1 dB reduction in sound pressure level (SPL) using 0.12% of the main jet mass flow. However, when the leading edge injection of the same mass flow rate was modulated at a frequency similar to that of the dominant vortex shedding (which caused the noise production), noise reductions of 10 dB were observed. Schlieren photographs illustrated the effectiveness of the oscillatory AFC at suppressing the dominant vortices (Fig. 2.3).

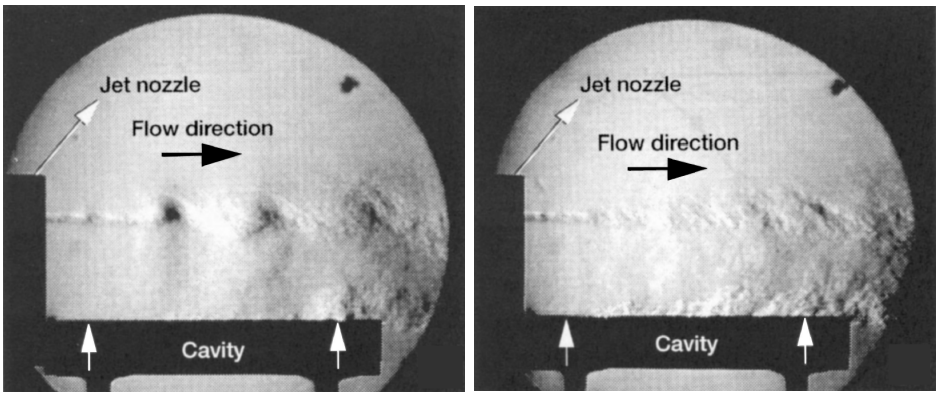

(a) Unexcited (b) Excited

Figure 2.3: Schlieren photography: flow injection suppressing cavity tone resonance, taken from Raman [92]

2.5 Flow control actuators

A flow control actuator is a device used to implement an AFC scheme, either steady or unsteady. It must meet requirements of control authority, bandwidth (in the case of unsteady flow control), efficiency, and robustness [34]. To illustrate the bandwidth requirements further, consider a wall-normal separation control scheme (Fig. 2.2b), where the intention is to modulate the flow in order to reduce the mass flow requirements as much as possible. The frequency of excitation required is relatively high, with $F^+ = 1$ commonly reported as the most effective frequency to prevent separation [17, 85, 104, 105], and $F^+ = 3 - 4$ for reattachment [104]. If this scheme were applied to a commercial aircraft wing in cruise, $U \sim O\,(100)$ ms^{-1}, $L \sim O\,(1)$ m, giving $f \sim O\,(100)$ Hz. The blade passing frequency inside a gas turbine is around 10 kHz [79], so that unsteady excitation inside the gas turbine, for example to prevent turbine tip leakage [121], would require excitation frequencies on $O(10)$ kHz.

The available actuators are reviewed by Cattafesta & Sheplak [15], and fall into the categories of plasma, fluidic, or moving object.

2.5.1 Plasma actuators

Plasma actuators work by applying a large potential difference across a pair of asymmetric electrodes separated by a dielectric material. The voltages required typically vary between 1 and 30 kV [15]. The result is that the air adjacent to one of the electrodes is ionised and driven by the electric field, causing the so-called 'electric wind' [78]. Figure 2.4 shows an example of such a device known as a single dielectric barrier discharge actuator (SDBD). SDBDs are popular because they have no moving parts and a high bandwidth. However,

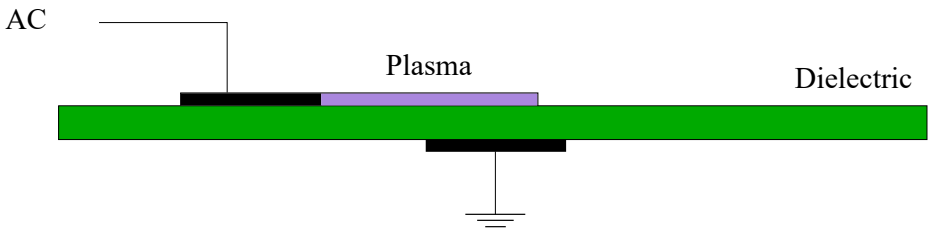

Figure 2.4: SDBD, adapted from [15].

they are limited by their control authority, with reports of the maximum possible electric wind velocity at around 8 ms^{-1} [32]. Additionally, they require a large electrical energy input, which could make them ineffectual for use in aerospace applications where the goal is to reduce fuel consumption.

2.5.2 Moving object actuators

The most common form of moving object actuator is a piezoelectric composite flap [15]. This works as a cantilever beam, so that when an AC signal is applied, the cantilever vibrates. The displacement of the tip of the cantilever produces perturbations which interact with the flow. This type of actuator was used for the first time by Wiltse & Glezer [131, 132] to manipulate a square jet, and to enhance mixing in a free shear flow. Reports of the gain-bandwidth of such devices range from 1 - 2 kHz for displacements O(10 - 100 μm) [58], and O(100 Hz) for displacements O(1 mm) [15]. These devices lack the robustness of a no-moving-parts actuator, and thus make them unattractive for use in safety-critical applications such as in the turbomachinery of commercial aircraft.

2.5.3 Zero-net mass flux devices

Zero-net mass flux (ZNMF) actuators are in principle where fluid is periodically ejected and ingested across an orifice, such that the net mass flux is zero [15]. The resulting train of vortices interact and form a synthetic jet, so that ZNMF actuators are also known as synthetic jet actuators [37]. Synthetic jet actuators were developed by Smith & Glezer [110]. The synthetic jet is formed from the working fluid of the system so that an external fluid source is not required. A typical realisation of a ZNMF actuator is a piezoelectric device, as shown in Figure 2.5. The membrane at the base of the device oscillates at the frequency of

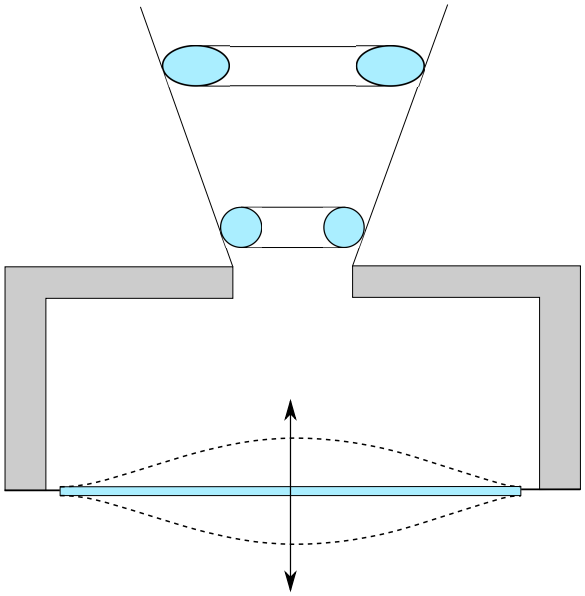

Figure 2.5: Piezoelectric ZNMF actuator, adapted from [15].

the AC voltage applied, which drives fluid into and out of the chamber. Piezoelectric devices typically have a resonant frequency in the kHz range, can achieve a maximum velocity up to 100 ms^{-1}, and have low power requirements as well as robustness [15]. Another style of ZNMF actuator is a electrodynamic device, where the diaphragm at the base of the device is instead driven by electrodynamic transduction. These actuators have a large displacement capability but are more cumbersome due to the weight of the magnet and the requirement to dissipate heat generated in the resistive coil [15].

2.5.4 Pulsed jet actuators

Pulsed jets, unlike steady jets, contain both AC and DC velocity components, and therefore have a net mass flux. They can be achieved by using a high-speed rotating siren valve [130] or a fast-acting solenoid valve [9]. A limitation of the pulsed jet is that the velocity signal it can produce can only be a variable duty-cycle square wave, as well as the requirement for an external flow source [15]. Combustion-driven pulsed jet actuators work by the ignition of a gaseous fuel and an oxidiser in a small combustion chamber to eject fluid out of an orifice [23]. In [23], frequencies greater than 150 Hz are achieved at pressure ratios of 5 bar, with the resulting jets showing penetration into a cross-flow with velocities up to Mach $M_n = 0.7$. These devices have a high control authority in terms of the ejection velocities achieved, but are limited to low bandwidths because of the finite time required for the combustion cycle [15]. Fluidic oscillators can also generate a pulsed jet, and are discussed in more detail in section 2.6.

2.6 Fluidic devices

2.6.1 Introduction

The field of fluidics originates from the Harry Diamond Laboratories (HDL) in 1959 [56]. In its early years, research efforts were primarily aimed at designing and understanding devices that could be used as logical elements in robust computing systems. Since then, several applications have benefited from the use of fluidic devices such as medicine, factory automation, and the aerospace industry [56]. Their design is based on the Coandă effect: the tendency of a jet of fluid to attach to an adjacent wall [21]. These devices are robust because they contain no moving parts [60] and can therefore operate in harsh environments unsuitable for mechanical components.

Coandă effect The Coandă effect is what gives all wall-attachment devices their stability. Figure 2.6 shows a nozzle with a sudden expansion, leading to a diverging section. Fluidic devices typically consist of variations of this basic geometry, and the Coandă effect can be explained by its analysis. When the nozzle is supplied with a pressurised fluid, flow issues

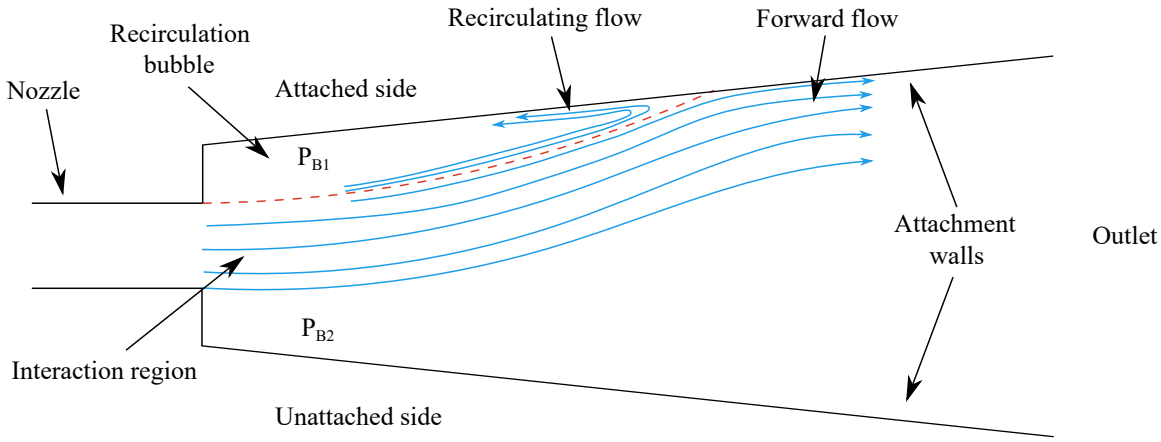

Figure 2.6: Basic fluidic device geometry: nozzle with sudden expansion to diverging section

into the interaction region. Mass flow is entrained into the jet as it leaves the nozzle, which causes it to spread out. The entrainment of ambient fluid into the jet causes a pressure reduction because the space is confined and the entrainment must be supplied from the outlet. The pressure on either side of the jet will not be perfectly equal, either due to a manufacturing bias or a difference in the random statistical variations in entrainment. This provides a small pressure difference across the jet, which pushes it towards the side with lower pressure, thus further confining that side and reducing the ease with which the entrainment flow is supplied, while on the other side the entrainment flow is supplied more readily from the outlet. This encourages the pressure difference, so that it is a positive feedback process. Eventually the jet 'attaches' to the wall on one side, which means that it strikes the wall and splits. The upstream flow is recirculated into the fully-confined space between the jet and the wall (the recirculation bubble) in order to supply the entrainment flow, and the downstream flow continues to the outlet on the attached side (forward flow). This is the steady state shown in Fig. 2.6. The recirculating flow provides a negative feedback mechanism that acts to increase the pressure in the recirculation bubble and push the jet off the wall. This balances the effect of the entrainment flow, which is to suck the jet towards the wall. In the steady state, these two flows are equal and the jet remains stably attached to one side with a constant pressure difference across it which supplies the centripetal force required for the jet to maintain a curved shaped. This steady state is

described by Euler's streamline curvature theorem [2], given by

$$\frac{\mathrm{d}P}{\mathrm{d}y} = \frac{\rho u^2}{R}, \tag{2.4}$$

which integrates to

$$\Delta P = \frac{J}{R}, \tag{2.5}$$

where $\Delta P = P_{\mathrm{B2}} - P_{\mathrm{B1}}$, J is the jet momentum flux per unit depth, and R is the radius of jet attachment. This equation implicitly assumes that the jet curvature is constant with streamwise distance (constant R), and therefore that ΔP is also constant along the jet up to the attachment point.

A fluidic diverter is shown in Fig. 2.7. It can be seen that control ports and a splitter

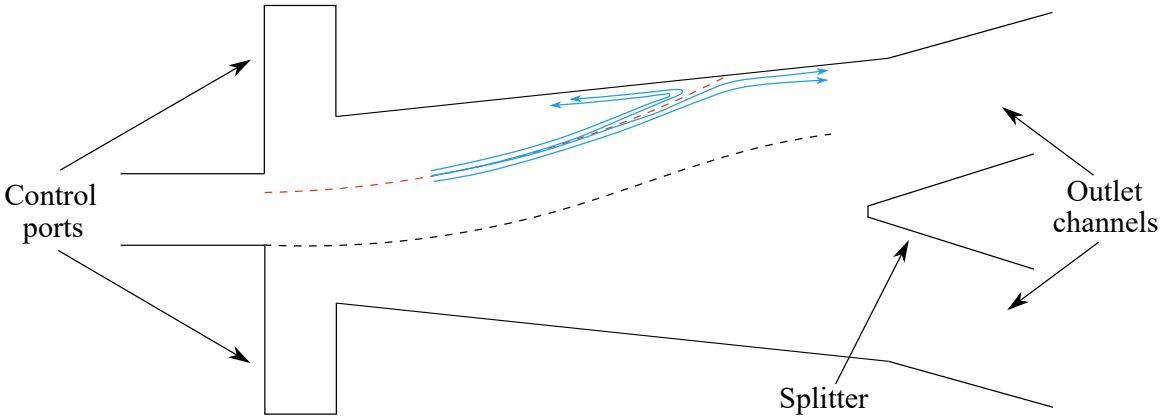

Figure 2.7: Fluidic diverter

have been added to the basic geometry in Fig. 2.6. The jet attaches to one of the two attachment walls as described above, and the Coandă effect provides stability. The splitter has the effect of dividing the flow so that it exits via one of two outlets, making it a bistable device. Traditionally, such devices are switched between their two stable states by transverse injection or extraction of flow at control ports adjacent to where the jet emerges into the device or by providing a pressure difference across the control ports that is large enough to overcome the Coandă effect [56]. When this happens, the flow becomes unattached and is driven over to the other side of the device before reattaching to the opposite wall, thus transitioning between the two stable states [25]. If mass flows are used to control the device,

typically only 10 - 20% of the main jet flow is required to overcome the Coandă effect and switch the jet [113].

Fluidic switching devices fall into two categories: those with a feedback mechanism, such as in [123, 93, 56, 47, 48, 91, 112, 84], and those controlled using active techniques, such as in [131, 77, 43, 46, 44, 76, 74, 75, 72, 73].

2.6.2 Passively-controlled fluidic devices - oscillators

Fluidic oscillators represent a passive means of controlling a fluidic device. They are a variant of the fluidic diverter, and produce an oscillating output when supplied with a pressurised fluid by their design rather than by an external input. Such devices have been used in several industrial applications such as windscreen washer fluid nozzles [118], flow rate measurement devices [128], and flow control applications including cavity tone suppression [92], mixing enhancement [123, 93], and boundary layer separation control [16]. Progress in fluidic oscillator development has been reviewed by Gregory [45] and Raghu [91].

In the most common design, known as a 'relaxation fluidic oscillator' [45], feedback channels connect the control ports to the outlet channels, as in Fig. 2.8, which shows the two flow paths that the device oscillates between. The working of the device is as follows, with reference to Figure 2.8: flow starts to travel through Channel A and becomes attached to the left-side wall. Some flow enters Feedback Path A and the resulting pressure pulse that reaches the top of the feedback path provides a pressure difference across the jet in the interaction region, deflecting the jet towards Channel B. Once a pressure difference that is sufficient to overcome the Coandă effect has built up across the jet in the interaction region, the jet reattaches to Channel B, as in Figure 2.8b. The same process then happens in reverse, so that the flow oscillates between Outlets A and B. The oscillation frequency has been shown to be related to the inlet-to-outlet pressure ratio and the geometry of the device, notably the splitter distance, d_s (Fig. 2.8a), and the feedback path lengths [91].

Another style of fluidic oscillator exists where the control ports are connected together

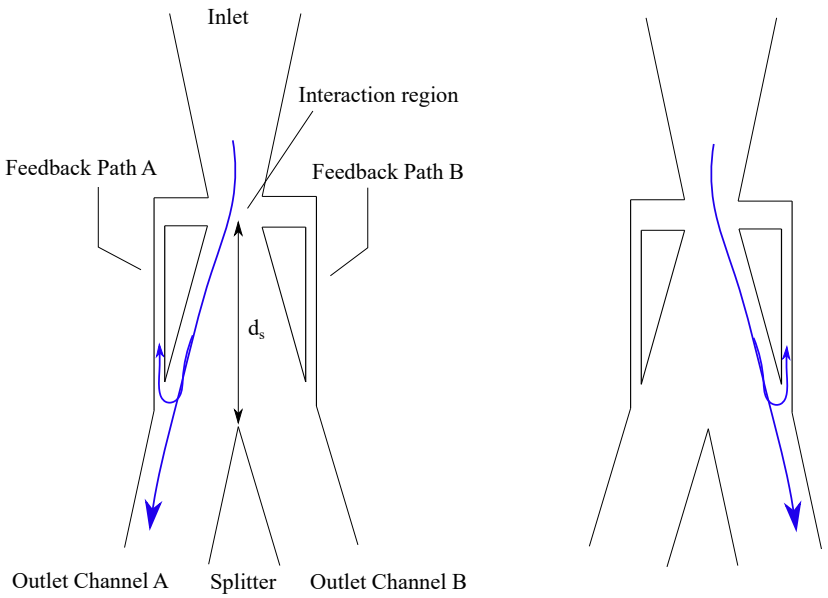

(a) Flow path 1 (b) Flow path 2

Figure 2.8: Fluidic oscillator in its two flow paths.

rather than to their corresponding outlets. This device was first suggested by Spyropoulos in 1964 [112], and is shown in Fig. 2.9. Spyropoulos investigated the operation of this de-

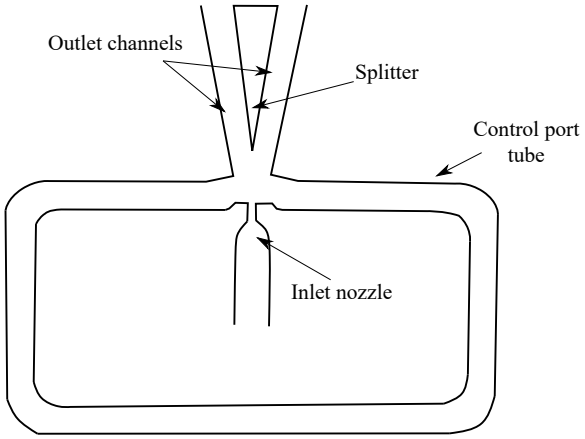

Figure 2.9: 'Sonic oscillator', adapted from [112].

sign, which he named a 'sonic oscillator', by varying the pressure ratio and control port tube (the tube connecting the control ports together) length and diameter. He found a linear relationship between the device pressure ratio and the oscillating frequency, and determined that the mechanism of operation of the device was related to the transmission of pressure and expansion waves through the control port tube. A decade later, Viets [123] developed Syproulos's design to reduce the pressure losses; removing the splitter and shortening the

nozzle. Viets's goal was to use the device as a means of increasing the mixing in the outlet of a thrust-augmenting ejector, and named the device a flip-flop jet nozzle. Oscillations of up to 100 Hz at flow velocities up to Mach $M_n = 0.5$ were achieved.

Raman et al. [93] studied a flip-flop jet nozzle like that in Viets [123]. Raman et al. incorrectly credited Viets with the wave propagation mechanism theory, which first came from Spyropoulos [112]. Raman et al. [93] suggested that part of the mechanism must be related to mass flow through the control port tube in order for the pressures to be equalised, and studied the effect of nozzle pressure ratio and control port tube length & volume independently on the oscillation frequency. It was found that the frequency increased with nozzle pressure ratio and control port tube cross sectional area, but decreased with control port tube length. It was suggested that the dependence on control port tube length was a result of the additional wave propagation time, while the increased frequency with cross sectional area implies a reducing resistance to the mass flow in the tube which equalises the pressure. It was also found that the output velocity of the device was largely independent of control port tube length and volume at a given pressure ratio.

Raghu [90] developed a microfluidic oscillator that had no feedback paths and relied on the interaction of two jets inside a specially designed chamber. Gregory [47, 48] also studied the device, shown in Fig. 2.10. This device produces a sweeping output rather than the

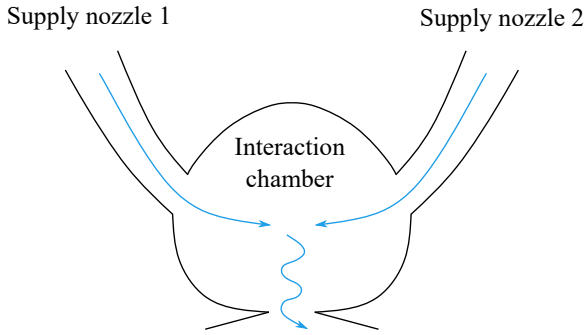

Figure 2.10: Microfluidic or jet interaction oscillator, developed by Raghu [90].

square wave-like output of the feedback path-style devices. Gregory [48] reported output oscillation frequencies up to 22 kHz, albeit with low flow rates of $O(1$ l/min). A linear

relationship between the flow rate and the output oscillation frequency was demonstrated.

One limitation of fluidic oscillators in terms of their use as flow control actuators is that their oscillating frequency is related to the flow rate through them. This reduces their degree of controllability compared with an actively controlled fluidic device. However, if it could be possible to lock the phase of their output onto a reference signal, such as the vortex generation signal on a stalled aerofoil or the blade passing frequency in a gas turbine, they could represent a simpler solution to problems that require unsteady flow injection than a fully actively controlled device. In a numerical study, Gokoglu et al. [38] showed that plasma devices positioned prudently in each feedback path of a fluidic oscillator may have sufficient authority to alter the operating frequency of the device. This has not yet been demonstrated experimentally, but represents a worthy research challenge. However, before this problem can be tackled, the operating mechanism(s) of fluidic oscillators must be understood more completely.

2.6.3 Actively-controlled fluidic devices

2.6.3.1 Non-acoustic control

The task of decoupling the output oscillation frequency from the flow rate was first tackled by Milelr [77], who designed and built an electronic-to-fluidic transducer. At the control ports the design used piezoelectric bender actuators operated at different frequencies in order to harness frequency beating. This meant that the output pressure was a function of the difference between the actuator frequencies, so that a DC signal proportional to this difference frequency could be produced. The resulting acoustic signal reached frequencies of up to 1 kHz, but at pressures of only 100 Pa.

Fluidic diverters are traditionally switched with a control mass flow or pressure at each of the control ports. A comparatively small flow or pressure is required relative to the main flow or total pressure. Such devices were studied by Culley [25], who used solenoid valves to control the pressures at the control ports of several geometries of diverter and achieved

oscillating frequencies of up to 312 Hz. However, while the introduction of solenoid valves at the control ports was a sensible means of studying the fluidic diverter, it introduces moving parts which nullifies the reliability of the device. As commented by Culley in his conclusion, other means of applying a disturbance at the control ports would be more suited for most applications.

Gregory [43, 46] used a piezoelectric bender in a fluidic amplifier to produce an oscillating output. The piezoelectric bender was placed down the centreline of the device, and the flow oscillated between the outlets at the same frequency as the perturbations of the tip of the bender. The piezoelectric bender used had a resonant frequency of 121 Hz, but the device was able to sustain output oscillations over frequencies from DC up to 250 Hz which were nearly independent of flow rate. At a pressure ratio of 1.14, output oscillations of up to 1.2 kHz were achieved. This study was able to decouple the output oscillation frequency from the flow rate, and, critically, at pressure ratios that may be useful in turbomachinery applications. However, the piezoelectric bender lacked robustness and was likely susceptible to high-cycle fatigue.

Another approach for active control is to use a plasma actuator. In Gregory [44], SDBDs were placed on the walls in the control ports of a fluidic diverter so that the electric wind blew toward the jet, as shown in Figure 2.11. The device works as follows, with reference to Figure 2.11: when initially attached to Wall A, there is a separation bubble for at the wall for some of its length because of the discontinuity in the wall due to the control ports and the step change from contraction to expansion. When the SDBD in Control port A is operated, the induced electric wind adds momentum to the jet and causes the separation bubble to grow in size. Once the bubble has extended along the entire length of the wall A, the jet separates and the momentum of the electric wind in the wall-normal direction moves the jet across to attach to Wall B. The study focused on minimising the duration of an individual switch rather than repeated switching in an oscillatory manner. Results indicate that the effect of increasing the jet velocity is to increase both the switching time and the standard deviation in switching time for a given power level applied to the plasma

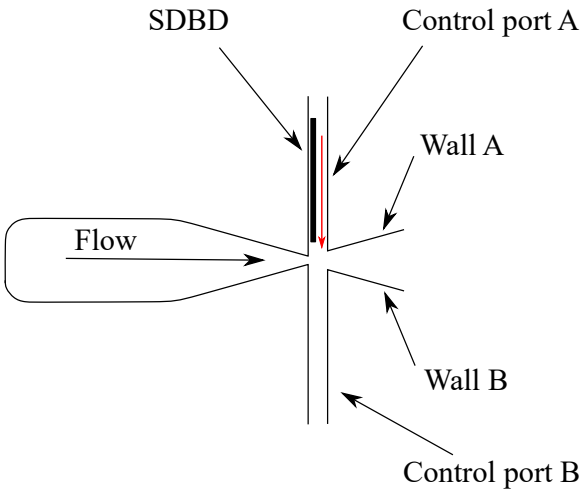

Figure 2.11: Plasma-fluidic amplifier, adapted from [44]. Red arrow shows direction of electric wind.

actuator. For example, a jet at 5 ms^{-1} was switched in 19 $\pm$ 1.5 ms with 400 mW of power applied to the SDBD, whereas at 8 ms^{-1}, the switching time is 43 $\pm$ 26 ms for the same power input. If operated in an oscillatory manner with SDBDs in both control ports, the switching frequency ranged from 8 Hz when using high flow velocities and low plasma powers to 26 Hz for low velocities and high powers.

A synthetic jet actuator was used by Martin et al. [76] to control a fluidic diverter. The actuator was designed to have a resonance frequency matching the resonance of the cavity, which acted like a Helmholtz resonator. When the synthetic jet velocities were measured over different actuator frequencies, two resonance peaks of similar amplitude were discovered at 630 and 1000 Hz respectively. However, the device could only be operated at the 630 Hz peak, implying that the switching mechanism was not dictated solely by the momentum of the synthetic jet. A parametric study revealed that there were lower limits to both the amplitude and number of cycles of the excitation in order that the device switched, and that these limits were a function of the Reynolds number of the flow. The device was operated in an oscillatory manner by amplitude modulating the excitation signals of the synthetic jets with a square waves out of phase with one another. The frequency of oscillation was varied from 5 to 25 Hz, with hot wire measurements in the channels indicating a velocity variation in the form of a sine wave. The amplitude of the variation decreased with frequency, which

was explained by the fact that increasing the frequency of the modulating square waves decreased the number of cycles per switch, such that the lower limit on excitation cycles was eventually reached.

2.6.3.2 Acoustic control

The use of an acoustic source to control a fluidic device is discussed in more detail because it is relevant to all of the following chapters. This approach originated in HDL for laminar proportional amplifiers (LPAs) [56], with more recent work by Mair et al. [73, 75, 72]. The switching mechanism is influenced both by local shear layer behaviour and bulk jet dynamics.

Shear layer excitation In order to understand the mechanism by which an acoustic source can control a fluidic device, it is necessary to consider the more fundamental case of a free jet. When a free, plane jet is unexcited, it emerges from its orifice and shear layers form on either side (Fig. 2.12). During the potential core region of the jet, vortices

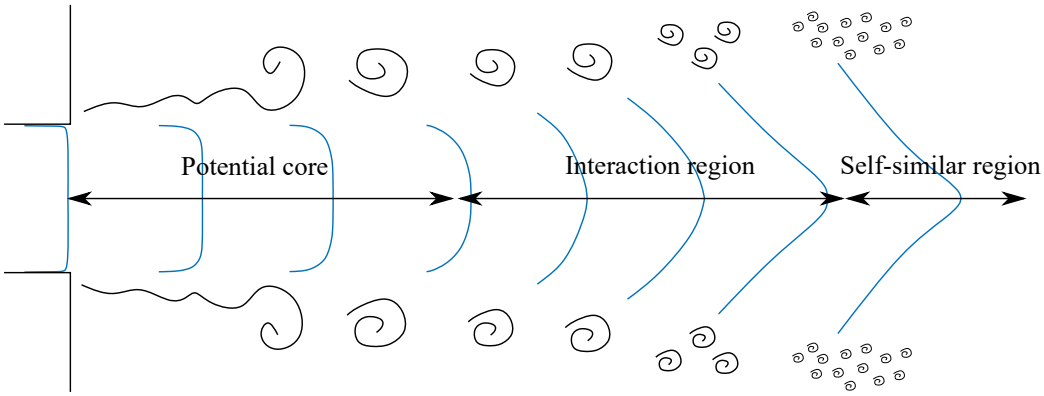

Figure 2.12: Free jet development

roll up in the shear layers [24]. The end of the potential core is defined as the point where the shear layers on both sides of the jet meet in the middle to create one continuous velocity profile, and is typically around three to five inlet nozzle diameters in length in an unexcited jet [98, 71]. Following the end of the potential core is a region wherein vortices may interact with one another, before their breakdown and the emergence of a self-similar velocity profile where the jet is deemed to be fully developed, by which point all large vortical

structures have disappeared and the turbulence is isotropic [133]. In the region where large scale structures exist, the frequency of the vortices passing a particular stationary reference point, henceforth referred to as the vortex frequency, is defined by the Strouhal number[1] referenced to the momentum thickness of the shear layer, given by

$$\mathrm{St}_\theta = \frac{f\theta}{\bar{u}}, \tag{2.6}$$

where f is the vortex frequency, θ is the momentum thickness and $\bar{u}$ is the mean jet velocity. Studies have found that the shear layer roll-up frequency is given by $\mathrm{St}_\theta = 0.012$ [51, 52, 135, 134], often called the shear layer mode. This is the naturally dominant disturbance frequency in the jet before the vortices roll up, and is therefore the frequency at which vortices are produced. It was shown by Crow & Champagne [24] and Zaman & Hussain [134] that acoustically exciting a jet shear layer can promote instabilities at the excitation frequency if the artificial instabilities dominate the natural instabilities at $\mathrm{St}_\theta = 0.012$. This encourages the shear layer to transition farther upstream than it would do naturally, and therefore the entrainment rate increases.

Another important non-dimensional jet frequency is the jet preferred mode, the terminology introduced by Crow & Champagne [24]. This frequency is given by

$$\mathrm{St}_D = \frac{fD}{u_{\max}} = 0.3, \tag{2.7}$$

where D is the jet diameter and $u_{\max}$ is the centreline velocity. Mair et al. [71] reported the greatest degree of jet spreading in a cannonical experiment that involved the excitation of a free circular jet when the excitation frequency matched the jet preferred mode. Mair [70] and Jiang et al. [54] reported that the equivalent value for a rectangular jet with $AR = 3$ is around $\mathrm{St}_{D_h} = 0.45$, where D_h is the hydraulic diameter, although Mair comments that this value may depend on AR.

[1] Strouhal number has the same formula as the non dimensional frequency F^+ discussed in section 2.4. The nomenclature F^+ appears to be favoured when dealing with actuation, while St seems to be preferred to describe the internal jet frequencies, e.g. the vortex shedding frequency discussed here.

The enhanced shear layer growth associated with excitation results in the shortening of the potential core (which has length L_{PC}) [24, 71]. For example, Mair et al. [71] reported the unexcited values were $L_{\mathrm{PC}} = 3$ to $3.5D$, corresponding to $L_{\mathrm{PC}} \approx 6$ to $7b$ for a rectangular jet with nozzle width b and aspect ratio $AR = 3$ (so $D_h \approx 2b$) if the hydraulic diameter is used to make the conversion. This value reduced to as low as $L_{\mathrm{PC}} = 1.5D$ when exciting at the jet preferred mode, $\mathrm{St}_D = 0.3$, equivalent to $L_{\mathrm{PC}} = 3b$ with the same conversion.

If the jet is attached to an adjacent, setback, and possibly inclined wall, the attachment point is typically further downstream than the end of the potential core [11]. The mass flow that is entrained from the unattached side of an attached jet can therefore be increased by the acoustic excitation. When excited from the unattached side immediately downstream of the inlet orifice, both sides of the shear layer are affected. The result of the increased entrainment is the lowering of the pressure on either side of the jet. The amount the pressure reduction depends on how well confined the jet is - if it is unconfined, the entrainment flow can be supplied without much depression. In a bistable fluidic diverter, there is a wall confining the unattached side as well as the attached side. The effect of unattached side excitation is that the pressure on the unattached side decreases more than on the attached side. This is not fully understood. One explanation is that the entrainment rate increase is biased towards the unattached side, although that is also not understood. Another reason could be that the unattached side entrainment occurs over a longer streamwise distance because it extends beyond the attachment point, so that an even increase in the entrainment rate on both sides would result in larger entrainment flow on the unattached side. In any case, the result is a reduction in the pressure difference across the jet, causing an increase in the radius of curvature and a downstream movement of the attachment point. The excitation therefore weakens the Coandă effect.

Jet demodulation As already mentioned in section 2.5.2, Wiltse & Glezer [131] studied a square jet by exciting it with piezoelectric actuators, which were driven with an amplitude modulated signal about their resonant carrier frequency. It is the carrier frequency to

which the shear layer reponded in the manner explained above. The novelty of amplitude modulation introduced by Wiltse & Glezer [131] demonstrated that the jet demodulated the excitation signal and responded at the modulation frequency. This is in agreement with the discussion above: exciting the jet with a constant amplitude tone results in a constant (DC) jet deflection, hence turning this tone off and on, i.e. modulating its amplitude, results in the jet following the modulating signal. This is an important result which is central to this thesis.

Application to fluidic devices Mair et al. [74] investigated the switching mechanism in a bistable fluidic device by using acoustic excitation from ZNMF piezoelectric transducers to switch the jet. The best results were obtained when the flow was excited from the control port on the opposite side to which the jet was attached. Excitation at the shear layer mode, $\mathrm{St}_\theta = 0.012$, yielded the shortest switching times. This indicated that the shear layer mode was the most effective excitation frequency for reducing the pressure difference across the jet sufficiently to overcome the Coandă effect and so cause the jet to detach before reattaching to the opposite side.

More recently, Mair et al. published more detailed results on the same device [73]. In this work, switching was again achieved by exciting the flow from the control port on the opposite side to which the flow was attached, and the mechanism was explained in more detail. It was found that the excitation lead to earlier spatial development of vortices in the shear layer, which caused the enhanced entrainment on both sides of the jet, but more so on the closer, unattached side. These results agreed with the classical explanation given by Crow & Champagne [24] and Zaman & Hussain [134].

Important results from Mair et al. [73] include a minimum sound pressure level of excitation to cause switching, around which the device switching time varied considerably. However, increasing the amplitude beyond this minimum threshold reduced the variation in switching time but did not change the mean switching time, which was shown to be purely a function of pressure ratio. The minimum energy required to switch a device was charac-

terised over a range of pressure ratios. Finally, when exciting at the optimal frequency for a given pressure ratio, which was again shown to match the shear layer mode $\mathrm{St}_\theta = 0.012$, the minimum switching time was characterised against pressure ratio, and shown to be proportional to its inverse. In another paper by Mair et al. [75], a similar device was switched at much higher pressure ratios using ultrasonic excitation. In this study, jets with velocities between 50 and 200 ms^{-1}, corresponding to pressure ratios up to 1.32, were switched. It was suggested that excitation of the $\mathrm{St}_\theta = 0.012$ mode does not cause switching, since at these higher jet velocities, the natural vortex shedding occurs at stations immediately downstream of the inlet nozzle orifice, such that excitation at this frequency can do nothing to encourage earlier vortex roll-ups. As such, it was proposed that the excitation at lower frequencies, at or close to subharmonics of the shear layer mode, can cause vortices to merge which reduces the pressure further and overcomes the Coandă effect.

2.6.4 Fluidic devices in application

The work by Raman et al. [92], who studied the suppression of resonance tones, has already been discussed in section 2.4. The actuator used to produce the unsteady AFC was a miniature feedback fluidic oscillator. The device produced frequencies up to 3 kHz and was positioned on the upstream edge of the cavity. As a reminder, it was possible to reduce the amplitude of the resonant tones by 10 dB using only 0.12% of the main jet flow. As a comparison, when steady blowing was used in the same position at the same flow rate, the amplitude reduction was only 1 dB.

A flow separation problem was considered by Cerretelli et al. [16]. In this work, a separated flow over a hump was reattached using both steady blowing and unsteady injection from two different fluidic oscillators. The steady blowing was able to fully reattach a flow with a freestream velocity of 25.9 ms^{-1} using a momentum coefficient $C_\mu \sim 8\%$. With unsteady injection, the most effective device operated at a frequency around 350 Hz, and was also able to reattach the flow with 60% reduction in the injected momentum required and a 30% reduction in blowing ratio.

Staats et al. [113] used a fluidic diverter operated with control mass flows actuated by solenoid valves as a means of unsteady flow injection into a compressor stator cascade. An unsteady boundary condition was applied by periodically closing vanes to block sections of the outlet duct as a means of mimicking the pressure disturbances from the combustor in a pulsed detonation engine. The goal of the fluidic injection was to avoid separation at the corner of a stator in the cascade by injecting flow close to the leading edge where a separation bubble formed. The fluidic actuator was most effective when operated at 30 Hz, and with a momentum coefficient $C_\mu \sim 2.5\%$, was able to reduce the total pressure loss through the cascade by 4% and increase the static pressure rise by 7.5%.

2.7 Control theory fundamentals

2.7.1 Introduction & fundamentals

This section contains background material on control theory and can be skipped by readers familiar with the topic. More information can be found in textbooks such as Banks [3]. All the flow control studies cited above used simple open-loop control methodology. Open-loop control refers to determining system inputs a priori rather than making use of sensor information in real-time. This is satisfactory in many cases. For instance, for constant blowing from the casing of a gas turbine to prevent tip leakage flow, feedback is not required. However, much secondary air can be saved if it is possible to blow only when a blade is passing by a given slot in the casing. This necessitates the design of a closed-loop controller in order to lock the input excitation onto the blade passing signal.

A second example relates to modulation of separation control blowing on an aerofoil. Instead of blowing (pulsed or steady) at all times, a closed-loop control system could use sensor information from the aerofoil to establish when stall is imminent in real-time and turn on the flow injection. This, when combined with pulsed blowing, could dramatically reduce the quantity of air required.

The primary objective of feedback control is to reduce uncertainty in the presence of noise

and disturbances. Necessarily this implies ensuring stability of the system, meaning that every signal in the system must be bound. Figure 2.13 is the block diagram of a generic SISO plant with transfer function, $G(s)$, which produces outputs that are affected by output disturbances, d_O to produce the signal, y. The input to the plant is the signal u produced

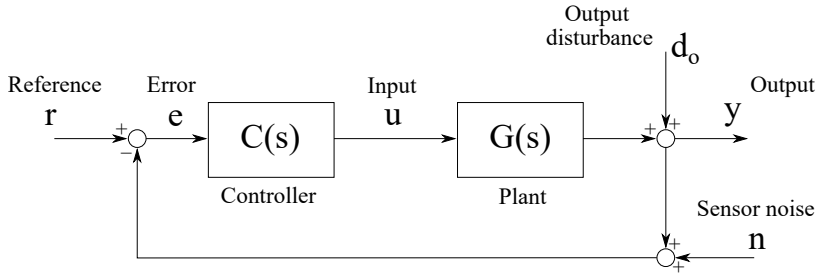

Figure 2.13: Generic control system block diagram

by the controller with transfer function, $C(s)$. The controller produces inputs in response to the error signal e, which is the difference between the desired reference for the output to follow, r and a noisy measurement of y. Note that disturbances have been placed at the output of the plant rather than its input for the purposes of this discussion, but it is possible to make similar arguments with input disturbances. The exogenous signals, r, n and d_O, affect the output, y. The transfer functions relating their Laplace transforms are

$$Y(s) = \frac{G(s)C(s)}{1+G(s)C(s)}R(s) - \frac{G(s)C(s)}{1+G(s)C(s)}N(s) + \frac{1}{1+G(s)C(s)}D_O(s) \tag{2.8}$$

$$S(s) = \frac{1}{1+G(s)C(s)} \tag{2.9}$$

$$T(s) = \frac{G(s)C(s)}{1+G(s)C(s)}, \tag{2.10}$$

where $S(s)$ and $T(s)$ are called the sensitivity and complimentary sensitivity transfer functions respectively. As can be seen in (2.8), $T(s)$ describes the relationship between the reference and the noise to the to the output, while $S(s)$ describes how the output disturbances affect the output. The ideal result would be $Y(s) = R(s)$ at all frequencies, although it is clear from (2.8) that this cannot be the case and a compromise must be struck. The

transfer functions $T(s)$ and $S(s)$ have the relationship

$$T(s) + S(s) \;=\; 1, \tag{2.11}$$

which is straightforward to derive from their definitions in (2.9) and (2.10). Consider the frequency response of these transfer functions with $s = j\omega$ substituted. Physical systems are strictly proper, which means that their transfer functions contain more poles than zeros, such that in the limit as $\omega \to \infty$, $|G(j\omega)| \to 0$. This is an intuitive result - physical systems do not respond to perturbations at arbitrarily high frequencies. It follows that

$$\lim_{\omega\to\infty} T(j\omega) \;=\; 0 \tag{2.12}$$

$$\lim_{\omega\to\infty} S(j\omega) \;=\; 1. \tag{2.13}$$

These results, along with (2.8), indicate that at high frequencies, the output cannot follow the reference and the noise will be filtered out. It also means that the disturbances cannot be removed at high frequencies, although the bandwidth of reference and disturbance signals tend to occur at lower frequencies, around those of the plant dynamics. At lower frequencies, around the plant bandwidth, it is possible to design $C(s)$ such that $T(j\omega) = 1$ and $S(j\omega) = 0$, so that $Y(j\omega) = R(j\omega) + N(j\omega)$. Here, the disturbances have been rejected completely, but the noise signal occurs unfiltered at the output. However, noise signals tend to have the opposite spectrum to the reference & disturbances signals: they occur at high frequencies rather than at those of the plant dynamics. At some value of ω, $T(j\omega)$ must 'cross-over' from $1 \to 0$ and $S(s)$ must cross-over from $0 \to 1$. This cross-over frequency can be determined by considering the frequency response of the plant, and the spectral content of the noise and disturbance signals. Ideally, the cross-over would occur above the roll-off of the plant dynamics spectrum to maximise the closed-loop system bandwidth and allow the output to track the reference and the controller to reject disturbances at as high a frequency as possible. On the other hand, $T(j\omega)$ must have rolled off to a sufficiently small value when ω reaches values where the noise signal becomes significant. The choice of this cross-over frequency represents one of the fundamental decisions to be made by the control engineer.

Sketches of example magnitude responses of $T(j\omega)$ and $S(j\omega)$ are shown in Fig. 2.14.

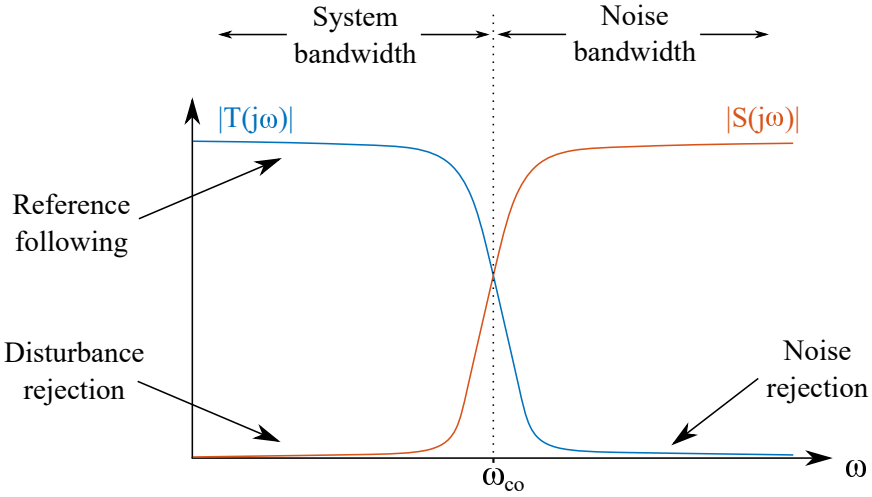

Figure 2.14: Example magnitude responses of $T(j\omega)$ and $S(j\omega)$, with cross-over frequency ω_{co}.

2.7.2 Optimal control: Linear-Quadratic Regulator

The branch of control theory used in this thesis is optimal control. Optimal control is a design methodology based on defining a cost function that is minimised by setting a linear control gain in terms of the parameters of the cost function and the plant dynamics. The plant dynamics can be expressed in terms of a state-space system as

$$\dot{x} = Ax + Bu \tag{2.14}$$

$$y = Cx, \tag{2.15}$$

where x are the system states, u are the inputs, and y are the outputs which are measured. The cost function to be minimised must apply a cost to the system states, so that the controller attempts to drive these to zero. This way the system states, x, can be transformed to $\delta x = x_0 - x$, where x_0 are the desirable states corresponding to $y = r$, i.e. the output tracking the reference, so that the controller acts to drive $\delta x \to 0$ so that $x \to x_0$ and $y \to r$. This point is made to demonstrate how driving the system states to zero can be used to achieve the control objective. However, the nomenclature for the states is left as x rather than δx for simplicity. In addition to placing a penalty on the states, the cost function must reflect the fact that making use of control inputs has a cost. Without this, the controller

would make the resulting control gain large to produce arbitrarily large control inputs to minimise the system states as quickly as possible. Control inputs are produced by real, physical actuators which have limits on the inputs they can produce and their slew rate. Such limits are nonlinear and are not included in the linear design process - the controller is unaware of them and attempts to drive $|u| \to \infty$ despite the range of inputs available, $\underline{u} < u < \bar{u}$. Therefore, a penalty on u is included in the cost function, which takes the form

$$J = \int_0^\infty x^{\mathrm{T}} Q x + u^{\mathrm{T}} R u \ \mathrm{d}t, \tag{2.16}$$

where Q is the state-cost matrix and R is the cost on control inputs. It is the parameters Q and R which are tuned by the control engineer to achieve the desired response. In terms of the previous discussion about the transfer functions $T(s)$ and $S(s)$, these parameters effectively set the cross-over frequency, among other things. A typical starting point is to choose Q so that linear combination of states that are costed is equal to the output, i.e. this term in the cost function becomes $y^{\mathrm{T}} y$, which is achieved by setting $Q = C^{\mathrm{T}} C$. In a SISO system, this leaves R as a scalar which can be used to set the cost of the input relative to that of the states. For example, in a 1-state, SISO system where Q and R are both scalars, the important quantity from the choice of Q and R is their ratio, Q/R.

The linear control law is given by

$$u = -K_{\mathrm{LQR}}\, x, \tag{2.17}$$

where K_{LQR} is the linear control gain to be determined by the derivation. The origin of the name of the control method, LQR, stands for Linear Quadratic Regulator. The 'Linear' refers to the linear input expression in terms of the system states, and 'Quadratic' refers to the form of the cost function. The derivation follows by finding the minimum of the cost function J in (2.16) constrained by the system dynamics in (2.14). After forming a set of simultaneous equations from stating the problem as a Lagrangian, the problem can be solved in two ways, the most numerically efficient of which is solving an algebraic

Riccati equation in the steady-state, which results in the solution of K_{LQR}. The resulting closed-loop system with the control law (2.17) has poles given by

$$\lambda\left(A - BK_{\mathrm{LQR}}\right). \tag{2.18}$$

Not only are these poles guaranteed to be in the left-half plane, and therefore the closed-loop system is certain to be stable, it is also possible to state sureties about the robustness of the closed-loop system. The notion of robustness is related to how much the system can change or what magnitude of disturbances or sensor noise can be added before stability is lost. These are pertinent questions because it was assumed that the plant dynamics (2.14) were known with certainty. In reality, these dynamics result from a theoretical analysis or experimental identification and are only known with a certain degree of confidence. This uncertainty means that while a controller may result in a stable closed-loop system for the nominal plant model, it may not be so for the true plant model. Uncertainty means that it is necessary quantify the robustness of a closed-loop system to changes in the plant model - or to disturbances or sensor noise which have an equivalent effect. Such robustness properties are often expressed in terms of gain and phase margin. The gain margin (GM) of a system is the factor of gain which can be added to the system while the phase margin (PM) is the amount of phase lag that can be introduced, before stability is lost. It is possible to show by frequency domain arguments that LQR has a gain margin guarantee of -6 dB (i.e. 6 dB attenuation) and $+\infty$ - that is to say that all amplifying gains are rejected while attenuations are acceptable down to -6 dB. The LQR phase margin is guaranteed to be at least 60^{o}. These margins give LQR sufficient robustness to be used in many applications.

2.7.3 Kalman filters

The previous section outlined the calculation of the controller that minimises the cost function (2.16) with the linear control law (2.17). The control gain, K_{LQR}, can be computed offline, but the system states, x, are required in real-time for the computation of the control input (2.17). The assumption that the states are known with complete accuracy is called full state feedback. However, it is the outputs, $y = Cx$, that are known, rather than the

states. The challenge is to determine the system states from the measurements, y, which is met by using an observer as part of the control system. An observer is effectively a simulation of the system that runs in real-time to produce estimates of the states which are used to calculate the control inputs. The state-space system for the observer is given by

$$\dot{\hat{x}} = \hat{A}\hat{x} + \hat{B}u + K_f y \tag{2.19}$$

$$\hat{y} = \hat{C}\hat{x}, \tag{2.20}$$

where $\hat{A}$, $\hat{B}$, and $\hat{C}$ are the observer state-, input-, and output-matrices respectively, K_f is the observer gain, $\hat{x}$ are the estimated states and $\hat{y}$ is the estimated output. The $K_f y$ term is the feedback information that allows the observer to track the real states, x. The matrices $\hat{A}$, $\hat{B}$, $\hat{C}$ are determined by considering the state prediction error, $e = x - \hat{x}$. The observer equation (2.19) is substituted from the state equation (2.14) to give the state prediction error dynamics, which are

$$\dot{x} - \dot{\hat{x}} = Ax - \hat{A}\hat{x} + Bu - \hat{B}u - K_f C x \tag{2.21}$$

$$\dot{e} = \left(A - \hat{A} - K_f C\right) x + \hat{A}e + \left(B - \hat{B}\right) u. \tag{2.22}$$

It is desirable for the prediction error dynamics to be independent of x and u, so choose $\hat{B} = B$, $\hat{A} = A - K_f C$ as well as $\hat{C} = C$, resulting in the error dynamics

$$\dot{e} = \left(A - K_f C\right) e. \tag{2.23}$$

The matrix K_f must be chosen so that $A - K_f C$ is stable, i.e. the real parts of its eigenvalues must lie in the open left-half plane. The state-estimate resulting from the observer is used to calculate the control law, $u = -K_{\mathrm{LQR}}\hat{x}$. The combined system of observer and controlled plant must be considered as a whole in order to guide the choice of the observer gain, K_f. The combined system with the reference added to the control law, $u = r - K_{\mathrm{LQR}}\hat{x} =$

$r - K_{\text{LQR}}(x - e)$, is given by

$$\frac{\mathrm{d}}{\mathrm{d}t}\begin{bmatrix} x \\ e \end{bmatrix} = \begin{bmatrix} A - BK_{\text{LQR}} & BK_{\text{LQR}} \\ 0 & A - K_f C \end{bmatrix}\begin{bmatrix} x \\ e \end{bmatrix} + \begin{bmatrix} B \\ 0 \end{bmatrix} r \tag{2.24}$$

The closed-loop dynamics are given by the eigenvalues of the combined A-matrix, which are $\lambda\left(A - BK_{\text{LQR}}\right)\lambda\left(A - K_f C\right)$, where $\lambda()$ denotes eigenvalues. This demonstrates the presence of both the observer ($\lambda\left(A - K_f C\right)$) and LQR closed-loop ($\lambda\left(A - BK_{\text{LQR}}\right)$) dynamics in the overall closed-loop dynamics. If the LQR has been designed with a control gain K_{LQR} to be optimal with respect to the cost function (2.16), the observer system poles should ideally not interfere with this response. This can be achieved by setting K_f such that the observer poles are faster than the LQR closed-loop poles so that the overall response is dominated by the response from our optimal control design. However, it is not possible to make the observer poles arbitrarily fast because of sensor noise. From a frequency domain perspective, the observer is a filter that outputs the state estimates from the measurements (system outputs). The faster the observer poles, the higher the roll-off frequency of the filter, and the more noise that is let into the state estimates. A trade-off is therefore required between recovering the LQR closed-loop dynamics and rejecting sensor noise.

A model for the disturbances and sensor noise is added to the system, which informs the choice of K_f. Adding these result in the new state-space system

$$\dot{x} = Ax + Bu + Fw \tag{2.25}$$

$$y = Cx + v, \tag{2.26}$$

where w and v are assumed to be Gaussian white noise and represent the disturbances and sensor noise respectively with covariances W and V. A Kalman filter is the sensing equivalent of LQR, which is to say that it is the optimal observer with respect to some cost function. The cost function is defined as the prediction error, $e(t) = x(t) - \hat{x}(t)$. With the

addition of the disturbances and noise, the error dynamics become

$$\dot{e} \;=\; \big(A - K_f C\big)\, e \;+\; Fv \;-\; K_f w. \tag{2.27}$$

Assuming that the prediction error has zero-mean, the problem is defined by

$$\min_{K_f} \mathbb{E}\left[e(t)e(t)^{\mathrm{T}}\right]. \tag{2.28}$$

An expression for $e(t)$ can be found by integrating the error dynamics, and after several steps this leads to a differential equation for the covariance of the prediction error, which is called P. The value of P is then minimised with respect to K_f, resulting in a solution for K_f in terms of P. Substiution of resulting expression for K_f back into the differential equation for $\dot{P}$ yields a time-dependent Ricatti equation, allowing for the possibility of time-varying state equation parameters and disturbance & sensor noise covariances, A, B, C, F, W & V. The Riccati equation for the Kalman filter is

$$\dot{P} \;=\; AP + PA^{\mathrm{T}} - PC^{\mathrm{T}}W^{-1}CP + FVF^{\mathrm{T}}. \tag{2.29}$$

In most cases it is assumed that the plant dynamics are stationary, and therefore $\dot{P} = 0$, giving a steady-state algebraic Riccati equation. Solving this for P allows for the calculation of the Kalman filter gain, given by

$$K_f \;=\; PC^{\mathrm{T}}W^{-1}. \tag{2.30}$$

This gain is optimal with respect to the chosen values of W and V, rather like how the LQR gain is optimal with respect to the cost weightings Q and R. While in theory the values of W and V can be measured, the reality is that the control engineer tunes them to get the desired tracking response. W is called the process noise, which represents both the magnitude of the disturbances but also the degree of plant uncertainty, while V is the sensor noise. Increasing the value of W relative to V causes the resulting Kalman filter to trust the measurements more - it is indicating that the cost of introducing to the system the noise

on the measurements is less than the cost of trusting the model. As might be expected, the Kalman filter has equivalent stability & robustness guarantees to LQR: guaranteed tracking stability with -6 dB gain margin and 60^{o} phase margin. However, when the Kalman filter is combined with LQR, the separate robustness guarantees disappear [29]. All is not lost, as the LQR-plant closed-loop system properties, including the robustness guarantees, can be recovered by speeding up the observer response so that the overall closed-loop system response is dominated by that of the LQR-plant, as stated previously. This is achieved by a two-step process: (1) making the assumption that $F = B$, which is equivalent to assuming that disturbances appear at the input to the plant, and (2) setting W and V such that $W/V \to \infty$ (in the case where W and V are scalars) [30]. This process is called loop transfer recovery (LTR), which refers to the recovery of the loop transfer function properties of the LQR-plant system for the overall Kalman filter-LQR-plant (also called LQG - Linear-Quadratic-Gaussian) system. Of course, the act of allowing $W/V \to \infty$ instructs the Kalman filter to trust completely the measurements, which is unlikely to be desirable in reality. It means that the roll-off frequency of the Kalman filter transfer function from measurements, y, to state estimates, $\hat{x}$, approaches ∞, thereby allowing all sensor noise into the system. In practice, the choice of W and V is another trade-off that the control engineer must judge, and their values ultimately depend on the plant, the bandwidth & magnitude of disturbances & sensor noise, as well as the control objectives. In summary, the design process for an LQG controller is as follows:

1. Design LQR by tuning Q and R to give desired full-state feedback response;
2. Calculate Kalman filter gain K_f with nominal W and V;
3. Conduct loop transfer recovery by setting $F = B$ and tuning W/V to give an acceptable recovery of the LQR-plant system in terms of the response and the stability margins, while still only allowing an acceptably small quantity of sensor noise into the loop.

2.8 Closed-loop flow control examples

The majority of practical feedback flow control examples in the literature [58, 87, 5, 4] deploy adaptive control algorithms, whose popularity in flow systems stems from the fact that the plants are often nonlinear and non-stationary. Adaptive control is founded on the assumption that the plant dynamics vary with time, and adaptive schemes like extremum seeking are well-suited to dealing with nonlinearities.

In [58], Kegerise et al. applied an adaptive generalised predictive control (GPC) algorithm to suppress the acoustic tones induced by the flow over a cavity. The actuator used was a piezoelectric bimorph cantilever beam, the length of which was in the streamwise direction with its tip situated at the cavity leading edge, and the sensors were pressure transducers on the surface of the cavity. The plant model was obtained by system identification at three Mach numbers ranging between $M_n = 0.275$ and $M_n = 0.38$. The predictive controller used a gradient descent method to optimise the plant model and controller coefficients at each time step. The controller was able to suppress multiple Rossiter modes (acoustic tones) [97] in the range of Mach numbers given, and the controller coefficients converged to a steady-state at a constant Mach number. The Bode sensitivity integral was shown to limit the performance of the controller in terms of the 'spillover' of the suppressed tones into the surrounding frequencies. The controller based on a plant model at a Mach number of $M_n = 0.275$ was run at slowly increasing Mach numbers. Although the controller was able to suppress the Rossiter modes up to a Mach number of $M_n = 0.29$, the system became unstable at higher velocities, which was shown to be caused by the convergence properties of the gradient descent algorithm.

In Pinier et al. in [87], leading edge separation was postponed until larger angles of attack on an aerofoil by a feedback controller. The modified linear stochastic measurements (MLSM) algorithm was applied, a technique that allows for the computation of the temporal coefficient associated with each POD mode, in this case based on an array of surface pressure measurements. It was shown that the first POD mode was related to the large

coherent structures associated with a separating boundary layer. The temporal coefficient associated with the first mode was computed in real time from sensor measurements with the MLSM algorithm. This signal was then low-pass filtered and used as the signal to modulate the resonant carrier tone of a piezoelectric actuator. This was based on the idea that when the flow was fully attached, the temporal coefficient associated with this mode would be small, so that the temporal coefficient was being used as an error signal and when separation began to occur, the controller would kick in. The effect was to prevent the flow from separating until larger angles of attack, although the physical mechanism behind this was not explained. Clearly, this type of feedback control was suboptimal, and the actuators were not using all of their authority. In addition, only proportional feedback was used, so that some degree of separation was required for the controller to act at all.

Chapter 3

Fluid dynamics of attached jets

3.1 Introduction

An attached jet is the basis of every fluidic device. Determining the physical mechanisms that govern how an attached jet responds to acoustic excitation is key to understanding the operation of acoustically-controlled fluidic devices. In this chapter, the fluid mechanics of an attached jet are studied with a view to creating a dynamic model that describes the jet's response to acoustic perturbation. Section 3.2 contains a detailed review of the relevant literature. In section 3.3 the equations for the model in the present work are explained, the control input is discussed, and the model is formed. A discussion is included in section 3.4, and conclusions are drawn in section 3.5.

3.2 Attached jets & fluidic devices

Fluidic devices fundamentally consist of a jet issuing from a nozzle and attaching to an adjacent wall that is setback and/or inclined. Further downstream, there may be vents, a splitter and outlet channels, but the most important dynamics occur between the nozzle exit and where the jet strikes the wall. Efforts to understand this more fundamental configuration of a jet attaching to an adjacent wall began with the work of Chapman [19], Borque & Newman [11] and Sawyer [99], the latter two of which both credit Dodds [27].

The example of a setback wall with no incline, as studied by Borque & Newman, is shown in Fig. 3.1. With reference to the figure, the jet attaches to the wall because of the Coandă

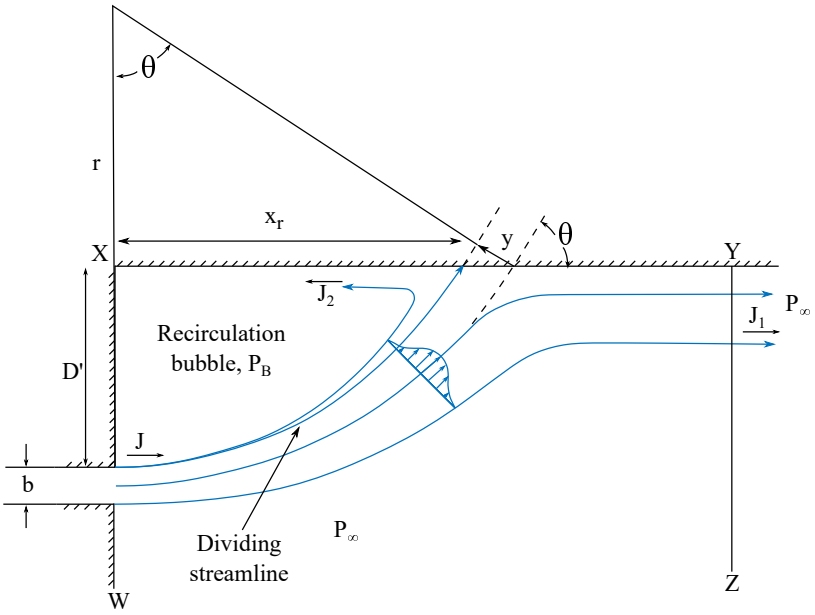

Figure 3.1: Setback wall geometry considered by Borque & Newman, adapted from [11]

effect, the principle that gives fluidic devices their stability. Mass flow is entrained into the jet after it leaves the nozzle orifice, causing it to spread out. On the lower side, this mass flow is supplied by the fluid in the free space below the jet. On the upper side, the space is confined so that the mass is not immediately replaced, since fluid must be drawn from further downstream. This results in a reduction of pressure on the upper side, while the pressure on the lower side remains at P_∞. The pressure difference vertically across the jet causes it to bend toward the upper side, further confining the space on that side which in turn reduces the pressure, eventually leading to the jet 'attaching' to the wall, which means that it strikes the wall at an angle (θ in Figure 3.1). Once this happens, the adverse pressure gradient on the jet in the direction parallel to the wall as well as the angle at which the jet strikes the wall results in a mass flow which recirculates back into the confined space between the jet and the wall. This can be seen in Figure 3.1 - the dividing streamline begins at the upper edge of the inlet orifice, and separates the flow that continues downstream from the flow that recirculates, which have momenta J_1 and J_2 respectively. The confined space between the jet and the upper wall is known as the recirculation bubble. The recirculated

fluid supplies the entrainment flow and provides a negative feedback mechanism that slows down the pressure reduction in the bubble. Eventually, the attachment point (defined by x_r in Figure 3.1) moves sufficiently far upstream that the recirculation mass flow balances the entrainment mass flow, which stabilises the bubble pressure (P_{B}) and therefore the position of the jet. Bourque & Newman [11] assumed that the pressure in the recirculation bubble was uniform, so that the jet formed a circular arc of constant curvature. It was also assumed [11] that the jet took the Görtler velocity profile, and that its width was small relative to the radius of the jet centreline, R. These assumptions were shared by the vast majority of the subsequent articles [99, 64, 67, 68, 31, 41, 18]. The aim in [11] was to predict the position of the jet attachment point on the wall (x_{R}). Sawyer [99] published at a similar time to Borque & Newman [11], and the articles were broadly in agreement. Levin & Manion [64] combined the two separate cases of setback and inclined walls considered in [11].

Following these articles, several attempts were made to model bistable fluidic devices. In most cases the basis of dynamic modelling efforts were the steady state attachment models given by Borque & Newman and Sawyer [11, 99]. The geometry of the fluidic devices considered in the literature may also include vents, a splitter, and control ports in addition to setback and/or inclined attachment walls. An example is shown in Fig. 3.2, which is adapted from Epstein [31]. With reference to the figure, the device works by injecting

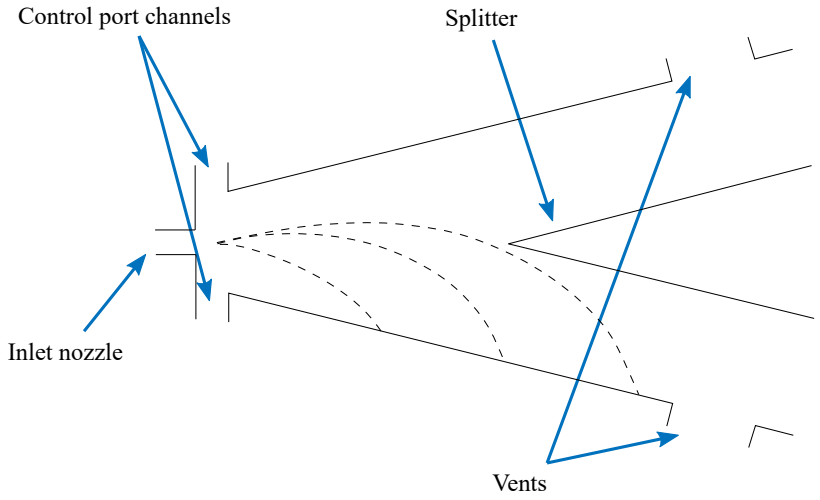

Figure 3.2: Typical fluidic diverter geometry, adapted from Epstein [31]

flow through the control port channel into the device on the attached side. There are several mechanisms by which this can cause the jet to detach and reattached to the opposite side, and the relevant mechanism for a particular device depends on the geometry. These mechanisms can be split into three categories [31]

i) End wall switching, where the jet detaches once the bubble has grown sufficiently along the attachment wall to reach a vent;

ii) Splitter switching, where the jet attachment point is moved downstream to the extent that the jet interacts with the splitter, causing an instability about the splitter leading edge which causes switching;

iii) Opposite wall switching (Fig. 3.3), where the momentum of the control jet is sufficient to deflect the main jet across to the opposite wall and form an attachment point, such that the jet then curves back round to the attachment point on the original wall. Both attachment points are then transported downstream with the jet until they reach the splitter, at which point the jet fully attaches to the opposite wall.

End wall switching occurs when either the wall setback is not small enough for opposite wall switching to occur (Lush [68] suggested $D < 2b$, where b is the inlet nozzle width, for opposite-wall switching to occur) or equivalently when the control jet has insufficient momentum to deflect the main jet to strike the opposite wall. Ozgu & Stenning studied a fluidic device with a small setback that operated using opposite-wall switching [86], and used hydrogen bubbles to visualise the switching transient with water as the working fluid. A series of snapshots from [86] is shown in Fig. 3.3 to illustrate the switching mechanism. Splitter switching occurs if the splitter is placed sufficiently far upstream that the jet can interact with it before either of the other two mechanisms occur. For example, the geometry of the device in Fig. 3.2 indicates that this device will operate using splitter switching. Mair comments that the device depth (into the page in Fig. 3.2) can affect the switching performance of a fluidic device, but that the switching mechanisms are inherently 2-D [70]. In this thesis, the nozzle aspect ratio (AR) takes a value of $AR = 3$ throughout, and the devices are modelled as 2-D.

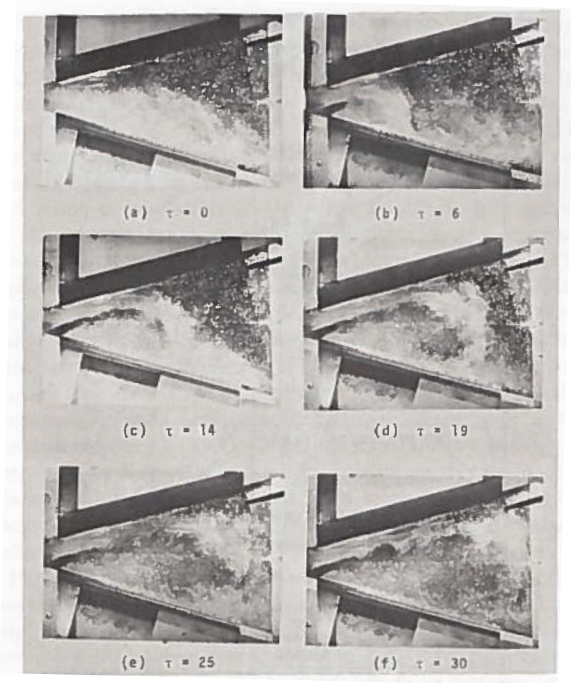

Figure 3.3: Snapshots during opposite-wall switching transient from [86], visualised using hydrogen bubbles in water. The flow is initially attached to the lower side.

Muller [80, 81] appears to have been the first to model fluidic device switching times. The time taken for the jet to detach was modelled by postulating that the condition for detachment is for the recirculation bubble to reach a critical volume. The origin of this idea was based on the fact that Muller's fluidic device was of the vented variety and so end wall switching would occur once the attachment point reached the vent, which corresponds to growing the bubble to a particular size. Muller then used a quadratic function to describe the difference between the flow entrained out of the bubble and the flow recirculated back into it. The coefficients of the function depended on the switching mechanism and hence the control flow rate. Muller referred to 'dynamic switching' and 'slow switching', which are equivalent to the opposite wall and end wall switching mechanisms described above.

Lush [67, 68] approached the modelling of the end wall switching mechanism in a bistable device by splitting up the switching process into phases. The device Lush studied is shown in Fig. 3.4. The first of these is the bubble growth phase, which is stable because steady

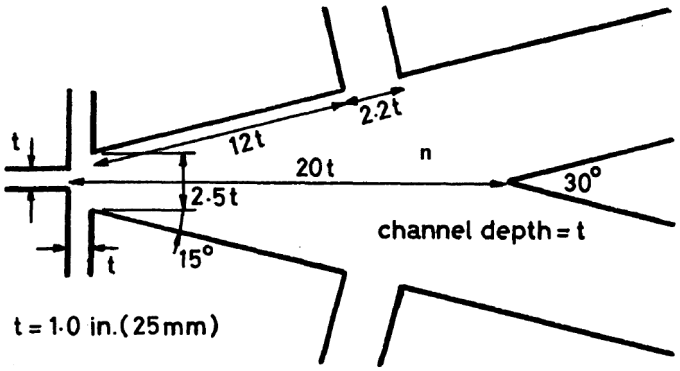

Figure 3.4: Fluidic amplifier studied by Lush [67]. Note that the definition of the setback distance highlighted as $2.5t$ is double the setback distance in this thesis (D), which is defined from the device centreline to the corner between the side wall and the control port.

state jet attachment positions in this regime can be supported by injecting a constant, subcritical control flow. The jet remains attached throughout this period.

In this thesis, focus is placed on a mode of operating fluidic diverters that differs from the traditional, full-switching approach. In this alternative mode, the jet remains attached to one side throughout and is partially deflected so that a portion of the flow exits via the unattached side outlet channel. It is the dynamics of the attached jet that govern the device operation in this continuous-modulation approach. As such, the phase of switching before the jet detaches described in Lush [67, 68] and others is the subject of the following sections, in which the components of the various modelling efforts of relevance are presented. Emphasis is placed on Lush's model as a starting point.

3.2.1 Görtler velocity profile

As in Bourque & Newman [11], Sawyer [99], and many others [64, 31, 41, 18], Lush used the Görtler velocity profile for the jet. The profile is given by

$$u = \frac{1}{2}\sqrt{\frac{3J\sigma}{\rho(s+s_0)}}\operatorname{sech}^2(\eta) \tag{3.1}$$

$$v = \frac{1}{4}\sqrt{\frac{3J}{\rho\sigma(s+s_0)}}\left[2\eta\operatorname{sech}^2(\eta) - \tanh(\eta)\right] \tag{3.2}$$

$$\eta = \frac{\sigma y}{s + s_0}, \tag{3.3}$$

where u is the streamwise velocity, v is the transverse velocity, σ is the jet spread parameter ($\sim 1/E$, where E is the entrainment rate), J is the jet momentum flux per unit depth, s is the distance along the jet centreline from the centre of the inlet orifice, s_0 is the distance along the jet centreline from the virtual origin of the jet to the inlet orifice, and y is the local coordinate perpendicular to the jet centreline at a given station s. The jet momentum flux per unit depth is given by $J = \dot{m}^2/\rho b d^2$.

The Görtler profile can be derived by taking Prandtl's assumption that the eddy viscosity of a free turbulent jet is proportional to the width of the jet and the centreline velocity [60]. This means that the eddy viscosity is assumed to be constant across the jet at any downstream station. A brief derivation of the velocity profile is given in Appendix A - readers are referred to Kirshner & Katz [60] for a complete derivation. Use of eddy viscosity as a concept implies the assumption of isotropic turbulence [122, p. 67-68]. This is a reasonable assumption for a free jet that emanates from an infinitesimally narrow slit, which is assumed in the Görtler profile. However, in practice a jet issues from a nozzle, which means that it has a velocity profile that depends on the upstream conditions and the nozzle entry length. Additionally, large scale structures are present in the jet shear layer which are not in general isotropic. The velocity profile of a real jet morphs into a Görtler profile some distance downstream of the nozzle orifice once the shear layer eddies break down and the turbulence becomes isotropic. This process is shown in Fig. 3.5. Assuming a Görtler profile from the

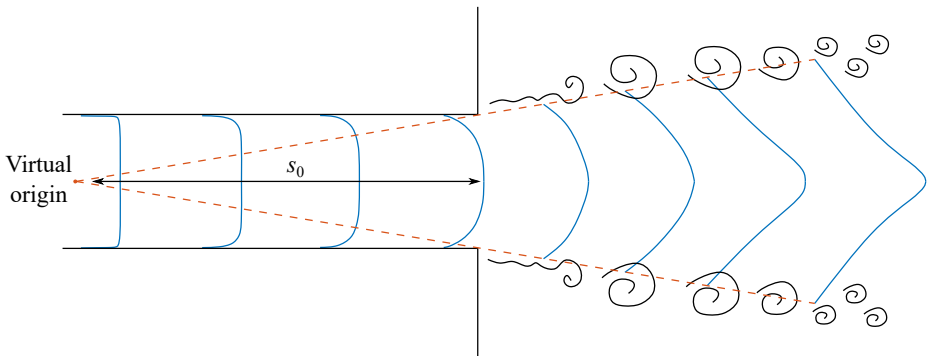

Figure 3.5: Jet issuing from finite nozzle with velocity profile developing into the Görtler profile.

nozzle orifice requires the definition of a virtual origin of the jet further upstream, such that the jet width grows to match the nozzle edges in some way. The validity of this assumption hinges on the resemblance of the velocity profile at the nozzle exit to the Görtler profile, which determines the length downstream of the nozzle where the free jet assumption, and therefore the use of the Görtler profile, becomes reasonable. It should be noted that the entrainment of flow into the jet is built into the Görtler profile.

3.2.2 Jet virtual origin

The virtual origin of the jet is called s_0, see (3.1 - 3.3). Lush [67, 68] used a continuity condition to set s_0. The Görtler profile assumes an initial mass flow rate of zero at its origin, and grows proportional to $s^{\frac{1}{2}}$ as it entrains the surrounding fluid. The virtual origin, s_0, can be used to set the origin of the profile such that by the time it has reached the nozzle orifice, it has entrained sufficient fluid to match the inlet mass flow rate. Integrating the velocity profile (3.1) between $y = 0$ and $y \to \infty$ with $s = 0$ and equating this to half of the inlet mass flow rate results in

$$\frac{\dot{m}}{2} = \int_{y=0}^{y=\infty} d\rho u \, \mathrm{d}y = \int_{y=0}^{y=\infty} \frac{d\rho}{2} \sqrt{\frac{3J\sigma}{\rho s_0}} \operatorname{sech}^2\left(\frac{\sigma y}{s_0}\right) \mathrm{d}y, \tag{3.4}$$

which can be evaluated and rearranged to give

$$s_0 = \frac{\sigma b}{3}. \tag{3.5}$$

This was the approach taken by the vast majority of the published articles on the topic [11, 99, 64, 41, 67, 68, 18].

3.2.3 Dividing streamline

Chapman [19] introduced the idea of the dividing streamline (DSL). He studied the flow over a backward-facing step, as shown in Fig. 3.6a. He suggested that particles on the free stream-side of the DSL (green shaded region in Fig. 3.6b) have sufficient total pressure to overcome the adverse pressure gradient along the wall, whereas those on the wall-side of

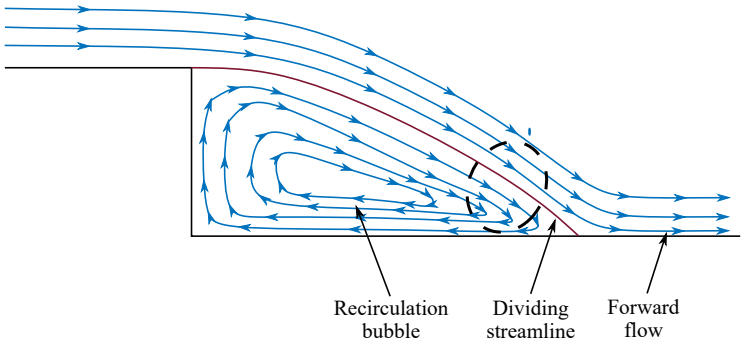

(a) Overview — circled region blown up in (b).

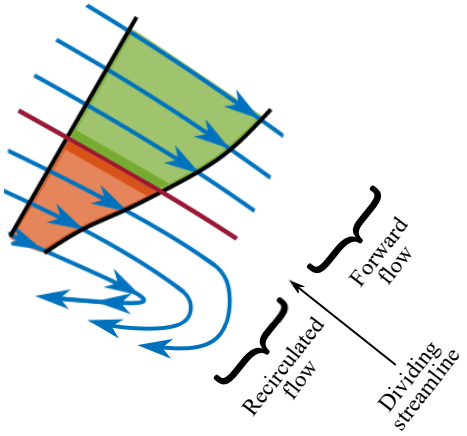

(b) Detail showing velocity profile

Figure 3.6: Sketch of setup studied by Chapman [19], highlighting dividing streamline.

the DSL (red shaded region) do not and are sucked into the bubble. Particles on the DSL represent the limiting case and stagnate against the wall. This is essentially an energy argument. Chapman used a Blasius profile to describe the separated boundary layer. To apply Chapman's energy approach to our case would require knowledge of the total pressure of particles on the dividing streamline, as well as the downstream pressure P_∞, both of which are difficult to determine.

There is a lack of consensus in the literature as to the definition of the DSL, which has resulted from the addition of control flows to models that were originally uncontrolled. Most generally, the DSL marks the edge of the jet in the sense that integrating across the profile between $y = 0$ and $y = y_{\mathrm{DSL}}$, results in half of the inlet mass flow. By continuity, in the steady state and in the absence of control flows, the DSL must originate from the edge

of the inlet orifice and divide the flow at the attachment point. The integral that defines the DSL is the same as that used to determine s_0, with s left as a variable rather than set to 0. The equation of the DSL is given by

$$y_{\mathrm{DSL}} = \frac{s + s_0}{\sigma} \operatorname{atanh}\left(\sqrt{\frac{\sigma b}{3(s + s_0)}}\right). \tag{3.6}$$

However, if a control flow is added, then the streamline originating at the edge of the inlet orifice will join the forward flow, and the streamline that separates the forward flow from the recirculated flow will originate in the control flow. Lush [67] included both a DSL and a reattaching streamline (RSL) because of the presence of a control flow. These are shown in Fig. 3.7. It is the RSL that divides the flow between recirculating and forward flow,

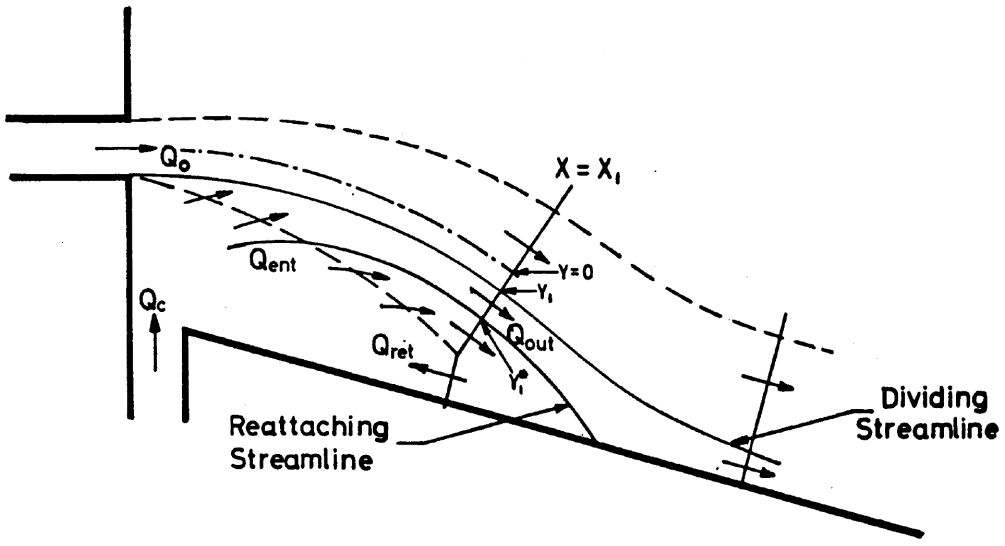

Figure 3.7: Fluidic amplifier studied by Lush [67] showing various streamlines.

while the DSL is still defined by the continuity condition in (3.6). The quantities of flow entrained or recirculated can be calculated by integration of the velocity profile with the relevant limits relating to these streamlines.

3.2.4 Bubble growth model

Since Lush [67] was studying a vented device that operated by end wall switching, he borrowed Muller's [80] idea that the bubble volume must reach a critical value before switching occurs. Lush used knowledge of the assumed velocity profile to derive an expression for the rate of change of the bubble volume, given by

$$\frac{\mathrm{d}V}{\mathrm{d}t} = Q_c - Q_{\mathrm{out}}, \tag{3.7}$$

where V is the bubble volume, Q_c is the control flow rate entering the device from the control port, and Q_{out} is the net flow exiting the bubble, which is the entrainment flow less the recirculated flow. In the steady state, $\mathrm{d}V/\mathrm{d}t = 0$, so $Q_{\mathrm{out}} = Q_c$. It follows from this that when $Q_c = 0$, $Q_{\mathrm{out}} = 0$, implying that the entrainment and recirculated flows are equal in the absence of control flows, as expected.

3.2.5 Jet curvature equation

The jet curvature equation describes a steady relationship between the pressure difference across a curved jet and the radius of curvature. It can be derived from Euler's equation,

$$\frac{\mathrm{d}P}{\mathrm{d}y} = \frac{\rho u^2}{R}, \tag{3.8}$$

where P is the pressure, y is the cross-stream coordinate, u is the streamwise velocity, ρ is the fluid density, and R is the radius of curvature. Integrating this equation across the jet gives

$$\Delta P = \frac{\int \rho u^2 \mathrm{d}y}{R}, \tag{3.9}$$

$$\Delta P = \frac{J}{R}. \tag{3.10}$$

This result was used to relate the pressure difference across the jet to its radius of curvature both in steady state [11, 99, 64, 18] and dynamic [41, 67, 68, 31, 18] models in all but one study to the knowledge of the author. The use of (3.10) in a dynamic model implies a 'quasi-steady jet' assumption, for which justification was provided by Lush [67] and Chang

[18], but not by others.

Lush's quasi-steady jet argument Lush [67] suggested that the inertial terms of the Navier-Stokes equation dominate the unsteady term, that is to say

$$u\frac{\partial u}{\partial x} \gg \frac{\partial u}{\partial t}. \tag{3.11}$$

To support this, he made a scaling argument. The substitutions made were as follows:

- u was replaced with u_0, the mean nozzle velocity;
- x was replaced with l, a length scale in the x-direction, which was chosen to be the attachment wall length (control port to vent);
- $\tau_s = t_s u_0/b$ was substituted for time, a non-dimensional switching time parameter that Lush called Strouhal^{-1} number, where t_s is switching time and b is the nozzle width.

Making these substitutions gives the condition

$$\tau_s \gg \frac{l}{b}. \tag{3.12}$$

Lush suggested that τ_s should be an order of magnitude greater than l/b for the unsteady term to be ignored safely. The values of τ_s calculated from switching time measurements were on the order of 100, while $l/b \approx 10$ for the device, satisfying (3.12).

Chang's quasi-steady jet argument Chang [18] suggested that to use (3.10) in a dynamic model of jet switching, the switching time must be much larger than the transport time of particles through the fluidic device, i.e.

$$\frac{d_s}{U} \ll t_s \;\Leftrightarrow\; D_s \ll \tau_s \tag{3.13}$$

where d_s is the distance between the nozzle orifice and the splitter, U is the mean velocity at the nozzle exit, t_s is the switching time of the device, $D_s = d_s/b$ is the nondimensionalised

splitter distance (by the nozzle width, b), and $\tau_s = t_s U/b$ is the nondimensionalised switching time. For Chang [18], $\tau_s \approx 20 D_s$. This agrees with Lush's argument - the conditions are equivalent.

Ries's jet curvature equation To the knowledge of the author, only Ries [96] has made efforts to derive a non-steady jet curvature equation. Ries's [96] work considered the first phase of switching described by Lush [67]; the bubble growth phase. In his derivation of an unsteady JCE, Ries started from the Navier-Stokes radial momentum equation in polar coordinates without the viscous terms, given by

$$\frac{\partial u_r}{\partial t} + u_r \frac{\partial u_r}{\partial r} + \frac{u_\phi}{r}\frac{\partial u_r}{\partial \phi} - \frac{u_\phi^2}{r} = -\frac{1}{\rho}\frac{\partial P}{\partial r}. \tag{3.14}$$

Note that the variable ϕ is related to the streamwise distance s by $s = R\phi$. Ries's first step is to discard the unsteady term, $\frac{\partial u_r}{\partial t}$, and the $\frac{\partial u_r}{\partial \phi}$ term, stating that u_r is independent of time and ϕ, leaving

$$u_r \frac{\partial u_r}{\partial r} - \frac{u_\phi^2}{r} = -\frac{1}{\rho}\frac{\partial P}{\partial r}. \tag{3.15}$$

Ries [96] goes on to substitute $r = R + y$, where r is the distance from the centre of curvature of the jet to a point in the velocity profile, and y is the radial (cross-stream) distance from the jet centreline to the point in the velocity profile. Differentiating this substitution gives

$$u_r \;=\; \dot{R} + v, \tag{3.16}$$

where $v = \mathrm{d}y/\mathrm{d}t$ is the cross-stream velocity with the profile given by (3.2). The velocity u_ϕ is replaced by u so that (u, v) are the local tangential and radial velocities at a point in the jet (s, y). Noting that $\mathrm{d}r = \mathrm{d}y$ and substituting (3.16) into (3.14) leads to

$$\left(\dot{R} + v\right)\frac{\partial\left(\dot{R} + v\right)}{\partial y} - \frac{u^2}{R + y} = -\frac{1}{\rho}\frac{\partial P}{\partial y}. \tag{3.17}$$

Ries [96] assumed that $R \gg y$ and $\mathrm{d}R/\mathrm{d}t \gg v$, leading to

$$\dot{R}\frac{\partial v}{\partial y} - \frac{u^2}{R} = -\frac{1}{\rho}\frac{\partial P}{\partial y}. \tag{3.18}$$

The next step was to multiple both sides by ρ and integrate (3.18) with respect to y between the limits of $y = -\infty$ and $y = \infty$, giving

$$\dot{R}\int_{-\infty}^{\infty}\rho\frac{\partial v}{\partial y}\,\mathrm{d}y \;-\; \frac{1}{R}\int_{-\infty}^{\infty}\rho u^2\,\mathrm{d}y \;=\; -\int_{-\infty}^{\infty}\frac{\partial P}{\partial y}\,\mathrm{d}y. \tag{3.19}$$

Evaluating the terms leads to

$$[v]_{-\infty}^{\infty}\,\dot{R} - \frac{J}{\rho R} = -\frac{1}{\rho}\,[P]_{-\infty}^{\infty}\,. \tag{3.20}$$

Ries [96] then makes a sign error by evaluating $[v]_{-\infty}^{\infty} = +2v_{\max}$. If evaluated correctly ($[v]_{-\infty}^{\infty} = -2v_{\max}$), the differential equation in R is unstable because the coefficients of $\dot{R}$ and $1/R$ have the same sign. The term $[v]_{-\infty}^{\infty}$ is a function of s, which Ries deals with by taking its average value by integrating from $s = 0$ to $s = R\theta$, where θ is the swept angle of the jet (see Fig. 3.1). The result is an unsteady jet curvature equation

$$\dot{m}\sqrt{\frac{3}{\sigma b d^2}}\frac{1}{\sqrt{\theta}}\frac{1}{\sqrt{R}}\frac{\mathrm{d}R}{\mathrm{d}t} \;-\; \left(\frac{\dot{m}^2}{\rho b d^2}\right)\frac{1}{R} \;=\; \Delta P. \tag{3.21}$$

Comparing (3.21) with the steady-state version derived from the Euler equation (3.10) indicates that Ries's approach yields the same result in the steady state, with the addition of the unsteady term in $\dot{R}$.

3.2.6 Momentum conservation at the attachment point

Borque & Newman [11] proposed two models to resolve the momentum flux conservation at the attachment point. The form of the momentum equation depends on the position and size of the control volume taken around the attachment point.

Attachment point theory The attachment point theory was applied to the straight, setback wall configuration, as shown in Fig. 3.8, which is a duplicate of Fig. 3.1 for convenience. This theory assumes a small control volume local to the attachment point,

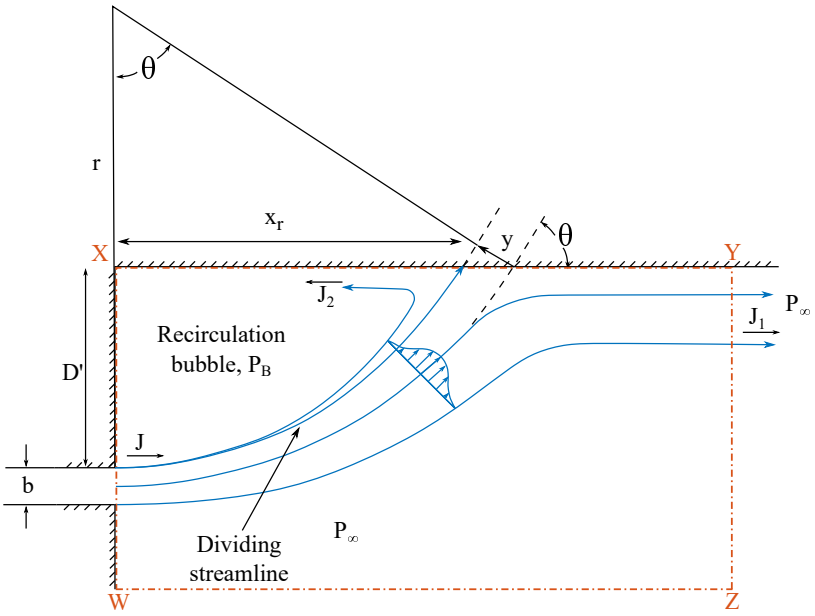

Figure 3.8: Setback wall geometry considered by Borque & Newman, adapted from [11] - duplicate of Fig. 3.1.

giving the momentum equation

$$J\cos(\theta) = J_1 - J_2, \tag{3.22}$$

where J_1 and J_2 are the forward and recirculated momenta, and $J\cos(\theta)$ is the component of the main jet entering the control volume in the direction parallel to the wall, as in Fig. 3.8.

Control volume theory The second theory, the control volume theory, takes the control volume given by WXYZ in Fig 3.8. In this theory, the momentum equation takes the form

$$J - J_1 = (P_\infty - P_\mathrm{B})\left(D' + \frac{b}{2}\right), \tag{3.23}$$

where D' is the setback distance of the start of the attachment wall relative to the edge of the inlet nozzle. The prime is used because the setback is defined in this thesis as

$D = D' + b/2$, the distance from the upstream corner of the attachment wall to the nozzle axis. The bubble pressure, P_{B}, is the pressure adjacent to the back wall along the line WX in Fig. 3.1, while P_∞ is the pressure downstream of the attachment point at line YZ. Through use of the steady JCE (3.10) and geometric relations, (3.23) can be reduced to

$$J\cos(\theta) \;=\; J_1. \tag{3.24}$$

The difference between the attachment point and control volume theories, (3.22) and (3.24), is the inclusion of the recirculated momentum term, J_2. As explained by Kirshner & Katz [60, p. 393], the discrepancy arises from the assumption of constant pressure in the bubble. If the recirculated momentum, J_2, reaches the back wall and stagnates or is turned by it, then the pressure at the wall will be greater than the average bubble pressure. If the recirculated momentum stagnates against the back wall, (3.24) applies, whereas if J_2 is dissipated by frictional losses and does not reach the back wall (resulting in the back wall pressure being the same as the mean bubble pressure), (3.22) applies. Therefore, the appropriate choice of control volume depends on the losses in the bubble. It should be noted that authors of the work following [11] unanimously opted for the attachment point theory [80, 81, 31], including Lush [67, 68], presumably because Bourque & Newman reported better experimental agreement in terms of the steady state attachment position, x_{R}, in [11]. However, Kirshner & Katz [60, p. 393] note that this better experimental agreement is more often found in studies where the wall is parallel to the axis of the inlet orifice rather than inclined.

3.2.7 Bubble pressure model

A model for the bubble pressure was not required in most of the studies discussed because of the assumption of a quasi-steady jet. Using this assumption makes the relationship between the radius of curvature of the jet, R (or its swept angle, θ,) and the pressure difference across the jet, ΔP an algebraic rather than a differential one, such that the steady JCE (3.10) could be used to compute ΔP from knowledge of R. Two cases where equations were formulated for the recirculation bubble pressure are discussed here.

Goto & Drzewiecki bubble pressure model An additional method of calculating the bubble pressure was devised by Goto & Drzewiecki [41]. Their main contribution to the literature was the inclusion of the supply nozzle, control ports, vents, and outlets as lumped parameters, allowing for the calculation of the pressures at each of these points given the flow velocities. Knowledge of these pressures allowed for more accurate switching time calculations, as the influence of the various geometric features was incorporated; for example, the effect of the back-pressure from the outlets. In order to close their model equations, an equation for the bubble pressure was required, which took the form of a forced vortex. This required calculation of the reattaching streamline pressure as a boundary condition for the vortex, which could be achieved by applying a continuity condition to the device as a whole. Goto & Drzewiecki's [41] bubble model accounts for the static pressure reduction due to the swirl of the flow. However, this is not the only cause of the depression in the bubble - there is a total pressure reduction due to the entrainment of flow from the jet. It is unclear if this effect is accounted for in the calculation of the entrainment streamline pressure.

Ries's bubble pressure model Ries [96] used the ideal gas law to describe the pressure in the recirculation bubble, as given by

$$P_{\mathrm{B}} = \left(\frac{R_g T}{M_m}\right) \frac{m_{\mathrm{B}}}{V_{\mathrm{B}}}, \tag{3.25}$$

where V_{B} is the bubble volume, m_{B} is the instantaneous mass in the bubble, R_g is the universal gas constant, M_m is the molar mass of air, and T is the temperature of the gas. Ries then used this relationship statically, updating the bubble mass in his simulations by calculating its net change at each time step. The rate of change of bubble mass was given by

$$\frac{\mathrm{d}m_{\mathrm{B}}}{\mathrm{d}t} = \dot{m}_{\mathrm{c}} + \dot{m}_{\mathrm{r}} - \dot{m}_{\mathrm{e}}, \tag{3.26}$$

where $\dot{m}_{\mathrm{c}}$, $\dot{m}_{\mathrm{r}}$, and $\dot{m}_{\mathrm{e}}$ are the control, recirculation, and entrainment mass flows respectively.

3.2.8 Bubble volume

The standard approach [67, 68, 41, 96, 18] is to find a geometric expression for the bubble volume in terms of device parameters and jet variables.

3.2.9 Model validation

For the steady state models of attached jets described here, the validation approach taken was a comparison between the experimentally-determined and model-predicted position of the attachment point. The parameters varied to test the models included geometric values like the wall setback distance and incline angle, as well as the flow rate. For the dynamic models of fluidic diverters, the validation generally consisted of a comparison between measured and predicted summary values like switching time. The predicted values were typically obtained from the model by running numerical simulations.

3.3 Dynamic model

No published articles consider the modelling of fluidic devices actuated by means other than control flows, for example acoustic excitation. This section introduces the model in the present work. The assumptions are as follows:

1. The jet centreline follows a circular arc with radius R;
2. The width of the jet is small compared with the radius of the jet centreline, R;
3. The jet has a Görtler velocity profile;
4. The recirculation bubble on each side of the jet has a uniform pressure distribution;
5. The fluid in the recirculation bubbles acts as an ideal gas;
6. The jet has constant density,

none of which are novel. The model is described in a modular fashion with components being directly comparable to those in section 3.2, starting with the assumed velocity profile.

3.3.1 Görtler velocity profile

The Görtler profile is duplicated here for convenience.

$$u = \frac{1}{2}\sqrt{\frac{3J\sigma}{\rho(s+s_0)}}\mathrm{sech}^2(\eta) \tag{3.27}$$

$$v = \frac{1}{4}\sqrt{\frac{3J}{\rho\sigma(s+s_0)}}\left[2\eta\,\mathrm{sech}^2(\eta) - \tanh(\eta)\right] \tag{3.28}$$

$$\eta = \frac{\sigma y}{s+s_0}, \tag{3.29}$$

where u is the streamwise velocity, v is the transverse velocity, σ is the jet spread parameter ($\sim 1/E$, where E is the entrainment rate), J is the jet momentum flux per unit depth, s is the distance along the jet centreline from the centre of the inlet orifice, s_0 is the distance along the jet centreline from the virtual origin of the jet to the centre of the inlet orifice, and y is the local coordinate perpendicular to the jet centreline at a given station s.

3.3.2 Jet virtual origin

It was explained in section 3.2.2 that the virtual origin is typically [11, 99, 64, 41, 67, 68, 18] set by matching the mass flow rate across the entire cross-stream domain of the jet to the mass flow of the physical jet that is being modelled. An alternative is to inflate the value of $\dot{m}$ in the definition of u in (3.27) and set the upper limit of the integral to $y = b/2$. This results in the correct mass flow across the nozzle at its exit, rather than the correct mass flow spread across the whole profile between $-\infty$ and ∞. This is illustrated in Fig. 3.9, which shows the streamwise (u) velocity profile. The red areas in the figure represent the mass flow that is outside of the nozzle if the integral limits are set to $\pm\infty$. If $\dot{m}$ in the expression for J in (3.27) is replaced with $\xi\dot{m}$, then integrating the profile at $s = 0$ from $y = 0$ to $y = b/2$ and equating it to half the mass flow rate gives

$$\frac{\dot{m}}{2} = \int_0^{\frac{b}{2}} d\rho u\,\mathrm{d}y = \int_0^{\frac{b}{2}} d\rho \left[\frac{3\xi^2\dot{m}^2\sigma}{4\rho^2 b d^2(s+s_0)}\right]^{\frac{1}{2}} \mathrm{sech}^2\left(\frac{\sigma y}{s+s_0}\right)\mathrm{d}y \tag{3.30}$$

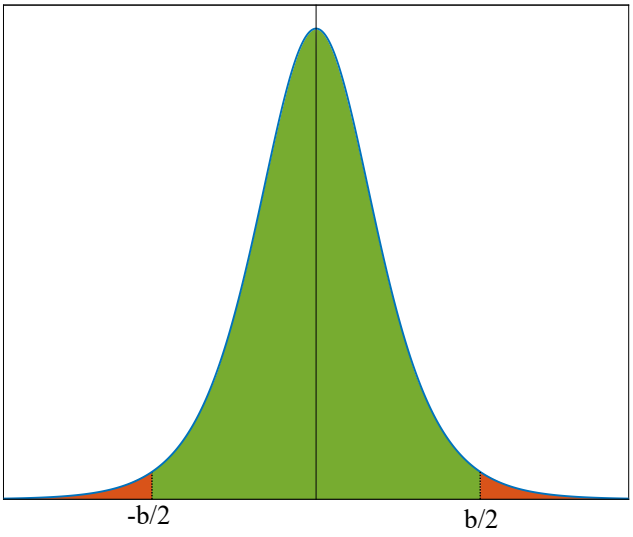

Figure 3.9: Görtler streamwise velocity profile: highlighting the difference in setting the integral limits to $\pm\infty$ and $\pm b/2$

$$\xi\sqrt{\frac{3s_0}{\sigma b}}\tanh\left(\frac{\sigma b}{2s_0}\right) - 1 = 0. \tag{3.31}$$

The resulting equation, (3.31), has no solutions for $\xi < 1.07$, one solution for $\xi = 1.07$ and two solutions for $\xi > 1.07$. The single solution case corresponds to matching the velocity profile mass flow to give the correct inlet mass flow in the nozzle at its exit, so $\xi = 1.07$ is taken, giving $s_0 = 0.46\sigma b$. The argument for this approach is that it respects the fact that the nozzle has a finite width, while the traditional approach indicates a nozzle of infinite width. On the other hand, the drawback is that truncating the Görtler profile does not respect the no-slip condition at the nozzle walls. The difference between the virtual origin in the present model, $s_0 = 0.46\sigma b$, and the traditional value, $s_0 = (1/3)\sigma b$, is shown to have significant consequences for future calculations in sections 3.3.3 and 3.4.2.1.

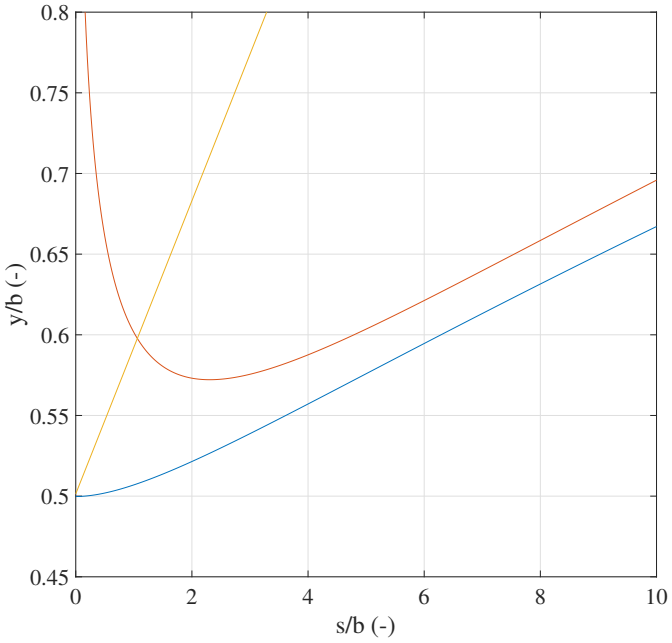

Figure 3.10: Dividing streamline with $\xi = 1.07$ & $s_0 = 0.46\sigma b$ (present work, blue), $\xi = 1$ & $s_0 = \sigma b/3$ (previous authors, red) and edge of shear layer according to $\eta = 1.09$ (yellow). In all cases, $\sigma = 12$.

3.3.3 Dividing streamline

With the addition of the inflating factor ξ, the equation of the DSL differs from that in section 3.2.3, and is given by

$$y_{\mathrm{DSL}} = \frac{s + s_0}{\sigma} \operatorname{atanh}\left(\frac{1}{\xi}\sqrt{\frac{\sigma b}{3(s + s_0)}}\right). \tag{3.32}$$

This agrees with Borque & Newman [11] if $\xi = 1$ and $s_0 = \sigma b/3$. The DSL as given by (3.32) with $\sigma = 12$ (a value typically used in the literature, for example by Borque & Newman [11] in their setback wall model) is plotted for these values of ξ and s_0, as well as $\xi = 1.07$ and $s_0 = 0.46\sigma b$, in Fig. 3.10. The DSL using Borque & Newman's approach has $y_{\mathrm{DSL}} \to \infty$ as $s \to 0$, whereas the DSL from the present analysis is 'well-behaved' and coincides with the edge of the nozzle at $y_{\mathrm{DSL}} = b/2$. This represents a marked improvement over the traditional approach, which has been used extensively in the literature [99, 64, 41, 67, 68, 18]. It will be necessary later to evaluate the jet velocity profile on the DSL, which is possi-

ble when it is physically reasonable as in the present work. This is one advantage of the approach taken to define the virtual origin in section 3.3.2. A second advantage is its influence on the jet dynamic responses, which is demonstrated in section 3.4.2.1 to be significant.

It is instructive to consider the transverse velocity profile given by (3.28) when determining the DSL. A normalised v, given by $\bar{v} = 2\eta\,\mathrm{sech}^2(\eta) - \tanh(\eta)$, is plotted in Fig. 3.11. The

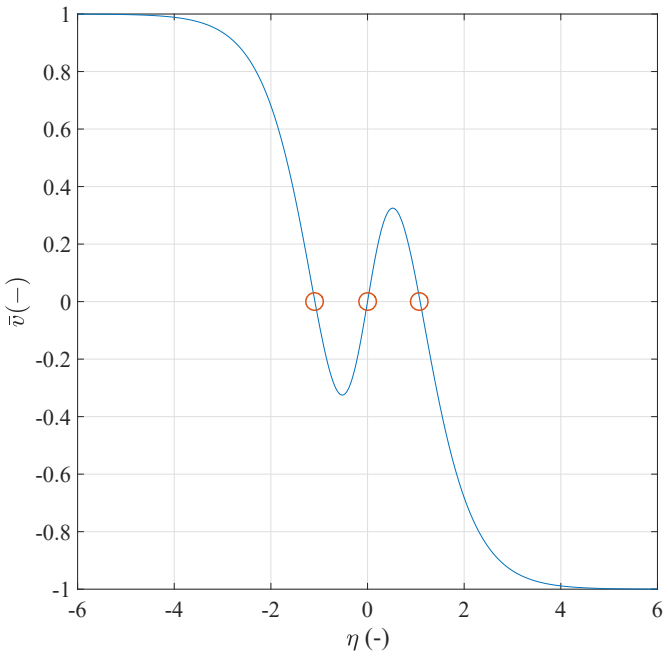

Figure 3.11: Normalised transverse Görtler velocity profile, with zero-crossings marked in red circles.

function is odd as should be expected, and there is a solution at $\eta = 0$ corresponding to the centre of the jet. There are also solutions at $\eta = \pm 1.09$, which come about as a result of (a) the jet spreading out from its centreline, such that the transverse velocity close to the centreline must have the same sign as η, and (b) the jet entraining flow from the surrounding fluid, such that far from the centreline the transverse velocity must be towards the centre of the jet, i.e. the opposite sign to η. These two factors mean there must be a point where the transverse velocity passes through 0, which occurs at $\eta = \pm 1.09$. This point is the edge of the shear layer, which is different from the DSL. Beyond this value of η in a free jet, the fluid has not been affected by the presence of the jet through viscous effects, i.e. it has not had streamwise momentum imparted on it through viscous shear. This is not reflected in the

streamwise velocity profile, u, which only reaches 0 in the limit as $\eta \to \pm\infty$. The limits of the model domain are therefore taken to be the edges of the shear layer defined by $\eta = \pm 1.09$.

For the model to be physically reasonable, the edge of the shear layer should coincide with the DSL at the edge of the nozzle orifice, then spread at a faster rate than the DSL. To test this, it is asserted that edge of the shear layer must pass through $y = b/2$ at $s = 0$, then the position of the jet virtual origin, s_0, required to achieved this is calculated. Substituting these values into the expression for η (3.29) and setting $\eta = \eta_{\mathrm{SL}} = 1.09$ gives

$$\eta \;=\; \frac{\sigma b}{2 s_0} \;\Rightarrow\; s_0 \;=\; 0.46 \sigma b, \tag{3.33}$$

which is in agreement with the previous calculation of s_0. Using this value of s_0 and $\sigma = 12$, the edge of the shear layer, given by

$$y_{\mathrm{SL}} \;=\; \frac{\eta_{\mathrm{SL}}(s + s_0)}{\sigma}, \tag{3.34}$$

is plotted along with the DSLs in Fig. 3.10. The figure shows that with this definition, the shear layer spreads at a faster rate than the DSL, as desired. Therefore this value of s_0 allows:

1. A physically reasonable DSL that starts at the edge of the nozzle orifice and spreads out, with the spread quickly becoming linear.

2. A shear layer which grows from the edge of the nozzle orifice and spreads faster than the DSL.

The final part of point 1. above is significant - examination of the DSL in the present work in Fig. 3.10 (the blue curve) shows that the curve does indeed spread linearly from only a short distance downstream of the nozzle orifice. Smoke and ink flow experiments show that the edges of jets grow linearly with downstream distance, which led Prandtl to assume that eddy viscosity is proportional to the centreline velocity and jet width [60, p.165] - the starting point derivation of the Görtler profile (see (A.2) in Appendix A). Therefore, the

DSL can be thought of as the edge of the jet, and the edge of the shear layer is the boundary of the model domain.

3.3.4 Jet curvature equation

As discussed in section 3.2.5, the jet curvature equation has been used most commonly in its steady state format, with Ries [96] making attempts to develop an unsteady version. The motivation for developing a novel, unsteady jet curvature equation is that the quasi-steady jet assumption is dubious. Kirshner & Katz [60] suggest that the quasi-steady assumption is the weakest element of all of the models in the literature, and the reason for its use is its simplicity. This is discussed at the close of this section. This derivation has a similar starting point to that of Ries [96], although a different conclusion is reached. The radial incompressible Navier-Stokes momentum equation in polar coordinates is the starting point,

$$\frac{\partial u_r}{\partial t} + u_r \frac{\partial u_r}{\partial r} + \frac{u_\phi}{r}\frac{\partial u_r}{\partial \phi} - \frac{u_\phi^2}{r} = -\frac{1}{\rho}\frac{\partial P}{\partial r} + \frac{\mu}{\rho}\left[\frac{1}{r}\frac{\partial}{\partial r}\left(r\frac{\partial u_r}{\partial r}\right) - \frac{u_r}{r^2} + \frac{1}{r^2}\frac{\partial^2 u_r}{\partial \phi^2} - \frac{2}{r^2}\frac{\partial u_\phi}{\partial \phi}\right]. \tag{3.35}$$

To aid with the derivation, reference is made to Fig. 3.12. Note that the variable ϕ in (3.35)

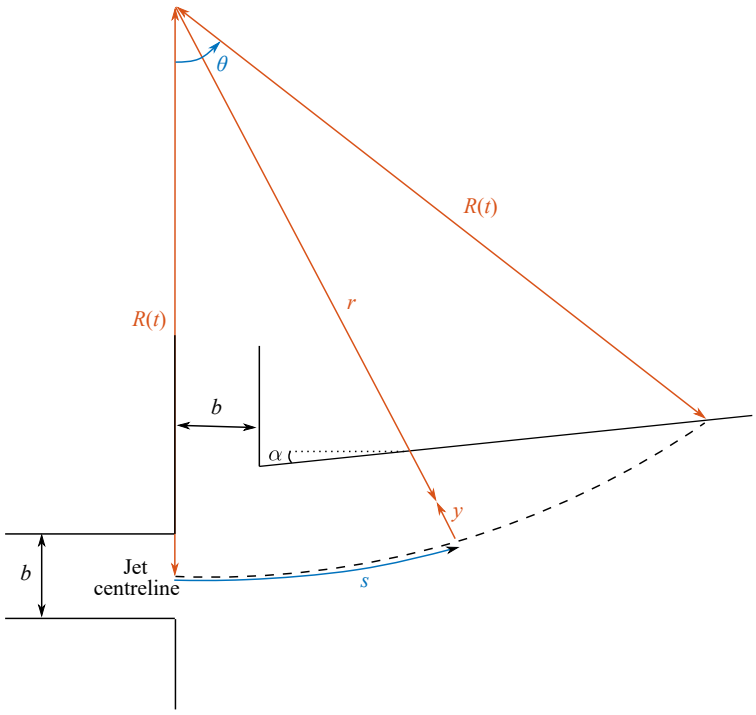

Figure 3.12: Device diagram: basic geometry

is related to s in Fig. 3.12 via $s = R\phi$. The assumptions made are:

- Viscous terms are negligible;
- No variation in radial velocity along the tangential direction, i.e. $\frac{\partial u_r}{\partial \phi} = R\frac{\partial u_r}{\partial s} = 0$;
- $R = R(t)$ is spatially constant and depends only on time.

These assumptions are justified by calculation of the relevant terms after the main derivation below. The expression $r = R - y$ can be seen from Fig. 3.12. Taking the time-derivative of this gives $u_r = \dot{R} - v$, where $v = \mathrm{d}y/\mathrm{d}t$. It is noted that $u_\phi = u$, so that (u, v) are the local tangential and radial velocity at a point in the jet, (s, y). Substituting these expressions into (3.35) and applying the above assumptions leads to

$$\left(\ddot{R} - \frac{\partial v}{\partial t}\right) - \left(\dot{R} - v\right)\frac{\partial v}{\partial r} - \frac{u^2}{r} = -\frac{1}{\rho}\frac{\partial P}{\partial r}. \tag{3.36}$$

From here, $r = R - y$ is substituted such that $\mathrm{d}r = -\mathrm{d}y$. It is assumed that $R \gg y$ (for the u^2 term), giving

$$\left(\ddot{R} - \frac{\partial v}{\partial t}\right) + \left(\dot{R} - v\right)\frac{\partial v}{\partial y} - \frac{u^2}{R} = \frac{1}{\rho}\frac{\partial P}{\partial y}. \tag{3.37}$$

As explained in section 3.2.5, Ries [96] took the integral with respect to y between the limits of $y = -\infty$ and $y = \infty$. Ries assumed that the pressure at $y = \infty$ is the bubble pressure, $P_{y=\infty} = P_\mathrm{B}$, and that $P_{y=-\infty} = P_\infty$ on the other side of the jet at $y = -\infty$ (although Ries uses $r = R + y$ so the signs of y are flipped). It was also explained that Ries made a sign error in evaluating the resulting equation, which was given by

$$[v]_{-\infty}^{\infty}\,\dot{R} - \frac{J}{\rho R} = \frac{1}{\rho}\,[P]_{-\infty}^{\infty}\,. \tag{3.38}$$

The form of the function v is shown in Fig. 3.11, which shows that $[\bar{v}]_{-\infty}^{\infty} = -2$, whereas Ries seems to evaluate $[\bar{v}]_{-\infty}^{\infty} = +2$. Note that this is not simply a result of the different sign convention for y. Additionally, Ries appears to neglect s_0 in the definition when averaging the resulting equation over the length of the jet centreline. Returning to (3.38) and evaluating (correctly) $[\bar{v}]_{-\infty}^{\infty} = -2$, the result is a negative coefficient of $\mathrm{d}R/\mathrm{d}t$, which makes the resulting differential equation unstable (perturbations about the equilibrium value of R

corresponding to a particular $[P]_{-\infty}^{\infty}$ result in $R \to 0$).

Returning to (3.37), the problem with Ries's approach of integrating with respect to y and setting the limits to $y = \pm\infty$ is that these limits do not represent the edges of the jet, and as such assuming $P_{y=\infty} = P_B$ (where P_B is the pressure in the attached side recirculation bubble) is dubious. Since the edge of the jet has been identified as the DSL, the limits are set to be $\pm y_{\mathrm{DSL}}$, where y_{DSL} is found at a given downstream station, s, with the expression in (3.32). This choice of limits makes setting $P_{y_{\mathrm{DSL}}} = P_B$ a more reasonable proposition than $P_{y=\infty} = P_B$, and is valid given the assumption of constant pressure in the bubble. Continuing with the derivation, (3.37) is integrated with respect to y between the limits $\pm y_{\mathrm{DSL}}$.

$$2y_{\mathrm{DSL}}\ddot{R} - \left[\frac{1}{2}v^2\right]_{-y_{\mathrm{DSL}}}^{y_{\mathrm{DSL}}} + [v]_{-y_{\mathrm{DSL}}}^{y_{\mathrm{DSL}}}\dot{R} - \frac{\bar{J}}{\rho R} = \frac{1}{\rho}[P]_{-y_{\mathrm{DSL}}}^{y_{\mathrm{DSL}}}, \tag{3.39}$$

where $\bar{J}$ is the momentum of the jet integrated across the nozzle exit. The term $\left[\frac{1}{2}v^2\right]_{-y_{\mathrm{DSL}}}^{y_{\mathrm{DSL}}}$ is equal to 0 because v is an odd function with respect to y, so v^2 is even and $\left[v^2\right]_{-a}^{a} = 0$. The evaluation of the term $[v]_{-y_{\mathrm{DSL}}}^{y_{\mathrm{DSL}}}$ results in a function of s. As underlined in the preceding discussion, the DSL is closer to the jet centreline than the edge of the shear layer for all values of s, except $s = 0$ where they coincide. This means that the value of η_{DSL} at each downstream station $s \geq 0$, will be in the range $0 < \eta_{\mathrm{DSL}} \leq \eta_{\mathrm{SL}}$. Referring to the plot of $\bar{v}$ in Fig. 3.11: the zero-crossings marked by the red circles correspond to $\eta = \eta_{\mathrm{SL}}$, so that $[v]_{-y_{\mathrm{DSL}}}^{y_{\mathrm{DSL}}}$ will always be non-negative for all $s \geq 0$. This means that the resulting differential equation will be stable; subject to the sign of the acceleration term coefficient. To remove the s-dependence from the $\dot{R}$ term coefficient, the equation is averaged between $s = 0$ and the attachment point, $s = R\theta$, as in Ries [96]. The coefficient of the term is given by

$$\zeta = \frac{1}{R\theta}\int_{s=0}^{s=R\theta} [v]_{-y_{\mathrm{DSL}}}^{y_{\mathrm{DSL}}}\,\mathrm{d}s \tag{3.40}$$

$$\zeta = \frac{1}{R\theta}\int_{s=0}^{s=R\theta} \frac{1}{2}\sqrt{\frac{3J}{\rho\sigma(s+s_0)}}\left[2\,\mathrm{atanh}\,(\chi)\,\mathrm{sech}^2\left(\mathrm{atanh}\,(\chi)\right) - \chi\right]\,\mathrm{d}s \tag{3.41}$$

$$\text{where } \chi = \frac{1}{\xi}\sqrt{\frac{\sigma b}{3(s+s_0)}}. \tag{3.42}$$

This is a reasonable step because the radius of curvature and the bubble pressure have been assumed to be constant in space, so the $\frac{\mathrm{d}R}{\mathrm{d}t}$ term must be independent of s for consistency.

The coefficient of the second order term in (3.39), $2y_{\mathrm{DSL}}$, is calculated by taking the mean value of y_{DSL} at $s = 0$ and $s = R\theta$ for simplicity. This is justified because y_{DSL} is approximately linear with respect to s (see Fig. 3.10), and yields the new coefficient for $\ddot{R}$, given by

$$\gamma = y_{\mathrm{DSL}}\big|_{s=0} + y_{\mathrm{DSL}}\big|_{s=R\theta}. \tag{3.43}$$

Substituting γ into the equation and solving the integral in (3.41) gives

$$\gamma\ddot{R} + \zeta\dot{R} - \frac{\bar{J}}{\rho R} = \frac{1}{\rho}\Delta P \tag{3.44}$$

$$\text{where } \zeta = \frac{1}{R\theta}\sqrt{\frac{bJ}{\rho}}\left[2\ln\left(1-\chi^2\right) + \frac{2\left(\chi^2+1\right)\,\mathrm{atanh}(\chi)}{\chi} - \ln(\chi)\right]_{\chi_1}^{\chi_2} \tag{3.45}$$

$$\text{and } \chi_1 = \frac{1}{\xi}\sqrt{\frac{\sigma b}{3s_0}},\ \ \chi_2 = \frac{1}{\xi}\sqrt{\frac{\sigma b}{3(R\theta+s_0)}}, \tag{3.46}$$

where ln() is the natural logarithm. Equations (3.44 - 3.46) are a novel jet curvature equation. As a comparison with Ries, the value of ζ is plotted against σ in Fig. 3.13 along with Ries's coefficient of $\dot{R}$, for $\dot{m} = 4.31 \times 10^{-3}$, which corresponds to $R = 14.9\,b$ and $\theta = 0.521$ rad for a device with setback $D = 2b$ and wall incline $\alpha = 6^{\mathrm{o}}$. These parameters are provided for reference but are not relevant to the comparison drawn. It can be seen in Fig. 3.13 that there is a significant difference between the coefficient in the present work compared with Ries. The coefficient is larger in Ries, so if a first order approximation were taken (ignore $\ddot{R}$ term in (3.44)), the response of the JCE is slower than in the present work. However, the inclusion of the second order term turns the value of ζ into a damping factor and changes the nature of the dynamics.

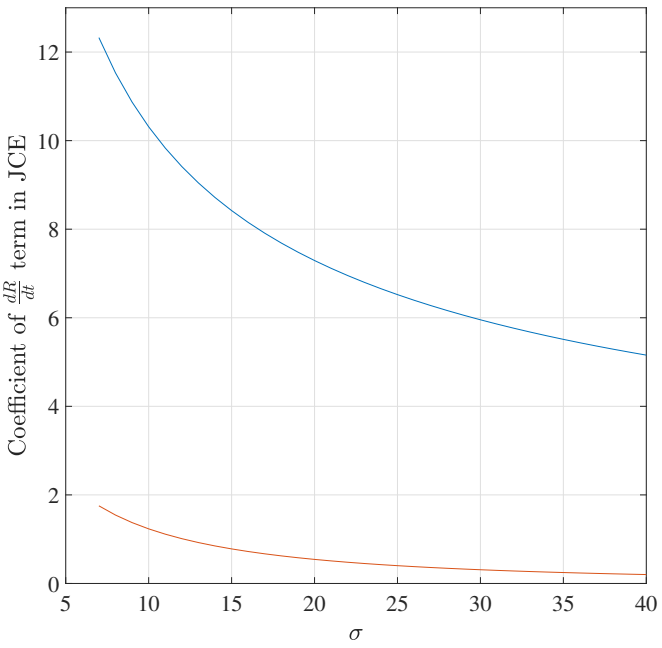

Figure 3.13: Coefficient of the $\dot{R}$ term in the jet curvature equation: Ries (3.21) [96] (blue) and the present work (3.45) (red).

Nicholls 2020	Ries 1972 [96]	Other authors
$\gamma\ddot{R} + \zeta\dot{R} - \frac{\bar{J}}{\rho R} = \frac{1}{\rho}\Delta P$	$\dot{m}\sqrt{\frac{3}{\sigma b d^2}}\frac{1}{\sqrt{\theta}}\frac{1}{\sqrt{R}}\dot{R} - \frac{J}{R} = \Delta P$	$-\frac{J}{R} = \Delta P$

Table 3.1: Jet curvature equation summary comparison

Justification of assumptions The decision to ignore viscous terms and the inertial term, $\frac{u_r}{r}\frac{\partial u_r}{\partial \phi}$, is justified here. Firstly, the inertial term can be expanded by substitution of $r = R - y$ and once again assuming $R \gg y$, giving

$$\frac{u}{r}\frac{\partial u_r}{\partial \phi} = \frac{u}{R}R\frac{\partial}{\partial s}\left(\dot{R} - v\right) = -u\frac{\partial v}{\partial s}, \tag{3.47}$$

where $\frac{\partial v}{\partial \phi} = R\frac{\partial v}{\partial s}$ and $\frac{\partial R}{\partial s} = 0$ have been used because R is purely a function of time. The function $\frac{\partial v}{\partial s}$ is an odd function in y, and u is an even function in y, such that their product is also odd. When the equation is integrated between $\pm y_{\mathrm{DSL}}$, the remaining term from (3.47) therefore goes to zero.

The viscous terms can be expanded to

$$\frac{\mu}{\rho}\left[\frac{1}{r}\frac{\partial}{\partial r}\left(r\frac{\partial u_r}{\partial r}\right)-\frac{u_r}{r^2}+\frac{1}{r^2}\frac{\partial^2 u_r}{\partial \phi^2}-\frac{2}{r^2}\frac{\partial u_\phi}{\partial \phi}\right]=\frac{\mu}{\rho}\left[-\frac{1}{R}\frac{\partial v}{\partial y}-\frac{\partial^2 v}{\partial y^2}-\frac{\dot{R}}{R^2}+\frac{v}{R^2}-\frac{\partial^2 v}{\partial s^2}-\frac{2}{R}\frac{\partial u}{\partial s}\right]. \tag{3.48}$$

The terms $\frac{\partial^2 v}{\partial y^2}$, v/R^2, and $\frac{\partial^2 v}{\partial s^2}$ in the above expression are odd, so that they disappear when integrated with respect to y between $\pm y_{\mathrm{DSL}}$. This leaves the expression

$$-\frac{\mu}{\rho}\int_{-y_{\mathrm{DSL}}}^{y_{\mathrm{DSL}}}\left(\frac{\dot{R}}{R^2}+\frac{2}{R}\frac{\partial u}{\partial s}\right)\mathrm{d}y, \tag{3.49}$$

where for the second term, use is made of continuity

$$\frac{\partial u}{\partial s}+\frac{\partial v}{\partial y}=0\Rightarrow\int\frac{\partial u}{\partial s}\mathrm{d}y=-v. \tag{3.50}$$

This cartesian form of the continuity equation was assumed in the derivation of the v-velocity in the Görtler profile, which assumes a straight jet. In order to account for the curvature of the jet, the continuity equation in polar coordinates can be used, with the Görtler profile providing the local radial and tangential velocities. This is given by

$$\frac{\partial\left(ru_r\right)}{\partial r}+\frac{\partial u}{\partial \phi}=0\;\Rightarrow\;\frac{v}{R}+\frac{\partial v}{\partial y}=\frac{\partial u}{\partial s}. \tag{3.51}$$

The importance of the addition of the centrifugal v/R term to the cartesian form of the continuity equation can be determined by evaluating it along with $\frac{\partial v}{\partial y}$ assuming the v-velocity profile determined from the cartesian form, (3.28). Substituting values ($\sigma = 7.7$, $R = 17b$, $s = 0{-}10b$) indicates that v/R is typically two orders of magnitude less than $\frac{\partial v}{\partial y}$. As such, it can be assumed that the centrifugal forces on the velocity profile are negligible. This conclusion is supported by velocity profile calculations based on measurements provided by Sawyer [99], which show no sign of asymmetry. Continuing with the evaluation of (3.49) gives

$$-\frac{\mu}{\rho}\left(\frac{2y_{\mathrm{DSL}}\dot{R}}{R^2}-\frac{2}{R}\left[v\right]_{-y_{\mathrm{DSL}}}^{y_{\mathrm{DSL}}}\right). \tag{3.52}$$

The impact of these terms on the system dynamics depends heavily on the value of μ. Turbulence closure achieved through a RANS-type model relies on the Boussinesq assumption, which is that the effect of the Reynolds stresses on the bulk flow is to increase the effective dynamic viscosity. This assumption has already been made implicitly by using the Görtler velocity profile, which assumes isotropic turbulence. The value used for the effective viscosity depends on the eddy viscosity ratio (EVR), the ratio between the effective turbulent viscosity and the molecular dynamic viscoity. EVR is typically determined experimentally, but this was not not possible. In the model, as the EVR is increased at a middling flow rate (260 slpm), the contribution of the first viscous term in (3.52) to the $\dot{R}$ term coefficient becomes one order of magnitude smaller than the other contributions when EVR $= 2 \times 10^4$. At this value, the second term is two orders of magnitude smaller than the centripetal contribution to the $1/R$ term coefficient, $\bar{J}/\rho R$. This value of EVR is unreasonably large, hence the viscous terms can be safely ignored.

Reflection on quasi-steady jet arguments It is interesting to consider the arguments made by Lush [67] and Chang [18], which they used to justify the use of the steady-state curvature equation, in light of the derivation provided in the present work. These arguments were first discussed in section 3.2.5.

Lush [67] used a scaling argument to show that an inertial term in the cartesian Navier-Stokes streamwise momentum equation dominated the unsteady term if the transport time of particles through the device is significantly less than the switching time. The same argument was made by Chang [18]. There are three points that counter this argument. Firstly, it was from the inertial term that the unsteady damping term (in $\dot{R}$) in the JCE originated, so Lush's argument would support removal of the acceleration term, $\ddot{R}$, but not the damping term, $\dot{R}$. Second, the relevant velocity was taken to be the streamwise velocity in Lush's scaling argument, but the bulk jet motion is in the cross-stream direction, and so should be compared with the cross-stream velocity, v.

The final point is that Lush [67] and Chang [18] used the overall switching time for compar-

ison with the transport time. However, since they used the steady-state JCE for modelling the first phase of switching, i.e. the subject of the present work, the attached jet response time would be more appropriate. This value is typically a lot smaller than the total switching time - in fact, this is the basis for the proposed operation of fluidic diverters using partial deflections of the jet rather than fully switching it. Therefore, while the transport time may be much less than the total switching time, this is not necessarily true for the attached jet response time. Calculations based on the roll-off frequency of the model responses in chapter 4 indicate that the jet response time is in fact comparable to the transport time.

To conclude, the origin of the terms in the JCE developed in the present work only become apparent when they are derived from the Navier-Stokes momentum equation itself. For example, Kirshner & Katz [60] and Lush [67] describe how the quasi-steady jet assumption ignores the 'acceleration' term of the jet curvature. However, the acceleration term in fact corresponds to the $\ddot{R}$ term, so the quasi-steady assumption also ignores the damping term, $\dot{R}$.

Unmodelled influences on jet curvature The weakness in the method used in the present work is that the values of $[v]_{-y_{\mathrm{DSL}}}^{y_{\mathrm{DSL}}}$ are (a) unlikely to be accurate close to the nozzle orifice unless, as already stated, the velocity profile at the nozzle exit resembles that of a Görtler profile, and (b) the Görtler profile is for a free jet, but the jet is attached so that the velocities on the attached side must be resolved into wall-parallel directions by the time the attachment point is reached at $s = R\theta$. The values of v differ from those given by the profile, which adds uncertainty to the value of v on the DSLs. With this in mind, a shape factor, κ_1, is applied to the values of v at $\pm y_{\mathrm{DSL}}$ so that they become $\kappa_1 v|_{\pm y_{\mathrm{DSL}}}$. The value of κ_1 is left as a floating constant. A fit parameter, κ_2, is applied to the coefficient of the acceleration term, $\ddot{R}$, which is also set later.

3.3.5 Bubble volumes

The bubble volumes are given by

$$V_{\mathrm{B1}} = f(\theta) = \frac{R^2}{2}\left(\theta - \sin^2(\theta)\tan(\alpha) - \frac{1}{2}\sin(2\theta)\right) + nb^2 \tag{3.53}$$

$$V_{\mathrm{B2}} = V_{\mathrm{const}} - V_{\mathrm{B1}}, \tag{3.54}$$

where the attached side bubble volume V_{B1} was found geometrically, and the unattached side volume is assumed to share the device volume with the attached side bubble and the jet (which is taken to have a constant volume), giving the simple expression for V_{B2} above. The wall incline angle is given by α, and n is a constant signifying the volume per unit depth of the control port channel.

3.3.6 Ideal gas law

The ideal gas law is applied to both the attached and unattached sides of the jet, which have subscripts 1 and 2 respectively. This approach (applied to one side) was taken in [96].

$$P_{\mathrm{B1}} = \left(\frac{R_g T}{M_m}\right)\frac{m_{\mathrm{B1}}}{V_{\mathrm{B1}}} \tag{3.55}$$

$$P_{\mathrm{B2}} = \left(\frac{R_g T}{M_m}\right)\frac{m_{\mathrm{B2}}}{V_{\mathrm{B2}}}, \tag{3.56}$$

where P_{B1} and P_{B2} are the bubble pressures on each side, m_{B1} and m_{B2} are the masses in each bubble, V_{B1} and V_{B2} are the volumes of the bubbles, R_g is the universal gas constant, M_m is the molar mass of air and T is the temperature of the gas. These last three parameters are constant. The pressure difference term in the JCE (3.44) is given by $\Delta P = P_{\mathrm{B1}} - P_{\mathrm{B2}}$ (which is negative).

Equations (3.55) & (3.56) are differentiated, giving

$$\frac{\mathrm{d}P_{\mathrm{B1}}}{\mathrm{d}t} = \left(\frac{R_g T}{M_m}\right)\left[\frac{1}{V_{\mathrm{B1}}}\frac{\mathrm{d}m_{\mathrm{B1}}}{\mathrm{d}t} - \frac{\dot{V}_{\mathrm{B1}} m_{\mathrm{B1}}}{V_{\mathrm{B1}}^2}\right] \tag{3.57}$$

$$\frac{\mathrm{d}P_{\mathrm{B2}}}{\mathrm{d}t} = \left(\frac{R_g T}{M_m}\right)\left[\frac{1}{V_{\mathrm{B2}}}\frac{\mathrm{d}m_{\mathrm{B2}}}{\mathrm{d}t} - \frac{\dot{V}_{\mathrm{B2}} m_{\mathrm{B2}}}{V_{\mathrm{B2}}^2}\right]. \tag{3.58}$$

Expressions for V_{B1} & V_{B2} were derived in section 3.3.5, and were shown to depend only on the swept angle, θ. The terms $\dot{V}_{\mathrm{B1}}$ & $\dot{V}_{\mathrm{B2}}$ can therefore be substituted via the chain rule as $\mathrm{d}f/\mathrm{d}t = (\mathrm{d}f/\mathrm{d}\theta)\,\dot{\theta} = f'\dot{\theta}$ and $\mathrm{d}\left(V_{\mathrm{const}} - f\right)/\mathrm{d}t = -(\mathrm{d}f/\mathrm{d}\theta)\,\dot{\theta} = -f'\dot{\theta}$. This, along with substitutions for P_{B1} & P_{B2}, leads to

$$\frac{\mathrm{d}P_{\mathrm{B1}}}{\mathrm{d}t} = \frac{1}{f}\left[\left(\frac{R_g T}{M_m}\right)\frac{\mathrm{d}m_{\mathrm{B1}}}{\mathrm{d}t} - P_{\mathrm{B1}} f'\dot{\theta}\right] \tag{3.59}$$

$$\frac{\mathrm{d}P_{\mathrm{B2}}}{\mathrm{d}t} = \frac{1}{V_{\mathrm{const}} - f}\left[\left(\frac{R_g T}{M_m}\right)\frac{\mathrm{d}m_{\mathrm{B2}}}{\mathrm{d}t} + P_{\mathrm{B2}} f'\dot{\theta}\right]. \tag{3.60}$$

3.3.7 Mass flows on the attached side

The mass in the attached side bubble is given by the time-integral of the difference between the entrainment and recirculation mass flows on this side, which are found with reference to Fig. 3.14. In the figure, 'SL1' is 'streamline 1' and should not be confused with the

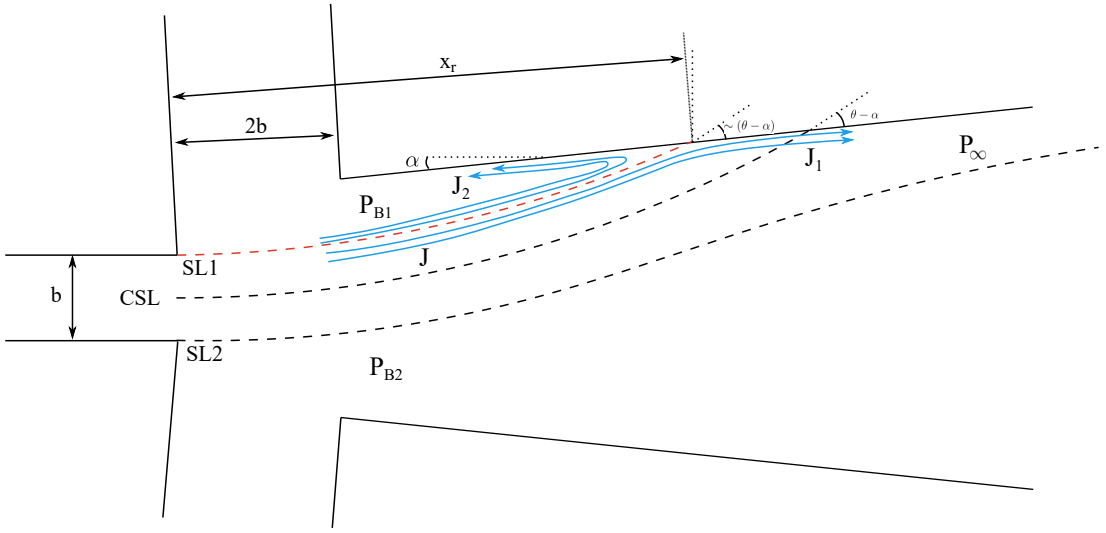

Figure 3.14: Flow on the attached side around the attachment point, where the streamlines labelled 'SL1' and 'SL2' are the same as the dividing streamlines on each side in the steady state. The streamline labelled 'CSL' is the central streamline or jet centreline.

shear layer; likewise 'SL2' is 'streamline 2'. In the steady state, these are the same as the dividing streamlines on each side respectively. Streamline 1 separates the recirculating flow (with momentum J_2) from the flow that continues downstream (with momentum J_1). The jet centreline is given by 'CSL' for 'central streamline'.

As discussed in section 3.2.3, Lush [67] introduced the idea of separating the dividing and reattaching streamlines (DSL and RSL). The RSL is equivalent to SL1 in the present work. A difference between Lush's model and the present work is that Lush's RSL did not have to agree with the DSL in the steady state - that is to say the RSL did not have to originate at the edge of the nozzle orifice. This steady state discrepancy between the DSL and RSL would occur in the presence of a steady control flow insufficient to cause the jet to switch.

The entrainment mass flow rate on the attached side can be found by integrating the velocity profile between the dividing streamline and the edge of the shear layer at the attachment point ($s = R\theta$), given by

$$\dot{m}_{\mathrm{e1}} \;=\; d\rho \int_{y_{\mathrm{DSL}}}^{y_{\mathrm{SL}}} u \,\mathrm{d}y, \tag{3.61}$$

which, once evaluated with the definition of y_{DSL} in (3.32) substituted, gives

$$\dot{m}_{\mathrm{e1}} \;=\; \frac{\dot{m}}{2}\left(\sqrt{\frac{3\xi^2\left(R\theta + s_0\right)}{b\sigma}}\tanh\left(\eta_{\mathrm{SL}}\right) \;-\; 1\right), \tag{3.62}$$

where $\eta_{\mathrm{SL}} = 1.09$. The same result can be found from

$$\dot{m}_{\mathrm{e1}} \;=\; d\rho \int_{0}^{y_{\mathrm{SL}}} u \,\mathrm{d}y \;-\; \frac{\dot{m}}{2}. \tag{3.63}$$

This agreement is expected because of the definition of the dividing streamline. The recirculated flow can be found by integrating the velocity profile between SL1 (corresponding to y_1 and η_1) and the edge of the shear layer at the attachment point, given by

$$\dot{m}_{\mathrm{r1}} \;=\; d\rho \int_{y_1}^{y_{\mathrm{SL}}} u \,\mathrm{d}y \;=\; \sqrt{\frac{3\xi^2\dot{m}^2\left(R\theta + s_0\right)}{4b\sigma}}\left(\tanh\left(\eta_{\mathrm{SL}}\right) \;-\; \tanh\left(\eta_1\right)\right). \tag{3.64}$$

In the steady state, SL1 is the same as the attached side DSL and $\dot{m}_{r1} = \dot{m}_{e1}$. Note that the expressions for both $\dot{m}_{e1}$ and $\dot{m}_{r1}$ have been evaluated at $s = R\theta$. To clarify: SL1 refers to the whole streamline at $y = y_1$ and is not evaluated in s, while η_1 is defined at $s = R\theta$, and is given by

$$\eta_1 = \frac{y_1 \sigma}{R\theta + s_0}. \tag{3.65}$$

3.3.8 Mass flows on the unattached side

A novel aspect of the present work is the modelling of the unattached side flows, which are shown in Fig. 3.15. The flow is shown to spread out across the entire channel some distance

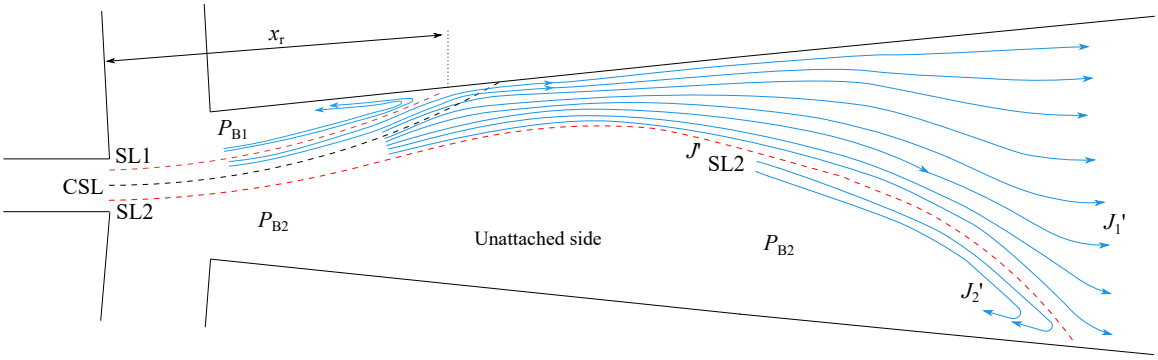

Figure 3.15: Flow on the unattached side showing the flow dividing. 'SL2' is streamline 2, which separates the flow that recirculates into the unattached side bubble from the flow that continues downstream. Note that the upper wall is the attached side, and the lower wall is the unattached side.

downstream of the attachment point. The channel has been assumed to be sufficiently long for this to occur before termination with an exit slot to atmospheric conditions. As such, forward flow must exist across the entire width of the exit slot, and an attached point must exist on the unattached side wall some distance downstream of the attached side attachment point, as shown in Fig. 3.15. The region in Fig. 3.15 on the unattached side between SL2 and the lower wall can be thought of as a recirculation bubble, although it is much larger and less well-defined than on the attached side. Its pressure is assumed to be uniform and to take the value P_{B2}. In Fig. 3.15, 'SL2' is the streamline that divides the flow on the unattached side: the flow below this streamline is recirculated into the unattached side recirculation bubble, while flow above continues downstream to the outlet.

The entrainment and recirculation flows on the unattached side are given by

$$\dot{m}_{\mathrm{e}2} = d\rho \int_{-\eta_{\mathrm{SL}}}^{0} u \, \mathrm{d}y - \frac{\dot{m}}{2} = \frac{\dot{m}}{2} \left(\sqrt{\frac{3\xi^2 \left(x_{\mathrm{US}} + s_0\right)}{b\sigma}} \tanh\left(\eta_{\mathrm{SL}}\right) - 1 \right) \tag{3.66}$$

$$\dot{m}_{\mathrm{r}2} = d\rho \int_{-\eta_{SL}}^{-y_2} u \, \mathrm{d}y = \frac{\dot{m}}{2} \sqrt{\frac{3\xi^2 \left(x_{\mathrm{US}} + s_0\right)}{b\sigma}} \left(\tanh\left(\eta_{\mathrm{SL}}\right) - \tanh\left(\eta_2\right) \right) \tag{3.67}$$

$$\eta_2 = \frac{y_2 \sigma}{x_{\mathrm{US}} + s_0}, \tag{3.68}$$

where η_2 is the non-dimensional position of SL2 at $s = x_{\mathrm{US}}$ in Fig. 3.15, and x_{US} is the length of SL2. In the steady state, SL2 is equal to the unattached side DSL and $\dot{m}_{\mathrm{r}2} = \dot{m}_{\mathrm{e}2}$. These expressions are the same as their equivalents on the attached side, with the only notable difference that the entrainment length has changed from $s = R\theta$ to $s = x_{\mathrm{US}}$.

3.3.9 Momentum equation on the attached side

Bourque & Newman found that the form of the momentum flux conservation equation around the attachment point depended on the control volume used [11]. A small control volume around the attachment point led to the attachment point theory, which indicates that the flow divides according to the angle of the jet as it strikes the wall, and does not depend on the bubble pressure. A larger control volume that occupied the whole region from the nozzle orifice to beyond the attachment point resulted in the control volume theory. In the present work, the control volume is taken to be in between these extremes with a length L_1 perpendicular to the wall, and is shown in Fig. 3.16. The momentum equation from the

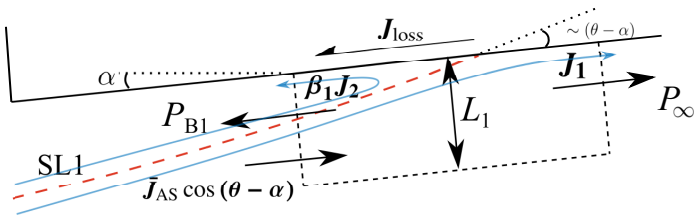

Figure 3.16: Control volume on the attached side around the attachment point.

analysis of this control volume takes the form

$$\left(P_{\mathrm{B1}} - P_\infty\right) L_1 - J_{\mathrm{loss}} = \left(J_1 - \beta_1 J_2\right) - \bar{J}_{\mathrm{AS}} \cos\left(\theta - \alpha\right), \tag{3.69}$$

where P_∞ is the pressure downstream of the control volume, J_2 is the momentum of the recirculation flow, J_1 is the momentum of the flow that continues downstream, $\bar{J}_{\text{AS}}$ is the fraction of the inlet momentum which enters the control volume, and J_{loss} represents the momentum lost to the wall through shear stresses within the control volume and is taken to be constant relative to the inlet momentum.

To understand how the momentum and pressure varies along the wall and the consequences of choosing a particular control volume, it is instructive to consider the simpler situation of a jet striking a wall. This is shown with the jet perpendicular to the wall in Fig. 3.17. The

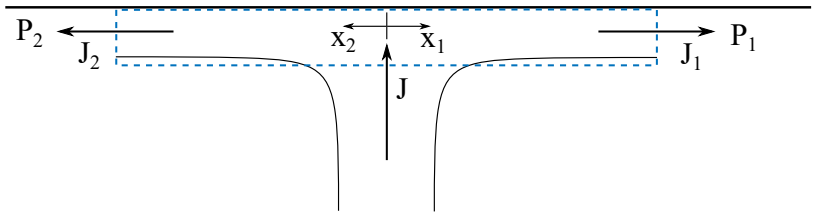

(a) Diagram of pressure and momentum.

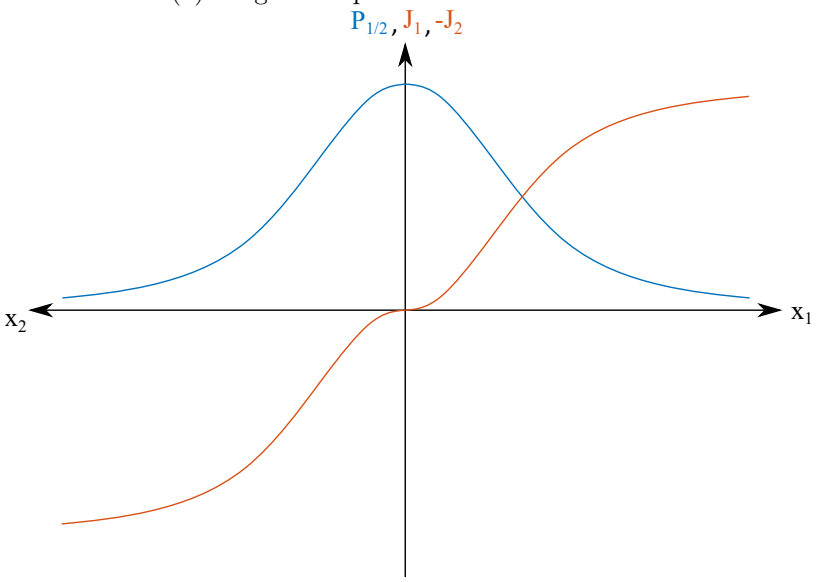

(b) Pressure and momentum on either side of the splitting point.

Figure 3.17: Jet striking wall perpendicularly in the absence of external pressure gradients.

pressure and momentum along the wall in either direction from the striking point are shown in Fig. 3.17b. This shows how the pressure at the wall, which was provided by recovering the dynamic head associated with jet momentum, J, is transferred back to the dynamics heads with momenta J_1 and J_2 in the wall-parallel direction. Consider now three changes

to the situation in Fig. 3.17:

1. The jet strikes the wall at an angle θ rather than perpendicularly;
2. A depression is superimposed adjacent to the wall on one side of the jet;
3. A back wall exists perpendicular to the main wall beyond the depression against which any flow in that direction stagnates.

These changes are shown in Fig. 3.18. This is effectively the same situation as in the control

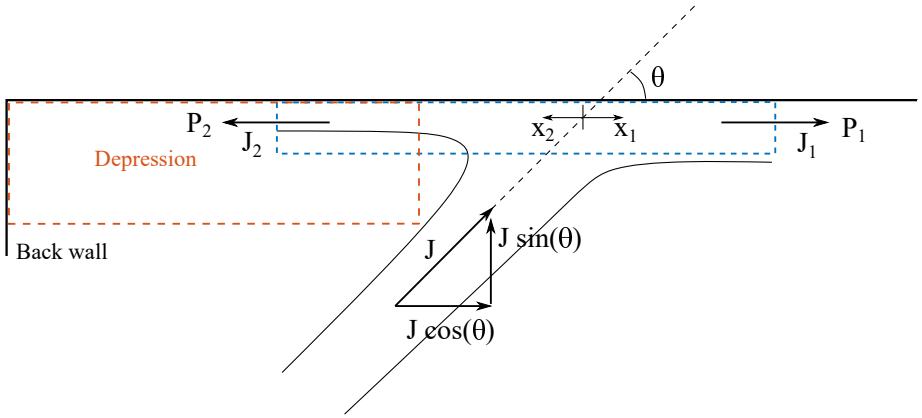

(a) Diagram of pressure and momentum.

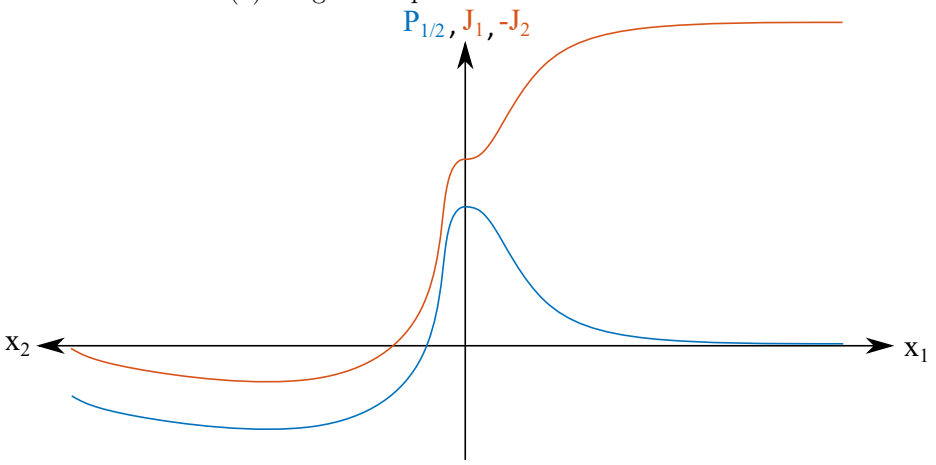

(b) Pressure and momentum on either side of the splitting point.

Figure 3.18: Jet striking a wall at an angle, θ, with both a depression and a perpendicular 'back wall' on one side.

volume in Fig. 3.16. It can be seen in Fig. 3.18b that the recirculated flow is first driven by the high pressure associated with the attachment point at small values of x_2, and later stagnates against the back wall so is recovered as pressure again. Since the bubble pressure

is assumed to be uniform, the upstream control volume edge must coincide with the mean pressure in the bubble. This is like choosing a value of P_2 in Fig. 3.18b then choosing the value of J_2 at the same position, x_2. On the downstream side, the value chosen for P_1 similarly fixes the downstream edge of the control volume and therefore the appropriate value of J_1 can be determined. Therefore, the parameter β_1 in (3.69) indicates the fraction of the recirculated momentum that corrects to the recirculation flow dynamic head that has not yet been recovered as pressure and which exits the control volume at its upstream boundary - β_1 is left as a floating constant. On the downstream side, the value of P_2 in Fig. 3.18b is equivalent to P_∞ in Fig. 3.16. The value taken is $P_\infty = 0$, which justifies the inclusion of the entirety of the forward momentum, J_1, in (3.69), rather than applying a factor similar to β_1. This means choosing the downstream control volume edge to be positioned sufficiently far along the wall so that the entirety of the pressure rise at the attachment point has been transferred back to dynamic pressure, with associated momentum, J_1.

Sawyer [99] measured the pressure along the attachment wall at several points, as well as along the wall in the spanwise direction. He demonstrated that the attachment wall measurements were in good agreement with the mean pressure in the flow column perpendicular to the attachment wall. That is to say that the measurements made at a given downstream station at the wall were in agreement with the mean pressure along the cross-stream direction from the measurement position on the wall across the bubble up to the jet. These measurements were taken at several setback values and are shown in Fig. 3.19, where the annotations are relevant to the present work rather than to Sawyer's. In the figure, x is the distance along the attachment wall from the back wall. Sawyer identified the attachment point to coincide with the maximum pressure, so that the region of x-values before the attachment point contains the recirculation bubble.

The value of setback in the present work is $D = 2b$, which is around half the smallest setback considered by Sawyer [99]. Considering the smallest setback curve in Fig. 3.19, the shape of the pressure variation along the wall agrees with the sketch in Fig. 3.18b. These data therefore support the arguments made above regarding the position of the con-

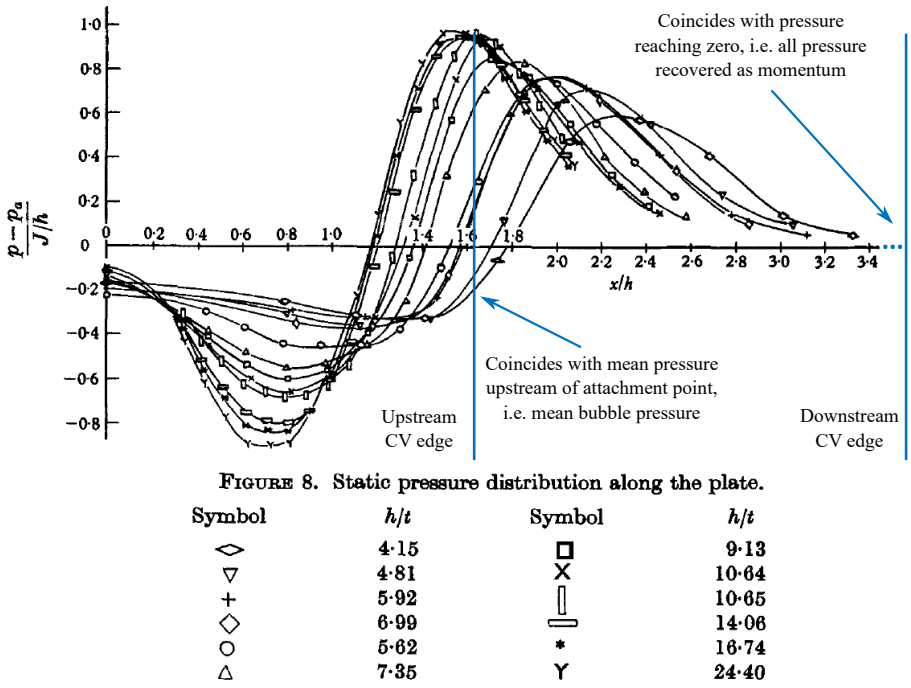

FIGURE 8. Static pressure distribution along the plate.

Symbol	h/t	Symbol	h/t
◇	4·15	□	9·13
▽	4·81	X	10·64
+	5·92	▯	10·65
◇	6·99	▬	14·06
○	5·62	*	16·74
△	7·35	Y	24·40

Figure 3.19: Sawyer's [99] measurements of pressure along the attachment wall for varying setback lengths. Note the nomenclature: x is the distance along the attachment wall, h is the attachment wall setback (D in present work), and t is the nozzle width (b in present work.) The wall incline angle is $\alpha = 0^{\circ}$ and $\mathrm{Re} = 9.5 \times 10^4$. Annotations relate to arguments made in the present work.

trol volume in the present work, the notional edges of which are included as annotations in Fig. 3.19 on the smallest setback curve. It should be noted that Sawyer opted for the attachment point theory, but made use of a 2$^{\text{nd}}$ control volume around the upstream side of the attachment point to make similar arguments about pressure recovery to those discussed above.

Momentum equation with acoustic excitation Instead of taking the attachment point theory approach from Borque & Newman [11], retaining the pressure term in the momentum equation is important in the present work. Otherwise, it would not be possible to support steady state deflection positions other than the unexcited case. The effect of acoustic excitation is to increase the jet spreading on both sides of the jet, but more so on the side at which the excitation is directed [24, 134, 73]. This fact is used here to explain why the pressure term in the momentum equation is required.

Figure 3.20 shows a timeline of flow snapshots around the attachment point for the case

where the pressure term is absent from the momentum conservation equation (3.69) - the thickness and number of streamlines represents the quantity of mass flow in each case. The

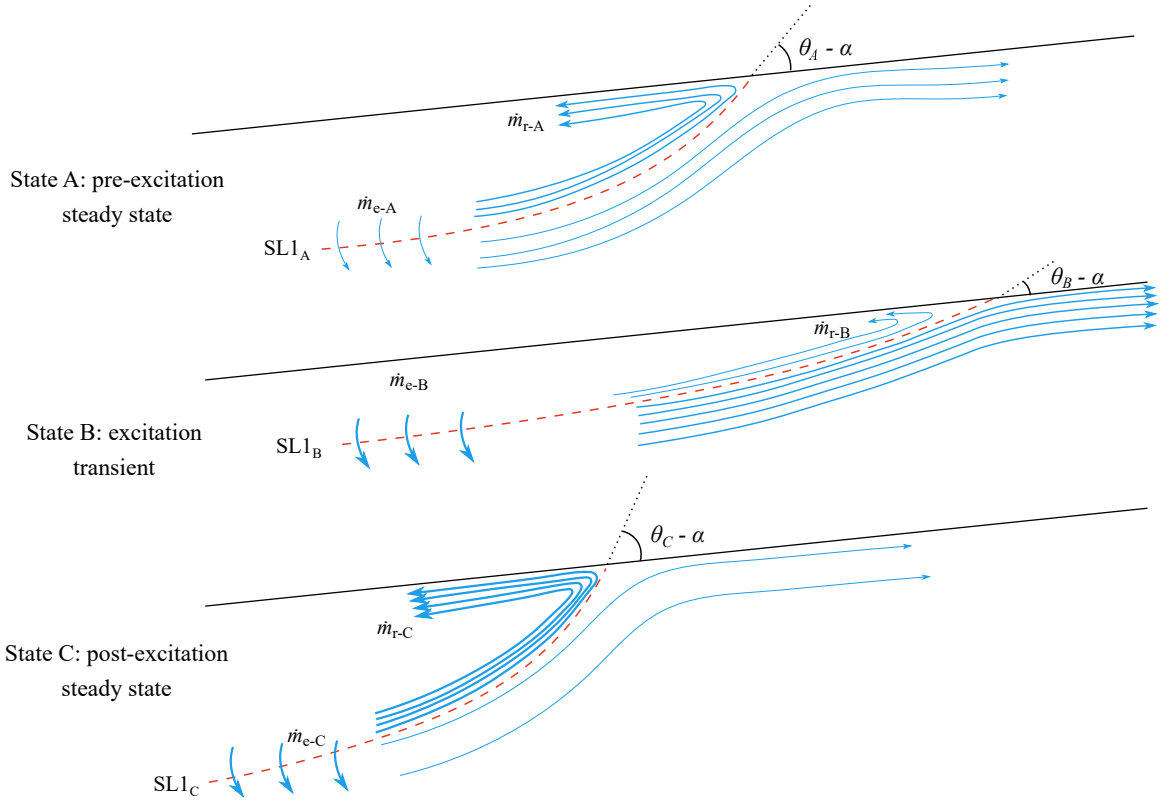

Figure 3.20: Flow around the attachment point during the excitation transient if the pressure term is removed from the momentum conservation equation, (3.69). The thickness and number of streamlines represents the quantity of mass flow.

unexcited situation is shown in the top diagram in Fig. 3.20 (State A). Consider the events that take place when the excitation is turned on, for now taking $J_{\text{loss}} = 0$ in (3.69). First, the entrainment increases on the unattached side more than the attached side, reducing the magnitude of the pressure difference across the jet, ΔP in (3.44), which in turn causes the radius of curvature to increase (θ decreases) and the attachment point to move downstream. This is shown in the middle diagram in Fig. 3.20 (State B). The behaviour that follows depends on the form of the momentum equation. Taking the attachment point theory from Bourque & Newman [11] means removing the pressure term in (3.69) and setting $\beta_1 = 1$. In this case, the only effect of the excitation and the corresponding downstream movement of the attachment point on the momentum balance (3.69) would be the reduction in θ. Since the jet is now striking the wall at a less direct angle ($\theta - \alpha$ is smaller), less flow is recir-

culated, as represented by the streamlines in Fig. 3.20 (State B). However, the excitation has caused the attached side entrainment flow to increase, so the recirculation flow must increase to the same value to reach a steady state.

Without a pressure term in the momentum equation, the only means by which the recirculation flow can increase is by the jet striking the wall at a more direct angle ($\theta - \alpha$ must increase), i.e. stronger attachment. The bubble pressure therefore continues to drop until the absolute pressure difference across the jet is *greater* than it was before the excitation. The end result is that acoustic excitation *strengthens*, rather than weakens, the Coandă effect, as shown by the bottom diagram in Fig. 3.20 (State C) - this is the opposite of what is observed in reality.

If instead the pressure term is included in the momentum equation, the recirculation flow is able to increase to the new, acoustically-excited level of entrainment through the direct action of the stronger pressure gradient created by, $P_{\mathrm{B1}} - P_{\infty}$, as opposed to requiring that the jet strikes the wall at a more acute angle. Numerous articles concerning re-attaching jet models, both of the steady and unsteady varieties, have made use of the attachment point theory [11, 99, 64, 67, 68, 18, 41, 31]. It has only been made apparent through use of acoustic excitation that this is an over-simplification that leads to the incorrect conclusion.

3.3.10 Momentum equation on the unattached side

In a similar vein, a control volume is taken around the attachment point on the unattached side in Fig. 3.15, which is shown in Fig. 3.21. The control volume has a length L_2 perpendicular to the streamwise direction, and the other variables mirror those on the attached side. Analysis of the control volume gives the momentum equation

$$(P_{\mathrm{B2}} - P_{\infty})\, L_2 \;=\; J_1' - \beta_2 J_2' - \bar{J}_{\mathrm{US}} + J_{\mathrm{loss}}', \tag{3.70}$$

where $\bar{J}_{\mathrm{US}}$ is the fraction of the jet entering the control volume, J_1' is momentum of the forward flow, $\beta_2 J_2'$ is the momentum of the flow that is recirculated into the unattached

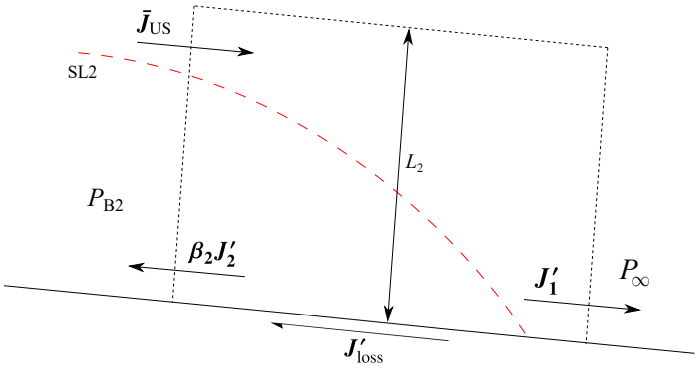

Figure 3.21: Control volume on the unattached side around the attachment point.

side recirculation bubble, J'_{loss} is a shear stress term, and P_∞ is the pressure downstream of the control volume. Similar to the attached side, the parameter β_2 indicates the fraction of the recirculated momentum corresponding to the quantity of dynamic pressure converted from static pressure at the upstream edge of the control volume, which is once again chosen to coincide with the mean pressure in the unattached side recirculation bubble. As on the attached side, $P_\infty = 0$.

3.3.11 Momentum terms

The various momentum terms are found by integrating the velocity profile. On the attached side

$$\bar{J}_{\mathrm{AS}} = \int_0^{y_{\mathrm{SL}}} \rho u^2 \,\mathrm{d}y \qquad J_2 = \int_{y_1}^{y_{\mathrm{SL}}} \rho u^2 \,\mathrm{d}y \qquad J_1 = \int_0^{y_1} \rho u^2 \,\mathrm{d}y, \tag{3.71}$$

which evaluate to

$$\bar{J}_{\mathrm{AS}} = \tfrac{3}{4}\left(t_{\mathrm{SL}} - \tfrac{1}{3}t_{\mathrm{SL}}^3\right) \qquad J_2 = \tfrac{3}{4}\left(t_{\mathrm{SL}} - \tfrac{1}{3}t_{\mathrm{SL}}^3 - \left(t_1 - \tfrac{1}{3}t_1^3\right)\right) \qquad J_1 = \tfrac{3}{4}\left(t_1 - \tfrac{1}{3}t_1^3\right), \tag{3.72}$$

where $t_{\mathrm{SL}} = \tanh(\eta_{\mathrm{SL}})$ and $t_1 = \tanh(\eta_1)$. On the unattached side, the terms are

$$\bar{J}_{\mathrm{US}} = \int_{-y_{\mathrm{SL}}}^{0} \rho u^2 \,\mathrm{d}y \qquad J_2' = \int_{-y_{\mathrm{SL}}}^{-y_2} \rho u^2 \,\mathrm{d}y \qquad J_1' = \int_{-y_2}^{0} \rho u^2 \,\mathrm{d}y \tag{3.73}$$

which evaluate to

$$\bar{J}_{\mathrm{US}} = \tfrac{3}{4}\left(t_{\mathrm{SL}} - \tfrac{1}{3}t_{\mathrm{SL}}^3\right) \qquad J_2' = \tfrac{3}{4}\left(t_{\mathrm{SL}} - \tfrac{1}{3}t_{\mathrm{SL}}^3 - \left(t_2 - \tfrac{1}{3}t_2^3\right)\right) \qquad J_1' = \tfrac{3}{4}\left(t_2 - \tfrac{1}{3}t_2^3\right), \tag{3.74}$$

where $t_2 = \tanh(\eta_2)$, y_2 corresponds to the position of SL2, and η_2 is defined specifically as the point on SL2 where $s = x_{\mathrm{US}}$.

3.3.12 Radius of jet centreline

The jet radius, R, is related geometrically to the swept angle, θ, by

$$R = g(\theta) = \frac{y_{\mathrm{co}} - x_{\mathrm{co}}\tan(\alpha)}{1 - \cos(\theta) - \sin(\theta)\tan(\alpha)}, \tag{3.75}$$

where x_{co} and y_{co} are the position of the corner between the side wall and the control port relative to the centre of the nozzle orifice.

3.3.13 Nonlinear model

The preceding equations can be manipulated to produce a nonlinear model with states θ, $\dot{\theta}$, P_{B1}, P_{B2}, given by

$$\ddot{\theta} = \frac{\frac{1}{\rho}\Delta P + \frac{\bar{J}}{\rho g} - \zeta g'\dot{\theta} - \gamma g''\dot{\theta}^2}{\gamma g'} \tag{3.76}$$

$$\dot{P}_{\mathrm{B1}} = \frac{c_3\dot{m}}{2}\left[1 - \tanh\left(\frac{y_1\sigma}{R\theta + s_0}\right)\sqrt{\frac{3\xi^2(g\theta + s_0)}{b\sigma}}\right] f^{-1} - P_{\mathrm{B1}}f'f^{-1}\dot{\theta} \tag{3.77}$$

$$\dot{P}_{\mathrm{B2}} = \frac{c_3\dot{m}}{2(V_{\mathrm{const}} - f)}\left[1 - \tanh\left(\frac{y_2\sigma}{x_{\mathrm{US}} + s_0}\right)\sqrt{\frac{3\xi^2(x_{\mathrm{US}} + s_0)}{b\sigma}}\right] + \frac{P_{\mathrm{B2}}f'}{(V_{\mathrm{const}} - f)}\dot{\theta}, \tag{3.78}$$

where $c_3 = \frac{R_{\mathrm{g}}T}{M_{\mathrm{m}}}$ is a constant and $\tanh\left(\frac{y_1\sigma}{R\theta + s_0}\right) = t_1$ is given by

$$-\frac{1}{4}(1 + \beta_1)t_1^3 + \frac{3}{4}(1 + \beta_1)t_1 - \frac{3}{4}\left(t_{\mathrm{SL}} - \frac{1}{3}t_{\mathrm{SL}}^3\right)\left(\beta_1 + \cos(\theta - \alpha)\right) + \frac{J_{\mathrm{loss}}}{J} - \frac{P_{\mathrm{B1}}L_1}{J} = 0, \tag{3.79}$$

which results from manipulating the momentum equation on the attached side (3.69). Additionally, $\tanh\left(\frac{y_2\sigma}{x_{\mathrm{US}}+s_0}\right) = t_2$ is given by

$$-\frac{1}{4}\left(1+\beta_2\right)t_2^3 + \frac{3}{4}\left(1+\beta_2\right)t_2 - \frac{3}{4}\left(t_{\mathrm{SL}} - \frac{1}{3}t_{\mathrm{SL}}^3\right)\left(\beta_2+1\right) + \frac{J'_{\mathrm{loss}}}{J} - \frac{P_{\mathrm{B2}}L_2}{J} = 0, \tag{3.80}$$

which, similarly, results from the unattached side momentum equation (3.70).

3.3.14 Modelling the acoustic control input

Experimental results [24, 134, 73] confirm that the effect of acoustic excitation is to increase the jet spreading on both sides of the jet, but more so on the side at which the excitation is directed. Mair et al. [70] demonstrated this clearly through PIV experiments, as well as the shortening of the jet potential core. In the present work the excitation is always on the unattached side, so that a constant acoustic tone should be expected to result in a biased offset in jet spreading from the natural values on either side. The spreading is indicated by the parameter σ in the model. Up to now, its value has been taken to be the same throughout. Different values of σ are introduced here for either side of the jet, σ_{AS} and σ_{US}, while the average of these values, σ_{mean}, is used in the evaluation of the jet curvature equation. This also results in three jet virtual origins because $s_0 = 0.46\sigma b$, leading to $s_{0_{\mathrm{AS}}}$, $s_{0_{\mathrm{US}}}$, and $s_{0_{\mathrm{mean}}}$.

In order to validate the model, the intention is to perturb the jet dynamically. As such, a time-varying input, $\sigma_\sim$, is added to the expressions for entrainment and recirculation on the unattached side only, to account for the bias in the effect of the excitation. When first tested, including $\sigma_\sim$ on the attached side had a negligible effect on the system dynamics. However, more detailed analysis has shown that the dynamics are insensitive to fractions of $\sigma_\sim$ appearing in the attached side ideal gas law, (3.77), up to a limit, at which point a bifurcation occurs and there is a reversal of the jet response to acoustic excitation. In other words, above this limit, excitation strengthens rather than weakens the jet attachment. This model feature is discussed in section 4.12.3, where the effect of the excitation on the

attached side spreading relative to the unattached side spread is bounded. For now, $\sigma_\sim$ is confined to be added to σ_{US}, and by extension to σ_{mean}. The nonlinear model with the control input added is given by

$$\ddot{\theta} = \frac{\frac{1}{\rho}\Delta P + \frac{\bar{J}}{\rho g} - \zeta g'\dot{\theta} - \gamma g''\dot{\theta}^2}{\gamma g'} \tag{3.81}$$

$$\dot{P}_{\text{B1}} = \frac{c_3\dot{m}}{2}\left[1 - t_1\sqrt{\frac{3\xi^2\left(g\theta + s_{0_{\text{AS}}}\right)}{b\sigma_{\text{AS}}}}\right] f^{-1} - P_{\text{B1}}f' f^{-1}\dot{\theta} \tag{3.82}$$

$$\dot{P}_{\text{B2}} = \frac{c_3\dot{m}}{2\left(V_{\text{const}} - f\right)}\left[1 - t_2\sqrt{\frac{3\xi^2\left(x_{\text{US}} + s_{0_{\text{US}}}\right)}{b\left(\sigma_{\text{US}} + \sigma_\sim\right)}}\right] + \frac{P_{\text{B2}}f'}{\left(V_{\text{const}} - f\right)}\dot{\theta}, \tag{3.83}$$

where t_1 and t_2 are found from the momentum equations (3.79) and (3.80). The coefficient ζ is given by

$$\zeta = \frac{\kappa_1}{R\theta}\int_{s=0}^{s=R\theta}\frac{1}{2}\sqrt{\frac{3J}{\rho\sigma_{\text{mean}}(s + s_{0_{\text{mean}}})}}\left[2\,\text{atanh}\left(\chi\right)\,\text{sech}^2\left(\text{atanh}\left(\chi\right)\right) - \chi\right]\,\text{d}s \tag{3.84}$$

$$\text{where } \chi = \frac{1}{\xi}\sqrt{\frac{\sigma_{\text{mean}}b}{3(s + s_{0_{\text{mean}}})}}. \tag{3.85}$$

The coefficient γ is found from

$$\gamma = \kappa_2\left(y_{\text{DSL}}\big|_{s=0} + y_{\text{DSL}}\big|_{s=R\theta}\right), \tag{3.86}$$

where κ_2 is the fit parameter described in section 3.3.4, and y_{DSL} is found from

$$y_{\text{DSL}} = \frac{s + s_{0_{\text{mean}}}}{\sigma_{\text{mean}}}\,\text{atanh}\left(\frac{1}{\xi}\sqrt{\frac{\sigma_{\text{mean}}b}{3(s + s_{0_{\text{mean}}})}}\right). \tag{3.87}$$

Finally, the system output is taken to be the bulk jet position as indicated by θ.

3.3.14.1 Summary of unknowns

A nonlinear system has been derived. Several parameters were added to the system equations without indication of their value. These are: L_1, L_2, $\frac{J_{\text{loss}}}{J}$, $\frac{J'_{\text{loss}}}{J}$, x_{US}, V_{const}, σ_{AS}, σ_{US}, β_1, β_2, κ_1, and κ_2. It is assumed that they are constant with respect to the states, and

their values are determined in due course.

3.4 Discussion

In this section, the potential sources of error in the assumptions and equations used in the model are discussed.

3.4.1 Görtler profile

Attached rather than free jet The Görtler profile is for a free rather than an attached jet. By the time particles have travelled to the attachment point, their velocities must be resolved into the wall-parallel direction. Additionally, the jet is confined on the attached side and there is a recirculation bubble adjacent to it. Sawyer [99] calculated the Görtler profile projection onto the direction parallel to the wall at two stations with $\sigma = 15$ and set the profile momentum using measurements with pitot-static tubes. The calculated profiles were compared with scaled plane jet measurements made by Förthmann [33], both of which are shown in Fig. 3.22. The close agreement of these calculated profiles supports the use of the Görtler profile in any modelling efforts. Note for reference that the attachment point of the jet at this setback distance in Sawyer [99] was $x = 11.2b$, so that the profiles in Fig. 3.22 represent slices at 31% and 65% of the length of the jet between the nozzle orifice and the attachment point. However, the interaction of the jet with the wall might have more significant consequences on the profile when the setback is smaller, as in the present work. Additionally, Sawyer did not provide the length of the slot from which the jet issues, which determines how well-developed the profile is at the nozzle exit.

The jet velocity profile appears to be symmetric, as indicated by Fig. 3.22 and by the lack of the importance of the centrifugal term, v/R, in the continuity equation, as evidenced in (3.50) in section 3.3.4. This appears to contradict the statement that the entrainment rates on each side of the jet are different. Sawyer [100] investigated this apparent inconsistency, confirming a symmetric profile for a jet where the entrainment rate on attached/unattached side was decreased/increased by 50% relative to that of a plane jet. Sawyer [100] went on

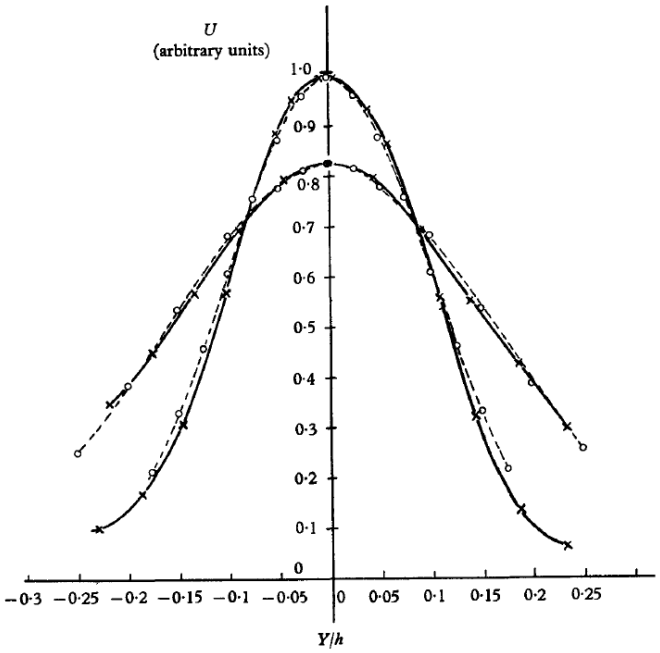

Figure 3.22: Sawyer's [99] velocity profiles: calculated from projection of Görtler profile into wall-parallel direction with $\sigma = 15$ (+) and scaled plane jet measurements made by Förthmann [33] (o) at $x = 3.42b$ and $x = 7.33b$, where x is the distance along the attachment wall. The wall incline angle is $\alpha = 0^{\circ}$, the setback is $D = 5.62b$ and the Reynolds number is $\mathrm{Re} = 9.5 \times 10^4$.

.

to demonstrate using a first-order mixing length argument that this result is expected.

Shear layer development A brief derivation of the profile was offered in Appendix A, where it was explained that the starting point of the derivation is Prandtl's assumption that the eddy viscosity is proportional to jet width and centreline velocity at a given downstream station. The use of eddy viscosity as a concept implicitly assumes the Boussinesq approximation that the effects of turbulence can be summarised by an additional turbulent viscosity term, which is independent of orientation and therefore also assumes isotropic turbulence [122, p. 67-68].

As mentioned in section 2.6.3.2, the jet potential core is typically around three to five inlet nozzle diameters in length, depending on the excitation provided [71]. The turbulence cannot be considered isotropic for stations upstream of the end of the potential core - vortices exist beyond the potential core for some distance. For reference, the length of the jet

centreline between the orifice and the attachment point, i.e. $s = R\theta$, takes values around $s \approx 10b$ in the present work, so that the potential core could last for approximately half of the length of the jet. The adopted strategy in this thesis has been to match the Görtler profile to the nozzle exit conditions by a continuity argument.

A better approach might be to characterise the velocity profile experimentally at several stations downstream of the nozzle orifice to determine the station where it becomes possible to match the Görtler profile. For the purposes of this discussion, this station is named the critical station. There are two indicators that could be used to judge the location of the critical station. Firstly, the profile itself should start to resemble a $\text{sech}^2(\eta)$ shape, and a least-square error fit could be conducted with an error threshold. Gori et al. [39] studied a jet emerging from a rectangular nozzle at Reynolds numbers with respect to the nozzle width ranging from $\text{Re} = 3400$ to $\text{Re} = 35,300$. The time-averaged velocity profile was determined with PIV measurements at several stations downstream of the nozzle orifice, and the range of Reynolds numbers considered overlaps those in the present work. The location of the critical station can be judged visually from the profiles given, and depends on the Reynolds number. In general, the larger the Reynolds number, the further downstream the critical station. This is assumed to be a result of the differing velocity profiles at the nozzle orifice. In the largest Reynolds number case, $\text{Re} = 35,300$, the most downstream station is shown below with a visually-fitted $\text{sech}^2(\eta)$. The value of σ for the fitted $\text{sech}^2(\eta)$ can be

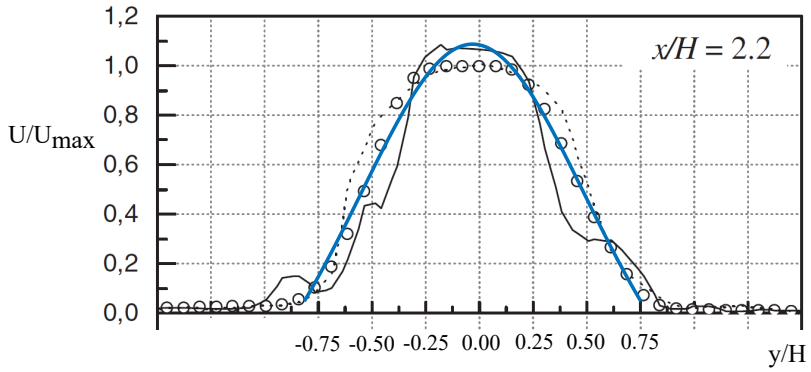

Figure 3.23: Gori et al.'s [39] time-averaged PIV velocity profile measurements at $s = 2.2b$ (o), with fitted $\text{sech}^2(\eta)$, $\text{Re} = 3.53 \times 10^4$ ($\sigma = 13$, blue curve). Dashed and solid black curves are instantaneous velocity measurements. Note that $H = b$.

.

determined from the values of η used and how they match the values of y in the profile. The values used for s and s_0 were $s = 2.2b$ and $s_0 = 0.46\sigma b$ as per the present model. Solving for the spread factor gives $\sigma = 13$, which is reasonable in light of the discussion of the value of σ in 4.12.2. The trend in the profiles at increasingly downstream stations is towards the Görtler profile. The fit given in Fig. 3.23 at $s = 2.2b$ provides at least a qualitative idea of the degree of error in assuming such a profile at this station. The experiments conducted by Gori et al. [39] were based on a free rather than an attached jet, which may introduce errors. However, the profiles offered by Sawyer [99] in Fig. 3.22 suggest these errors are negligible, at least for values of setback several times larger than in the present work.

The second indicator for the location of the critical station could come from considering that the Görtler profile assumes that eddy viscosity is constant across the jet. Eddy viscosity is related to turbulence intensity [122, p. 67-68], which can be measured with a hot wire. Therefore, a threshold for the variation in turbulence intensity across the jet could be used to determine the critical station.

A composite condition based on both indicators may be most effective. Once achieved, a second velocity profile could be obtained at a station further downstream. This would give an indication of how the profile is developing, and allow the spread factor and virtual origin coefficient (i.e. the constant in $s_0 = C\sigma b$; $C = 0.46$ in the present work) to be set to match both profiles. This approach would allow the profile development to be captured more accurately in the model. Sawyer [100] used a similar strategy, and obtained good agreement between predicted and experimentally-determined attachment lengths. However, it should be noted that the goal in the present work is to capture the system dynamics rather than the steady state conditions. The relatively large effort involved in matching the velocity profiles and subsequent complexity added to the model may not yield a justifiable improvement. The purpose of the model is learn about the attachment dynamics using the simplest possible description of the physics.

3.4.2 Bubble pressure model

The ideal gas law was used to model the bubble pressure in the present work. The ideal gas law allows for the calculation of the total pressure in the bubble, but does not take into account the reduction in static pressure due to the dynamic pressure associated with the swirling flow. This swirling effect was discounted as secondary to the principal cause of the pressure reduction around the jet, which was taken to be entrainment. This was justified because the device geometry means that the bubble is significantly elongated and the forced vortex model used by Goto & Drzewiecki [41] would be inappropriate. It is difficult to quantify the error that this introduces without knowing the velocity distribution in the recirculation bubble. The wall pressure measurements made by Sawyer [99] have already been discussed in section 3.3.9, but pertain to arguments in the present section. Sawyer's plots are duplicated in Fig. 3.24 for convenience, with the annotations made in section 3.3.9 removed. The trend observed is that as the setback is reduced, the ratio of

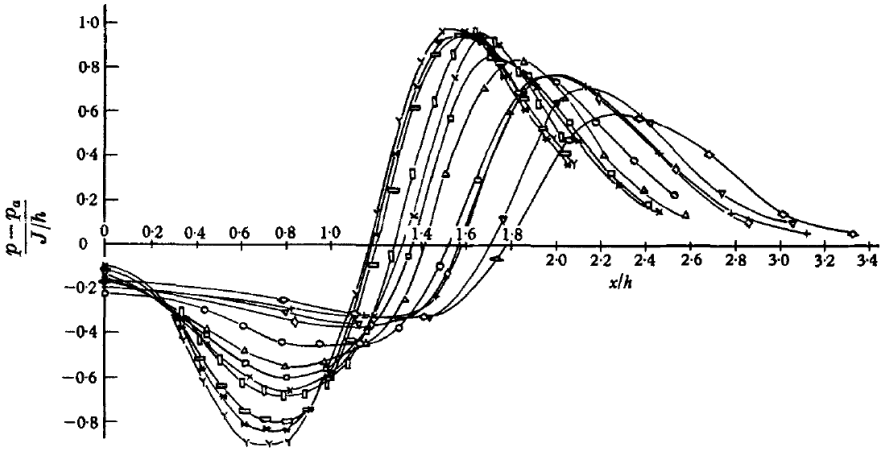

FIGURE 8. Static pressure distribution along the plate.

Symbol	h/t	Symbol	h/t
◇	4·15	□	9·13
▽	4·81	×	10·64
+	5·92	▯	10·65
◇	6·99	▭	14·06
○	5·62	*	16·74
△	7·35	Y	24·40

Figure 3.24: Duplicate of Fig. 3.19 with annotations removed: Sawyer's [99] measurements of pressure along the attachment wall for varying setback lengths. Note the nomenclature: x is the distance along the attachment wall, h is the attachment wall setback (D in present work), and t is the nozzle width (b in present work.) The wall incline angle is $\alpha = 0^{\circ}$ and $\mathrm{Re} = 9.5 \times 10^4$.

.

the minimum to the mean pressure in the bubble region reduces. The cause of the pressure

variation in the bubble is the swirling of flow. The pressure contour map provided by Sawyer [99] shows the spatial pressure variation in the bubble as concentric quasi-circular lines, matching the distribution of a forced vortex as modelled by Goto & Drzewiecki [41]. This map was provided at a setback distance of $h = 5.62t$ in Sawyer's nomenclature, i.e. $D = 5.62b$ in the present nomenclature, and the corresponding curve in Fig. 3.24 shows that the bubble pressure varies spatially by a factor of 2. However, for the smaller setback lengths, this variation reduces, indicating that the more elongated geometry is not conducive to the formation of a vortex in the bubble. Given that the value of setback in the present work is $D = 2b$, which is less than half the smallest setback considered by Sawyer [99], it seems reasonable to assume that the bubble pressure variation will be minimal, justifying the exclusion of the dynamic pressure due to the swirling flow.

3.4.2.1 Jet virtual origin

The jet virtual origin was set to match the mass flow rate integrated across the nozzle orifice in the model to the experimental value, which required the inlet mass flow to be inflated by a parameter, $\xi = 1.07$. This differed from the traditional method of integrating across the entire velocity profile. The result is a higher-momentum jet for the same measured values of P_{AS} and P_{US}, which affects both the steady state and dynamic properties of the model. The steady state radius of attachment calculated from (3.10) is larger (more weakly attached), and the dynamic magnitude response is more damped (lower resonant peak and roll-off frequency). If the traditional approach is taken, resulting in the virtual origin given by $s_0 = \sigma b/3$, the shape factor κ_1 must be increased from $\kappa_1 = 2.8$ to $\kappa_1 = 4$ in order to reduce the magnitude response resonances and recover the agreement with the experimental data obtained in Fig. 4.17 (introduced in chapter 4). This supports the approach taken in the present model because it requires less tuning via the shape factor, and suggests the jet virtual origin used in this paper is closer to the reality than the traditional method.

3.5 Conclusion

This chapter has dealt with modelling the fluid dynamics of an attached jet from first principles. A novel unsteady jet curvature equation was developed through use of the Görtler velocity profile and the radial Navier-Stokes momentum equation, and a nonlinear dynamic model was built around it. The effect of acoustic excitation was included for the first time. The validity of the model is demonstrated in the next chapter.

Chapter 4

Model validation

4.1 Introduction

A dynamic model for an attached jet was developed from first principles in Chapter 3. It was found that the dynamics governing the motion of the jet contain equations associated with recirculation bubble expansion and the bulk motion of the jet itself. The model can be used to predict the jet response to acoustic excitation through its effect on entrainment rates and therefore the jet spread parameter, σ. This chapter deals with the experimental validation of the model. For this purpose, experimental data are required. Wiltse & Glezer demonstrated that jets demodulate acoustic signals [131]. This is consistent with the observed effect of the excitation: a constant acoustic tone causes a constant, DC offset in the jet position. Amplitude-modulating the excitation tone causes the jet to respond at the modulation frequency, as shown in [131]. Use is made of this to perturb the jet in this chapter.

A canonical diverging channel is used in this validation study, with inputs and outputs provided by a mid-range loudspeaker and static & total pressure tappings respectively. The experimental setup is described in section 4.2, and data obtained through measurements of the unexcited conditions at a range of flow rates are presented in section 4.3. Experimental equivalents to the model input and output are determined in section 4.4. Section 4.5 explores the system nonlinearities, and offers a strategy to invert them. The experimentally-

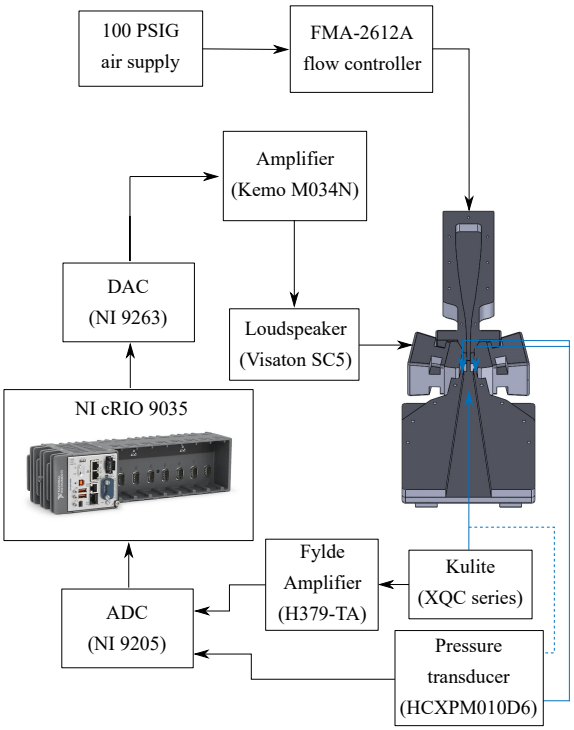

Figure 4.1: Experimental setup for model validation

determined dynamic jet responses are presented and discussed in section 4.7. Following this, the steady state data required to calculate the model operating points for linearisation purposes are illustrated in section 4.8, and bounds on the system transport delay are calculated in section 4.9. The model is linearised in section 4.10. The crux of the chapter is in section 4.11, where the model frequency responses are compared with the experimental data, and an assessment of the agreement is made. Section 4.12 provides a more detailed discussion of the model performance, with additional analysis to explain inconsistencies with the experimental data. A discussion of the parameters is provided, and details are given of a Monte Carlo analysis conducted on the model to ascertain its sensitivity to key inputs. Finally, conclusions are drawn in section 4.13.

4.2 Experimental setup

An overview of the experimental setup is shown in Fig. 4.1. The FPGA (field programmable gate array) used is the National Instruments (NI) cRIO-9035, with the NI 9205 Analogue Input (AI) card and NI 9263 Analogue Output (AO) card. The loudspeaker used is the

Sensor name	Alias	Range	Accuracy
HCXPM005D6	PT A-5	-5 to 5 mbar	±0.5 %
HCXPM010D6	PT A-10	-10 to 10 mbar	±0.5 %
HCXM100D6	PT A-100	0 to 100 mbar	±0.5 %
Kulite XCQ	PT B	350 mbar	±0.5 %

Table 4.1: Sensor data summary

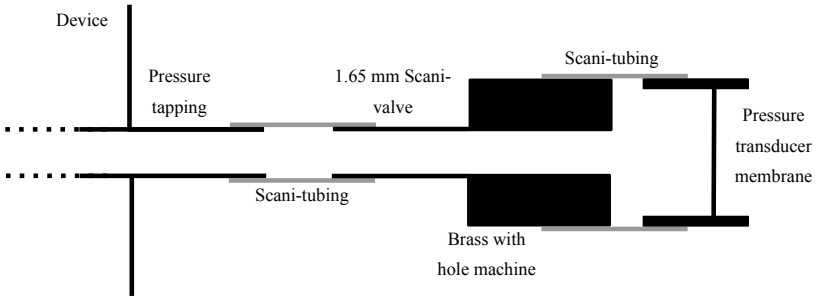

Figure 4.2: Measurement connection diagram for PT A

Visaton SC5 8 Ω, the audio amplifier is the Kemo 40 W M034N, and the pressure transducers are the First Sensor 5 & 10 mbar HCXPM-series and 100 mbar HCXM-series transducers (henceforth referred to as PT A-5, PT A-10, and PT A-100), which have a response time of 100 μs, and the Kulite XCQ-series pressure transducer (PT B). PT A-5, PT A-10, and PT A-100 were used to measure steady pressures, while PT B recorded the unsteady signals produced when the jet was perturbed dynamically. References to 'PT-A' should be assumed to refer to PT A-5 when the values given do not exceed 500 Pa, to PT A-10 for pressures between 500 and 1000 Pa, and to PT-100 for pressures exceeding 1000 Pa. The sensors used are summarised in Table 4.1. A measurement connection (MC) was required to connect PT A to the total pressure tapping on the device. This consisted of a length of 1.65 mm Scanivalve tubing to connect the tapping to an adapter, which comprised a short length of 1.6 mm Scanivalve soldered to a thicker brass cylinder with the same internal diameter. A second piece of Scanivalve tubing of appropriate (larger) diameter connected the adapter to the pressure transducer. A diagram of the measurement connection is shown in Fig 4.2.

The dynamics studied in the present work are those of the bulk jet rather than those associated with shear layer instabilities. This would usually inform the choice of sampling

rate, i.e. choosing a sampling rate at least double the highest frequency of the dynamics. However, in this case it was necessary to generate input waveforms, and it was convenient to match the loop rate of the signal generation code to the sampling rate. The frequency of the input signals required was $O(1\text{kHz})$, and to synthesize these signals accurately a loop rate at least one order of magnitude greater was required. The loop and sampling rates were therefore set to $f_s = 50$ kHz in all cases. An analogue, first order, 25 kHz anti-aliasing filter was applied to the pressure transducer measurements before sampling by the FPGA, and the flow controller used was the Omega FMA-2612A.

The measurement locations are just downstream of the inlet orifice, adjacent to the jet (P_{AS} and P_{US} - static pressures, measured by PT A) and on the central axis of the device approximately 17 nozzle widths ($17b$) downstream of the inlet orifice (P_{out} - total pressure, measured by either PT A or PT B depending on the experiment). These are shown in Fig. 4.3a, with device dimensions in Fig. 4.3b. Note that both control port channels are terminated with the loudspeakers, but only one was used throughout this paper. Each control port channel is a straight, rectangular channel which is then lofted to a larger, circular cross-section to match the loudspeaker.

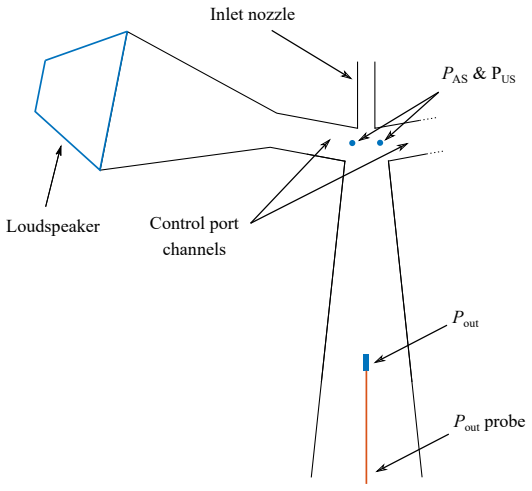

(a) Measurement locations for model validation experiments: P_{AS} & P_{US} are static pressure measurements, P_{out} is a total pressure measurement.

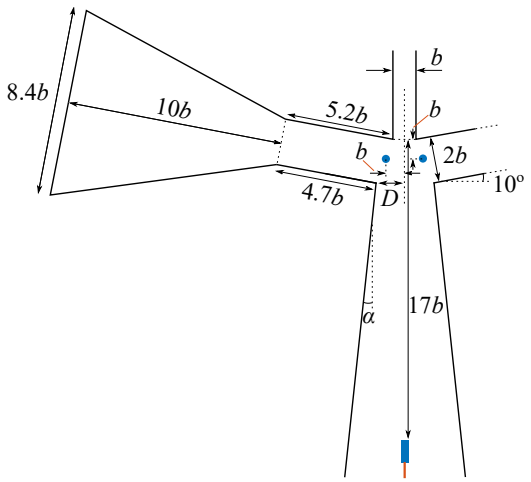

(b) Device dimensions. Note that $D = 2b$, $\alpha = 6°$, $b = 5$ mm.

Figure 4.3: Diverging channel used in validation experiments. Control port and loudspeaker shown on one side only; device is symmetric about nozzle axis.

4.3 Unexcited conditions

The jet position described by the curvature, R, refers to the mean profile. When the jet is perturbed dynamically, it can no-longer be called the mean profile. References to the bulk jet position are intended to signify the quasi-mean profile, as opposed to the turbulent fluctuations. This position, and therefore the jet curvature, may vary with flow rate. Using the jet curvature equation derived in chapter 3, which is given by

$$\gamma \frac{\mathrm{d}^2 R}{\mathrm{d}t^2} + \zeta \frac{\mathrm{d}R}{\mathrm{d}t} - \frac{\bar{J}}{\rho R} = \frac{1}{\rho} \Delta P, \tag{4.1}$$

and setting $\ddot{R} = \dot{R} = 0$, the steady state JCE is given by

$$-\frac{\bar{J}}{R} = \Delta P. \tag{4.2}$$

The pressures on either side of the jet, P_{AS} & P_{US}, were characterised vs flow rate without excitation from the loudspeaker. The jet momentum flux per unit depth, $\bar{J}$, was calculated by integrating the profile across the nozzle, and so the radius of curvature R could be calculated from (4.2). The pressures and radius of curvature are plotted against flow rate in Fig. 4.4. The radius of curvature increases slightly with flow rate, but is largely constant, with an average of $16.8b$ over the flow rates used.

4.4 Input & output selection

The parameter used to validate the model is the jet position, which is indicated by θ in the model and is related geometrically to R by $R = g(\theta)$ in (3.75). It is difficult to measure either θ or R directly, so the measurement used to indicate the jet position is P_{out}, the total pressure given by a probe on the central axis.

It has been explained that a constant acoustic excitation tone causes a constant degree of additional jet spreading. As such, the input in the model is the jet spread factor, σ. The experimental input is therefore the voltage applied to the audio amplifier, $g_{\mathrm{ex}}(t)$, which

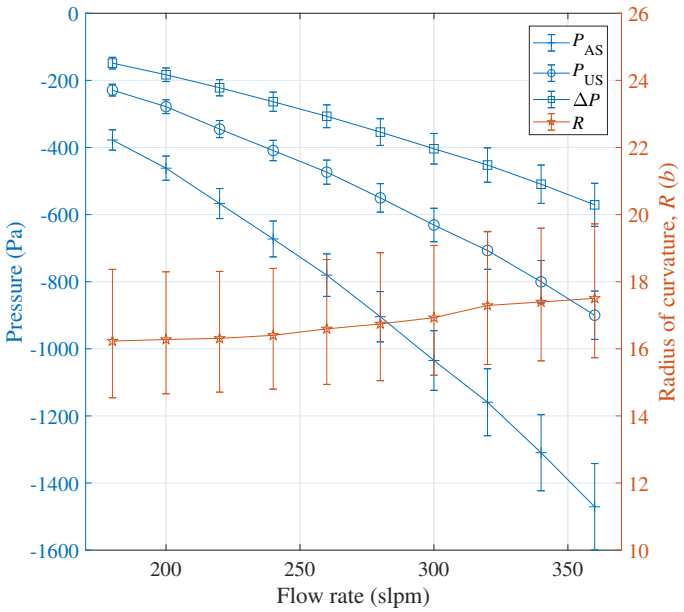

Figure 4.4: Attached side pressure, P_{AS} (blue, crosses), unattached side pressure, P_{US} (blue, circles), pressure difference, ΔP (blue, squares) and radius of curvature, R (red, stars), vs flow rate, no excitation. Error bars represent one standard deviation.

drives the loudspeaker in the control port channel on the unattached side of the device.

This choice of experimental input and output reflects the trend of the equivalent model input and output. Increasing $g_{\mathrm{ex}}(t)$ causes more jet spreading and the attachment is weakened. This is reflected by an increasing P_{out} caused by the movement of the jet away from the wall and towards the channel centreline. The equivalent for the model is that σ decreases when the jet spreading is larger, and θ decreases when the jet is deflected. The goal is to linearise the model at each flow rate and consider perturbations about each operating point.

Exciting the jet with a constant tone,

$$g_{\mathrm{ex}}(t) \;=\; A \sin\left(2\pi f_{\mathrm{c}} t\right), \tag{4.3}$$

results in a nonlinear response depending on the frequency and amplitude of the tone,

$$P_{\mathrm{out}} \;=\; g_{\mathrm{resp}}\left(A, f_{\mathrm{c}}\right) + P_{\mathrm{out}\,0}, \tag{4.4}$$

where $P_{\text{out}\,0}$ is the unexcited level. The jet can be perturbed dynamically by varying the amplitude of the input dynamically, i.e. amplitude modulating a carrier tone. This is represented by

$$g_{\text{ex}}(t) = g_{\text{c}}(t)g_m(t) = \sin(2\pi f_{\text{c}}t)(A\sin(2\pi f_m t) + B). \tag{4.5}$$

The intention was to vary the amplitude of the input, but the frequency has also changed from f_c to the frequency of the amplitude modulation (AM) signal in (4.5). This signal contains the side-bands, $f_c \pm f_m$, as well as the carrier, f_c. Since the jet demodulates the applied signal, its response is

$$\begin{aligned} P_{\text{out}} \;=\; \left[g_{\text{resp}}\left(A, f_{\text{c}} - f_m\right) + g_{\text{resp}}\left(A, f_{\text{c}} + f_m\right)\right] \left|G(2\pi f_m)\right| \sin\left(2\pi f_m t + \phi\right) ... \\ ... + g_{\text{resp}}\left(B, f_{\text{c}}\right) + P_{\text{out}\,0}. \end{aligned} \tag{4.6}$$

The first term is the jet response to the time-varying modulation signal with frequencies $f_c \pm f_m$, and the second term is the response to the constant part of the modulation signal. The time-varying response is made up of:

i) $\left[g_{\text{resp}}\left(A, f_{\text{c}} - f_m\right) + g_{\text{resp}}\left(A, f_{\text{c}} + f_m\right)\right]$, the nonlinear response that depends on the amplitude, carrier tone frequency, and modulation tone frequency at the input.

ii) $\left|G(2\pi f_m)\right|$, the magnitude response of the bulk jet dynamics - the subject of the model derived in chapter 3.

iii) ϕ, the combination of the phase response of the bulk jet dynamics, $\arg\left(G(2\pi f_m)\right)$, as well as the phase lag due to the system transport delay.

The demodulation process is sketched in Fig. 4.5. In light of this, the system input changes from 'the voltage applied to the audio amplifier' to be the time-varying part of the modulation signal in (4.5), i.e.

$$u(t) \;=\; A\sin(2\pi f_m t). \tag{4.7}$$

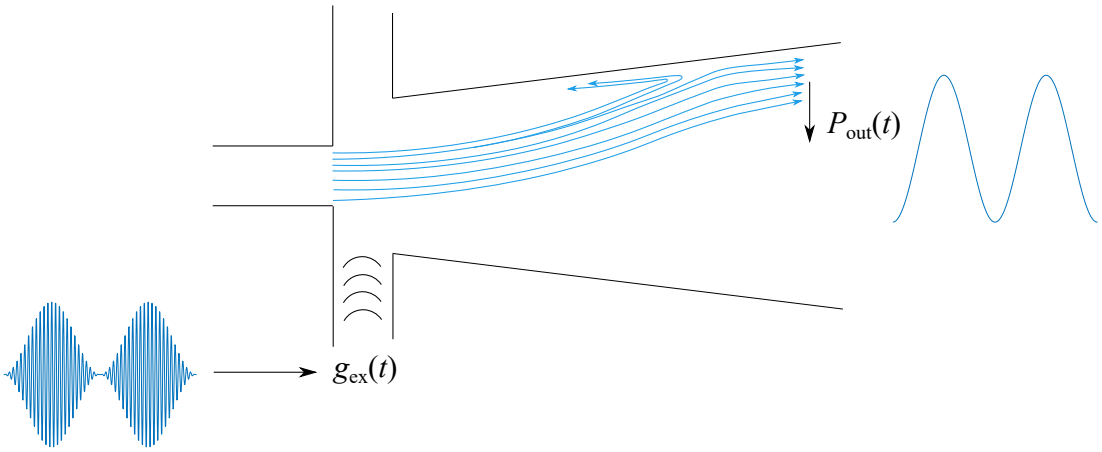

Figure 4.5: Excitation signal demodulation process by jet.

4.5 Nonlinearities

The potential for system nonlinearities is reflected in the jet response at the output in (4.6) by the function $g_{\text{resp}}(A, f)$, which depends on the tone amplitude and frequency. Fixing the amplitude of the tone applied to the audio amplifier and varying the frequency causes a response called the static jet deflection response or static jet deflection curve (SDC); these terms are used interchangeably. Similarly, fixing the frequency of the tone and varying its amplitude results in the nonlinear amplitude response.

Each source of nonlinearity is shown in Fig. 4.6. First, the audio amplifier & loudspeaker both respond nonlinearly when the input voltage exceeds a certain value. The control port channel cavity response is a function of frequency, contributing to the static jet deflection response. The response of the shear layer to the acoustic signal emitting from the end of the control port channel may depend nonlinearly on both the amplitude and frequency of the excitation. Finally, the measurement at P_{out} is effectively a point measurement in the velocity profile, which is unlikely to be linear - a Görtler profile has been assumed in the model - so that a variation in the jet position will cause a nonlinear variation in P_{out}.

Careful placement of the measurement probe that provides P_{out}, along with restricting the excitation amplitudes to small values, reduces the amplitude nonlinearity until it is

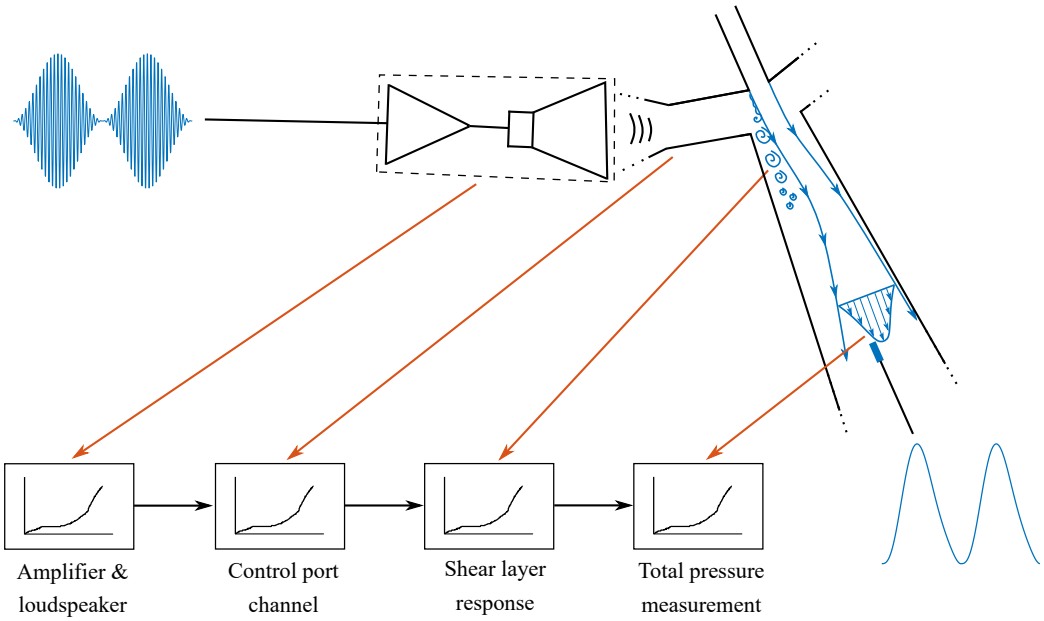

Figure 4.6: Origin of system nonlinearities

approximately linear. It was found that positioning the probe 17 inlet nozzle widths downstream of the inlet orifice gave fairly linear responses (quantified below). Examples of these responses at different input tone frequencies and flow rates are shown in Fig. 4.7. There are several curves which have more significant nonlinearities than the average - notably those at input tone frequencies of 3500 Hz. The strong response at 3500 Hz results from a device resonance that occurs when a standing wave is setup between the loudspeakers[1].

If these mappings are applied to a sinusoidal signal, the degree of nonlinearity in each curve impacts the amount of power in the harmonics at the mapping output. However, the important quantity is the jet response at the fundamental frequency, which depends weakly on the degree of nonlinearity when the mapping is a monotonically increasing function, as in this case. Warping a sinusoid by each of the curves in Fig. 4.7 showed that in all cases at the mapping output, the power loss at the fundamental frequency relative to the input never exceeds 1 dB. Therefore, the curves are assumed to be linear. The gradient of the mapping, i.e. the gain, does affect the fundamental frequency output amplitude. However, that is a function of frequency rather than amplitude, and is dealt with in section 4.6.

[1]Note that the attached side loudspeaker is inert throughout and provides an acoustic boundary against which waves reflect.

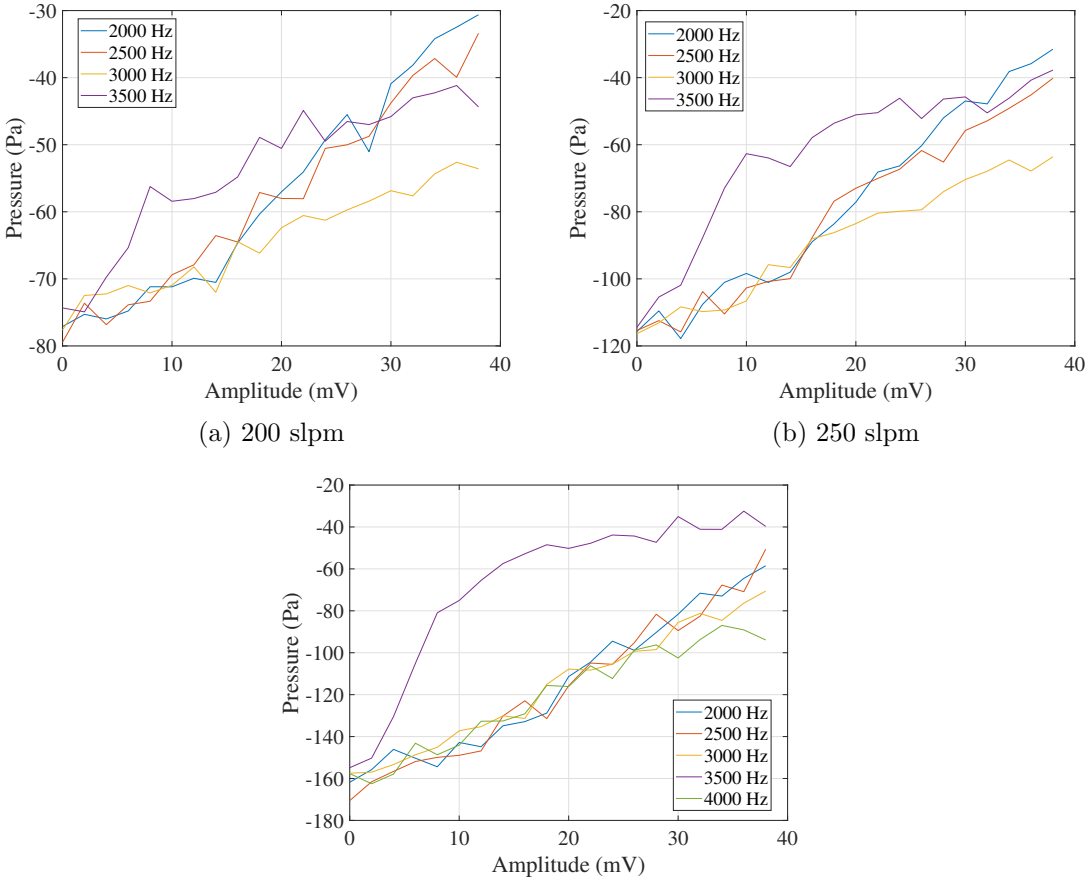

(a) 200 slpm

(b) 250 slpm

(c) 300 slpm

Figure 4.7: Jet deflection amplitude response as indicated by the measurement P_{out} against input amplitude for several tone frequencies and flow rates. Note that these are gauge pressures relative to atmospheric conditions.

The function $g_{\text{resp}}(A, f)$ has been shown to be linear with respect to A, so A can be removed as an input.

4.6 Static deflection curve

This leaves the static jet deflection response, or static deflection curve (SDC), as the only source of nonlinearity in $g_{\text{resp}}(f_c)$. It is clear from Fig. 4.7 that holding the input amplitude constant and varying the input frequency will not give a constant output - this is equivalent to drawing a vertical line at a given amplitude on Fig. 4.7 and plotting its intersection with each curve. The static deflection curves were determined by driving the amplifier with a

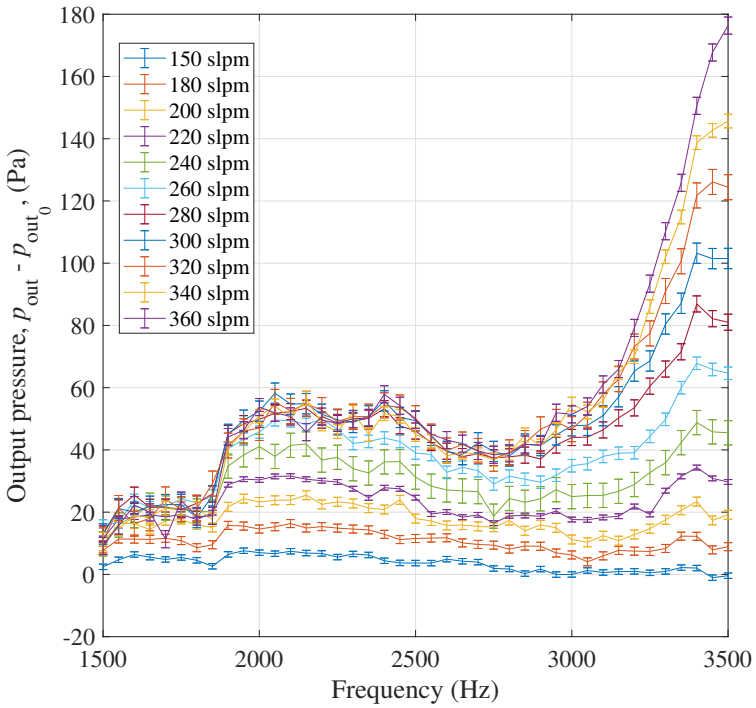

Figure 4.8: Static deflection curves at $A = 20$ mV.

tone at a range of frequencies, given by

$$g_{\text{ex}}(t) = A \sin(2\pi f_c t), \tag{4.8}$$

where $A = 20$ mV was chosen because it is in the middle of the range of amplitudes tested in Fig. 4.7, and the frequency was incremented from $f_c = 1500$ Hz to $f_c = 3500$ Hz in steps of 50 Hz. The duration of each tone was 4 seconds, and the experiment was repeated four times. The mean value of P_{out} in each 4-second run at each frequency was sampled, and the ensemble average of each of the four runs was taken to give a value of P_{out} at each value of f_c at each flow rate. The mean of the unexcited output, P_{out_0}, was sampled for 8 seconds between runs to give four values at each flow rate. The mean and standard deviation of each unexcited level was calculated: the former was removed from each value of P_{out}, while the latter provided an estimate for the uncertainty at each flow rate. The resulting static deflection curves are shown in Fig. 4.8.

4.6.1 Effect on the dynamic response

Without inversion, the static deflection curves have an impact on the measured dynamic response. This effect is called the quasi-steady jet response, denoted $\psi_{f_c}(f_m)$, which is defined as

$$\psi_{f_c}(f_m) = \left[g_{\text{resp}}(f_c - f_m) + g_{\text{resp}}(f_c + f_m)\right]. \tag{4.9}$$

It should be noted that inverting the static deflection curve is the same thing as inverting the quasi-steady jet response. The former is the name of the nonlinearity at the modulated frequency, $f_c \pm f_m$, while the latter is its effect at the base band frequency, f_m. The subscript f_c is used in ψ because it depends on the carrier tone frequency chosen. The statements 'invert the static deflection curves' and 'invert the quasi-steady jet response' are used interchangeably.

When perturbing the jet dynamically, the input signal is an AM signal given by

$$g_{\text{ex}}(t) = \sin(2\pi f_{\text{c}} t)\left(A\sin(2\pi f_{\text{m}} t) + B\right). \tag{4.10}$$

Evaluating the sine product yields an input and corresponding output given by

$$g_{\text{ex}}(t) = \frac{A}{2}\cos\left(2\pi(f_c - f_m)t\right) - \frac{A}{2}\cos\left(2\pi(f_c + f_m)t\right) + B\sin(2\pi f_c t) \tag{4.11}$$

$$P_{\text{out}} = A\,\psi_{f_c}(f_m)\left|G(2\pi f_m)\right|\sin(2\pi f_{\text{m}} t + \phi) + g_{\text{resp}}(B, f_c) + P_{\text{out}\,0}. \tag{4.12}$$

The output magnitude response at f_m is a combination of the jet dynamic response and the quasi-steady jet response. The differences between (4.12) and (4.6) are that the amplitude nonlinearity has been assumed linear, and the effects of the SDCs have been summarised in $\psi_{f_c}(f_m)$.

4.6.2 Inversion at the output

The strategy adopted for removing the quasi-steady deflection curve is to invert it at the output. The carrier frequency can be chosen carefully to reduce the effects of the SDCs in

Fig. 4.8, thereby lowering any errors introduced through their inversion due to experimental uncertainty. The key is to choose a value of f_c such that the corresponding quasi-steady jet response, $\psi_{f_c}(f_m)$, is small at all values of f_m used. The quasi-steady deflection curve for $f_c = 2500$ Hz is shown in Fig. 4.9. This was calculated from the SDCs in Fig. 4.8 through

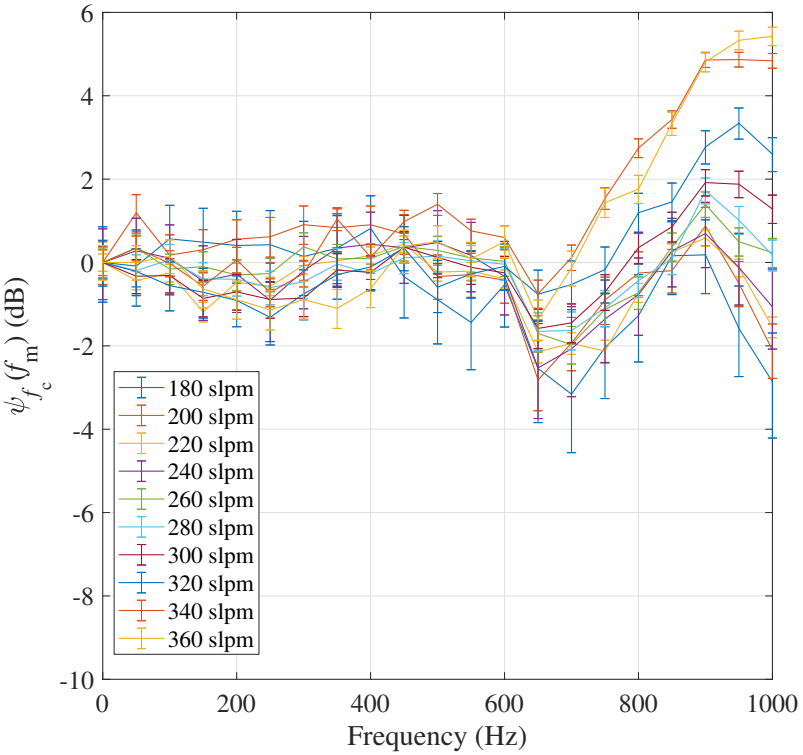

Figure 4.9: Quasi-steady jet deflection curve at $f_c = 2500$ Hz, $\psi_{f_c}(f_m)$, at several flow rates.

(4.9). The values are relatively small at this value of f_c, making it a good choice.

4.7 Dynamic response identification

The dynamic jet responses were identified experimentally using an AM input given by

$$u_c(t) = \sin(2\pi f_c t)\left(A\sin(2\pi f_m t) + B\right), \tag{4.13}$$

where $B = 20$ mV, $A = 20$ mV, and $f_c = 2500$ Hz. The value of f_m was stepped between $f_m = 20$ Hz and $f_m = 880$ Hz in increments of 20 Hz. The response from each tone at each flow rate was sampled for 4 seconds, which was repeated 10 times. The signal-to-noise

ratio was improved by taking the ensemble average, which was possible because the phase of the input signals was reset at the start of each 4-second run. The input signal was also recorded. The empirical transfer function estimate (ETFE) was used to estimate the frequency response from the input and output time series. The ETFE is calculated using

$$\hat{G}(\omega) = \frac{\Phi_{yu}(\omega)}{\Phi_{uu}(\omega)}, \tag{4.14}$$

where $\Phi_{yu}(\omega)$ and $\Phi_{uu}(\omega)$ are the cross-spectral density of the output and the input and the power spectral density of the input respectively. The magnitude responses both with and without SDC inversion are shown in Fig. 4.10. The data were truncated for values of

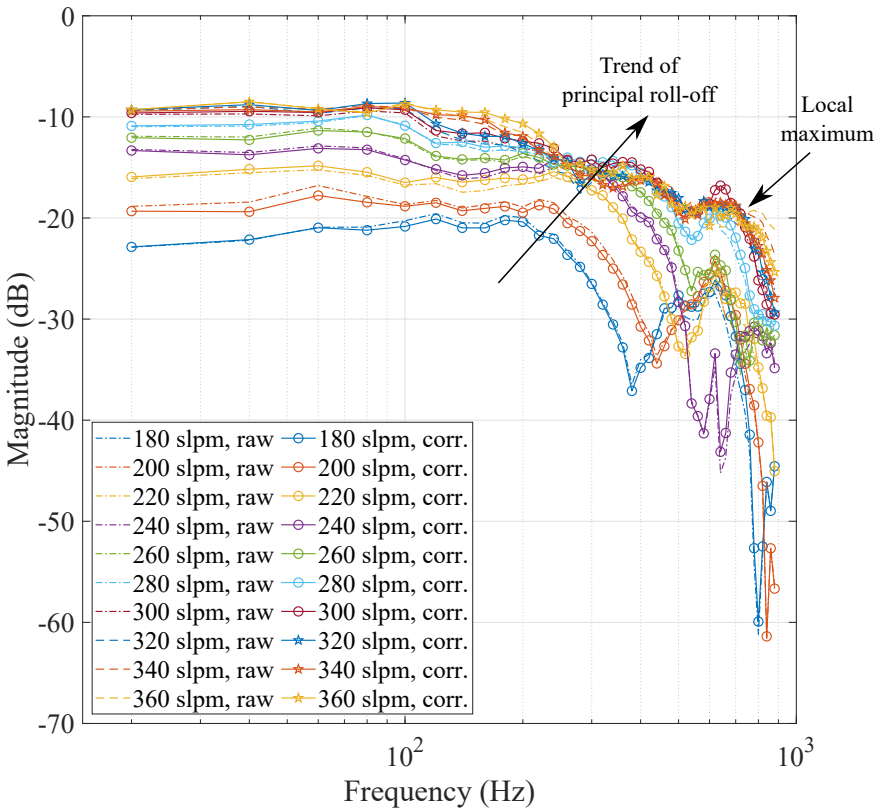

Figure 4.10: Dynamic magnitude responses (ETFEs): raw, without SDC inversion (dash-dot and dash-dash); and with SDC inversion (circles and stars).

f_m where the response at f_m to the input was dominated by the jet noise. The main points from these responses are:

1. The effect of the static deflection curves is small, particularly in the system bandwidth.

2. There is a roll-off that increases with flow rate, which is highlighted in Fig. 4.10. The DC level stops increasing with flow rate at around 320 slpm, but the roll-off contuinues to increase. This is called the principal roll-off hereafter.

3. There is a local maximum at $\sim$ 650 Hz that is static with respect to flow rate.

The phase responses are shown in Fig. 4.11. The phase lag is dominated by the transport

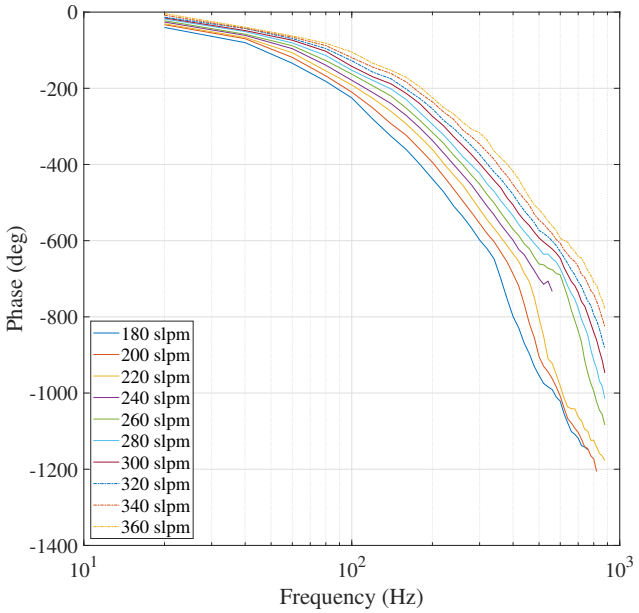

Figure 4.11: Dynamic phase responses (ETFE)

delay between particles being acted on by the input at the nozzle orifice to being recorded when they arrive at the pressure transducer. This is illustrated by Fig. 4.11 through consideration of the ratio between the phase lag of the smallest and largest flow rates - the largest flow rate (360 slpm) is double the smallest (180 slpm.) The nozzle velocities between these extreme cases should also be approximately a factor of two apart, and hence the transport delay at 360 slpm should be roughly half that at 180 slpm. For example, at 100 Hz the ratio is 2.1, while at 300 Hz it is 2.2. The phase response around the region of the local maximum in the magnitude response at 650 Hz appears to deviate from its trend.

The local maximum described in point 3. above is a result of loudspeaker nonlinearities demodulating the applied AM signal and producing tones at f_m, which are picked up directly by the pressure transducer. The amplitude and phase of these demodulated tones were characterised by running the dynamic response experiment described above with the flow turned off. The resulting data are shown in Fig. 4.12, along with the 180 slpm (corrected) magnitude response from Fig. 4.10 and its corresponding phase response from Fig. 4.11. As shown in the figure, the local maximum coincides with the peak in the no-flow dynamic

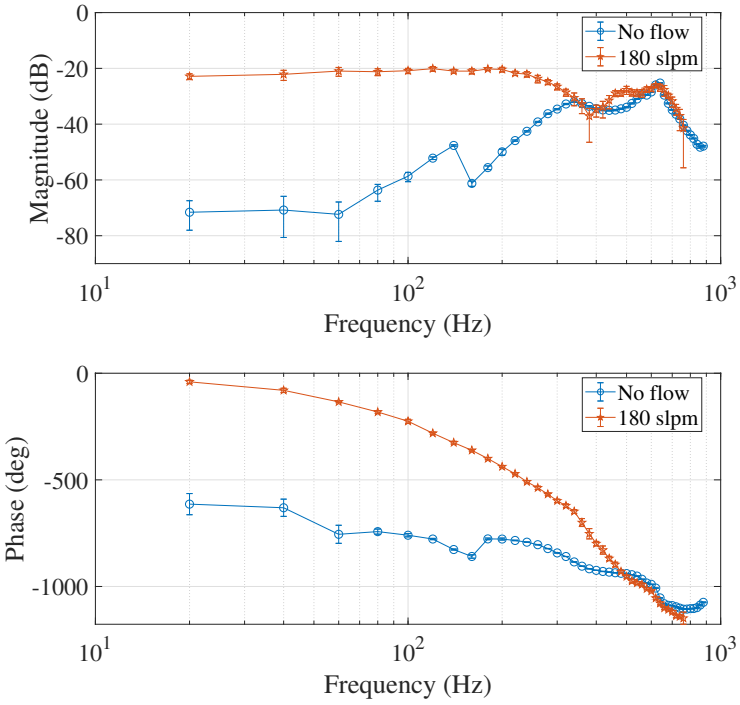

Figure 4.12: Dynamic responses: No flow (blue, circles), and 180 slpm (red, stars), for comparison.

magnitude response in both magnitude and frequency, while the phases also agree.

4.8 Solution of the system equilibrium

Now that experimental dynamic jet response data have been acquired, equivalent data must be produced from the model so that a comparison can be drawn. This means linearising the nonlinear system derived in chapter 3 at each of the flow rates tested in Fig. 4.10 & 4.11 and considering the resulting frequency responses. An operating point must be determined

for the linearisation at each flow rate. An operating point is a system equilibrium, i.e. values of θ, P_{B1}, and P_{B2} where $\ddot{\theta}$, $\dot{\theta}$, $\dot{P}_{\mathrm{B1}}$, and $\dot{P}_{\mathrm{B2}}$ are equal to zero. There are also unknown parameters, summarised in section 3.3.14.1, which must be set. To establish which parameters have to be determined from the experiments, the solution of the system differential equations in the steady state is considered, given by

$$\frac{\frac{1}{\rho}\Delta P + \frac{\bar{J}}{\rho g} - \zeta g'\dot{\theta} - \gamma g''\dot{\theta}^2}{\gamma g'} = 0 \tag{4.15}$$

$$\frac{c_3\dot{m}}{2}\left[1 - \tanh(\eta_1)\sqrt{\frac{3\xi^2\left(g\theta + s_{0_{\mathrm{AS}}}\right)}{b\sigma_{\mathrm{AS}}}}\right] f^{-1} - P_{\mathrm{B1}}f'f^{-1}\dot{\theta} = 0 \tag{4.16}$$

$$\frac{c_3\dot{m}}{2\left(V_{\mathrm{const}} - f\right)}\left[1 - \tanh(\eta_2)\sqrt{\frac{3\xi^2\left(x_{\mathrm{US}} + s_{0_{\mathrm{US}}}\right)}{b\sigma_{\mathrm{US}}}}\right] + \frac{P_{\mathrm{B2}}f'}{\left(V_{\mathrm{const}} - f\right)}\dot{\theta} = 0. \tag{4.17}$$

Substituting $\dot{\theta} = 0$ and manipulating the above equations yields

$$\text{-}\Delta P = \frac{\bar{J}}{g} \tag{4.18}$$

$$\tanh\left(\eta_1\right)\sqrt{\frac{3\xi^2\left(g\theta + s_0\right)}{b\sigma}} = 1 \tag{4.19}$$

$$\tanh\left(\eta_2\right)\sqrt{\frac{3\xi^2\left(x_{\mathrm{US}} + s_0\right)}{b\sigma}} = 1. \tag{4.20}$$

The first equation, (4.18), has reduced to the standard steady state jet curvature equation. The ideal gas law steady states have reduced in equations (4.19) and (4.20) to statements that the entrainment flow must be equal to the recirculation flow on each side of the jet in the steady state. The definition of the entrainment flow is based on the position of the dividing streamline, and manipulation of (4.19) and (4.20) results in $\eta_1 = \eta_{\mathrm{DSL}_{\mathrm{AS}}}$ and $\eta_2 = \eta_{\mathrm{DSL}_{\mathrm{US}}}$. Recalling the definition of the DSL at the attachment point ($s = g\theta$), this gives

$$\eta_1 = \operatorname{atanh}\left(\frac{1}{\xi}\sqrt{\frac{\sigma_{\mathrm{AS}}b}{3\left(g\theta + s_{0_{\mathrm{AS}}}\right)}}\right) \tag{4.21}$$

$$\eta_2 = \operatorname{atanh}\left(\frac{1}{\xi}\sqrt{\frac{\sigma_{\mathrm{US}}b}{3\left(x_{\mathrm{US}} + s_{0_{\mathrm{US}}}\right)}}\right). \tag{4.22}$$

Finally, the momentum equations of each side of the jet must be added as constraints to the equilibrium, copied here from the previous chapter

$$-\frac{1}{4}\left(1+\beta_1\right)t_1^3 + \frac{3}{4}\left(1+\beta_1\right)t_1 - \frac{3}{4}\left(t_{\mathrm{SL}} - \frac{1}{3}t_{\mathrm{SL}}^3\right)\left(\beta_1 + \cos\left(\theta-\alpha\right)\right) + \frac{J_{\mathrm{loss}}}{J} - \frac{P_{\mathrm{B1}}L_1}{J} = 0 \tag{4.23}$$

$$-\frac{1}{4}\left(1+\beta_2\right)t_2^3 + \frac{3}{4}\left(1+\beta_2\right)t_2 - \frac{3}{4}\left(t_{\mathrm{SL}} - \frac{1}{3}t_{\mathrm{SL}}^3\right)\left(\beta_2 + 1\right) + \frac{J'_{\mathrm{loss}}}{J} - \frac{P_{\mathrm{B2}}L_2}{J} = 0. \tag{4.24}$$

Together, equations (4.18) & (4.21 - 4.24) are algebraic equations that must be solved simultaneously to find the values of the states in the equilibrium. The unknown states and parameters are

$$\{\ \theta,\quad P_{\mathrm{B1}},\quad P_{\mathrm{B2}},\quad \eta_1,\quad \eta_2,\quad \sigma_{\mathrm{AS}},\quad \sigma_{\mathrm{US}},\quad \kappa_1,\quad \kappa_2,\quad x_{\mathrm{US}},\quad V_{\mathrm{const}},\quad \beta_1,\quad \beta_2,\quad J_{\mathrm{loss}},\quad J'_{\mathrm{loss}},\quad L_1,\quad L_2\ \}, \tag{4.25}$$

a total of 17 unknowns and 5 equations. A summary of the approach is shown in Table 4.2. It is first noted that it is possible to measure P_{B1} and P_{B2} because they correspond to the measurements P_{AS} and P_{US} in Fig. 4.3a. The values of θ, η_1, η_2, L_1, and L_2 are not straightforward to measure, so are left to be determined by the solver.

The attached side spread factor, σ_{AS}, is fixed to be the free jet value, $\sigma_{\mathrm{AS}} = 7.7$. The fact that the jet is curved and attached causes less entrainment on the attached side [100], which would indicate that $\sigma_{\mathrm{AS}} > 7.7$. However, the increased entrainment due to the acoustic excitation decreases the value of σ_{AS}, so it is left as the free jet value. The spread factor on the unattached side, σ_{US}, should be lower than that on the attached side due to the naturally greater entrainment and because of the excitation. The value used is $\sigma_{\mathrm{US}} = 5.7$, although it should be noted that the system is relatively insensitive to σ_{US}. The values of σ_{AS} and σ_{US} are discussed in section 4.12.2.

Unknown	**Physically-reasonable range**	**Nominal value**	**Range for Monte Carlo Analysis**
θ	-	Solve JCE (4.18)	-
P_{B1}	-	Measure (P_{AS})	-
P_{B2}	-	Measure (P_{US})	-
η_1	-	Solve AS IGL (4.19)	-
η_2	-	Solve US IGL (4.20)	-
L_1	$0 \leq L_1 \leq D$	Solve AS mom. eqn. (4.23)	-
L_2	$0 \leq L_2 \leq 3D$	Solve US mom. eqn. (4.24)	-
κ_1	-	2.8	-
κ_2	-	0.8	-
σ_{AS}	-	7.7	$6.16 \leq \sigma_{\mathrm{AS}} \leq 9.24$
σ_{US}	-	5.7	$4.16 \leq \sigma_{\mathrm{US}} \leq 7.24$
x_{US}	-	$20b$	-
V_{const}	$250 \leq \frac{V_{\mathrm{const}}}{b^2 d} \leq 750$	$500b^2d$	$250 \leq \frac{V_{\mathrm{const}}}{b^2 d} \leq 750$
β_1	$0 \leq \beta_1 \leq 1$	0.4	$0.2 \leq \beta_1 \leq 0.6$
β_2	$0 \leq \beta_2 \leq 1$	0.1	-
J_{loss}	$0 \leq J_{\mathrm{loss}} \leq \bar{J}/2$	0	$0 \leq J_{\mathrm{loss}} \leq 0.03\bar{J}$
J'_{loss}	$0 \leq J'_{\mathrm{loss}} \leq \bar{J}$	0	-

Table 4.2: Unknowns in solution of system equilibrium, with Monte Carlo analysis parameter ranges. Candidates for pre-testing for Monte Carlo analysis are below the double line.

The shape factor, κ_1, is effectively applied to the coefficient of the damping term, $\dot{R}$, in the jet curvature equation, through its scaling of the transverse velocities on the dividing streamlines, i.e. $\kappa_1 v|_{\pm y_{\mathrm{DSL}}}$. The value $\kappa_1 = 2.8$ was used in all flow rates to correct the model damping to fit the data. The fitting parameter, κ_2, was set to $\kappa_2 = 0.8$ to improve the fit as well, although leaving $\kappa_2 = 1$ also yields a decent fit.

The value of x_{US} is difficult to measure but the model is insensitive to it. It is set as $x_{\mathrm{US}} = 20b$ for all flow rates. This is also discussed in section 4.12.5. The volume shared by the bubbles on each side, V_{const} is set to $500b^2d$. The total channel volume is $\sim 1000b^2d$, but the jet takes up a portion of this volume, so the upper bound for the range is $750b^2d$. It is possible to bound the values of β_1 and β_2 because they represent the fraction of the recirculated momentum at the upstream edge of each of the control volumes. The bounds are therefore

$$0 \leq \beta_1 \leq 1; \qquad 0 \leq \beta_2 \leq 1. \tag{4.26}$$

Similarly, the side lengths of the control volumes, L_1 and L_2, must be physically reasonable, and are given the bounds

$$0 < L_1 \leq D; \qquad 0 < L_2 \leq 3D. \tag{4.27}$$

The bounds on the losses are given by

$$0 \leq J_{\mathrm{loss}} \leq \frac{\bar{J}}{2}; \qquad 0 \leq J'_{\mathrm{loss}} \leq \bar{J}, \tag{4.28}$$

where the upper limit for J_{loss} is only half of the jet momentum because only the top half of the jet momentum is included in the analysis of the attached side control volume. The fraction of the jet included in the unattached side control volume analysis had no effect on the equations because the additional momentum from including more of the jet at the entrance to the control volume at the upstream boundary as part of $\bar{J}_{\mathrm{US}}$ simply exited at the downstream boundary as part of J'_1 without being turned.

The solver was set up with θ, η_1, η_2, L_1, and L_2 as decision variables. The values of β_1 and β_2 were set beforehand. These parameters had a dominant effect on the resulting values of L_1 and L_2, and were set so that L_1 and L_2 satisfied their bounds given by (4.27). The values chosen were $\beta_1 = 0.4$ & $\beta_2 = 0.1$, although there was a range of values that would have satisfied the bounds in (4.27) and (4.26).

The unknowns in the solution of the equilibrium given by (4.25) have each been dealt with. To continue with solving for the equilibrium, the values of P_{B1} and P_{B2} are required at each flow rate. While these were determined for the unexcited case in Fig. 4.4, it is noted that their values at the operating points about which the jet is perturbed must be considered, i.e. the constant excitation which pulls the jet off the wall so that it can oscillate freely when excited dynamically. Experiments were conducted at each flow rate with the input set to the constant part of the AM signal in (4.13), given by

$$u_{\mathrm{equil}} = B\sin\left(2\pi f_c t\right), \tag{4.29}$$

where $B = 20$ mV. In one series of experiments, the pressure difference $\Delta P = P_{\mathrm{AS}} - P_{\mathrm{US}}$ was measured with two nominally identical versions of PT A-5. The combined mean values and uncertainties are shown in Fig. 4.13 both with the input in (4.29) and without excitation to highlight its effect. Note that for the uncertainty calculation, a 2^{nd} order notch filter around 2500 Hz was applied to both the excited and unexcited data to remove the excitation tone picked up directly by the pressure transducer, which otherwise inflated the excited uncertainty. In another experiment, the values of P_{AS} and P_{US} were sampled separately with each of PT A-5, PT A-10, and PT A-100 where the range of each was appropriate, with some overlapping cases. These data are shown for the unexcited case in Fig. 4.14a to demonstrate the agreement between the transducers, and Fig. 4.14b shows the pressures on each side for both the excited and unexcited cases, with the data taken from the relevant pressure transducer according to its valid measurement range. The direct measurement of ΔP was taken to reduce error because the system is sensitive to its value. For the purpose

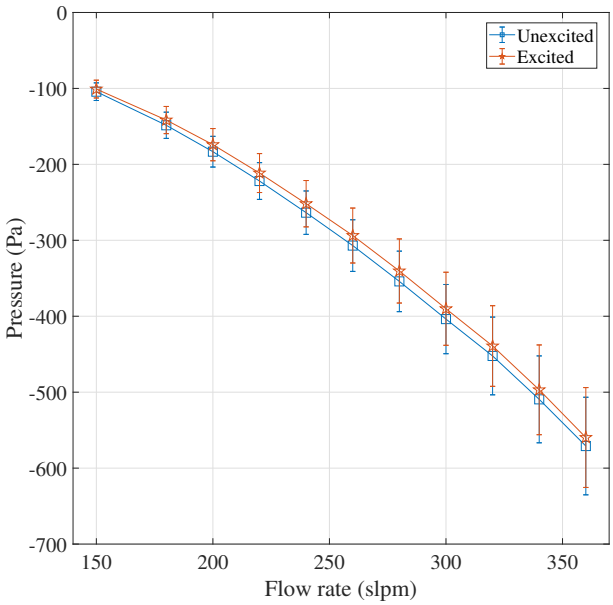

Figure 4.13: Pressure difference across jet vs flow rate: Excited with 20 mV, 2500 Hz tone (red, star), and unexcited (blue, square). Error bars represent one standard deviation.

of setting the operating points, the excited values of ΔP and the attached side pressure values were used, while the unattached side pressures were calculated from the other two values.

MATLAB's *fsolve()* with the trust-region dogleg algorithm was employed to solve the system of equations. The values of R were calculated from (4.18) using the mean values of ΔP from Fig. 4.14. These are shown alongside the unexcited values in Fig. 4.15. The radius of curvature is larger when the jet is excited, which indicates the weakening of the Coandă effect, as expected. Next, the values of L_1 and L_2 set by the solver are shown in Fig. 4.16. The figure shows that that control volume side lengths satisfy the bounds given in (4.27), and do not vary significantly with flow rate. The value of η_1 was almost constant with respect to flow rate, reducing by 1.5% from its value at 180 slpm to its final value at 360 slpm. Its mean value along with the truly constant value of η_2 are given by

$$\eta_1 = 0.432 \pm 0.021, \qquad \eta_2 = 0.278 \pm 0.020, \tag{4.30}$$

where the uncertainty results from a Monte Carlo analysis that is described later.

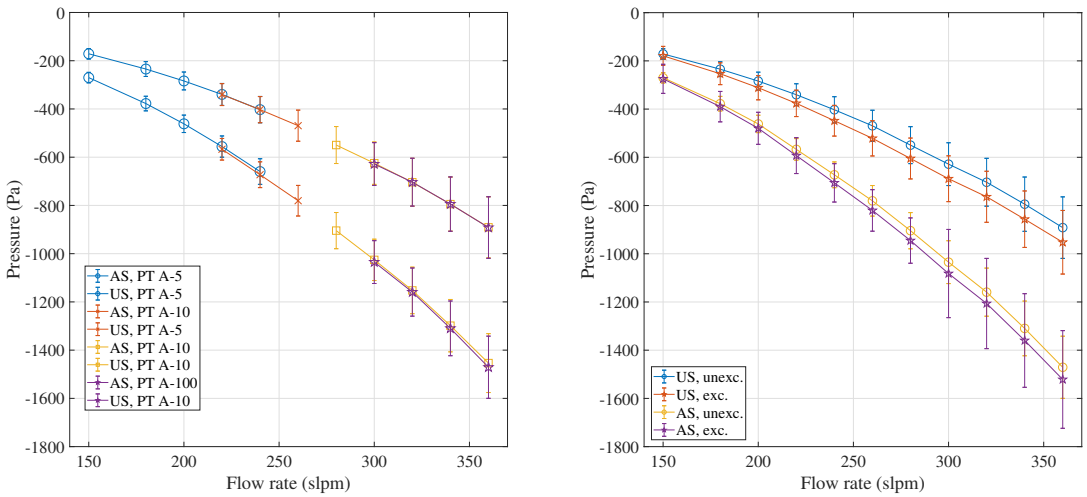

(a) Unexcited bubble pressures for several pressure transducers.

(b) Excited and unexcited bubble pressures for chosen pressure transducers.

Figure 4.14: Measured bubble pressures vs flow rate.

4.9 Transport delay calculations

It was argued in section 4.7 that the transport delay dominates the phase response. In this section, the value of the transport delay is bounded. A delay results in a phase lag that increases linearly with frequency, with a transfer function given by

$$G_{\text{delay}}(s) = e^{-sT_d}, \tag{4.31}$$

where the time delay T_d can be estimated by considering the maximum jet velocity averaged along the path between the nozzle orifice and the position of PT B, which is called $\bar{u}_{\max}$. The largest reasonable value of $\bar{u}_{\max}$ is the mean of the centreline velocity between the nozzle orifice and the station of the probe, $s = s_{\text{pr}} = 17b$. Its value is estimated by the averaging the centreline velocities at the nozzle orifice, $s = 0$, and at $s = s_{\text{pr}}$, and can be found from

$$\max(\bar{u}_{\max}) = \frac{1}{2}\left[u_{\max}|_{s=0} + u_{\max}|_{s=s_{\text{pr}}}\right] = \frac{1}{2}\left[\frac{1}{2}\sqrt{\frac{3J\sigma_{\text{pr}}}{\rho s_0}} + \frac{1}{2}\sqrt{\frac{3J\sigma_{\text{pr}}}{\rho\left(s_{\text{pr}} + s_0\right)}}\right]. \tag{4.32}$$

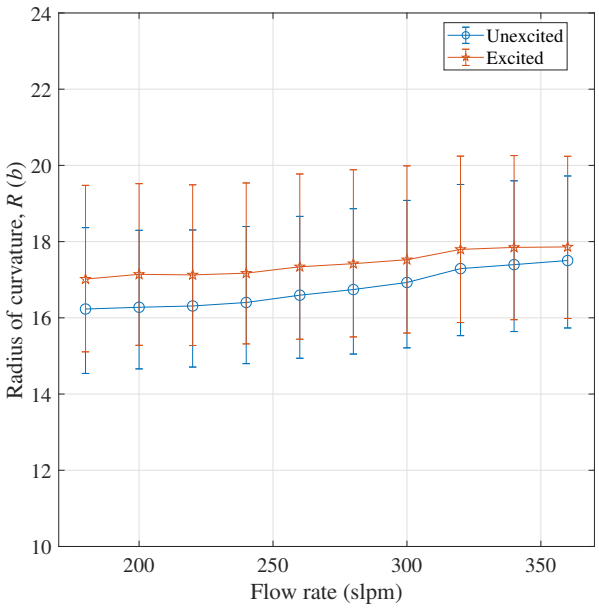

Figure 4.15: Radius of curvature, R, calculated from ΔP data: excited (red, stars) and unexcited (red, circles) values.

The lowest reasonable estimate of $\bar{u}_{\max}$ is given by the value of u at a value of η corresponding to the probe position at s_{pr}, called η_{pr}. The channel has an approximate width of $6b$ at s_{pr}, and the centreline is assumed to be one nozzle width from the wall. This places the probe, which is in middle of the channel, at $y = 6b/2 - b = 2b$ from the jet centreline. The spread factor was assumed to be equal to the free jet value, $\sigma = 7.7$, for this calculation. It may be smaller on the unattached side close to the nozzle orifice due to the excitation ($\sigma_{\mathrm{US}} = 5.5$), but the average value of σ along the jet from the nozzle orifice to the probe station is likely to be larger than this. The lowest reasonable estimate of $\bar{u}_{\max}$ is therefore given by

$$\min\left(\bar{u}_{\max}\right) = \frac{1}{2}\sqrt{\frac{3J\sigma}{\rho\left(s_{\mathrm{pr}} + s_0\right)}}\,\mathrm{sech}^2\left(\eta_{\mathrm{pr}}\right). \tag{4.33}$$

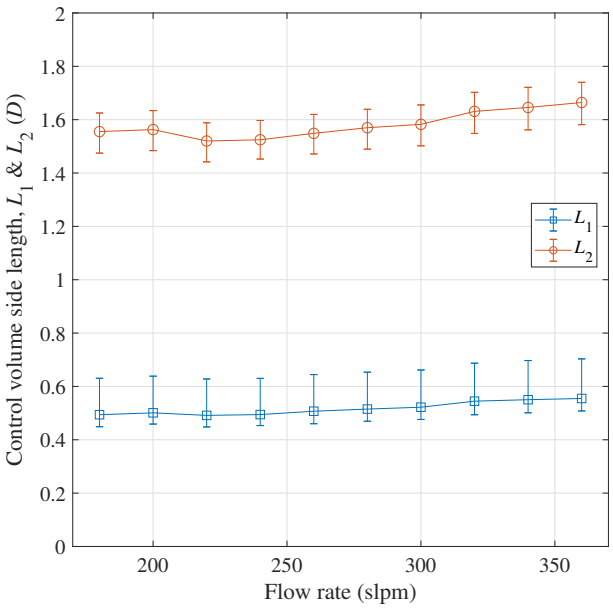

Figure 4.16: L_1 (blue, squares) and L_2 (red, circles) vs flow rate. Error bars indicate parameter sensitivity from Monte Carlo analysis. Note that the y-axis has units of D, the setback distance.

4.10 Model linearisation

Linearising the nonlinear equations (3.76 - 3.78) leads to the state space system

$$\begin{bmatrix} \dot{x}_1 \\ \dot{x}_2 \\ \dot{x}_3 \\ \dot{x}_4 \end{bmatrix} = \begin{bmatrix} \frac{\partial \dot{\theta}}{\partial \theta} & \frac{\partial \dot{\theta}}{\partial P_{\mathrm{B1}}} & \frac{\partial \dot{\theta}}{\partial P_{\mathrm{B2}}} & \frac{\partial \dot{\theta}}{\partial \dot{\theta}} \\ \frac{\partial \dot{P}_{\mathrm{B1}}}{\partial \theta} & \frac{\partial \dot{P}_{\mathrm{B1}}}{\partial P_{\mathrm{B1}}} & \frac{\partial \dot{P}_{\mathrm{B1}}}{\partial P_{\mathrm{B2}}} & \frac{\partial \dot{P}_{\mathrm{B1}}}{\partial \dot{\theta}} \\ \frac{\partial \dot{P}_{\mathrm{B2}}}{\partial \theta} & \frac{\partial \dot{P}_{\mathrm{B2}}}{\partial P_{\mathrm{B1}}} & \frac{\partial \dot{P}_{\mathrm{B2}}}{\partial P_{\mathrm{B2}}} & \frac{\partial \dot{P}_{\mathrm{B2}}}{\partial \dot{\theta}} \\ \frac{\partial \ddot{\theta}}{\partial \theta} & \frac{\partial \ddot{\theta}}{\partial P_{\mathrm{B1}}} & \frac{\partial \ddot{\theta}}{\partial P_{\mathrm{B2}}} & \frac{\partial \ddot{\theta}}{\partial \dot{\theta}} \end{bmatrix}\Bigg|_{\mathrm{OP}} \begin{bmatrix} x_1 \\ x_2 \\ x_3 \\ x_4 \end{bmatrix} + \begin{bmatrix} \frac{\partial \dot{\theta}}{\partial \sigma_\sim} \\ \frac{\partial \dot{P}_{\mathrm{B1}}}{\partial \sigma_\sim} \\ \frac{\partial \dot{P}_{\mathrm{B2}}}{\partial \sigma_\sim} \\ \frac{\partial \ddot{\theta}}{\partial \sigma_\sim} \end{bmatrix}\Bigg|_{\mathrm{OP}} u, \tag{4.34}$$

where x_1, x_2, x_3, and x_4 represent perturbations in the states θ, P_{B1}, P_{B2}, and $\dot{\theta}$ from their equilibrium positions. Recalling that the output selected is the jet position, θ, the output equation is given by

$$y = \begin{bmatrix} \frac{\partial y}{\partial x_1} & \frac{\partial y}{\partial x_2} & \frac{\partial y}{\partial x_3} & \frac{\partial y}{\partial x_4} \end{bmatrix}\Bigg|_{\mathrm{OP}} \begin{bmatrix} x_1 \\ x_2 \\ x_3 \\ x_4 \end{bmatrix} + \frac{\partial y}{\partial \sigma_\sim}\Bigg|_{\mathrm{OP}} u, \tag{4.35}$$

which can be resolved without knowledge of the operating point to

$$y = \begin{bmatrix} 1 & 0 & 0 & 0 \end{bmatrix} \begin{bmatrix} x_1 \\ x_2 \\ x_3 \\ x_4 \end{bmatrix}. \tag{4.36}$$

Summarising the state space system using the standard nomenclature gives

$$\dot{\mathbf{x}} = \mathbf{A}\mathbf{x} + \mathbf{B}u \tag{4.37}$$

$$y = \mathbf{C}\mathbf{x}. \tag{4.38}$$

Taking Laplace transforms of equations (4.37) & (4.38) and rearranging gives the SISO transfer function

$$G(s) = \mathbf{C}\left(s\mathbf{I} - \mathbf{A}\right)^{-1}\mathbf{B}. \tag{4.39}$$

4.11 Dynamic jet response comparison

The system equilibrium has been solved for each flow rate, so the linearised system given by (4.34) and (4.36) can be evaluated. The various derivatives were derived symbolically in MATLAB and the steady state values were substituted. Note that the steady state value for the time-varying input, $\sigma_{\sim}$, was set to 0. This is because the difference in spreading on each side of the jet caused by the steady input, u_{equil} (see (4.29)), was absorbed into the difference between the values σ_{AS} and σ_{US}. That is to say, the difference between these values reflects not only the natural difference in jet spreading but also the bias in additional jet spreading caused by the excitation.

The dynamic responses from the model along with the corresponding experimental data are shown in Fig. 4.17. The model phase response is combined with the phase lag associated with the transport delay bounds calculated in section 4.9. The model fits the data well, particularly at the lower flow rates. The phase is within the calculated bounds,

although it is close to the lower bound. This could be because the transport delay is close to the value associated with the bound, or it may be the result of unmodelled dynamics. The local maximum at ∼650 Hz was established in section 4.7 as an artefact of the experiment and should be ignored. The error bars on the model frequency responses are the output of the Monte Carlo analysis, which is discussed in section 4.12.6. These give an indication of the sensitivity of the model to the parameters that were perturbed.

It is evident from the magnitude responses in Fig. 4.17 that the model predicts the principal roll-off, which dominates the experimental responses at low flow rates, but becomes less important as the flow rate increases. This is the result of a second roll-off around 100 Hz that influences the response at the higher flow rates. However, this feature is clearly secondary to the principal roll-off, which the model captures accurately. An important feature of the data is the trend of increasing roll-off frequency with respect to flow rate. To compare this trend in the experimental data with that in the model, the principal roll-off breakpoint frequency for each flow rate was estimated from the graphs of the experimental data in Fig. 4.17, along with what was judged an appropriate uncertainty bound. The model roll-off breakpoint frequency was calculated as the frequency where the response went below its DC value, which was deemed to be a reasonable qualitative equivalent to the points chosen in the experimental data. These roll-off breakpoint frequencies are shown in Fig. 4.18, along with a line of best fit for the experimental data, and the uncertainty in the line parameters. There is reasonable agreement between the model roll-off frequencies and the estimated principal roll-off frequencies. Clearly, the judgement of the principal roll-off frequencies is subjective, but the trend is apparent when the experimental magnitude responses are plotted on the same axes, as highlighted in Fig. 4.10.

4.12 Discussion

4.12.1 Principal and 100 Hz roll-offs

It was explained in section 4.11 that the model predicts the principal roll-off. A secondary feature exists in the magnitude response experimental data at the higher flow rates. The

magnitude response starts to roll-off at around 100 Hz for the 320 – 360 slpm curves, which is hereafter referred to as the 100 Hz roll-off. The cause of this feature is unclear, and this section provides two possible causes.

Firstly, the 100 Hz roll-off may not be associated with the bulk jet dynamics, but rather some other part of the system. One candidate is the shear layer response. It has been assumed that the shear layer responds instantly to the acoustic excitation, so that the jet spreading is the system input. This may be a poor assumption in some conditions.

A second possibility is related to the 'filling time' of the channel. When the jet is excited dynamically, the reattachment position varies at f_m. This means that the total pressure loss of the system between the nozzle orifice and the attachment point also varies at f_m. Consequently, the pressure immediately downstream of the nozzle orifice varies at the same frequency. The mass flow controller response is much slower than all non-zero values of f_m considered in this paper, so that it represents a constant restriction. The 100 psig source upstream of the mass flow controller therefore supplies the nozzle with a constant pressure at f_m. A constant pressure driving a time-varying total pressure loss results in a time-varying flow driven through the nozzle. The remainder of the channel from the attachment point to the outlet plane can be considered as a lumped volume supplied with a time-varying flow. The lumped volume entry plane is taken as the channel cross-section at the attachment point, and the exit plane is the outlet slot, through which flow is driven by the pressure in the lumped volume. Using this model, an order-of-magnitude estimate of the filling response frequency can be calculated. The loss coefficient of the lumped element is assumed to be $K_\mathrm{L} = 1$, and the geometry is used to calculate the entry and exit plane cross-sectional areas and the lumped volume. Linearising the filling dynamics results in the 1$^\mathrm{st}$ order system

$$\frac{\mathrm{d}P_\mathrm{c}}{\mathrm{d}t} = \frac{R_0 T \dot{m}_\mathrm{f}}{M_\mathrm{m} V} - 1500 P_\mathrm{c}, \tag{4.40}$$

where P_c is the lumped pressure that is measured by the probe, and $\dot{m}_\mathrm{f}$ is the time-varying flow filling the channel. The system has a roll-off breakpoint frequency of $1500/2\pi = 240$ Hz.

This filling response frequency is effectively independent of flow rate, so that it could not cause the principal roll-off, which follows the trend in Fig. 4.18. However, it is the correct order of magnitude to be the source of the 100 Hz roll-off, and it is suggested as a possible cause.

4.12.2 Spread factor, σ

The value of the spread factor should depend on the rate of entrainment. Reichardt [95] suggested that a free jet should take $\sigma = 7.7$, which was based on experimental data from a plane jet. Kirshner & Katz [60] suggested that the value of σ depends on the shape of the plenum from which the jet emerges. A plenum that encourages the production of large scale structures will result in a jet that spreads more and σ may be lower than 7.7. On the other hand, if the plenum is design to avoid the production of turbulence, the value of σ may exceed 7.7, which corresponds to less jet spreading. In both Bourque & Newman [11] and Sawyer [99], the setback distances considered were larger than in the present study. Neither of these studies considered the combination of an inclined and setback wall - Sawyer only considered a setback, while Bourque & Newman considered each separately. For Bourque & Newman's setback-only case, they found that $\sigma = 12$ gave the best fit to the data. Sawyer [99] suggested $\sigma \approx 10$ gave the best description of the development of the velocity profile between two measured stations. However, Sawyer also reported that $\sigma = 15$ gave the best results in terms of predicting the recirculated momentum (and therefore bubble pressure) and the attachment length. He concluded that $\sigma = 15$ was most appropriate for modelling purposes and that the discrepancy arose from the collective errors in the various assumptions made in the analysis. In a later paper, Sawyer [100] accounted for the difference in entrainment on either side of the jet and concluded that an overall spread factor of $\sigma = 7.7$ gave the best results when the attached side value exceeded the unattached side value. For Bourque & Newman's inclined wall, neither of their attachment models fit the data as well for a single value of σ, although it was suggested that the value is unlikely to stray far from 7.7. The values of α used in [11], the wall incline angle, were all greater than 30°, which is larger than the $\alpha = 6^{\circ}$ used in the present work. Lush [67, 68] suggested that σ should lie in the range $7.7 \leq \sigma \leq 14$, while Goto & Drzewiecki [41] used $\sigma = 10$. Epstein [31]

suggested that σ depends on the aspect ratio (AR) of the jet. For $AR = 1$, he found that $\sigma = 31.5$ gave the best fit for attachment distance, which was for smaller setback values with $D \leq 1$. Epstein suggested that Bourque found good agreement for $AR \to \infty$ with $\sigma = 10.5$. Chang [18] considered a device with $AR = 3.1$ and found that $\sigma = 10.5$ gave the best fit to the measured velocity profile.

It is clear that the plane jet value of $\sigma = 7.7$ used in the present work is towards the lower end of the values used in previous papers. The principal explanation for this is that none of the previous papers considered acoustically-excited jets. As discussed in section 3.3.14, the acoustic excitation promotes vortex production and increases entrainment, which has the effect of reducing the value of σ.

4.12.3 Effect of excitation on attached side spreading

It was explained in section 3.3.14 that the effect of including a fraction of the system input, $\sigma_\sim$, in the attached side ideal gas law, (3.77), depends on the quantity included. In this discussion, the fraction included is ϵ, so that σ_{AS} is replaced with $\sigma_{\mathrm{AS}} + \epsilon\sigma_\sim$ in (3.82), as well as in the calculation of $s_{0_{\mathrm{AS}}}$.

The following explanation may be easier to understand with the context of Fig. 3.15. When a constant acoustic excitation tone (no amplitude modulation) is switched on, the unattached side bubble pressure reduces because there is a net entrainment of flow into the jet in the transient. At the unattached side attachment point, a greater portion of the jet is sucked upstream by the reducing pressure. This increasing recirculation flow rate acts as a negative feedback to settle the unattached side bubble pressure. The pressure reduction decreases the magnitude of the pressure difference across the jet, which causes the attached side attachment point to move downstream and the radius of curvature to increase. On the attached side, even with $\epsilon = 0$ (which has been assumed up to this point), there are three things that cause the bubble pressure to decrease. Firstly, the larger value of R results in a longer entrainment length, so even with an unchanged attached side spread factor (which defines the entrainment per unit length rather than the total entrainment flow rate), the

entrainment flow rate increases. Second, the weaker attachment means that the jet strikes the wall at a less direct angle, which reduces the recirculation flow rate. The imbalanced entrainment and recirculation flow rates cause a net mass flow rate leaving the bubble, which reduces its pressure. Finally, the increased radius of curvature increases the bubble volume, which also reduces its pressure. At the attached side attachment point, more flow is sucked upstream by the reduced bubble pressure. This increased recirculation flow rate stabilises the bubble pressure and a steady state is reached when the recirculation flow rate increases to the larger entrainment flow rate.

The only difference to this chain of events when $\epsilon > 0$ is that the attached side entrainment flow rate increases directly under the action of the excitation. The increased entrainment on each side of the jet reduces the pressure on each side — the resulting difference, ΔP, determines the change in attachment strength. The net change in ΔP therefore depends on the effectiveness with which the change in entrainment can reduce the pressure. This effectiveness is determined by the entrainment length and by the impact of the resulting pressure reduction on the recirculation flow rate via the momentum equation on each side. These effects act against each other — the entrainment length on the unattached side is double the typical value on the attached side, but the larger value of L_2 compared with L_1 means the recirculation mechanism is more effective on the unattached side. With the parameter values used in this thesis, this stronger recirculation mechanism (inhibits bubble pressure reduction) outweighs the direct increase in entrainment length (drives bubble pressure reduction). Therefore, setting an even sensitivity to excitation on both sides of the jet ($\epsilon = 1$) means that excitation causes a larger reduction in bubble pressure on the attached side than the unattached side, so that the magnitude of the pressure difference across the jet is increased. The result is that excitation strengthens rather than weakens attachment. This not observed in reality.

It is possible to bound the value of ϵ to be less than the critical value, ϵ_0, where the steady state under the impact of excitation has no net effect on attachment strength. This value is only weakly dependent on flow rate — with the parameters used in the present

work, its range is $0.299 < \epsilon_0 < 0.314$, a 5% variation with an approximately linear (positive) dependence on flow rate. Increasing ϵ decreases the system DC gain, i.e. the steady state change in θ resulting from a given value of $\sigma_\sim$, until the critical value, ϵ_0, where the DC gain passes through 0 (excitation strengthens rather than weakens attachment). The goal of the model presented in this paper has been to describe the system frequency response; it has not attempted to predict the DC gain. This has resulted in a relatively conservative bound on ϵ, which limits the model to the observed behaviour of weakening, rather than strengthening, the attachment. However, it is possible to place a stricter bound on ϵ by considering the effect of its value on the system zero in $G(s)$. As ϵ increases, the zero approaches $-\infty$ at some limiting value, ϵ_1 ($\epsilon_1 < \epsilon_0$). When ϵ increases beyond ϵ_1, the zero re-appears at $+\infty$, then moves towards the origin, reaching its critical value (ϵ_0) when it arrives at $(0, 0)$. In the range $\epsilon_1 < \epsilon < \epsilon_0$, the zero is on the positive real axis, which means the system is non-minimum phase. This variety of linear systems has a characteristic feature in its transient step response, which is that the system output (θ in this case) 'goes the wrong way' initially, before reaching its steady state. For example, the step response of a non-minimum phase system with a positive DC gain would initially become negative in the transient, before increasing above the axis and settling to a positive steady value. The duration and magnitude of the inversion depends on the position of the zero – the closer to the origin, the more dominant and obvious the inversion. The step response to excitation in the experiment suffers from a weak signal-to-noise ratio, and while this can be improved with many repeats and temporal averaging, it is not possible to exclude the possibility of a very small inversion in the response. However, a probable bound that can be placed on ϵ is ϵ_1, the limiting value beyond which the system becomes non-minimum phase, which takes the value $\epsilon_1 = 0.193$ (the variation with respect to flow rate is smaller than the precision given). While ϵ was not included in the Monte Carlo analysis, its effect on the frequency response is negligible until its value is close to ϵ_0.

4.12.4 Shape factor, κ_1

The shape factor took the value $\kappa_1 = 2.8$. This was required to increase the damping because the system gave overly-resonant responses otherwise. The effect of reducing σ,

which corresponds to more spreading, is also to increase the damping. It may therefore be possible to achieve the correct damping level with $\kappa_1 = 1$ and a smaller value of σ. However, the shape factor was introduced to account for the fact that the transverse velocity profile, $v(\eta)$, may not closely resemble a Görtler profile because the jet is curved and attached rather than free, so a non-unity value is reasonable.

4.12.5 Unattached side entrainment length, x_{US}

The value of x_{US} was set to $20b$ rather arbitrarily. This appears to be a sensible value in that it is larger than the attached side entrainment length, $R\theta$. It was found that the model was insensitive to its value. This was a result of the pole associated with the unattached side bubble being at a high frequency relative to the rest of the model, so that it only affected the frequency response above the roll-off frequency.

4.12.6 Monte Carlo analysis

4.12.6.1 Parameter pre-testing

To evaluate the sensitivity of the model to each of its parameters, a Monte Carlo analysis was conducted. First, each parameter was pre-tested to determine which of them should be included in the analysis. The candidates for pre-testing are in the bottom half of Table 4.2, below the double line. The unattached side entrainment length x_{US}, fraction of unattached side recirculated momentum, β_2, unattached side viscous control volume losses, J'_{loss}, and the difference in spread parameter between the two sides, $\Delta\sigma$, had relatively little effect on the model frequency response and were not included in the Monte Carlo analysis. The remaining parameters that were included are: the attached side spread parameter, σ_{AS}, the constant volume shared between the bubbles on each side, V_{const}, the fraction of the attached side recirculated momentum, β_1, and the viscous losses in the attached side control volume, J_{loss}. Note that the unattached side spread parameter, σ_{US}, is listed as varying in the Monte Carlo analysis in Table 4.2, but this is simply a result of the fixed $\Delta\sigma = 2$ and varying σ_{AS}.

4.12.6.2 Parameter value range selection

The ranges in which the chosen parameters can vary was determined through a combination of experience and what is physically reasonable.

Attached side loss, $J_{\mathbf{loss}}$ The effect of increasing J_{loss} is to move the real part of a pair of complex conjugate poles towards the origin. With the other parameters set to their nominal values in Table 4.2, when $J_{\text{loss}} > 0.1J$, the real part of the poles becomes positive and the system becomes unstable. The damping factor for this pair of poles therefore decreases dramatically as $J_{\text{loss}} \to 0.1J$, which makes the resonance in the model frequency responses significantly larger. When other parameters tend to the extreme of their ranges, this instability occurs for $J_{\text{loss}} \geq 0.04J$. It is desirable to avoid this extreme behaviour because it is not observed in reality. The effect of including a small number of anomalous responses in the Monte Carlo analysis is to inflate the variance of the response curves unrealistically. As such, the range chosen was $0 \leq J_{\text{loss}} \leq 0.03J$.

Attached side spread factor, $\sigma_{\mathbf{AS}}$ There was no obvious means of determining a reasonable range of the value of σ_{AS}. It has a considerable effect on the system responses, mostly on the damping. The range selected was the nominal value $\pm 20\%$.

Shared bubble volume, $V_{\mathbf{const}}$ The effect of varying V_{const} is to modify the real pole associated with the unattached side bubble dynamics independently of the other poles. When it is increased, the pole approaches the origin, and its roll-off becomes more important. The limits chosen were those of the physically reasonable range in Table 4.2, given by $250 \leq V_{\text{const}}/b^2 d \leq 750$.

Fraction of the attached side recirculated momentum, β_1 As explained in section 4.8, the nominal value of β_1 was set to keep L_1 in its physically reasonable range. There was no obvious way of determining how to choose the range of values of β_1 for the Monte Carlo analysis, so $\pm 50\%$ of the nominal value was taken, giving $0.2 \leq \beta_1 \leq 0.6$.

Clearly, the choice of the parameter value ranges is subjective. The purpose of the analysis

is to determine the sensitivity of the model to its input parameters, hence reference to these ranges should be made when considering the resulting model uncertainty.

4.12.6.3 Implementation

Uniform probability density functions for each parameter range described above were used to produce random values for the Monte Carlo analysis. The number of values taken was $N_{\mathrm{MC}} = 2000$, and the equilibrium and linearisation was computed for each value. The standard deviation of the resulting model frequency responses was computed at each frequency, and these are included as error bars in Fig. 4.17.

The magnitude response positive error bars are larger above the nominal curves than the negative error bars in general. This is in part a result of choosing a nominal loss coefficient of zero, $J_{\mathrm{loss}} = 0$, which sits at one extreme of the range $0 \leq J_{\mathrm{loss}} \leq 0.03J$. The phase responses are relatively insensitive to parametric variation. This is because they are dominated by the transport delay, and the bounds on its value were independent of the parameters varied.

4.12.7 Summary

The values that the parameters have taken lie inside physically reasonable ranges and, most significantly, none are varied with respect to flow rate. This approach results in poorer fits for higher flow rates, but yields insight into which dynamics are described by the model, and which may derive from sources other than the bulk jet dynamics.

4.13 Conclusion

This chapter has dealt with validating the model developed in chapter 3. Steady state experimental data were used in the solution of the system equilibrium. A strategy was presented that identified the dynamic jet response to perturbation through inversion of system nonlinearities at the output. Experiments were conducted to determine the bulk jet dynamic response. These data were then used in a comparison with the linearised model

output and were found to agree reasonably well, particularly at lower flow rates. Two roll-off features were identified in the experimental data, one of which the model was shown to predict. The other roll-off was suggested to arise from unmodelled dynamics that may not be associated with the bulk jet motion; the shear layer response and channel filling time are possible sources. Finally, a discussion of the system parameters was provided, with a Monte Carlo analysis to provide a sense of the uncertainty in the model responses.

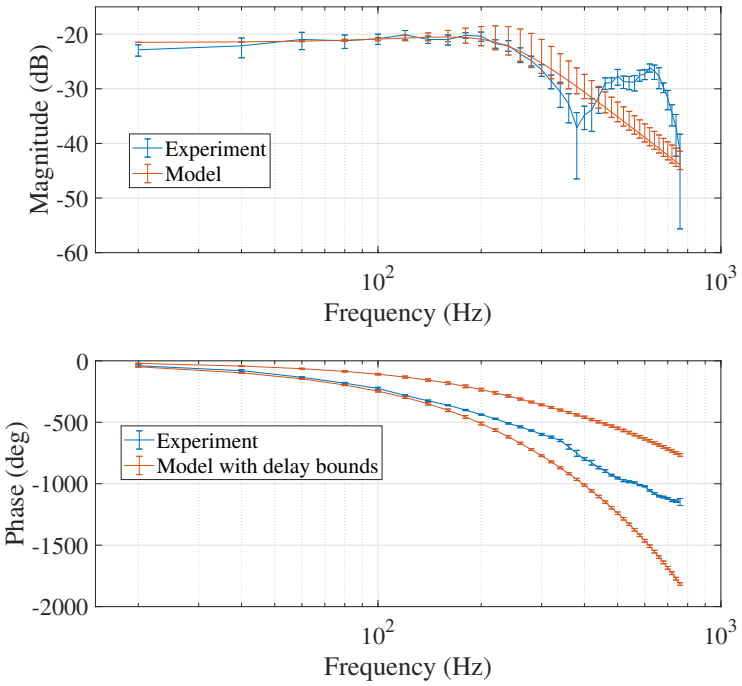

(a) 180 slpm

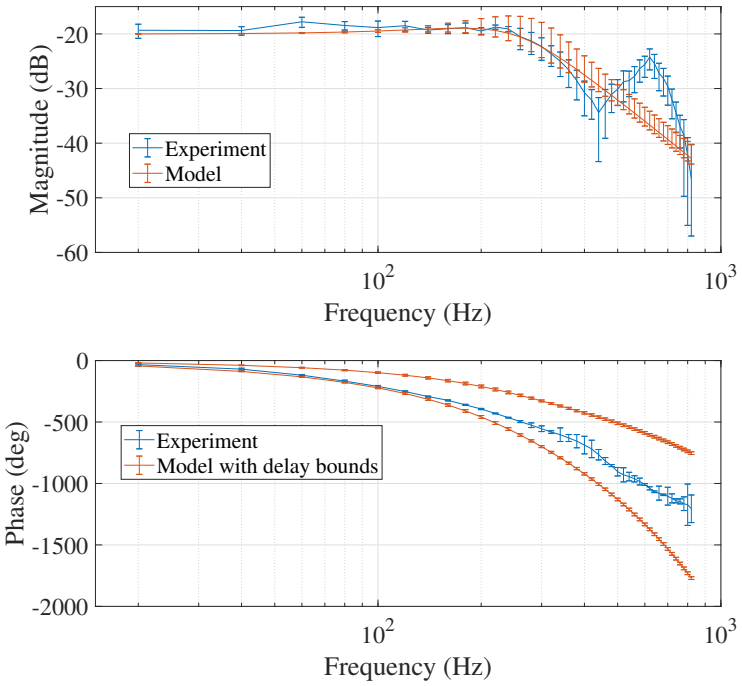

(b) 200 slpm

Figure 4.17: Dynamic jet responses: ETFE from experimental data (blue) and model output (red).

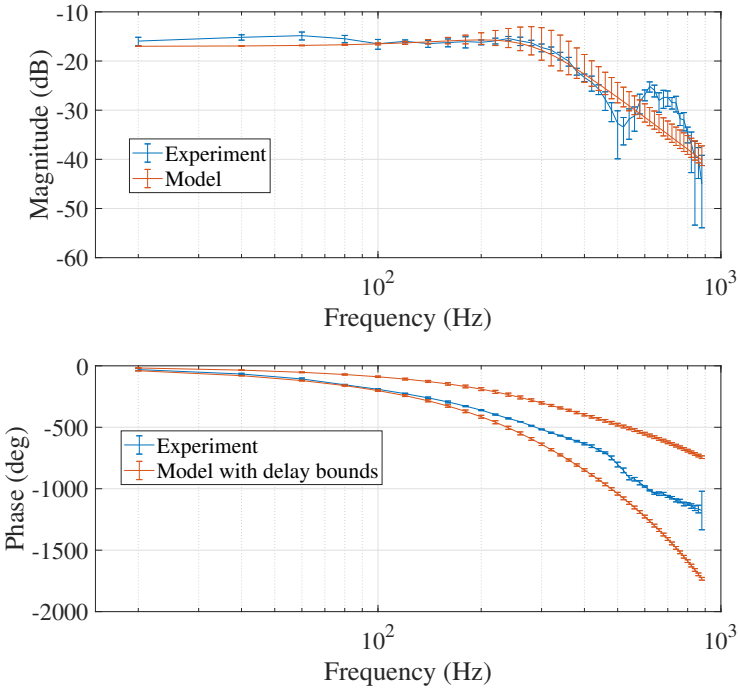

(c) 220 slpm

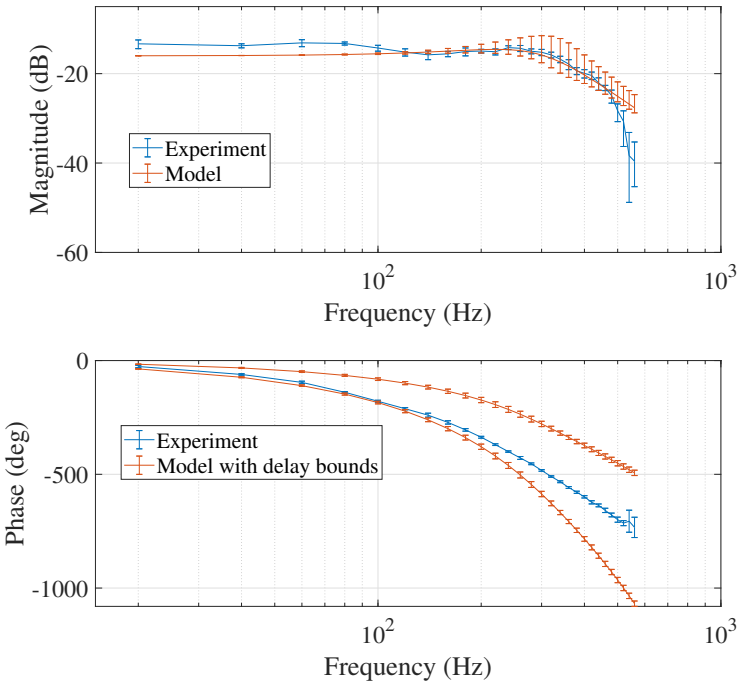

(d) 240 slpm

Figure 4.17: Dynamic jet responses: ETFE from experimental data (blue) and model output (red).

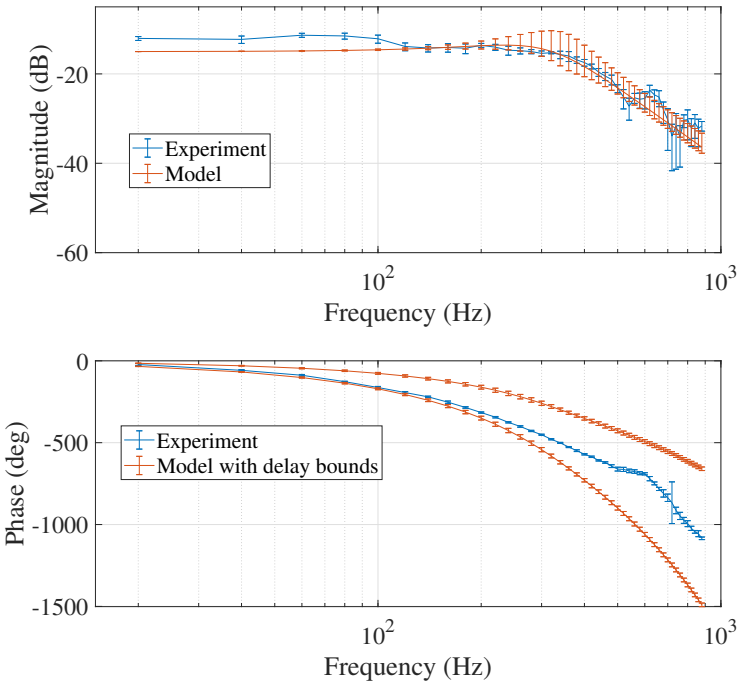

(e) 260 slpm

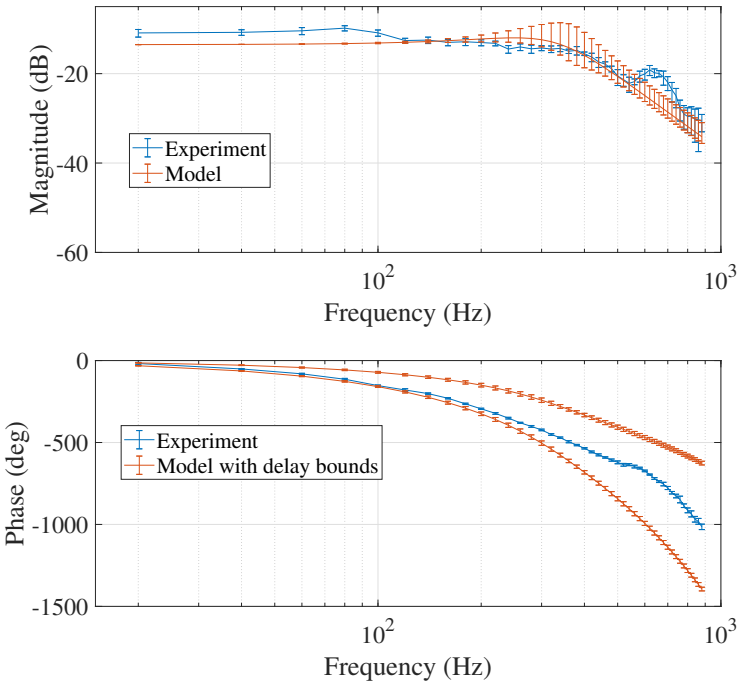

(f) 280 slpm

Figure 4.17: Dynamic jet responses: ETFE from experimental data (blue) and model output (red).

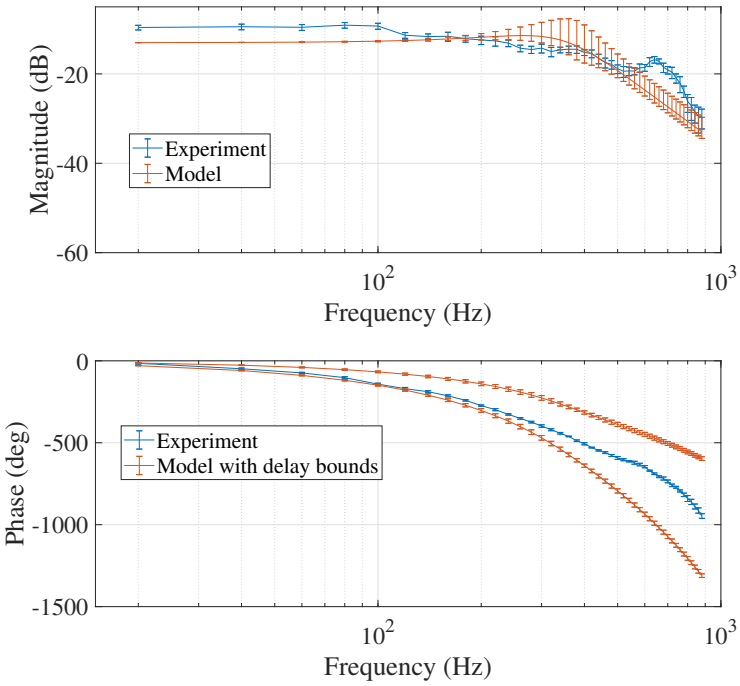

(g) 300 slpm

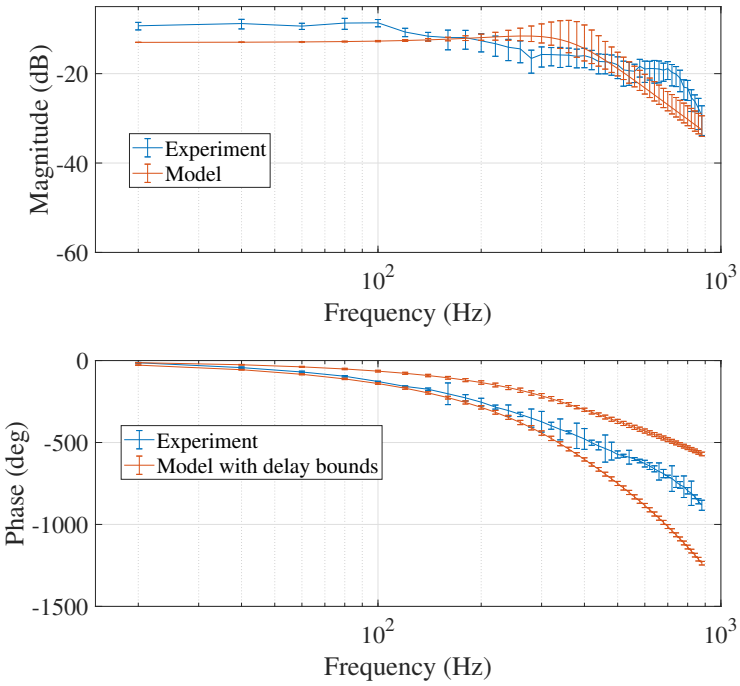

(h) 320 slpm

Figure 4.17: Dynamic jet responses: ETFE from experimental data (blue) and model output (red).

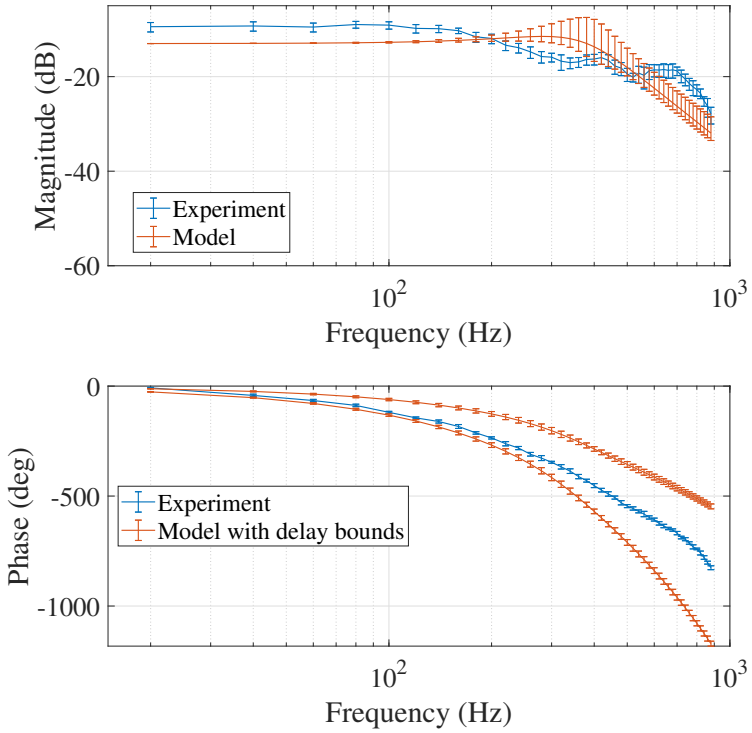

(i) 340 slpm

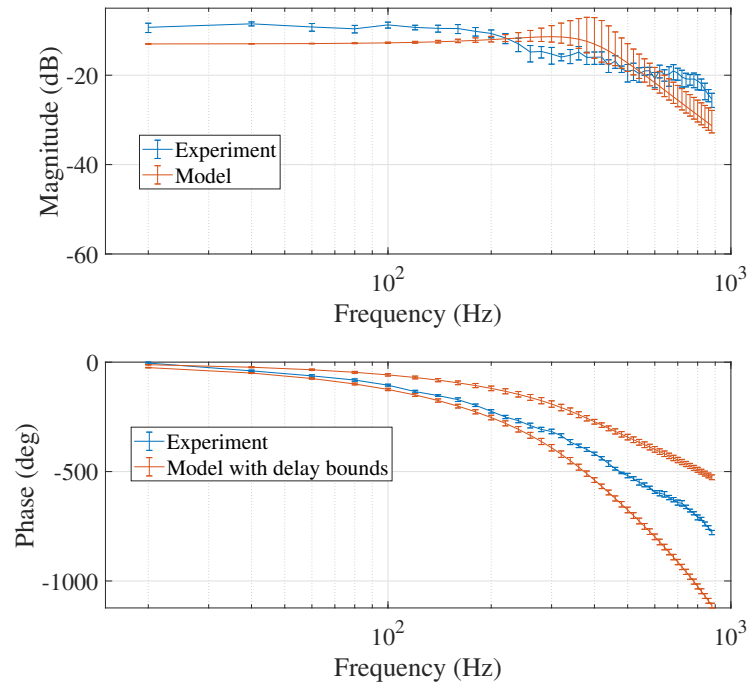

(j) 360 slpm

Figure 4.17: Dynamic jet responses: ETFE from experimental data (blue) and model output (red).

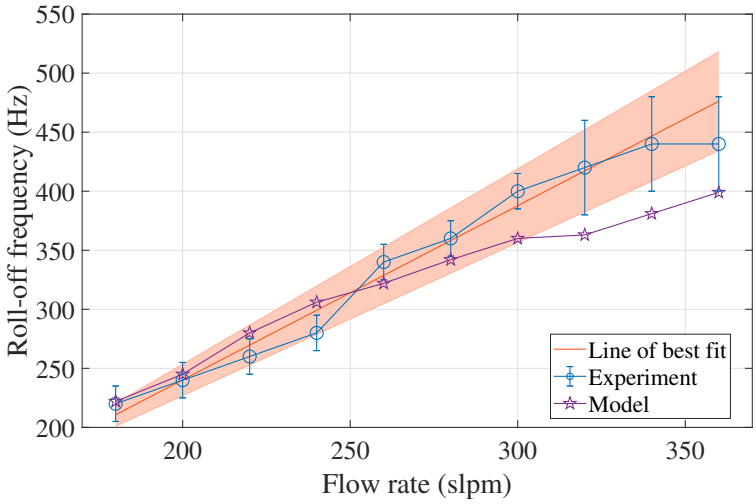

Figure 4.18: Dynamic response roll-off frequency vs flow rate: experiment principal roll-off (blue, circles) with suggested uncertainty, line of best fit (red) with its uncertainty (one standard deviation, shaded red), and model DC-level crossing (purple, stars)

Chapter 5

Closed-loop control of a fluidic amplifier

5.1 Introduction

The content of this chapter was published in the AIAA Journal [83]. It was conducted before the attached-jet model described in chapters 3 & 4 was developed, so the model was not available to determine the system dynamics. As such, black box system identification methods were required. However, the model fit to the experimentally-identified dynamics is included with adjusted parameters to account for the effect of the splitter and outlet channels among other things, which are not present in the more fundamental case of the attached jet.

This chapter demonstrates the closed-loop control of a novel piezo-fluidic amplifier that may be used in high-speed flow control applications [117, 6, 101]. The control technique described here is applicable to any device based on a fluidic jet. Piezo-fluidic amplifiers [74, 75, 72, 73] are governed by the same physics as the acoustically-excited attached jet explored in chapters 3 & 4. The purpose of this chapter is to demonstrate the effective closed-loop control of those dynamics, thereby enabling continuous output flow modulation according to a desired output trajectory.

There are comparatively few examples of feedback controllers based on dynamic models [50, 87, 94, 49]. The findings of Wiltse & Glezer [131] that jets demodulate acoustic signals, of which use was made in chapter 4, has also been applied in closed-loop control studies [120, 94]. For example, in [120], an adaptive closed-loop control scheme is used to explore the optimal AM or BM (burst modulated) forcing frequency of a synthetic jet actuator, which injected flow into the boundary layer of a NACA aerofoil to promote reattachment of the separated flow. A strain gauge was used to determine the lift and drag forces on the aerofoil, which were used to assess the degree of separation in the cost function for the adaptive control algorithm. This approach yielded a doubling of the lift-to-drag ratio.

Rapoport et al. [94] used a synthetic jet actuator to encourage a jet issuing from a nozzle terminated with a wide-angle diffuser to attach to the diffuser by thrust vectoring. The main jet responded to the modulation signal of an AM-driven synthetic jet. System identification was used to fit a second order dynamic model and a controller was designed using an internal model control (IMC) scheme. The controlled jet responded up to 30 - 50 Hz, achieving an order of magnitude higher bandwidth than conventional thrust vectoring mechanisms.

Mair et al. [73] used a highly reliable piezo buzzer to deflect the jet inside a Coandă diverter causing the device to switch its state. However, the response of the device was limited by the application of open-loop control only. The use of open-loop control has two main disadvantages: (*i*) no disturbance rejection, and (*ii*) significant variation of the switching time. The former makes the system susceptible to upstream and downstream pressure changes whereas the latter precludes the use of the device in applications that require strong synchronisation. In the present work, closed-loop control is used to tackle both of these deficiencies by utilising pressure measurements from the total pressure tappings in the output channels as feedback signals (see Fig. 5.1) and by relying on the demodulating properties of jet dynamics as first demonstrated by Wiltse & Glezer [131].

Section 5.2 describes the experimental setup. The system identification experiments used to

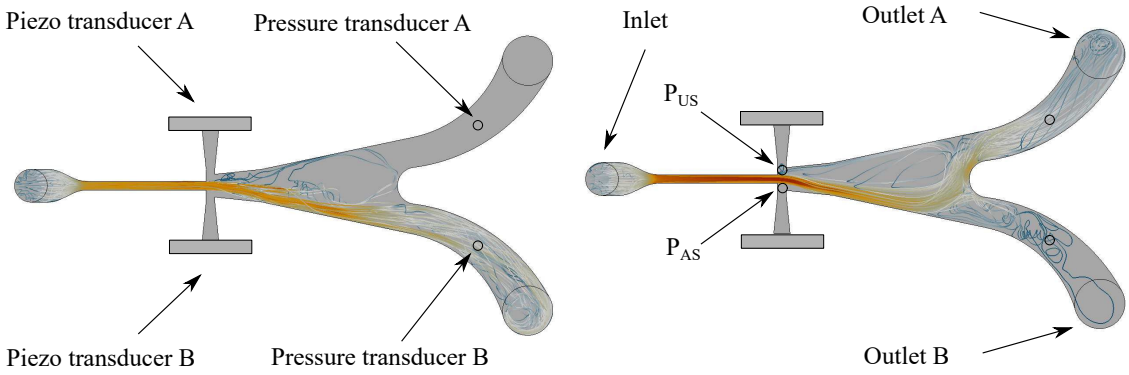

Figure 5.1: Fluidic amplifier used in this paper.

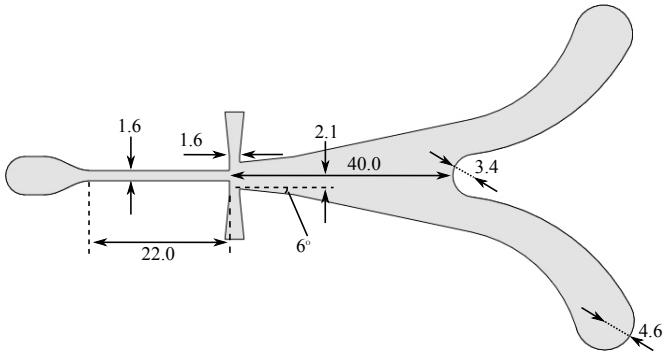

Figure 5.2: Device dimensions. Unless otherwise indicated, the units are mm. The depth of the fluid path is $d = 4.8$ mm.

determine the jet dynamics inside the device, similar to those in chapter 4, are detailed in section 5.3. Section 5.4 describes the design of the output-LQG controller. Finally, section 5.5 demonstrates experimentally the effectiveness of the closed-loop scheme in controlling the jet.

5.2 Experimental setup

The device used is shown in Fig. 5.1, with detailed dimensions given in Fig. 5.2. The inlet channel has a rectangular cross-section with width $b = 1.6$ mm by height $d = 4.8$ mm. The geometry for this device is very similar to that in chapter 4 up to a certain downstream distance: instead of an outlet slot there is a splitter which divides the flow into two outlet channels. In the unexcited case, the flow exits entirely through the outlet on the attached side, as explained in chapter 2. It has been described in detail in chapters 3 & 4 how the

Coandă effect is weakened by acoustic excitation. The result is that the jet is deflected away from the wall to which it is attached. For a fluidic amplifier, this means that the jet is pushed towards the unattached side outlet channel. In the limiting case that $R \to \infty$ (R is the jet radius of curvature), i.e. a straight jet, the flow would be divided equally between the two outlet channels by the splitter. Hence, increasing R by acoustically exciting the unattached side shear layer results in a portion of the jet exiting the fluidic device via the unattached side outlet.

The principal flow rate used was 40 lpm, corresponding to an approximate mean inlet channel velocity of 114 ms^{-1} and a Reynolds number based on the hydraulic diameter of 2.2×10^4. At this flow rate, it is not possible to make the jet switch, although large deflections of the jet are possible, and a portion of the flow can be directed out of the unattached side channel. Hence, the goal is to provide a second mode of operation for the device (in addition to the traditional full-switch, possible at lower flow rates). This mode operates at higher jet speeds relative to conventional operation so that a faster response is obtained, but does not lead to a full switch as a result of limited piezo amplitude. This results in lower effective gain (from piezo amplitude to total pressure in the unattached side outlet channel) as only part of the jet is directed out of the unattached side outlet. However, since the jet is never fully detached, the slow dynamics of detachment and reattachment are avoided [31]. This, in combination with higher jet speeds, ensures a faster device response, leading to higher effective bandwidth. The output used is the total pressure in the unattached side channel, as measured by a total pressure tapping in the centre of the channel. While it would be more accurate to use, for example, a hot-wire anemometer at the unattached side outlet orifice, this measurement strategy would not be sufficiently robust to be used in a real application.

The experimental setup is shown in Fig. 5.3. The elements of the setup are the same as those described in section 4.2, with a small number of differences. Instead of the Visaton loudspeaker, the actuator used was the Kingstate 108 dB Panel Mount Continuous External Piezo Buzzer. The piezo was used because it is highly reliable. The measurement

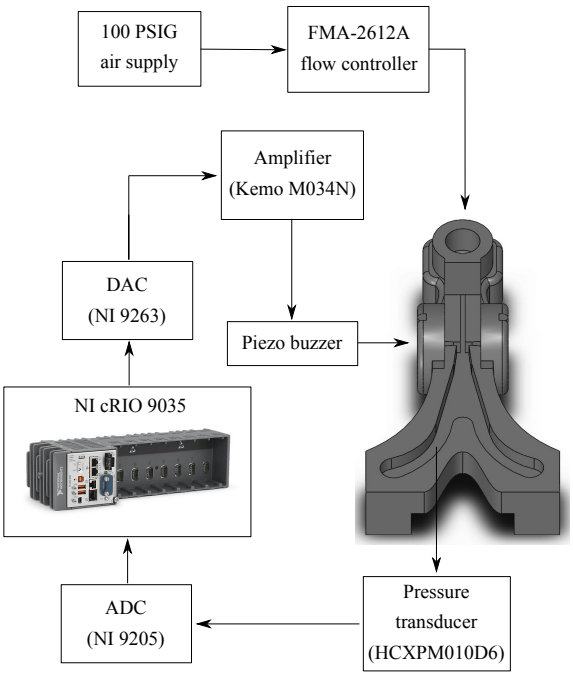

Figure 5.3: Experimental setup

connection described is the same format as shown in Fig. 4.2, but in this chapter there were two versions of it: MC 1 and MC 2. The latter version simply had the shortest possible lengths of each section of the connection, thus reducing its filling time and increasing its bandwidth. The First Sensor pressure transducer has a response time of 100 μs, but the limiting factor in the measurement frequency response is the filling associated with the measurement connection. Another pressure transducer, a Honeywell SDX series device, was also used but showed no improvement in the frequency response for the same reason. It is the measurement connection that causes the roll-off. The sampling rates and filtering used are also the same as in section 4.2.

5.3 System identification

5.3.1 Linearity

The sources of nonlinearity in this device are equivalent to those discussed in section 4.4, chapter 4. To reiterate briefly, these are are listed here.

1. The pitot in the unattached side outlet channel measures a point in the shear layer,

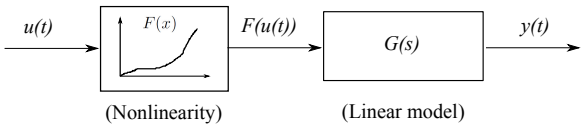

Figure 5.4: Approximation of plant: Hammerstein model

which is unlikely to be linear;

2. The piezo-amplifier system has a nonlinear input-output response;

3. The control port channel cavity response is a function of frequency;

4. The response of the shear layer to the acoustic signal emitting from the end of the control port channel has a nonlinear amplitude response and may also a function of excitation frequency;

Points 1, 2, and 4 contribute to the amplitude nonlinearity, while points 2, 3, and 4, contribute to the frequency nonlinearity, i.e. the static deflection curve. The system model can be approximated with a Hammerstein model, shown in Fig. 5.4, where the system amplitude nonlinearities have been incorporated into the static nonlinearity, $F(x)$.

The function $F(x)$ was determined at several flow rates by driving the audio amplifier at 2.75 kHz with amplitude linearly increasing from 0 to 10 V. The resulting characterisations are shown in Fig. 5.5 with corresponding fitted rational functions. Input amplitudes greater than $\sim$0.8 V are omitted because the resulting deflection was not strictly monotonically increasing. Unlike in chapter 4, the amplitude response is nonlinear. The curves in Fig. 5.5f are the scaled, inverted, fitted functions that were implemented in look-up tables for the dynamic system identification experiments in section 5.3.3 in order to preserve linearity. These curves demonstrate that the function $F(x)$ is relatively insensitive to flow rate, suggesting that any feedback controller will not be limited in tracking reference jet positions away from the design flow rate because of a variation in the system amplitude nonlinearity.

An experiment was conducted in order to determine the significance of the contributions to

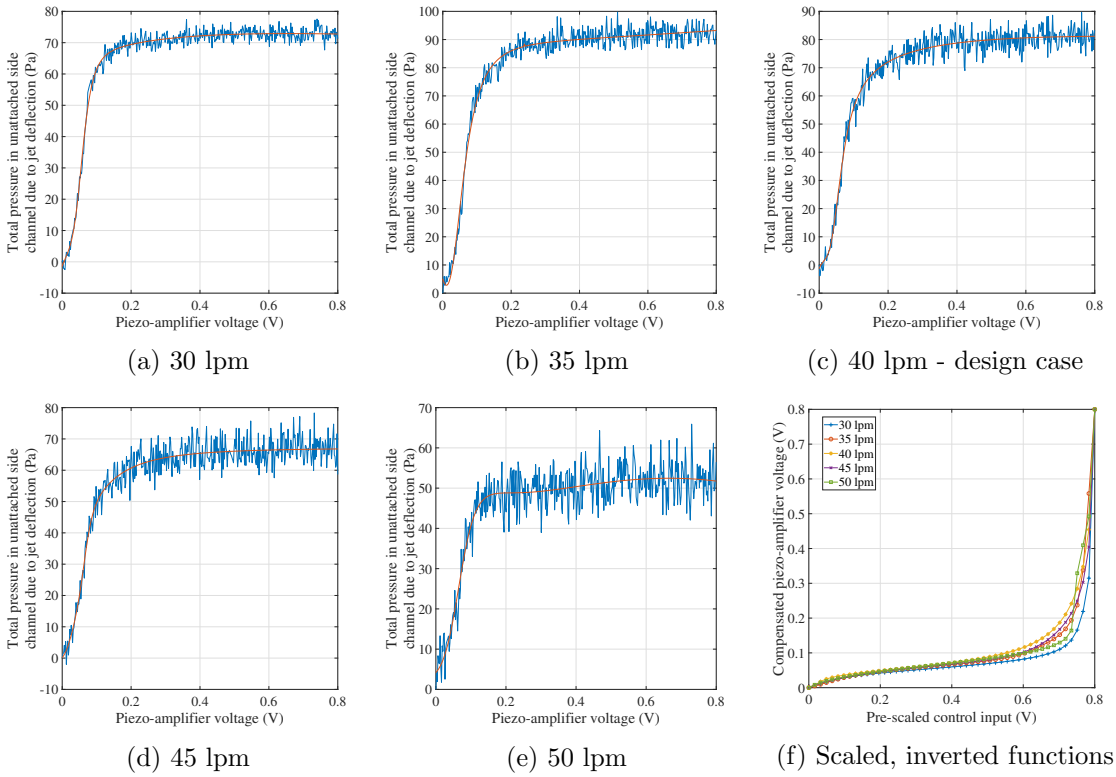

(a) 30 lpm (b) 35 lpm (c) 40 lpm - design case

(d) 45 lpm (e) 50 lpm (f) Scaled, inverted functions

Figure 5.5: System nonlinearities, $F(x)$, at several flow rates: ensemble averaged data (N = 2, blue) and fitted rational functions (red), $f_c = 2.75$ kHz; Fig. 5.5f shows the scaled, inverted functions for each flow rate for look-up table implementation.

the nonlinearity curves in Fig. 5.5, which represent the overall input-output nonlinearity at each flow rate. A 2.75 kHz tone was used to drive the piezo-amplifier system, linearly increasing in amplitude from 0 to 0.8 V over 50 seconds, and the resulting sound pressure level was measured by PT B (the Kulite) in one of the outlet channels. Note that the flow was switched off for this experiment. The time series was split into 400 sets of 6250 samples, and the RMS was taken of each set, resulting in a 400-sample curve. These data were scaled up to the amplitude of the 40 lpm input-output nonlinearity rational function so as to draw a comparison, and both of these curves are shown in Fig. 5.6. The RMS full scale error (i.e. error relative to the maximum value) of the input nonlinearity (red) relative to the overall nonlinearity (blue) is 4.2%. This justifies the use of a Hammerstein model structure, which assumes that the system nonlinearity is entirely at the input to the system (Fig. 5.4).

With the implementation of the LUTs to invert the amplitude nonlinearity, the jet de-

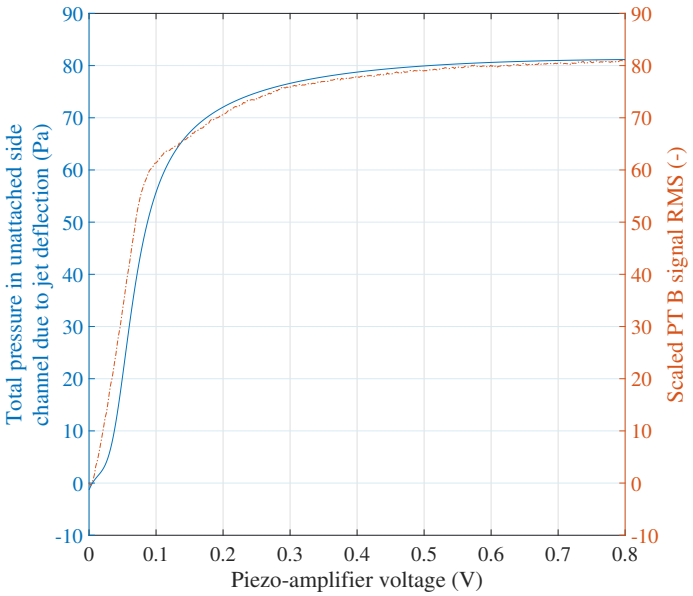

Figure 5.6: Input-output nonlinearity rational function at 40 lpm (solid blue) and scaled input nonlinearity as measured by PT B (Kulite) RMS (dash-dot red)

flection is now only dependent on the tone frequency. This was the situation in chapter 4, and the response to a tone with amplitude A with frequency f is $A\, g_{\text{resp}}(f)$.

5.3.2 Frequency sensitivity of the jet to perturbation: static deflection curves

When the piezo is driven by a single frequency tone in the range 1.3 to 4.8 kHz, the jet is deflected, resulting in a steady state increase in the unattached side total pressure. To identify frequencies at which the piezo-jet system is most responsive, the piezo on the unattached side was driven through the audio amplifier with a chirp input signal with an amplitude of 70 mV from 1.3 to 4.8 kHz over 100 s, i.e.

$$u(t) \;=\; A\sin\left[2\pi\left(\xi_{\text{ch}}t + \frac{\gamma_{\text{ch}}}{2}t^2\right)\right], \tag{5.1}$$

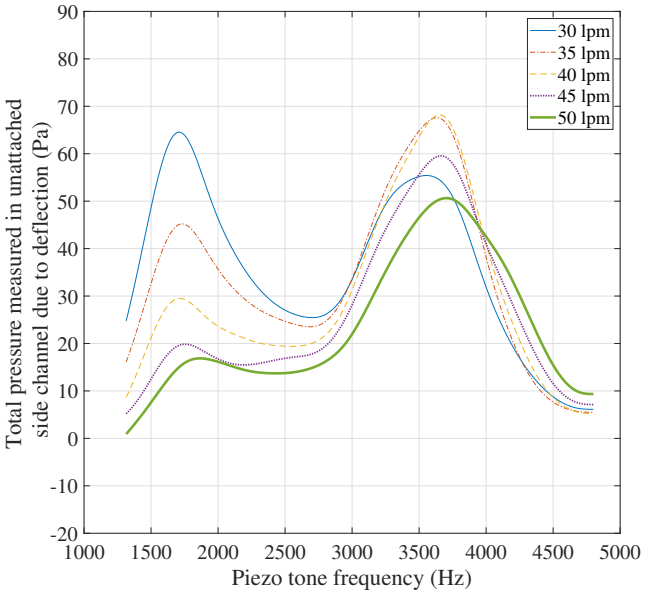

Figure 5.7: Static jet deflection vs perturbation tone frequency at several flow rates: 30 lpm (blue, solid), 35 lpm (red, dash-dot), 40 lpm (yellow, dash), 45 lpm (purple, dot), 50 lpm (green, bold solid)

where $\gamma_{\text{ch}} = 35$ Hzs^{-1}, and $\xi_{\text{ch}} = 1.3$ kHz. The signal mean was sampled to determine the degree of deflection, given by

$$y(t) \;=\; A\, g_{\text{resp}} \left(\xi_{\text{ch}} t + \frac{\gamma_{\text{ch}}}{2} t^2 \right). \tag{5.2}$$

Figure 5.7 shows the resulting static deflection curves. It should be noted that this curve shows deflections away from the natural bias, which is itself a function of flow rate. A method for inverting the static deflection curves at the output was presented in section 4.6. In this chapter, the aim is to control the jet in the closed-loop. Inverting the static deflection curves is therefore not possible when the input signal is generated in real-time in the time domain. This is explored in detail in section 5.3.3.

5.3.3 Jet Dynamics

5.3.3.1 Experimental identification

To identify the jet's dynamic behaviour, system identification experiments were carried out where the deflection was varied dynamically. The carrier signal at 2.75 kHz, $g_c(t) =$

$\sin(2\pi f_c t)$ (where $f_c = 2.75$ kHz), is amplitude modulated by another signal, $g_m(t)$. Just as described in chapter 4, the resulting jet is deflected dynamically and the deflection follows the shape of $g_m(t)$. As an example, if $g_m(t) = A\sin(2\pi f_m t) + B$, where f_m is low enough to avoid exciting the jet dynamics, the signal driving the audio amplifier is given by

$$g_{\text{ex}}(t) = g_c(t)g_m(t) = \sin(2\pi f_c t)F^{-1}\left\{(A\sin(2\pi f_m t) + B)\right\}, \tag{5.3}$$

where $F^{-1}(x)$ is the inverted system nonlinearity, i.e. the relevant curve in Fig. 5.5f, and the deflection varies between $g_{\text{resp}}\left(F^{-1}\left\{(B-A)\right\}, f_c\right)$ and $g_{\text{resp}}\left(F^{-1}\left\{(B+A)\right\}, f_c\right)$. It is important to note that while $F^{-1}\left\{(B-A)\right\}$ is included as in input to g_{resp} here, the LUT inversion provided by $F^{-1}\{\}$ ensures that the response is only linearly dependent on the amplitude. The dependence on f_c remains nonlinear. The system considered is between the time-varying component of the modulating signal, $g_m(t)$, and the total pressure in the unattached side channel.

The amplitude of the offset of the carrier signal, B in the example above, was chosen to be 0.3 V because it is in the middle of the range of possible input amplitudes, and the modulation signal amplitude, A above, was also 0.3 V, giving a 100% modulated input. The FPGA produces the signal $g_{\text{ex}}(t) = g_c(t)F^{-1}\left\{g_m(t)\right\}$. The signal $g_m(t)$ is an offset sinusoid which changes in frequency from 10 to 1960 Hz in 30 Hz steps over 200 s, so that

$$g_m(t) = A\sin\left(2\pi t\left(f_0 + f_1(t)\right)\right) + B, \tag{5.4}$$

where $f_1(t)$ increments by 30 Hz periodically. A stepped sinusoid input was chosen rather than a chirp signal because of the high noise levels in the device. A chirp signal spreads the input energy over a broad, continuous range of frequencies, and the jet response at each frequency was found to be dominated by its random fluctuations rather than the response to the input excitation. While the stepped sinusoid does not result in a continuous range of frequencies, the response it produces dominates at a discrete set of frequencies, thus allowing accurate magnitude and phase calculations.

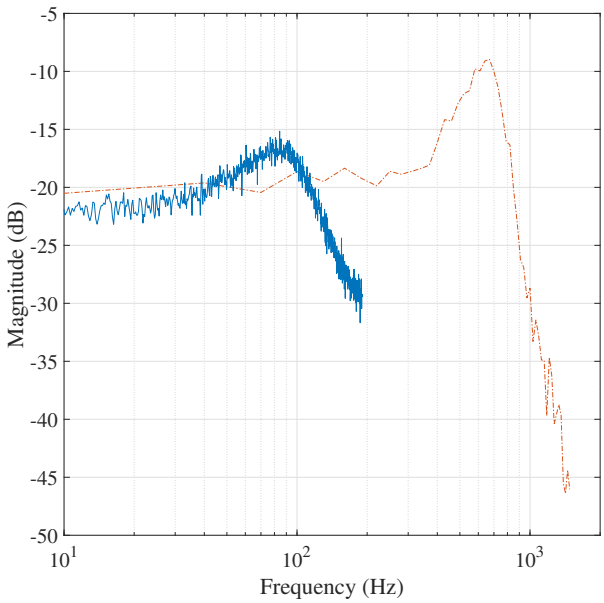

Figure 5.8: Open-loop Bode magnitude plot from ETFE at 40 lpm and $f_c = 2.75$ kHz. ETFE from MC 1 (blue, solid) and from MC 2 (red, dash-dot).

The dynamic system identification experiments were performed at several flow rates around the design case (40 lpm) in order to indicate the sensitivity of the plant to variations in the inlet flow rate, with the relevant nonlinearity compensator, $F^{-1}(x)$, from Fig. 5.5f, implemented in a LUT. The empirical transfer function estimate (ETFE) is defined as

$$\hat{G}(\omega) = \frac{\Phi_{yu}(\omega)}{\Phi_{uu}(\omega)}, \tag{5.5}$$

where $\Phi_{yu}(\omega)$ and $\Phi_{uu}(\omega)$ are the cross-spectral density of the output and the input and the power spectral density of the input respectively. Note that the input is taken as $u(t) = g_m(t) - B$, and the output is the total pressure in the unattached side outlet channel less its unexcited value. Initially, the response captured at 40 lpm using PT A and measurement connection 1 (MC 1) gave the blue curve in Fig 5.8. It was found that the roll-off in the response, at $\sim$ 150 Hz, was a result of the dynamics of the tube connecting the pressure tapping to the pressure transducer (MC 1), despite the faster response time of the transducer itself (100 μs). As such, the connection between the pressure tapping and the transducer was redesigned (MC 2), and the experiment was repeated. The corresponding response

is shown in red in Fig. 5.8. The same dynamic system identification was carried out at several flow rates in order to indicate the sensitivity of the plant to this parameter. The magnitude and phase responses of these data at each flow rate are shown in Fig. 5.9. The true jet deflection system roll-off was measured to be slightly higher by repeating the system identification experiments with PT B, which requires no measurement connection and has a higher bandwidth limitation. However, PT B suffers from poor temperature compensation which causes the mean signal to vary, making it unsuitable for use in a tracking problem. Therefore, the small reduction in bandwidth was considered acceptable and PT A was used for the purposes of control.

5.3.3.2 Extending the model

The model developed in chapter 3 was for the case of an attached jet. There are several differences in geometry between the model and the fluidic amplifer studied in the present chapter. However, as already discussed, the most important dynamics occur around the interaction region of the fluidic device - the part with a very similar geometry to the model. The model was therefore linearised at the operating points used at each flow rate in the dynamic system identification experiments. This meant exciting the jet with the constant carrier tone offset, $B = 0.3$ V and sampling the mean pressures P_{AS}, P_{US} (static tappings shown in Fig. 5.1), and $\Delta P = P_{\mathrm{AS}} - P_{\mathrm{US}}$ over 8 seconds with PT A. These data were used to solve for the model system equilibrium, with the appropriate geometric parameters inserted. The values of R were calculated using the steady state jet curvature equation (see (3.44) in chapter 3), and are plotted along with the values of P_{AS}, P_{US}, and ΔP in Fig. 5.10. Note that volumetric flow rates between 30 and 50 lpm were set during the experiments, but the mass flow rates in slpm were also recorded, which is the x-axis unit in Fig. 5.10.

The most noticeable differences between the values of R presented in the figure compared with those given for the equivalent experiments in chapter 4 are that they are larger and increase more with flow rate. The measurements taken for P_{AS} and P_{US} in the fluidic device were from tappings that had a diameter of approximately 1 nozzle width, compared with around 0.3 nozzle widths for the device used in chapter 4. This made it difficult to drill

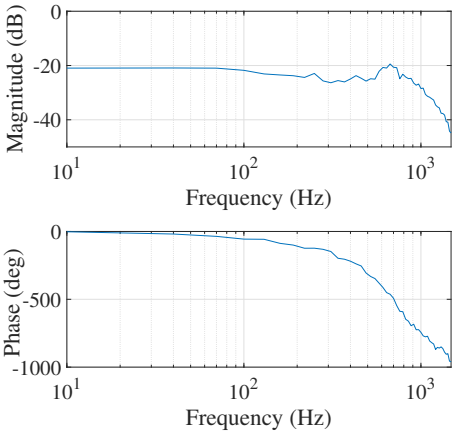

(a) 30 lpm

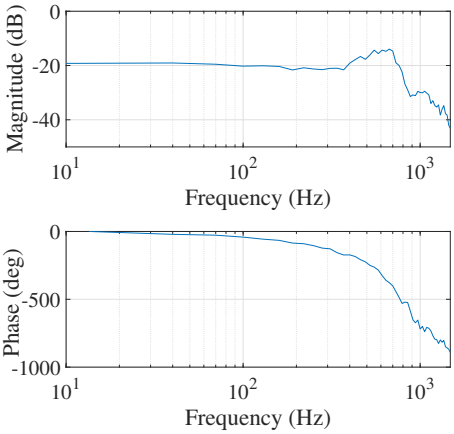

(b) 35 lpm

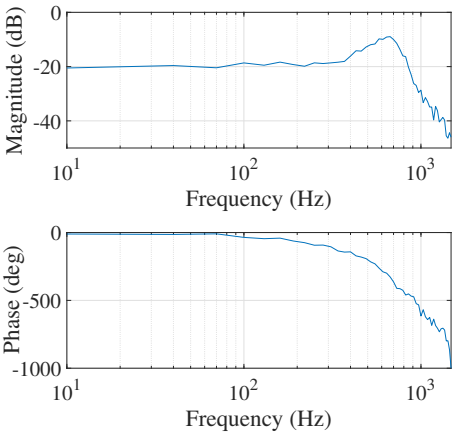

(c) 40 lpm - design case

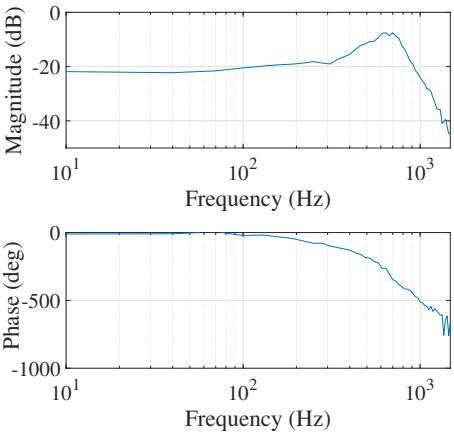

(d) 45 lpm

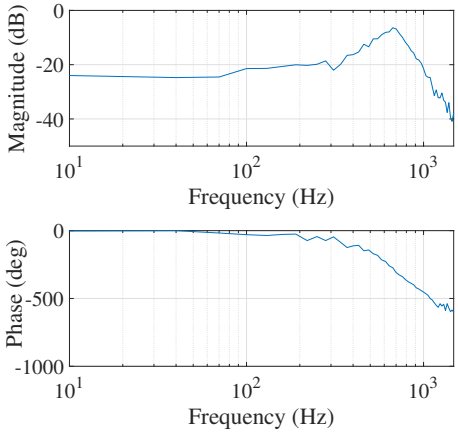

(e) 50 lpm

Figure 5.9: Open-loop Bode plots from ETFE with MC 2, $f_c = 2.75$ kHz.

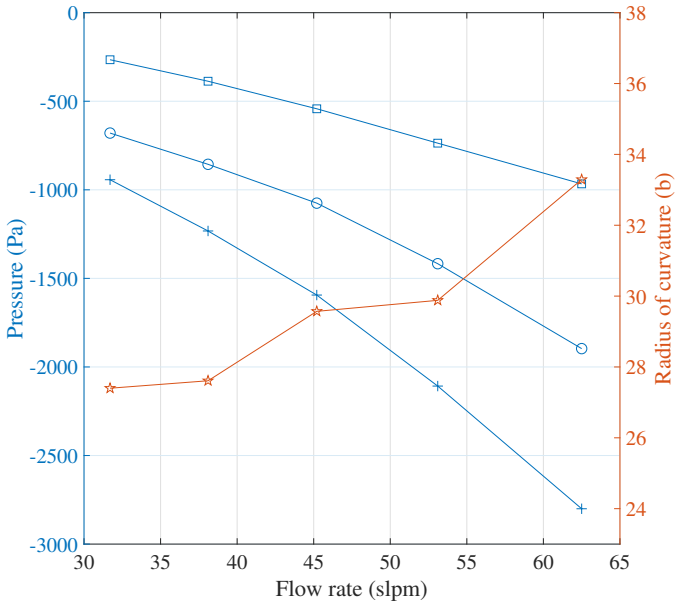

Figure 5.10: Pressures: P_{AS} (blue, crosses), P_{US} (blue, circles), ΔP (blue, squares), and radius of curvature (red, stars) vs flow rate. Data collected for fluidic device with constant excitation $u(t) = F^{-1}\{B\}\sin(2\pi f_c t)$; $B = 0.3$ V, $f_c = 2.75$ kHz.

the holes for the P_{AS} & P_{US} tappings in the fluidic device, leading to more uncertainty in those measurements, which could contribute to the larger value of R. However, they are not necessarily unreasonably large values of R because the splitter and outlet channels provide significant back pressure to the attachment point. This has the effect of weakening the Coandă effect, because the back pressure increases the pressure downstream of the attachment point, P_∞. The back pressure also increases with flow rate, which may explain why the value of R also follows that trend.

It may be the case that the piezo excitation is more effective at weakening the attachment and deflecting the jet in the fluidic device than the loudspeaker excitation is in the model validation device. When there is a splitter present and the jet is deflected so that part of it travels into the unattached side outlet channel, CFD simulations (not conducted by the author) have indicated that a vortex can be formed on the unattached side of the splitter by the deflected flow. This swirling flow reduces the local dynamic pressure, which effectively means lowering the unattached side pressure and encouraging further Coandă

weakening. This may help to explain why the acoustic excitation is more effective in the presence of a splitter. It is likely a combination of these points that explain the larger values of R.

The model responses were fitted to the experimental data in Fig. 5.9 and are shown in Fig. 5.11. As in chapter 4, bounds on the phase lag corresponding to the transport delay were added to the system phase response. The bounds for the velocity used to calculated the transport delay were similar: the average jet centreline ($y = 0$) velocity between the nozzle orifice ($s = 0$) and the measurement probe station ($s = s_{\mathrm{pr}}$) provided an upper bound on the velocity, while the profile velocity at the probe station ($s = s_{\mathrm{pr}}$) three nozzle widths from the centreline ($y = 3b$) was used for the lower bound.

The model appears to predict the roll-off frequency accurately for all flow rates but 30 lpm, and the phase response is found to be within the estimated bounds. However, the trend of increasing resonance with flow rate observed in the experimental data is not reflected in the model. The model inputs used to produce these curves differed from those in chapter 4 in several ways:

1. The attached side spread factor was set as $\sigma_{\mathrm{AS}} = 9$, cf. $\sigma_{\mathrm{AS}} = 7.7$ in chapter 4.
2. The shape factor was set as $\kappa_1 = 1$, cf. $\kappa_1 = 2.8$.
3. The fitting parameter applied to the $\ddot{R}$ term in the JCE was set as $\kappa_2 = 2$, cf. $\kappa_2 = 0.8$.
4. The values of β_1 and β_2 were reduced to their minimum reasonable values, $\beta_1 = \beta_1 = 0$, in order to keep L_1 and L_2 as close as possible to their physically reasonable ranges given in Table 4.2, cf. $\beta_1 = 0.4$, $\beta_2 = 0.1$.

There are three reasons for the failure of the model to predict the changing resonance, and for the required adjustments to the parameters. Firstly, unlike in the model validation experiments, the static deflection curves have not been accounted for in the experimental data presented in this chapter. This is tackled later in this section. Second, as stated in section 5.3.3.1, PT A was used to record the responses, which was explained to suffer from a lower

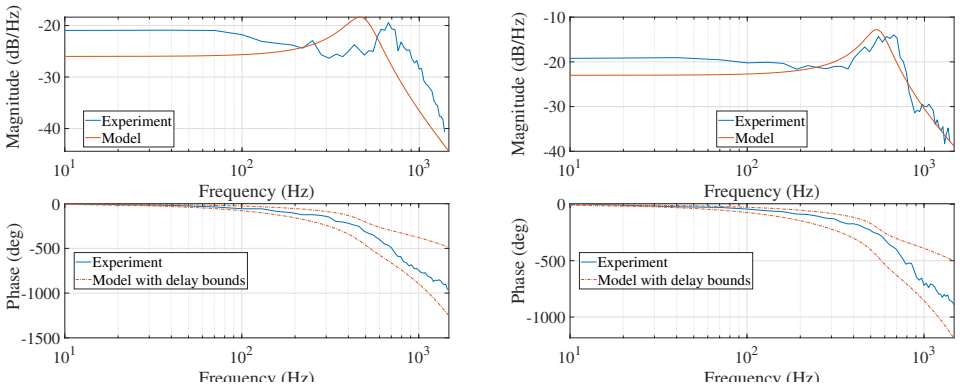

(a) 30 lpm

(b) 35 lpm

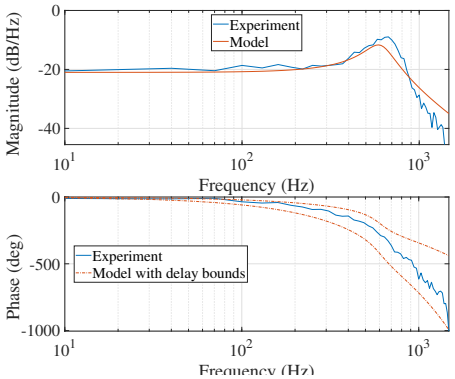

(c) 40 lpm - design case

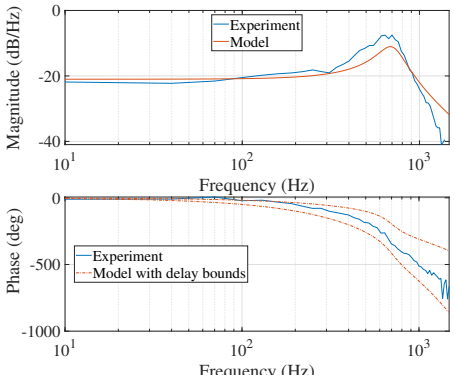

(d) 45 lpm

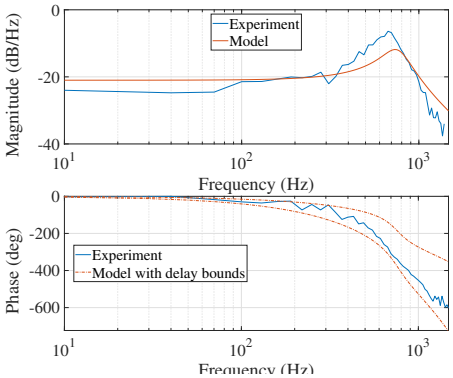

(e) 50 lpm

Figure 5.11: Open-loop Bode plots from ETFE with fitted model responses.

roll-off frequency than PT B (the Kulite). The responses are clearly therefore affected by the measurement response, which is unmodelled. Third, the effects of the splitter and outlet channels have not been considered. These can be modelled as volumes that fill, raising the static pressure to drive the flow through the impedance associated with the outlet on each side. They can therefore each be represented by an additional system pole associated with

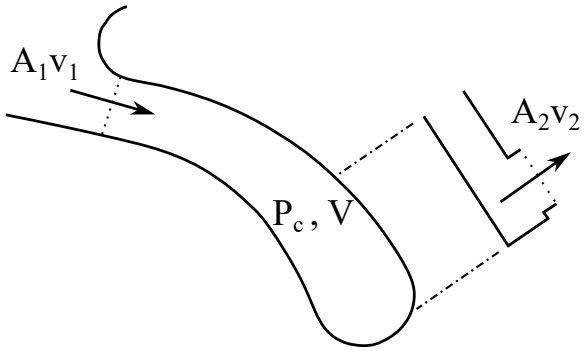

Figure 5.12: Outlet channel modelled as a volume with an impedance. Note that the dash-dot lines represent the side-view.

the filling time. When combined, they produce a complex conjugate pair, which has the effect of decreasing the damping and increasing the roll-off frequency. To understand this physically, consider the scenario where the acoustic excitation is perturbing the jet at a particular frequency, which causes it to oscillate between the outlet channels. As it moves towards the unattached side, that outlet channel is filled and the associated pressure rise (the back pressure) pushes the jet back towards the attached side. At the same time, the attached side channel is evacuated, which lowers the pressure there, having the same effect. This demonstrates how the filling and emptying of the outlet channels could increase the oscillation amplitude. In fact, this idea is central to the explanation of one of the modes of operation of the fluidic oscillator studied by Nicholls et al. [84].

To determine if the volume and impedance of the outlet channels could produce a response at the frequencies in question, some basic calculations are presented. A similar calculation was sketched out in section 4.12.1 where the filling volume was taken to be the entire diverging channel in the device. Fig. 5.12 shows a diagram of the outlet channel. The pressure in each outlet channel is determined by the ideal gas law, which, when differentiated, is given by

$$\dot{P}_c V = \dot{m} R_\mathrm{g} T = (\dot{m}_1 - \dot{m}_2) R_\mathrm{g} T, \tag{5.6}$$

where P_c is the mean pressure in the outlet channel, V is its volume, R_g is the gas constant for air, T is the temperature of the gas and $\dot{m}_1$ & $\dot{m}_2$ are the mass flow rates at the inlet and outlet of the outlet channel, as shown in Fig. 5.6. The inlet flow rate is given by

$\dot{m}_1 = \rho A_1 v_1$, while the outlet flow rate depends on the loss coefficient associated with the outlet channel. The outlet channel consists of a 90-degree elbow followed by a sudden expansion. These have associated loss coefficients of 0.9 and 1.0 respectively. The loss coefficient of the channel is therefore taken to be $K_\mathrm{L} = 2$. The outlet mass flow is given by

$$\dot{m}_2 \;=\; \rho A_2 v_2 \;=\; \rho A_2 \sqrt{\frac{2P_c}{K_\mathrm{L}\rho}} \;=\; A_2 \sqrt{\frac{2\rho P_c}{K_\mathrm{L}}}. \tag{5.7}$$

Substituting this into (5.6) and linearising with respect to P requires the derivative

$$\frac{\partial \dot{P}_c}{\partial P_c} \;=\; -\frac{\rho A_2 R_\mathrm{g} T}{V} \sqrt{\frac{1}{2\rho K_\mathrm{L} P_c}}. \tag{5.8}$$

The operating point is taken to be atmospheric conditions, i.e. $P_c = 1$ bar, $\rho = 1.2$ kgm^{-3}. The volume of the outlet channel is given by $V \approx 100\, b^2 d$, and the outlet is a circle with diameter $\sim 5b$, so $A_2 \approx 5.0 \times 10^{-5}$. Substituting these values gives the linearised system

$$\frac{\mathrm{d}P_c}{\mathrm{d}t} \;=\; \frac{R_\mathrm{g} T \dot{m}_1}{V} - 6100 P_c. \tag{5.9}$$

Taking the mass flow rate $\dot{m}_1$ as the input and taking the Laplace transform gives

$$sP_c\,(s) \;=\; \frac{R_\mathrm{g} T}{V} U\,(s) - 6100 P_c\,(s) \Rightarrow \frac{P_c\,(s)}{U\,(s)} \;=\; \frac{R_\mathrm{g} T}{V}\, \frac{1}{s + 6100}, \tag{5.10}$$

where $U\,(s)$ is the Laplace transform of the input ($U\,(s) \;=\; \mathcal{L}\,\{\dot{m}_1\}$). This first order system has a roll-off at $f = 6100/2\pi = 970$ Hz. The aim of this analysis was to estimate the response time of the static pressure in a single outlet channel to perturbations in the mass flow. A qualitative explanation of how a pair of such channels can combine to give an oscillatory 2$^{\mathrm{nd}}$ order system has been given above, but the analysis is restricted to one outlet channel for simplicity. The calculated frequency, 970 Hz, coincides with the frequencies of the resonances in Fig. 5.11. The argument presented is therefore a plausible contribution to the discrepancies between the model are the experimental data, as well as the required input parameter adjustments from their values in chapter 4.

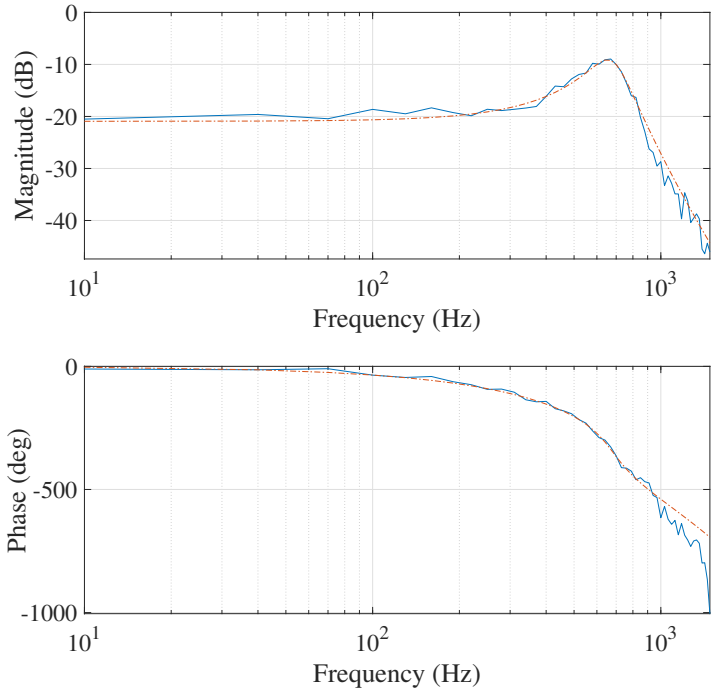

Figure 5.13: Open-loop Bode plot at 40 lpm: ETFE (blue, solid) and fitted transfer function (red, dash-dot).

5.3.3.3 Black-box identification

The previous section indicated that the responses gathered in Fig. 5.9 captured the dynamics that are to be controlled. For the purposes of developing a controller, a discrete-time transfer function model was fitted to $\hat{G}(\omega)$ (the ETFE, see (5.5)) for the design flow rate, 40 lpm, which is shown in Fig. 5.13. The transfer function was found using MATLAB's System Identification Toolbox, which was constrained by asserting that the model structure should be a 4^{th} order system. This was chosen based on the structure of the dynamic model derived in chapter 3. The transfer function is given by

$$H_{\text{plant}} = z^{-36} \frac{4.86\times10^{-6} z^{-1}}{1 - 3.88z^{-1} + 5.67z^{-2} - 3.68z^{-3} + 0.899z^{-4}}. \tag{5.11}$$

The estimated input-output delay is 36 time steps, which is 0.72 ms and corresponds to a transport delay in the device. This is the time taken for particles in the jet to travel from the inlet orifice, where upon they are acted by the piezo, to the pitot probe in the unattached

side outlet channel. This distance is approximately 50 mm, which gives an time-averaged jet speed of 69 ms^{-1} between these points. Based on the orifice mean jet velocity of around 114 ms^{-1}, this seems to be a reasonable value.

The curves in Fig. 5.9 demonstrate a significant variation in the plant dynamics with inlet flow rate away from the 40 lpm design case. In practice, it is possible that the device could be supplied with an unsteady pressure ratio, leading to varying and potentially unknown mass flow rates. The use of closed-loop control makes the system robust to these variations to some degree, which will be tested later.

5.3.3.4 Quasi-steady deflection curves

It was explained in section 4.6.1 that the effect of the static deflection curve on the dynamic response is called the quasi-steady deflection curve, which is defined by

$$\psi_{f_c}(f_m) = \left[g_{\text{resp}}(f_c - f_m) + g_{\text{resp}}(f_c + f_m) \right], \tag{5.12}$$

where it has been assumed that the amplitude nonlinearity has been inverted through use of the inverting curve $F^{-1}\{\}$. As a reminder, the response to the 100% AM input signal in given by (4.10) is

$$y(t) = A\,\psi_{f_c}(f_m)\,|G(2\pi f_m)|\,\sin(2\pi f_m t + \phi), \tag{5.13}$$

where G is the true jet dynamic transfer function, $|G|$ is its magnitude response and ϕ is its phase response combined with the transport delay. In the frequency domain, without compensating for $\psi_{f_c}(f_m)$, the response captured from system identification experiments is

$$\hat{G}(2\pi f_m) = A\,\psi_{f_c}(f_m) G(2\pi f_m). \tag{5.14}$$

In chapter 4, $\psi_{f_c}(f_m)$ was found from the static deflection curves through (5.12). An alternate means of determining the quasi-steady jet behaviour was used in this chapter because the work was completed before chapter 4. A simulation was created where two tones, initially at 2750 Hz and out of phase, linearly increased and decreased in frequency respectively

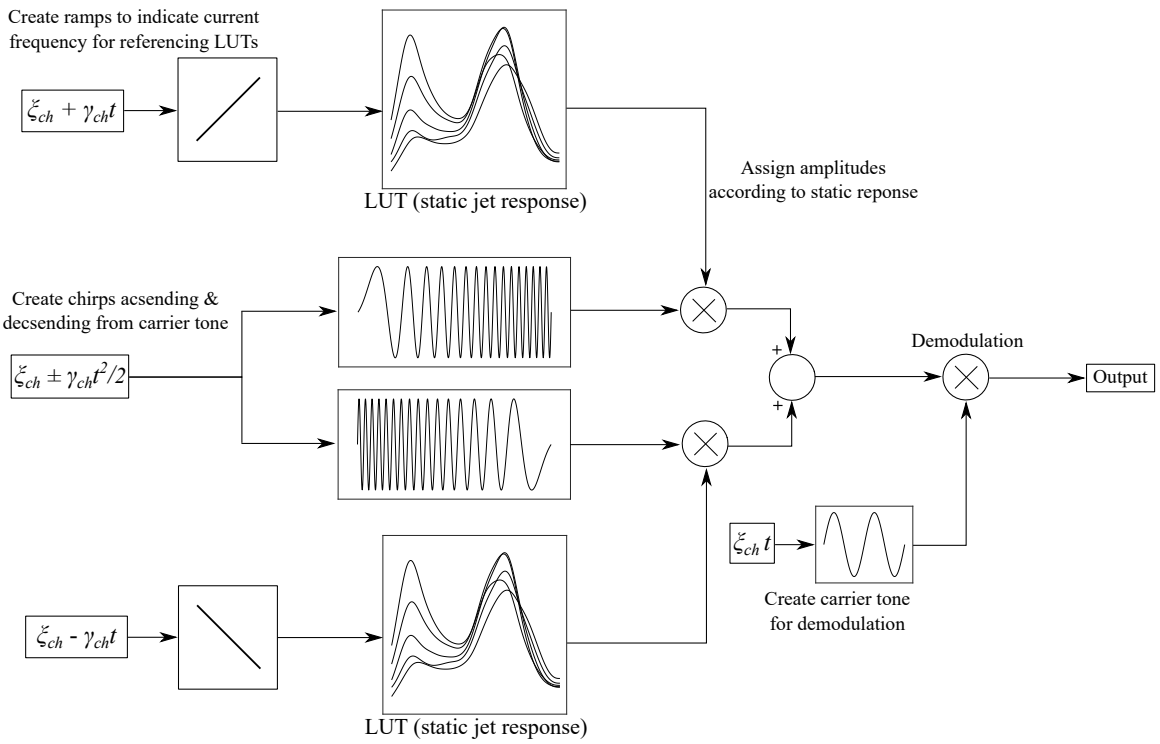

Figure 5.14: Block diagram of simulation used to determine quasi-steady jet response, $\psi(f)$, from static jet deflection response (Fig. 5.7).

at a rate of 28 Hzs^{-1} over 50 seconds. This corresponds to two copies of the signal in (5.1), with $\xi_{\text{ch}} = 2750$ Hz, $\gamma_{\text{ch}} = \pm 28$ Hzs^{-1}. The magnitudes of these tones were assigned by reference to a look-up table, which interpolated the values of the relevant static deflection curve in Fig. 5.7. The tones were then summed and the signal demodulated by multiplying by the 2750 Hz carrier tone. A block diagram of the simulation is shown in Fig. 5.14. The power spectral density of the resulting signal, $\psi_{f_c}(f)$, is plotted up to 1350 Hz in Fig. 5.15 at all of the flow rates considered.

The curve for 40 lpm and $f_c = 2.75$ kHz is referred to as $\psi_D(f)$. The similarity of the curves in Fig. 5.15 justifies the choice of carrier tone at 2750 Hz, since the resulting responses are independent of flow rate to within 1 dB, and the roll-off is higher than that of the dynamic response. To consider the effect of these quasi-steady curves on the dynamic response, the dynamic response identification was repeated at the design flow rate (40 lpm) with the amplitude of the modulating tone set to invert the shape of the 40 lpm quasi-steady response curve in Fig. 5.15. This was implemented in a look-up table ($\psi_D^{-1}\{f\}$), which was

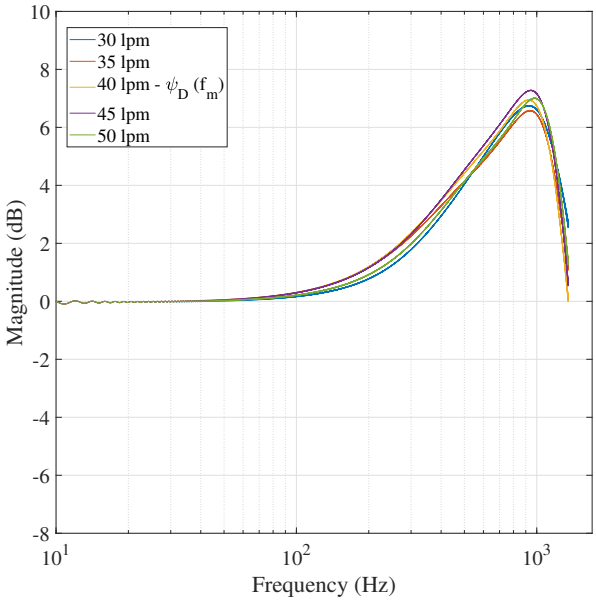

Figure 5.15: Quasi-steady state jet behaviour, $\psi_{f_c}(f)$, at several flow rates

referenced by the frequency of the modulating tone being produced, such that the audio amplifier signal was given by

$$g_{\text{ex}}(t) = \sin(2\pi f_c t) F^{-1}\left\{ {\psi_D}^{-1}\left\{f_0 + f_1(t)\right\} \sin\left(2\pi t\left(f_0 + f_1(t)\right)\right) + B \right\}. \tag{5.15}$$

A dynamic system identification was conducted at 40 lpm using (5.15), with the carrier offset set to 0.25 V (B in (5.15)). The expected result was predicted by numerically inverting $\psi_D(f_m)$ and applying it to the original 40 lpm magnitude response in Fig. 5.13, i.e. rearranging (5.14) to give $G = \psi_D^{-1}\left\{\hat{G}/A\right\}$. The ETFE resulting from the experiment, the predicted result given by $\psi_D^{-1}\left\{\hat{G}/A\right\}$, and the original response for 40 lpm from Fig. 5.13 are shown in Fig 5.16. There is good agreement between the predicted and measured magnitude responses, and the phase response is the same as the uncorrected data, $\hat{G}$, as expected. This demonstrates that (5.14) is a reasonable model for the effect of the quasi-steady jet response. However, it was not possible to implement $\psi_D^{-1}\{f_m\}$ in practice in a real-time controller because it is defined in the frequency domain has no corresponding phase response, such that a linear filter could not be used as a model. Additionally, the 36 T_s transport delay in the plant model (5.11) was ignored for the purposes of linear control,

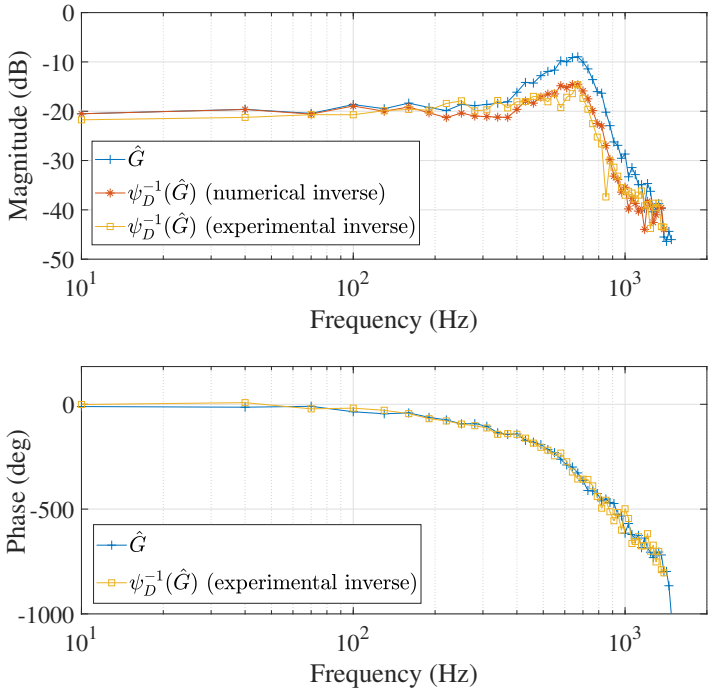

Figure 5.16: Dynamic responses at 40 lpm: original curve, $\hat{G}$ (blue, cross), predicted magnitude response from numerical inversion of quasi-steady jet response, $\psi_D^{-1}\left\{\hat{G}\right\}$ (red, star) and the result of experimentally inverting $\psi_D\left(f_m\right)$ (yellow, square).

which is justified in section 5.4.

5.4 Controller Design and Simulation

An LQR control strategy was adopted, and therefore required an observer to estimate the system states. Converting (5.11) to a state-space system,

$$\begin{aligned} \mathbf{x}(t+T) &= \mathbf{A}\mathbf{x}(t) + \mathbf{B}u(t) \\ y(t) &= \mathbf{C}\mathbf{x}(t) + Du(t), \end{aligned} \tag{5.16}$$

gave the matrices

$$\mathbf{A} = \begin{bmatrix} 3.88 & -2.83 & 1.84 & -0.899 \\ 2.00 & 0 & 0 & 0 \\ 0 & 1.00 & 0 & 0 \\ 0 & 0 & 0.500 & 0 \end{bmatrix}; \quad D = 0;$$

$$\mathbf{B} = \begin{bmatrix} 0.00391 \\ 0 \\ 0 \\ 0 \end{bmatrix}; \quad \mathbf{C} = \begin{bmatrix} 0.00297 & 0 & 0 & 0 \end{bmatrix}. \tag{5.17}$$

To clarify, the input, $u(t)$, is the amplitude of the tone that drives the audio amplifier, and the output, $y(t)$, is the total pressure in the unattached side outlet channel less its unexcited value. The equilibrium of the system is shifted by subtracting the steady state values of the states, input and output once the output has been driven to a reference signal, r. These are $\mathbf{x_0}$, u_0 and r respectively. New variables are introduced to describe variation from the steady state values, namely $\delta\mathbf{x}(t) = \mathbf{x}(t) - \mathbf{x_0}$, $\delta u(t) = u(t) - u_0$, and $\delta y(t) = y(t) - r$, so

that the system dynamics take the form

$$\begin{aligned} \delta\mathbf{x}(t+T) &= \mathbf{A}\delta\mathbf{x}(t) + \mathbf{B}\delta u(t) \\ \delta y(t) &= \mathbf{C}\delta\mathbf{x}(t). \end{aligned} \tag{5.18}$$

To eliminate steady state error, the plant is augmented with an integrator state defined by

$$z(t+T) = z(t) + \delta y(t), \tag{5.19}$$

such that when process and sensor noise is added, the dynamics become

$$\begin{aligned} \begin{bmatrix} \delta\mathbf{x}(t+T) \\ z(t+T) \end{bmatrix} &= \begin{bmatrix} \mathbf{A} & 0 \\ \mathbf{C} & 1 \end{bmatrix} \begin{bmatrix} \delta\mathbf{x}(t) \\ z(t) \end{bmatrix} + \begin{bmatrix} \mathbf{B} \\ 0 \end{bmatrix} \delta u(t) + \begin{bmatrix} \mathbf{F} \\ 0 \end{bmatrix} w(t) \\ \begin{bmatrix} \delta y'(t) \\ z'(t) \end{bmatrix} &= \begin{bmatrix} \mathbf{C} & 0 \\ 0 & 1 \end{bmatrix} \begin{bmatrix} \delta\mathbf{x}(t) \\ z(t) \end{bmatrix} + \mathbf{v}(t), \end{aligned} \tag{5.20}$$

where $\delta y'(t)$ and $z'(t)$ are the noisy measurements of $\delta y(t)$ and $z(t)$. The regulator minimised the cost function given by

$$J = \sum_{i=0}^{i=\infty} \left(\delta\mathbf{x}_i^{\mathrm{T}} \mathbf{Q} \delta\mathbf{x}_i + R\delta u_i^2 \right), \tag{5.21}$$

where $\delta\mathbf{x}_i = \delta\mathbf{x}(t+iT)$ and $\delta u_i = \delta u(t+iT)$. The tuned LQR cost parameters are

$$\mathbf{Q} = \begin{bmatrix} 1 & 0 & 0 & 0 & 0 \\ 0 & 0 & 0 & 0 & 0 \\ 0 & 0 & 0 & 0 & 0 \\ 0 & 0 & 0 & 0 & 0 \\ 0 & 0 & 0 & 0 & 10^3 \end{bmatrix}, \quad R = 10^6, \tag{5.22}$$

where $\mathbf{Q}$ is the state-error cost matrix and R is the cost of control actions. $\mathbf{Q}$ was chosen as per standard output-LQR, i.e. $\mathbf{C}^{\mathrm{T}}\mathbf{C}$, and the integrator cost was tuned manually. The states were not measured directly so a Kalman filter was used for state estimation. The

observer dynamics take the form

$$\begin{bmatrix} \delta\hat{\mathbf{x}}\,(t+T) \\ \hat{z}(t+T) \end{bmatrix} = \begin{bmatrix} \mathbf{A} & 0 \\ \mathbf{C} & 1 \end{bmatrix} \begin{bmatrix} \delta\hat{\mathbf{x}}(t) \\ \hat{z}(t) \end{bmatrix} + \begin{bmatrix} \mathbf{B} \\ 0 \end{bmatrix} \delta u(t) + \mathbf{K}_f \begin{bmatrix} \delta y'(t) - \delta\hat{y}(t) \\ z'(t) - \hat{z}(t) \end{bmatrix} \tag{5.23}$$

$$\delta\hat{y}(t) = \begin{bmatrix} \mathbf{C} & 0 \end{bmatrix} \begin{bmatrix} \delta\hat{\mathbf{x}}(t) \\ \hat{z}(t) \end{bmatrix}, \tag{5.24}$$

where $\hat{\delta\mathbf{x}}$, $\hat{\delta y}$ and $\hat{z}$ are the estimates of the state deviations, the output error and the integrator respectively. The augmented system matrices are substituted as follows

$$\begin{aligned} \mathbf{A}_{\text{aug}} &= \begin{bmatrix} \mathbf{A} & 0 \\ \mathbf{C} & 1 \end{bmatrix}, \quad \mathbf{B}_{\text{aug}} = \begin{bmatrix} \mathbf{B} \\ 0 \end{bmatrix}, \quad \mathbf{C}_{\text{aug}} = \begin{bmatrix} \mathbf{C} & 0 \\ \mathbf{0} & 1 \end{bmatrix}, \\ \mathbf{F}_{\text{aug}} &= \begin{bmatrix} \mathbf{F} \\ 0 \end{bmatrix}, \quad \mathbf{x}_{\text{aug}} = \begin{bmatrix} \delta\mathbf{x} \\ z \end{bmatrix}, \quad \mathbf{e}_{\text{aug}} = \begin{bmatrix} \delta\mathbf{x} - \delta\hat{\mathbf{x}} \\ z - \hat{z} \end{bmatrix}, \end{aligned} \tag{5.25}$$

leading to closed-loop dynamics given by

$$\begin{aligned} \begin{bmatrix} \mathbf{x}_{\text{aug}}(t+T) \\ \mathbf{e}_{\text{aug}}(t+T) \end{bmatrix} = &\begin{bmatrix} \mathbf{A}_{\text{aug}} - \mathbf{B}_{\text{aug}}\mathbf{K}_{\text{LQR}} & \mathbf{B}_{\text{aug}}\mathbf{K}_{\text{LQR}} \\ \mathbf{0} & \mathbf{A}_{\text{aug}} - \mathbf{K}_f\mathbf{C}_{\text{aug}} \end{bmatrix} \begin{bmatrix} \mathbf{x}_{\text{aug}}(t) \\ \mathbf{e}_{\text{aug}}(t) \end{bmatrix} \\ &+ \begin{bmatrix} \mathbf{F}_{\text{aug}} & \mathbf{0} \\ \mathbf{F}_{\text{aug}} & -\mathbf{K}_f \end{bmatrix} \begin{bmatrix} w(t) \\ \mathbf{v}(t) \end{bmatrix}, \end{aligned} \tag{5.26}$$

where $\mathbf{e}_{\text{aug}}$ is the state estimation error.

There is no automatic guarantee of robustness despite the individual gain and phase margin guarantees of the Kalman filter and LQR separately in continuous-time [29]. Furthermore, in the practical application considered here, discrete-time LQR has typically inferior stability margin properties [107]. It is well known that the loop-transfer recovery (LTR) methodology presented by Doyle and Stein in [30] for continuous-time systems allows the robustness properties of the full state feedback case to be recovered. It is also well understood that there lies a trade off between recovering these robustness margins and the system noise

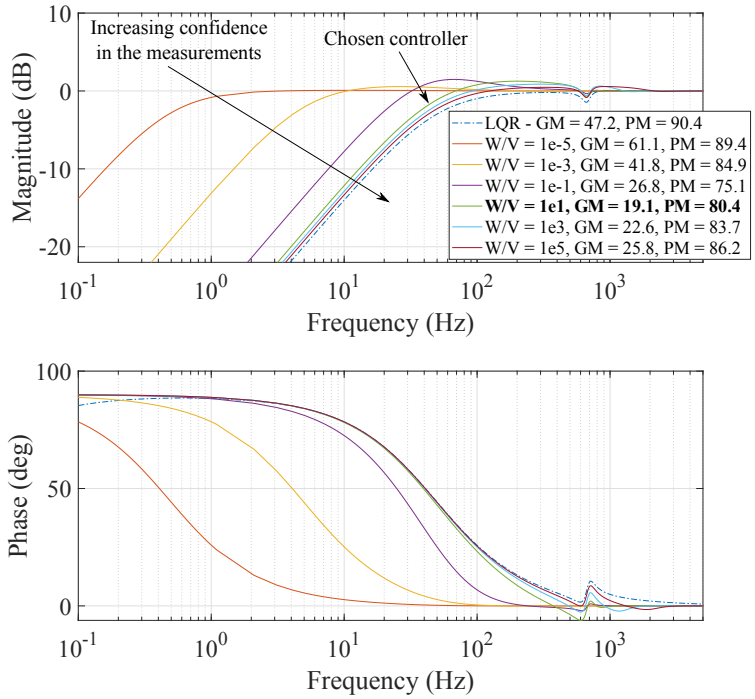

Figure 5.17: LTR procedure demonstrated with sensitivity functions for a variety of process-to-sensor noise ratios. Units for gain and phase margins in legend are dB and degrees respectively. LQR curve is dash-dot blue.

performance in continuous-time. In discrete-time it may not be possible to recover fully the LQR loop transfer properties [69]. The value of the sensitivity transfer function across the frequency space,

$$S(z) = \frac{1}{1 + C(z)H_{\text{plant}}(z)}, \tag{5.27}$$

determines a controller's ability to reject disturbances, follow the reference signal as well its noise performance [8].

The sensitivity transfer functions of the system with several process-to-sensor noise ratios are shown in Fig. 5.17 to demonstrate the LTR procedure. The integrator state measurement noise variance is fixed at $100\sigma_{y'}^2$, where $\sigma_{y'}^2$ is the sensor noise variance for the measurement $\delta y'(t)$. Fig. 5.17 shows that the LQG curves approach the LQR curve as the process-to-sensor noise ratio is increased. However, practical controller design is not as simple as choosing the system found by allowing $W/V \to \infty$, which would likely suffer from

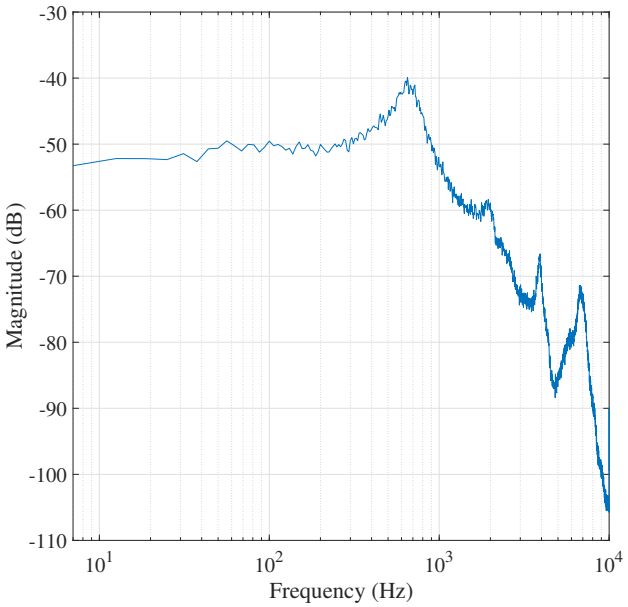

Figure 5.18: Jet spectrum: PSD of total pressure in unattached side channel at 40 lpm, no excitation.

poor noise performance. In order to select a value of W/V, the system noise spectrum must be considered. A time series was captured by sampling the unattached side channel pressure tapping whilst the jet was unexcited. The turbulence is technically an output disturbance but cannot be rejected by control action - the acoustic signals only control the jet position. Therefore, the turbulence can be thought of as sensor noise for control purposes. The power spectral density (PSD) of the time series is shown in Fig. 5.18. As can be seen in Fig. 5.18, the roll-off is caused in part by the measurement system, as described in section 5.3.3, and the frequency content is in the same bandwidth as the system. This means that choosing a larger W/V causes the controller not only to reject disturbances that can be controlled (e.g. fluctuations in the inlet mass flow) and follow the reference more effectively, but also to react to the jet turbulence. Therefore a compromise must be made to give both acceptable disturbance rejection and noise performance. The value of W/V chosen is 1e1, with a gain margin of 19.1 dB and a phase margin of 80.4°. The tuned LQR costs and Kalman filter variances that give these results are

$$W = 1, \quad \mathbf{V} = \begin{bmatrix} \text{1e-1} & 0 \\ 0 & \text{1e1} \end{bmatrix} \tag{5.28}$$

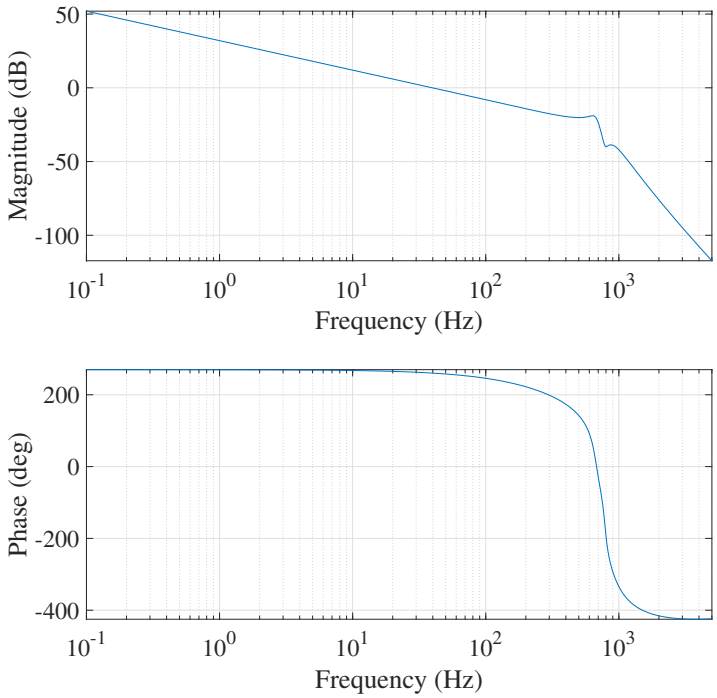

Figure 5.19: LQG transfer function Bode plot

where W and $\mathbf{V}$ are the process and sensor noise variance and covariance respectively. Note that the 5^{th} state in the system is the integrator state, and that the 2^{nd} dimension in the covariance matrix V is the variance of the integrator state measurement. The LQG controller magnitude response is shown in Fig. 5.19. The cross-over frequency for this controller is around 50 Hz, while the transport delay (0.72 ms) is a period corresponding to $\sim$ 1400 Hz. Therefore, since the closed-loop bandwidth is two orders of magnitude below this, the earlier decision not to include the input-output delay in the controller design process is justified.

5.5 Implementation and Results

The LQG controller simulated in Sec. 5.4 was implemented in the FPGA and the system block diagram is shown in Fig. 5.20. As shown in the diagram, a feed-forward term was added to help increase the speed of the initial rise of the step response, giving the control

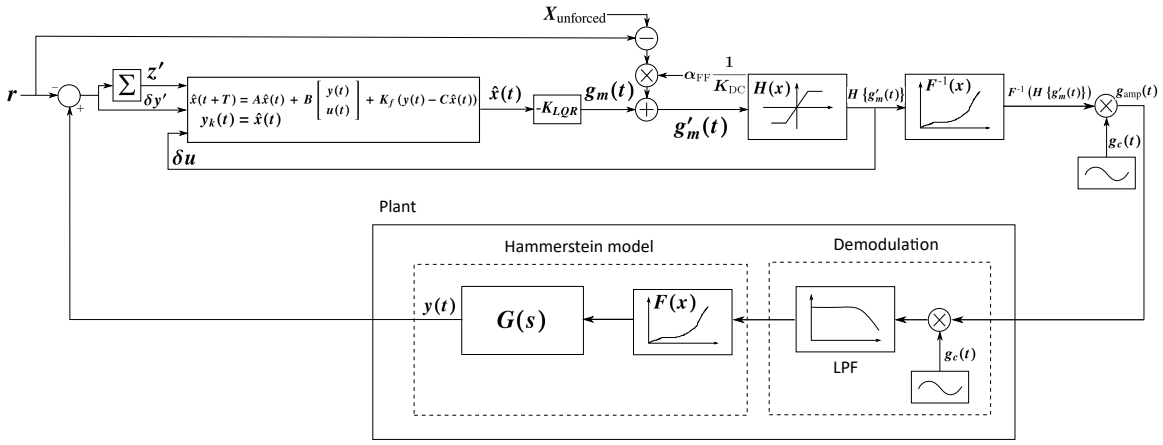

Figure 5.20: Closed-loop system block diagram

law

$$u(t) = -\mathbf{K}_{\text{LQR}} \begin{bmatrix} \hat{\delta\mathbf{x}}(t) \\ \hat{z}(t) \end{bmatrix} + u_{\text{FF}}(t), \tag{5.29}$$

where $u_{\text{FF}}(t)$ is the feed-forward term. The DC level measured by the pressure transducer due to the unforced response is X_{unforced}, K_{DC} is the DC gain of the model, and α_{FF} is a parameter used to vary the contribution from the feed-forward term when tuning the step response. The implementation of the control law is therefore

$$g'_m(t) = g_m(t) + \alpha_{\text{FF}} \frac{(r - X_{\text{unforced}})}{K_{\text{DC}}}. \tag{5.30}$$

It can be seen by comparison of (5.29) and (5.30) that $g_m(t)$ is the feedback term and $u_{\text{FF}}(t) = \alpha_{\text{FF}}\left(r - X_{\text{unforced}}\right)/K_{\text{DC}}$. Fig. 5.20 also shows that $g'_m(t)$ was limited to between 0 and 0.8 V, denoted by $H\left\{g'_m(t)\right\}$. This was necessary because the linear model fails to predict the plant behaviour outside this region. If $F^{-1}\left(g_m(t)\right) > 0.8$ V, the deflection does not increase because of the lack of strict monotonicity of the system characterisation in this range (see Sec. 5.3.1). The model indicates that values of $F^{-1}\left(g_m(t)\right) < 0$ V will cause the jet to deflect away from the centre of the device, which is not the case; the deflection is caused, in steady state, by $g_c(t)$, whose phase does not affect the direction of deflection. The audio amplifier signal is therefore $g_{\text{amp}}(t) = F^{-1}\left(H\left\{g_m(t)\right\}\right) g_c(t)$.

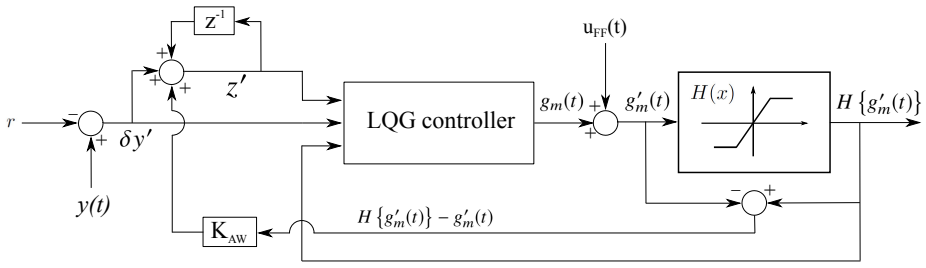

Figure 5.21: Anti wind-up scheme

The combination of an integrator state and input saturation limits necessitates an anti wind-up scheme to avoid an unstable integrator state. The details of this scheme are shown in Fig. 5.21, where the value of the anti wind-up gain, K_{AW}, was set by manual tuning, and took a value of 1e-5. This was not included in the overall closed-loop block diagram in Fig. 5.20 for brevity.

5.5.1 Step response

The ensemble averaged ($n_{\mathrm{ts}} = 50$) response of this system to a reference step from 0 to 74 Pa deflection in the unattached side channel was recorded in closed-loop, with the inlet flow at 40 lpm. As a comparison, an ensemble averaged ($n_{\mathrm{ts}} = 50$) full switch was recorded at a lower flow rate, such that the pressure in the initially unattached side channel was the same as the deflection in the closed-loop case once the jet had switched, i.e. 74 Pa. To achieve this, the flow rate was set to 15 lpm, and the amplitude of the piezo tone was set to 0.8 V. The ensemble-averaged time series were then filtered with a notch filter at 2.75 kHz to reduce the direct coupling between the piezo tone and the pressure transducer. A broad notch was also applied at 650 Hz to reduce the jet background noise in order to judge when the deflection first reached its steady state value. The resulting step responses are shown in Fig. 5.22a, while Fig. 5.22b shows an ensemble averaged control signal ($n_{\mathrm{ts}} = 50$), $g'_m(t)$ (see Fig. 5.20). In terms of rise time, the closed-loop response at 1.1 ms is thirty times faster than the open-loop full switch at 34 ms. However, this improvement comes from the faster jet dynamics at higher velocities and from using a feed-forward term in the control law rather than the feedback term. Nevertheless, using feed-forward control alone does not compensate for model uncertainty or disturbances such as mass flow variations.

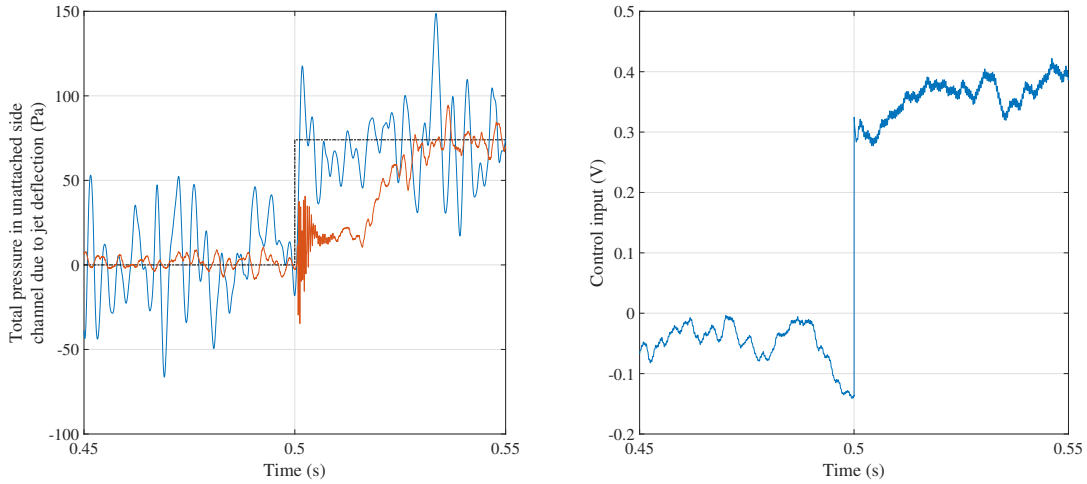

(a) Ensemble averaged & filtered step responses ($n_{\text{ts}} = 50$): closed-loop at 40 lpm (blue) and open-loop full switch at 15 lpm (red). Reference (dash-dot black).

(b) Control signal (ensemble averaged, $n_{\text{ts}} = 50$), $g'_m(t)$ in Fig. 5.20.

Figure 5.22: System step response: Open- and closed-loop system responses and closed-loop control input.

5.5.2 Disturbance rejection - mass flow variation

The controller's ability to reject disturbances was tested in two ways. First the inlet mass flow was varied. This was done in the steady state since the response time of the FMA-2612A was insufficient to test the closed-loop bandwidth of the controller. The flow rate was set to values between 19 and 54 lpm, which was the range of flow rates that the controller was able to reject whilst tracking a reference of 50 Pa deflection from the natural bias state. The mean control inputs required to maintain these deflections are shown in Fig. 5.23. The figure shows how the DC gain of the jet deflection system varies over different flow rates, with a broad maximum DC gain at the minimum of the curve, i.e. between 28 and 35 lpm.

5.5.3 Disturbance rejection - input disturbance

The response of the controller to input disturbances was tested at the design flow rate (40 lpm) by removing the feed-forward term whilst the controller was tracking a constant reference deflection of 50 Pa. The pressure in the unattached side channel due to the deflection and the control input signal are shown in Fig. 5.24. The signal processing for

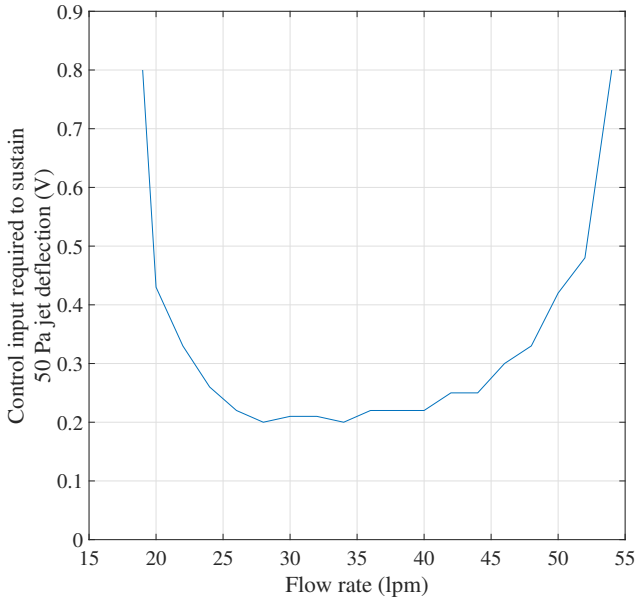

Figure 5.23: Mean control input required to maintain 50 Pa jet deflection over several flow rates.

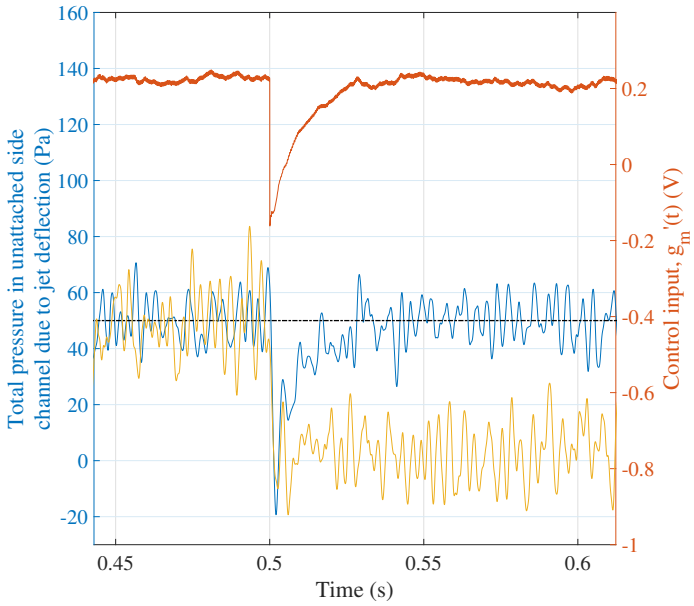

Figure 5.24: Controller response to input disturbances. Pressure in unattached side channel due to deflection: closed-loop response (blue) and open-loop response (yellow). Control signal ($g'_m(t)$) showing step change in $u_{\mathrm{FF}}(t)$ at $t = 0.5$s (red). Signal processing scheme described in text.

these data was as follows: as for the step responses in section 5.5.1, a 2.75 kHz high-Q factor notch as well as a broad notch at 650 Hz were applied to ensemble averaged time series ($n_{\text{ts}} = 50$). This was repeated 6 times and the resulting signals were also ensemble averaged. This additional ensemble averaging step was required due to the higher variance of the open-loop response times (relative to the mean). The input signal was ensemble averaged without any filtering ($n_{\text{ts}} = 350$). Fig. 5.24 indicates that the closed-loop response time to disturbances is around 28 ms, whereas the case with no feedback term has a faster response time (1.4 ms) but is unable to reject the input disturbance (as expected). It is interesting to consider the response times of the open- and closed-loop cases over several flow rates in order to evaluate the robustness of the input disturbance rejection properties to varying operating conditions. To see this, the same input disturbance experiment described above was carried out at several mass flow rates for both the open- and closed-loop cases. The response time was recorded for each case. For the closed-loop cases, this means the time to return to the reference of 50 Pa deflection, whereas for the open-loop cases, it is the time to reach the natural, undeflected jet position at each flow rate (i.e. 0 Pa in the Fig. 5.24). Each response time was normalised relative to the 40 lpm cases for open- and closed-loop respectively. These normalised times are shown in Fig. 5.25. The figure shows that response times vary significantly more in the open-loop case. In the closed-loop case the times vary by 7%, whereas the open-loop times vary by 35%. The ability not only to reject disturbances but also to reject them with a relatively consistent response over a wide range of operating conditions highlights the benefits of using feedback.

5.5.4 Performance summary of device control modes

The response times of the various device control modes are in Table 5.1. A comparison is drawn between the closed-loop response time to input disturbances, which is effectively the feedback term response time and is 28 ms, and the open-loop response time for the full switch at 15 lpm, i.e. the red curve in Fig. 5.22a, which is 34 ms. With the feedback term alone, this response time has been recovered and improved upon, with the added benefits of robustness to mass flow fluctuations and input disturbances. In practice, the controller also includes the feed-forward term (closed-loop response time to reference signal in Table 5.1),

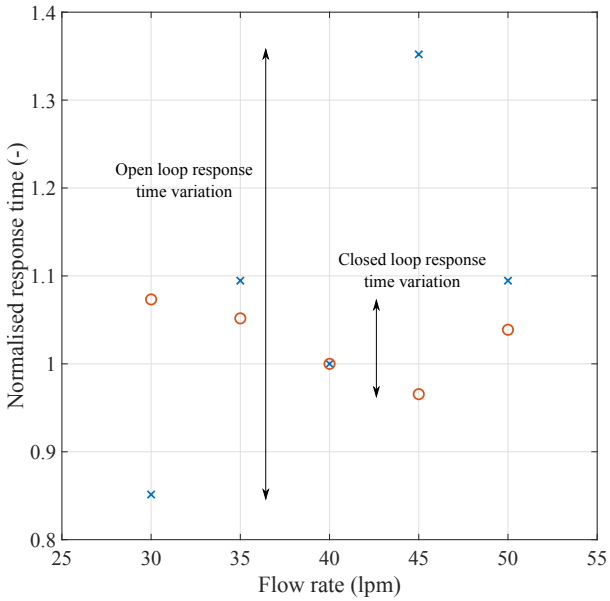

Figure 5.25: Controller response time to input disturbances relative to reference case (40 lpm): open-loop (blue, cross) and closed-loop (red, circle).

Control mode	**Resp. time to ref. sig. (ms)**	**Resp. time to inp. dist. (ms)**	**Variation in resp. time to inp. dist. (-)**
OL at 15 lpm (full switch)	34	∞	-
CL at 40 lpm (part. defl.)	1.1	28	7%
OL at 40lpm (part. defl.)	1.1	$1.4/\infty$	35%

Table 5.1: Response times for device control modes

which significantly reduces the time taken to respond to changes in the reference signal (1.1 ms) because of the faster jet dynamics at higher flow rates, while maintaining the robustness to mass flow and input disturbances due to the feedback term.

5.6 Conclusion

A novel, bistable fluidic amplifier was controlled by a piezoelectric buzzer. The degree of deflection of the jet was determined by making measurements with a pressure transducer connected to a total pressure tapping in the unattached side channel of the device. The sensitivity of the jet deflection in steady state to piezo tone frequencies (the static deflection

curve) was assessed, and the deflection was varied to identify the dynamic response. The model from chapter 3 was adapted to predict the experimental responses, and the required parameter adjustments were explained with analysis of the outlet channels of the device. A discrete linear model was developed from these data, and an LQG regulator was designed to drive the jet deflection to follow a reference. This controller was implemented on an FPGA and the resulting closed-loop controller brought a 114 ms^{-1} jet under control. The disturbance rejection performance of the controller was evaluated by varying the flow conditions and adding input disturbances.

The control design was limited by measurement noise (due to jet turbulence) in the system bandwidth, necessitating a small system gain and a low closed-loop bandwidth. In this case, the closed-loop design bandwidth was ∼79 Hz compared with an open-loop bandwidth of ∼900 Hz, an order of magnitude difference. This appears to be a significant problem in the feedback control of jets that severely limits the controller performance. However, the jet noise measured by the outlet channel pressure transducer is unlikely to be correlated to the jet noise measured elsewhere in the device. For example, the difference between the pressure measurements on either side of the jet could be used as a second measurement for the control system. The transport delay may represent a limiting factor in this case, but is sufficiently small (~ 0.72 ms) that the approximate limiting bandwidth, given by the inverse of the sum of the transport time and the time constant of the open-loop response, is $f_{\text{lim}} \approx 10^3/(0.72 + 1.1) = 550$ Hz. Using the second measurement raises some exciting possibilities for disturbance identification and rejection. Namely, the known transport delay between the two measurements would make it possible to distinguish between input and output disturbances by using the relevant correlations between the measurements as system states.

Chapter 6

Shear layer modulation

6.1 Introduction

So far in this thesis, focus has been placed on the bulk jet response to acoustic input. The chain of signal processing events in the system was highlighted in Fig. 4.6. The present chapter deals explicitly with the shear layer and its interaction with a modulated perturbation, adopting a signal processing viewpoint. This perspective yields new insights, with results that are relevant to any modulated perturbation that causes vortex roll-up in a shear layer. Reference is made to the data from the attached jet experiment from chapter 3.

In Wiltse & Glezer's initial discovery of the AM technique [131], an experiment was conducted to determine the mechanism that causes the demodulation in the shear layer. The flow speed was reduced to 2.75 ms^{-1} (although it was only 4 ms^{-1} for the rest of the experiments), and Schlieren photographs were provided showing the flow at several phases in the modulating period. Wiltse & Glezer highlight line vortices produced in the shear layer at the carrier tone frequency ($f_c = 510$ Hz), which roll up into larger vortices at the modulating frequency ($f_m = 12$ Hz) further downstream.

This mechanism suggests there is a requirement for many of the line vortices to merge into a single vortex at the modulating frequency. In Wiltse & Glezer's case, $510/12 = 42.5$ vortices are required on average to be present in the shear layer simultaneously to produce

a single vortex at the modulating frequency. The number of vortices present can be estimated by the ratio of the average distance between vortices and the space in the shear layer in which the vortices exist before breakdown to isotropic turbulence. Results from PIV experiments conducted by Mair [70] indicate a vortex convection speed of around 65% of the centreline jet velocity. Similarly, Kuo et al. [61] reported a vortex convection speed of 67% of the jet centreline velocity. Cattafesta et al. [14] used a cantilevered piezoelectric actuator, rather like that used by Wiltse & Glezer [131], to control the acoustic tones induced by flow over a cavity. In this study, the convection speed of the vortices produced by the actuator was found to be around 45% of the free stream flow.

If the convection speed is assumed to be in the range $0.4U \leq v_{\mathrm{SL}} \leq 0.65U$, where U is the mean velocity, the range of values for the distance between vortices in Wiltse & Glezer [131] is given by

$$L_v = v_{\mathrm{SL}}/f_c \approx 2.2 \text{ to } 3.5 \text{ mm} = 0.050 \text{ to } 0.082\, D_h, \tag{6.1}$$

where $D_h = 43.0$ mm is the hydraulic diameter of the square jet. A first approximation for the length along which vortices exist is the length of the potential core, although they do exist beyond this region for some distance before breaking down into isotropic turbulence. It was discussed in section 2.6.3.2 that Mair et al. [71] reported potential core lengths ranging from $3D$ when excited at the jet preferred mode to $7D$ when unexcited. To get a sense of the order of the average number of vortices present in the shear layer, the length of the region where vortices at f_c exist is taken to be $L_{\mathrm{ve}} \approx 5D_h$. This gives

$$N_v = \frac{L_{\mathrm{ve}}}{L_v} \approx 100 \text{ to } 61, \tag{6.2}$$

so that on average there would be between $100/42.5 = 2.4$ to $61/42.5 = 1.4$ vortices present at the modulating frequency, $f_m = 12$ Hz. Wiltse & Glezer's [131] proposed merging mechanism therefore seems plausible. However, the flow speed in question was very low, and it may be the case that the mechanism is different when there are too few vortices produced

at f_c to roll up into vortices at f_m.

Vukasinovic et al. [126] investigated the mechanism within the shear layer that causes the demodulation. They studied the flow over a backward-facing step controlled by a wall-normal synthetic jet actuator mounted upstream of the step. The synthetic jet was driven with a carrier frequency of $f_c = 2000$ Hz, with modulating frequencies in the range $f_m = 50$ Hz to $f_m = 300$ Hz. The modulating signal was a square wave rather than a sinusoid, so that the synthetic jet was switched on and off completely during excitation. Phase-locked PIV vorticity snapshots at several times through a modulation period at $f_m = 100$ Hz show the vortex train being produced during the excitation portion of the period only at the carrier tone frequency, $f_c = 2000$ Hz. The authors argue that the snapshots indicate that the vortices produced during the 'on' portion of the modulating period coalesce into a larger vortex produced at the modulating frequency. The mean velocity profiles provided at several downstream distances demonstrate that the excitation varies the degree of separation over the step at the modulating frequency, resulting from the variation in entrainment. This varying separation is equivalent to the jet deflection in the case of an attached jet. The important result from this paper for the present work is that the entrainment variation at f_m is caused by the modulation of the shear layer vortices which are originally produced at f_c, rather than the shear layer responding at f_m.

The difference between the study by Vukasinovic et al. [126] and the present work is that it is unclear if the synthetic jet actuator is equivalent to the acoustic excitation. The velocity disturbance resulting from the periodic blowing and sucking of air produces vortices a short distance upstream of the step in the case of the synthetic jet, while the acoustic excitation provides a dominating perturbation that the shear layer amplifies by rolling up into vortices. In the present work, the paradigm of shear layer modulation is that the size of a given vortex in the vortex train is determined by the mean amplitude of the modulating signal during the carrier period in which the vortex is produced. It is not suggested that the vortices merge because calculations of the number of vortices present in the shear layer simultaneously suggest this cannot be the case. Even if the vortices do merge, the

arguments made in this chapter are unaffected. The lock-on effect first discovered by Crow & Champagne [24], i.e. that the vortices are produced at the acoustic excitation frequency, which was observed in Wiltse & Glezer's Schlieren photographs [131], is also assumed here. The importance of these articles will be explained.

Two novel features of this chapter are the input over-modulation technique and a Nyquist sampling theorem analogy for the shear layer response. The over-modulation technique is explained in section 6.3, after the basic operations are introduced in section 6.2. Calculations to determine the shear layer response to the technique are detailed in section 6.4, and applications for its use are suggested in section 6.5. An analogy with the Nyquist sampling theorem is made in section 6.6. Finally, the conclusions of the chapter are drawn in section 6.7.

6.2 Basic operations

Up to this point, the origin of the static deflection curves (SDCs) in Fig. 4.8 has not been specified. The possibilities are shown in the diagram in Fig. 4.6. It is hypothesised that the SDCs originate in one or both of the amplifier-loudspeaker and the cavity response nonlinearities, which are now combined into the amplifier-loudspeaker-cavity response (ALCR) nonlinearity. The justification for this assumption is that Fig 4.8 indicates that the SDCs generally agree with one another. If the variation was the result of some fluid dynamical effect, it is supposed that some features would vary more obviously with flow rate. For example, the system appears to be very sensitive to inputs at around 3500 Hz, which is independent of flow rate.

The ALCR was determined directly by switching off the flow and placing the Kulite pressure transducer probe in two positions: first on the jet centreline and level with the centre of the control port orifice, and second $\sim$2 mm into the control port orifice (on the excitation side). The amplifier was then driven with a range of tone frequencies. The results, shown in Fig. 6.1, confirm a peak in the response at $f_c = 3500$ Hz, whose frequency was insensitive to the

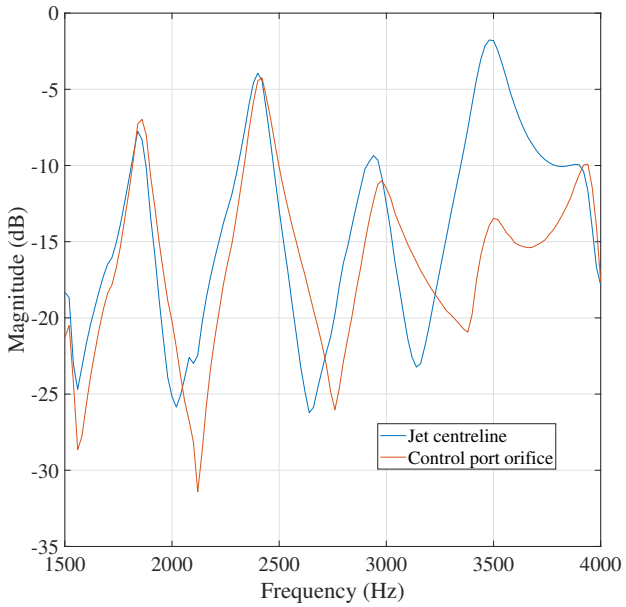

Figure 6.1: Cavity response measurements (flow off): jet centreline (blue), and control port orifice (red). The input amplitude was 10 mV.

small change in the probe position. The series of peaks and troughs are spaced around 550 Hz apart with the 3500 Hz peak superimposed. Clearly, this is not observed in the SDCs in Fig. 4.8, and the relationship between the cavity responses in Fig. 6.1 and the SDCs are not understood. Mair et al. [70] did see a correspondence between jet response and measured SPL, but in that case the excitation frequencies were ultrasonic so that the jet and the SPL measurement position were in the far field, while the lower frequencies and larger scale in the present work puts the measurement position in the near field.

Travelling wave calculations indicate that the interference between the fundamental and reflected waves at the jet centreline would give a maximum around 3500 Hz if the distance between the loudspeakers was $\sim 38b$, which is 120% of its value. The 550 Hz-spaced pattern would correspond to a larger reflection distance, most likely the axial length of the device from the back wall to the exit. If this is the case, then when flow is switched on, this reflection may not occur due to the jet turning the upstream-travelling waves away from the device axis. More generally, the jet is likely to have an effect on the sound field produced by the loudspeaker because the shear layer absorbs some of the acoustic energy.

Regardless, the important non-dimensional frequencies such as the jet preferred mode ($\mathrm{St}_D = 0.3$) would display a linear dependence on flow rate. The lack of any such dependencies in Fig. 4.8 justifies the hypothesis that the SDCs result from the ALCR and not fluidic dynamical effects.

The consequence of this hypothesis is that the quasi-steady jet response, $\psi_{f_c}(f_m)$, which is the effect of the SDCs on the dynamic response, occurs in the chain of signal processing events *before* the shear layer response. The signal that arrives as the input to the shear layer, i.e. the output of the ALCR, is named $u_{\mathrm{SL}}(t)$. When the input signal, $g_{\mathrm{ex}}(t)$, is set to the standard AM signal without SDC inversion, i.e. that given by (4.11), $u_{\mathrm{SL}}(t)$ is given by

$$u_{\mathrm{SL}}(t) = \frac{A}{2} g_{\mathrm{resp}}(f_c - f_m) \cos\left(2\pi (f_c - f_m) t\right) - \frac{A}{2} g_{\mathrm{resp}}(f_c + f_m) \cos\left(2\pi (f_c + f_m) t\right) ... \\ ... + B\, g_{\mathrm{resp}}(f_c) \sin(2\pi f_c t) . \tag{6.3}$$

The next stage of the system is the shear layer response to $u_{\mathrm{SL}}(t)$. The output of the shear layer response is related to jet spreading - the input to the model, σ. The operation performed on the signal by the shear layer, again assuming that $g_{\mathrm{resp}}(f)$ occurs purely as part of the ALCR, is:

Shear layer operations
1. The signal is demodulated down to base frequencies
2. The signal phase is ignored

The demodulation property is well-known, but the phase insensitivity of shear layers has not been discussed in the literature. It is not possible to make the jet attach *more* strongly the wall by flipping the phase of the excitation tone by π, hence the phase is not important.

6.3 Physics of shear layer operations

In this section, the shear layer operations stated above are explored through use of input over-modulation, i.e. AM signals that are modulated over 100% so that the phase of the modulating signal flips periodically at f_m.

It is instructive to consider the physics of the events that take place when the shear layer is excited: the signal $u_{\mathrm{SL}}(t)$ is the perturbation signal in the shear layer which encourages vortex roll-up at the carrier frequency, f_c, and results in a vortex train at f_c for a larger proportion of the streamwise length of the shear layer than would occur naturally. This was explained in section 2.6.3.2, and the result is that jet spreading is increased [24]. The effect of the modulation is to vary the amplitude of the disturbances at f_m, so that the degree of additional spreading varies at the same frequency. This explains the demodulation operation performed by the shear layer.

The signal $u_{\mathrm{SL}}(t)$ is over-modulated when the amplitudes A & B and $\psi_{f_c}(f_m)$ (see (6.3)) are such that

$$A\left(g_{\mathrm{resp}}\left(f_c - f_m\right) + g_{\mathrm{resp}}\left(f_c + f_m\right)\right) \;=\; A\psi_{f_c}(f_m) \;>\; Bg_{\mathrm{resp}}\left(f_c\right). \tag{6.4}$$

Consider the limiting case when the inequality in (6.4) is an equality, and the modulation at the input to the shear layer is at 100%. This means that the shear layer disturbance amplitude at f_c varies between 0 and $2Bg_{\mathrm{resp}}(f_c)$. When the carrier offset is reduced so that the over-modulation condition in (6.4) is met, the modulating signal falls below 0, and the sign of the amplitude of the carrier tone in u_{SL} changes. The consequence of the phase change is that at a specific point in the shear layer where before there was a positive disturbance, it has now flipped to a negative disturbance for the portion of modulating signal that is negative. For the vortex train, this means that there are two adjacent vortices or gaps between vortices where the phase changes. This is shown in Fig. 6.2, where Fig. 6.2a shows the shear layer response to a constant carrier tone, and Fig. 6.2b - 6.2d show the response to AM

signals with varying degrees of modulation. The diagrams in Fig. 6.2c & 6.2d demonstrate the phase of the vortex train flipping in the period where the modulating signal is negative.

It should be noted that Fig. 6.2 is not intended to suggest that all vortices in the train necessarily exist simultaneously - as they travel along the shear layer they will eventually break down into isotropic turbulence [133]. The number of vortices that exist at any given time was estimated as in section 6.1. In the present work, for the mass flow rates used,

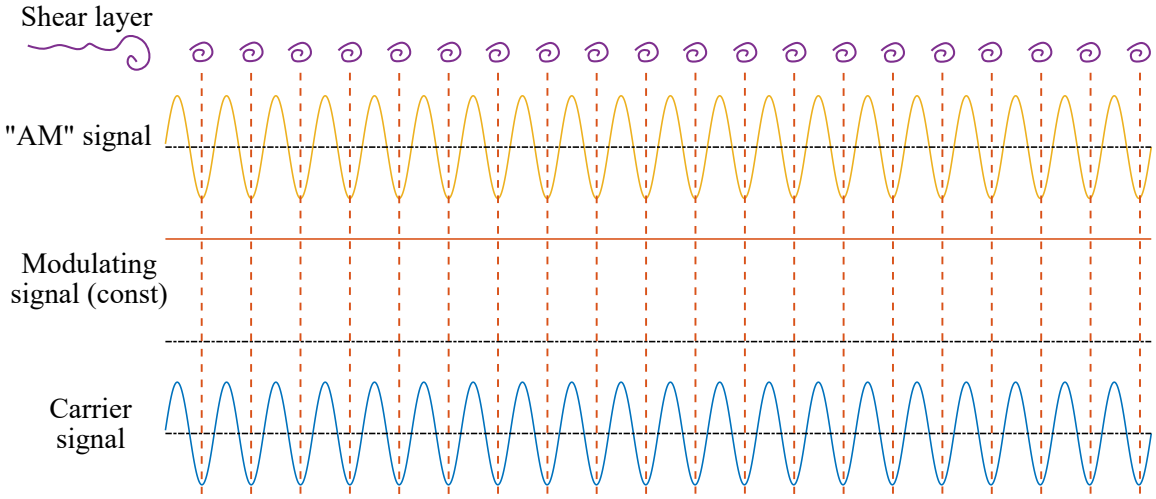

(a) Carrier tone with constant amplitude.

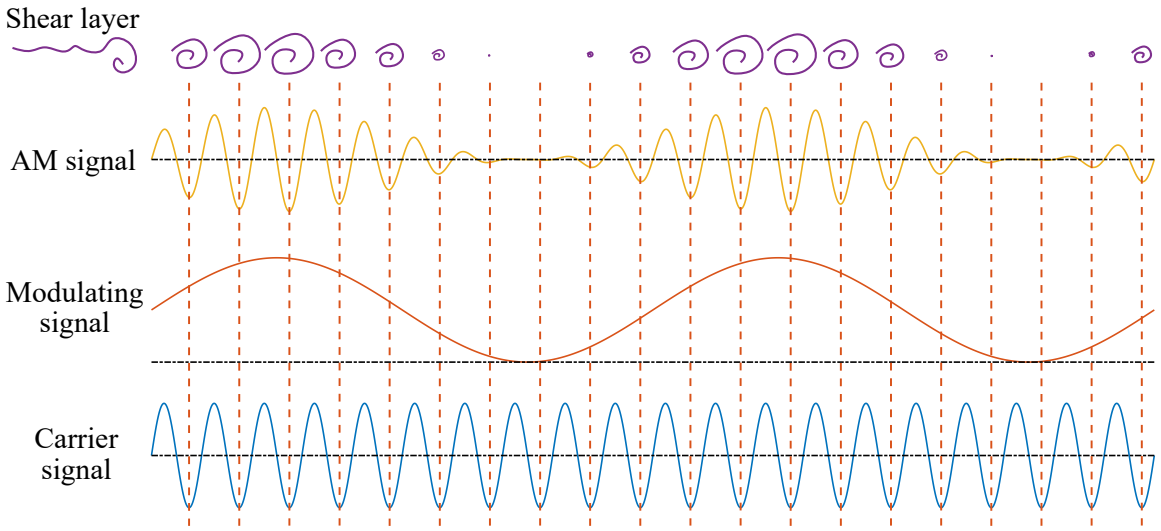

(b) Carrier tone with 100% amplitude modulation.

Figure 6.2: Shear layer response to constant carrier tone (constant modulation 'signal') (a) and 100% amplitude modulation signal (b); $u_{\mathrm{SL}}(t)$: constant, 100% AM.

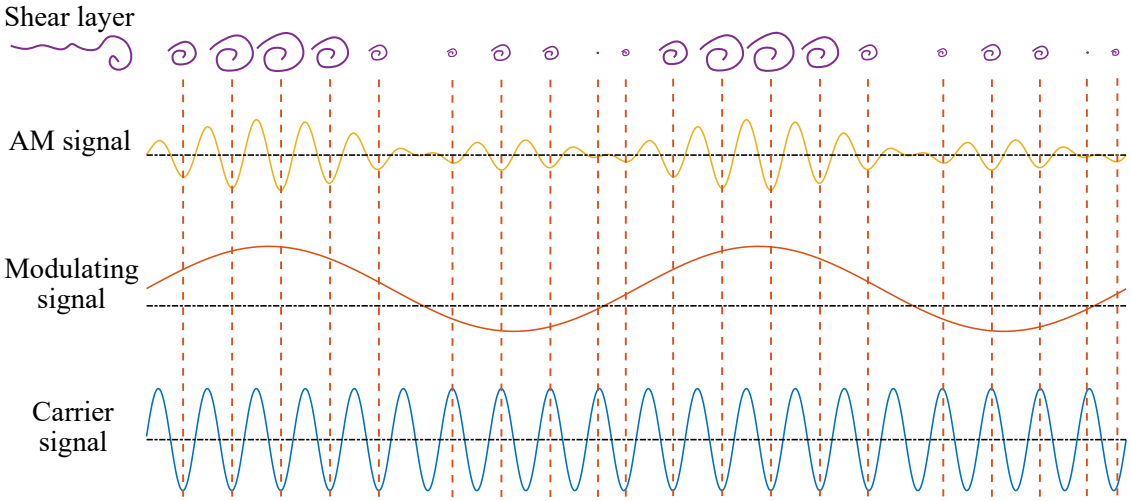

(c) Carrier tone with 160 % amplitude modulation.

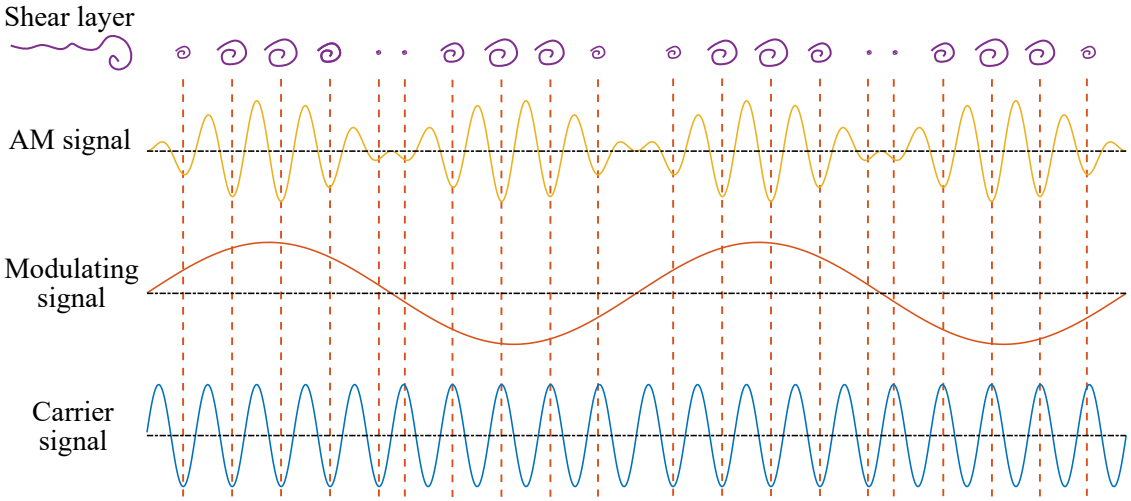

(d) Carrier tone with 200% amplitude modulation.

Figure 6.2: Shear layer response to 160% (c) and 200% (d) amplitude modulation signals; $u_{\mathrm{SL}}(t)$: 160% AM, 200% AM

the Görtler profile indicates that the mean jet velocity ranges from around 43 to 91 ms^{-1} at the nozzle orifice. The range for shear layer velocity (vortex propagation speed) used is the same as that in section 6.1, i.e. $0.4U \leq v_{\mathrm{SL}} \leq 0.65U$, which would suggest shear layer velocities in the range 17 to 59 ms^{-1}. At a carrier tone of $f_c = 2500$ Hz, the average distance between vortices is given by

$$L_v = v_{\mathrm{SL}}/f_c \approx 6.9 \text{ to } 19 \text{ mm} = 1.4 \text{ to } 4.7b. \tag{6.5}$$

Similar to section 6.1, the length of the region where vortices at f_c exist is taken to be $L_{\text{ve}} \approx 5b$, so that the average number of vortices is given by

$$N_v = \frac{L_{\text{ve}}}{L_v} \approx 1.1 \text{ to } 3.7. \tag{6.6}$$

Since the modulating frequency can be arbitrarily low, it seems unlikely that the mechanism for demodulation is the merging of vortices if there so few vortices present simultaneously. In fact, even in the low speed experiment in Wiltse & Glezer [131], if the modulation frequency was decreased, for example to $f_m = 1$ Hz, then there would be too few vortices present in the shear layer simultaneously to merge into vortices at this value of f_m. This justifies the approach taken in this chapter where vortex size is determined by the average modulation signal value during the carrier tone period corresponding to a given vortex. However, as stated in section 6.1, the arguments made are unaffected when merging is the mechanism.

Since f_c is generally at least an order of magnitude larger than f_m, there are many vortices produced per modulating period. For example, if $f_c = 1000$ Hz and $f_m = 100$ Hz, then there are 10 vortices per modulating period. If the degree of over-modulation is such that, for example, 40% of the period of the modulating signal is negative, then on average the phase of the vortex train with be flipped for 4 vortices. This is the example shown in Fig. 6.2c, while Fig. 6.2d shows the limiting 200% modulation case where the phase flips for half of the modulation tone period. The phase change in the vortex train demonstrates that negative modulation signals still result in increased jet spreading, which is the output of the shear layer response and depends on the size of the vortices in the train. This is the physical explanation behind the shear layer's insensitivity to phase.

It is interesting to consider the effect of the phase change on the vortex train when f_m is larger (although still smaller than f_c). In this case, the repeated vortex (or gap between vortices) that occurs may have an effect on the jet. If the phase of the carrier tone relative to the modulating signal is as shown in Fig. 6.2d, when the modulating signal goes negative there is a repeated vortex and hence a longer length of low pressure than usual. Similarly,

when the modulating signal phase flips again, there is a repeated absence of a vortex, and therefore a longer length of high pressure than usual. With the assumption of $f_c \gg f_m$, these effects can be assumed to occur much faster than the jet response to the phase change at $2f_m$ and can be safely ignored.

With the shear layer operations of demodulation and phase-insensitivity explained, it is observed that they can be combined into a single operation:

Shear layer operations
1. The modulus is applied

The modulus operation performs the demodulation and provides the insensitivity to phase observed. This single operation is analagous to a simple envelope detector that would demodulate an AM signal in a radio receiver, implemented by a full-wave rectifier. This insight is novel: previously, researchers have not focused on the phase-insensitivity of shear layers. To understand the output of the modulation operation, it is instructive to write the input in (6.3) in terms of the product of the carrier and modulating signals, given by

$$u_{\mathrm{SL}}(t) \;=\; \sin\left(2\pi f_c t\right)\left[A\psi_{f_c}(f_m)\sin\left(2\pi f_m t\right) \;+\; B\,g_{\mathrm{resp}}\left(f_c\right)\right]. \tag{6.7}$$

The output of the shear layer, denoted y_{SL}, which is assumed to be some analogue of jet spreading, is given by

$$y_{\mathrm{SL}}(t) \;=\; \left|\sin\left(2\pi f_c t\right)\left[A\psi_{f_c}(f_m)\sin\left(2\pi f_m t\right) \;+\; B\,g_{\mathrm{resp}}\left(f_c\right)\right]\right|. \tag{6.8}$$

Note that this does not include the jet dynamic response, $G(2\pi f_m)$, because that comes later in the system. For cases where the signal is not over-modulated, i.e. $A\psi_{f_c}(f_m) \leq B\,g_{\mathrm{resp}}\left(f_c\right)$, the modulating signal is always positive and the modulus only affects the carrier tone. This results in the power shifting from f_c to DC and harmonics of f_c, and is the standard operation of an envelope detector, implemented by a full-wave rectifier. The output can be

re-written as

$$y_{\mathrm{SL}}(t) \;=\; \left|\sin\left(2\pi f_c t\right)\right| \left|A\psi_{f_c}(f_m)\sin\left(2\pi f_m t\right) \;+\; B\, g_{\mathrm{resp}}\left(f_c\right)\right| \tag{6.9}$$

$$y_{\mathrm{SL}}(t) \;=\; \left[C + D\sin\left(2\pi 2 f_c t\right) + ...\right] \left|A\psi_{f_c}(f_m)\sin\left(2\pi f_m t\right) \;+\; B\, g_{\mathrm{resp}}\left(f_c\right)\right|. \tag{6.10}$$

The result is that the modulus of the modulating signal in (6.9) is mixed with DC and harmonics of f_c. Since it is assumed that there will be no response at the harmonics of f_c, the effect of the modulus on the base band frequencies is simply to scale all terms by a constant, which can be calculated as the constant in the Fourier series to be $C = 0.64$. The constant is applied to all terms, and since it is the relative amplitudes of each term in the modulus of the modulating signal that is relevant, the constant is ignored (i.e. treat $C = 1$). Applying these assumptions results in the shear layer output given by

$$y_{\mathrm{SL}} \;=\; \left|A\psi_{f_c}(f_m)\sin\left(2\pi f_m t\right) \;+\; B g_{\mathrm{resp}}\left(f_c\right)\right|. \tag{6.11}$$

The effect of the modulus operation on (6.11) depends on the degree of modulation. When over-modulated, a fraction of the power at the fundamental, f_m, is shifted to DC and harmonics of f_m, as was the case with the carrier tone above. In the 200% modulation case, all power is removed from f_m, and the result is a signal that is 100% modulated.

It can now be revealed from the arguments set forth in this section that this transfer of power from the fundamental f_m to DC and harmonics of f_m occurs *at the shear layer* link in the chain of signal processing events rather than before. The implications of this are interesting. If side-band-only transmission is used, that is to say that $B = 0$, so that the signal at $g_{\mathrm{ex}}(t)$ is 200% modulated, the jet responds primarily at DC and $2f_m$. However, the relevant frequency for the ALCR is f_m, and it is the shear layer nonlinearity that transfers the power away from the fundamental frequency. This over-modulation technique has been confirmed experimentally: the jet responds at $2f_m$ when $B = 0$. The output spectra of an example at 300 slpm where $f_c = 2500$ Hz, $f_m = 5$ Hz, and $B = 0$ (200% AM) is shown in Fig. 6.3. Detail around around $2f_m$ is shown in Fig. 6.3b, while the direct measurement of

the input tones at $f_c \pm f_m$ is highlighted in Fig. 6.3c.

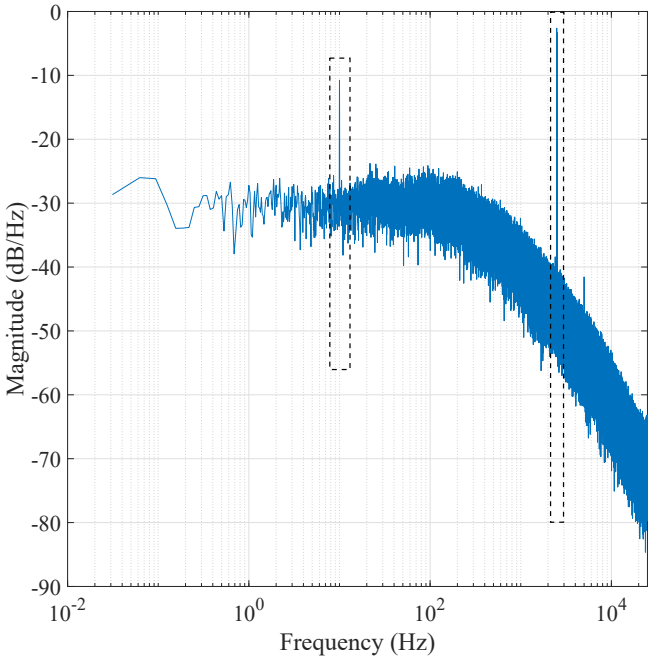

(a) Full output spectra

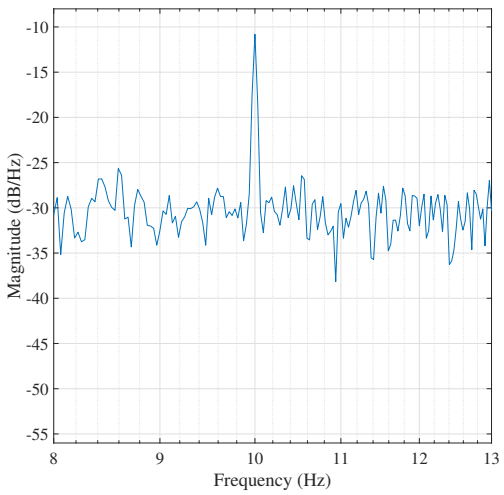

(b) Zoom on $2f_m = 10$ Hz

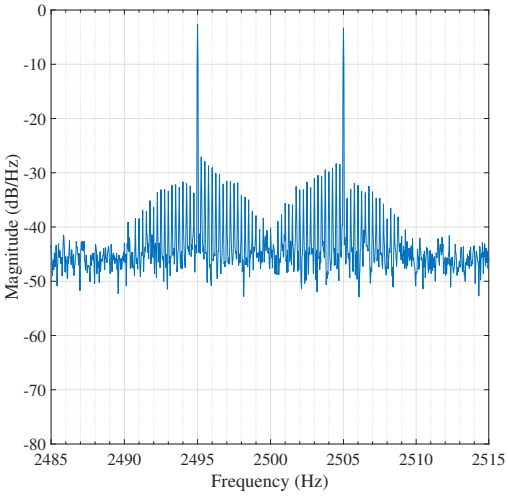

(c) Zoom on $f_c = 2500$ Hz

Figure 6.3: Power spectral density of output signal with over-modulated input: $f_c = 2500$ Hz, $f_m = 5$ Hz, and $B = 0$ (200% AM).

6.3.1 Jet preferred mode

It was established in section 2.6.3.2 that jet shear layers respond differently to different excitation frequencies. It was argued in section 6.2 that the jet sensitivity to excitation frequency (given by the SDCs) was purely a result of the amplifier-loudspeaker-cavity response rather than any fluid dynamical effects in the present work. Clearly, excitation of the jet preferred mode is a fluid dynamical effect, and it is interesting to consider its effect. With regular modulation, if the carrier tone is set to the jet preferred mode, i.e. the frequency corresponding to $\mathrm{St}_D = 0.3$ (or $\mathrm{St}_{D_h} = 0.45$ for a rectangular jet), then the expectation is that jet will be deflected to a relatively large degree. Assuming no ALCR effects so that the jet sensitivity is purely a function of fluid dynamical effects, the degree of modulation at the output might be expected to depend on the jet sensitivity to $f_c \pm f_m$. However, this is not the case because the shear layer responds and produces vortices at the time scale of the period of the carrier tone, and the size of a given vortex depends on the amplitude of the carrier averaged over a single period. This is rather like setting the time-scale of an FFT to be the period of the carrier tone rather than that of the modulating tone or larger. It is interesting to consider that in the case of 200% modulation, i.e. the technique proposed in section 6.2, the excitation signal does not actually contain the carrier tone frequency when considered over a time scale at least as large as the modulation tone period, but the shear layer vortices will be produced at f_c.

6.4 Quantifying the effects of input over-modulation

This section details the redistribution of power from the modulating signal into DC and the harmonics of the fundamental frequency, f_m. It has been shown that (6.11) is the shear layer output, which is something akin to jet spreading. In the over-modulation technique, $B = 0$ is used to achieve the maximum 200% over-modulation. The output signal is therefore

$$y_{\mathrm{SL}} = \left| A\psi_{f_c}(f_m) \sin\left(2\pi f_m t\right) \right|. \tag{6.12}$$

To determine the frequency content of this signal, the Fourier series coefficients can be found from the standard formulas. The odd sinusoid terms disappear because $\left|\sin\left(2\pi f_m t\right)\right|$ is an even signal, and the resulting Fourier series for (6.12) is given by

$$y_{\mathrm{SL}} \;=\; A\psi_{f_c}(f_m)\left(\frac{2}{\pi} \;-\; \frac{4}{\pi}\sum_{n=1}^{\infty}\frac{1}{4n^2-1}\cos\left(2\pi(2nf_m)t\right)\right) \tag{6.13}$$

$$y_{\mathrm{SL}} \;=\; A\psi_{f_c}(f_m)\left(\frac{2}{\pi} \;-\; \frac{4}{3\pi}\cos\left(2\pi(2f_m)t\right) \;-\; \frac{4}{15\pi}\cos\left(2\pi(4f_m)t\right) \;-\; ...\right) \tag{6.14}$$

The distribution of power between the terms is given in Table 6.1. This set of powers

Term	DC	$2f_m$	$4f_m + 6f_m + ...$
Power (%)	81.1	18.0	0.9

Table 6.1: Power distribution of terms in Fourier series of $\left|\sin\left(2\pi f_m t)\right)\right|$

appears to indicate a signal that has less than 100% modulation because the DC power term dominates. Inspection of (6.12) shows that this is not the case, and that the signal varies between $y_{\mathrm{SL}} = 0$ and $y_{\mathrm{SL}} = A\psi_{f_c}(f_m)$. If the harmonics above $2f_m$ are ignored and $A\psi_{f_c}(f_m) = 1$, the resulting signal is given by

$$y_{\mathrm{SL}} \;=\; 0.637 \;-\; 0.424\cos\left(2\pi 2 f_m t\right), \tag{6.15}$$

which is a 67% modulated signal. The higher harmonics account for the remaining 33% of the modulation, despite their powers only summing to 0.9% of the total.

The spectra of the various signals in the diagrams in Fig 6.2 are shown for each modulation case in Fig 6.4. These signals are:

- Carrier signal (blue): $y_c(t) = \sin\left(2\pi f_c t\right)$
- Modulating signal (red): $y_m(t) = A\sin\left(2\pi f_m t\right) + B$
- AM signal, shear layer input (yellow): $u_{\mathrm{SL}}(t) = \sin\left(2\pi f_c t\right)\left(A\sin\left(2\pi f_m t\right) + B\right)$
- Shear layer output (purple): $y_{\mathrm{SL}} = \left|A\sin\left(2\pi f_m t\right) + B\right|$

where $\psi_{f_c}(f_m) = 1$. The values for A and B for the four modulation percentages shown in each plot in Fig. 6.4 are given in Table 6.2. Note that the colour of each time-domain plot

Fig.	6.4a	6.4b	6.4c	6.4d
Mod. %	0	100	160	200
A	0	1	1	1
B	1	1	0.4	0

Table 6.2: Modulation cases and corresponding values of A and B

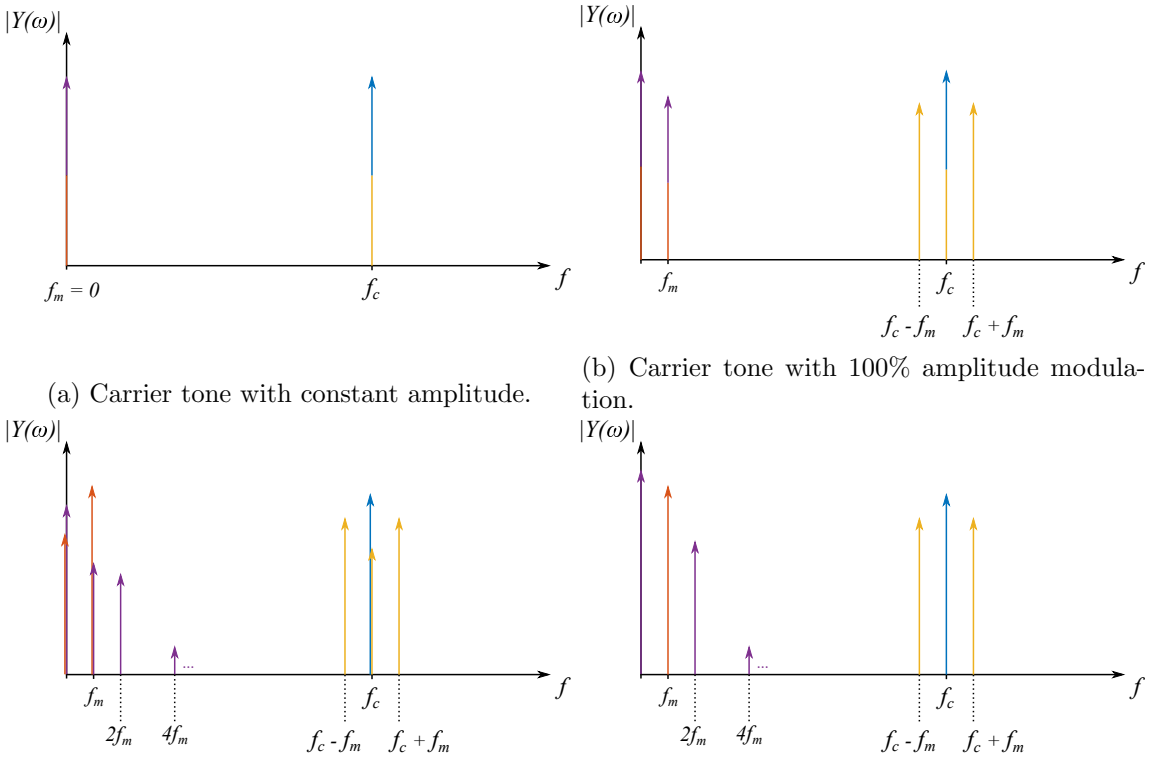

(a) Carrier tone with constant amplitude.

(b) Carrier tone with 100% amplitude modulation.

(c) Carrier tone with 160 % amplitude modulation.

(d) Carrier tone with 200% amplitude modulation.

Figure 6.4: Spectra at several AM percentages: Carrier (blue); Modulation signal (red); AM input to shear layer, $u_{\mathrm{SL}}(t)$ (yellow); shear layer response, $y_{\mathrm{SL}}(t)$ (purple). Note that signals around $2f_c$ have been neglected.

in Fig. 6.2 matches its frequency-domain representation in Fig. 6.4. The 200% modulation case in Fig. 6.4d demonstrates the distribution of power in Table 6.1. For reference, if a 100% AM case results in power P_{f_m} dB at f_m, then setting $B = 0$ will produce a response at $2f_m$ given by

$$P_{2f_m} = P_{f_m} - 7.44\,\mathrm{dB}. \tag{6.16}$$

This was tested at 300 slpm by conducting dynamic response experiments at 100% AM at $f_m = 2, 5, 10, 20$, and 40 Hz, then repeating them at 200% AM with $f_m = 1, 2.5, 5, 10$, and 20 Hz. In both cases, $f_c = 2500$ Hz because the SDCs are flat in this region, so that choosing low values for f_m keeps $f_c \pm f_m$ in the flat region and avoids exciting the bulk jet dynamics. An example comparison is shown in Fig. 6.5, and all of the comparison data are summarised in Table 6.3. The final row shows the average amplitude ratio to give a power

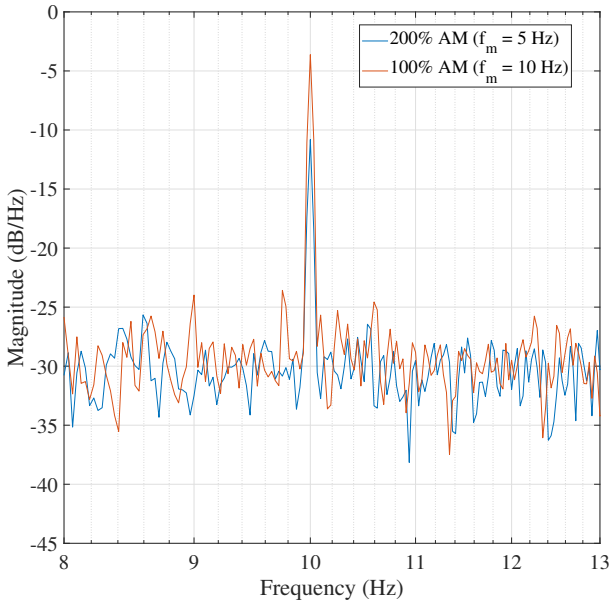

Figure 6.5: Output spectra at 300 slpm: 100% AM, $f_m = 10$ Hz (red), and 200% AM, $f_m = 5$ Hz (blue).

Response frequency (Hz)	**Magnitude, 100% AM (dB)**	**Magnitude, 200% AM (dB)**	**Magnitude ratio (dB)**
2	-5.16	-11.58	6.42
5	-4.10	-11.63	7.53
10	-3.62	-10.81	7.19
20	-2.15	-10.04	7.89
40	-1.38	-9.68	8.30
Avg. ratio (dB)			**7.49**

Table 6.3: Magnitude response comparison: 100% and 200% modulation at several values of f_m.

ratio of 7.49 dB, cf. the calculated value of 7.44 dB in (6.16).

Note that this 7.44 dB ratio is not strictly a 'fair' comparison because the input power

is not the same in both cases, since the 200% AM input differs only by setting $B = 0$. If the amplitude of the side bands at $f_c \pm f_m$ is increased to match the total input power of the 100% modulation case, then the resulting power ratio is

$$P_{2f_m} = P_{f_m} - 2.67\,\text{dB}, \tag{6.17}$$

an amplitude ratio of 1.4. While the focus has been on the response at $2f_m$, the over-modulation input theoretically results in a 100% modulated signal at the shear layer output when the harmonics of $2f_m$ are included. However, the shear layer response will likely roll-off at some frequency and the bulk jet dynamics certainly will.

6.5 Applications for input over-modulation

The input over-modulated technique has several possible applications, which are discussed here.

High Q-factor acoustic cavity In an acoustically-controlled device, it is desirable to design the cavity to amplify a relatively narrow range of acoustic tone frequencies corresponding to the resonance of the acoustic source used so that the sound pressure level achieved is maximised. However, if the device in question is to be used dynamically or in any operating mode other than the steady state, the acoustic transient will be limited by the bandwidth of the source-cavity frequency response resonance. For example, in the case of the ultrasonically-controlled fluidic diverters studied by Mair et al. [70], the acoustic cavity was designed to have a bandwidth of 2 kHz around a resonant frequency of 25 kHz, giving a $Q = 12.5$. In this case, the tolerances associated with the rapid prototyping manufacturing technique used limited the value of Q. However, it would have been undesirable to make Q significantly larger, since the effective bandwidth of the source-cavity system is 1 kHz at $Q = 12.5$. This is because it is the bandwidth on either side of the source resonance that limits the response time. This bandwidth has an associated time constant of 1 ms, and the device switching times demonstrated were around 5 ms at a pressure ratio of 1.07 ($M_n = 0.3$). The acoustic cavity response time therefore already makes up 20% of

the overall switching time. Further to this, the jet in the device was fully switched rather than partially deflected as in the present work. Therefore, when operated using partial deflections instead of full-switching, the jet response time in Mair's device [70] is less than 5 ms because the jet response time only makes up a fraction of the total switching time, the latter of which also includes detachment and reattachment times [67, 31]. Therefore, the value $Q = 12.5$ may already limit the jet response time in Mair's device, in which case the amplitude-gain product would be diminished.

The over-modulation technique could be applied to Mair's device when operated in the continuous-modulation mode described in the present work. The high-Q shape of the cavity response precludes f_m from exceeding 1000 Hz, but if the carrier offset is removed to give 200% modulation, the shear layer responds at $2f_m$, so that it is possible to drive output oscillations up to 2000 Hz while enjoying the high-gain amplitude response of the cavity up to 1000 Hz.

Resonant actuator In a similar vein to the acoustic cavity example above, any actuator with a strong response around a resonant frequency that decays quickly as the frequency moves away from the resonance could benefit from this technique. For example, the cantilevered piezoelectric actuators used by Wiltse & Glezer [131] and Cattafesta et al. [14] could increase their effective bandwidth with over-modulation.

Dynamic response identification The static deflection curves have been hypothesised to result from the ALCR. The SDCs in Fig. 4.8 are largely flat between 2000 and 3000 Hz. It would be beneficial to keep $f_c \pm f_m$ in this 'well-behaved' region because experimental uncertainty is likely to be greater outside of this region. The 'well-behaved' region can effectively be extended by use of the over-modulation technique: $f_c \pm f_m$ can remain in the 2 - 3 kHz band, while the jet response can be evaluated up to $2f_m = 1000$ Hz. The quasi-steady jet deflection curves in Fig. 4.9 show the increasing effects of the SDCs as f_m increases.

In this case, the effects of the SDCs on the dynamic responses were small. However, this is in part because the loudspeaker selected for the experiments has a relatively flat frequency response. In real applications, the actuators are not likely to have such flat responses. For example, the piezoelectric buzzer used in chapter 5, or the cantilevered piezoelectric actuators used by Wiltse & Glezer [131] and Cattafesta et al. [14]. In those cases, if the dynamic response needs to be determined for controller design purposes, the over-modulation technique may be used to extend any flat regions of actuator response.

As a demonstration, the 300 slpm dynamic response was measured up to 500 Hz using the procedure described in section 4.7: once for the 100% modulation case with $20 \leq f_m \leq 500$ Hz, and twice with $10 \leq f_m \leq 250$ Hz for the 200% modulation case. The input amplitudes were $A = B = 20$ mV for the 100% AM case, and $A = 20$ mV & $A = 20\sqrt{3} = 34.64$ mV, $B = 0$ for each of the over-modulation cases. The first over-modulation case was conducted to demonstrate the predicted -7.44 dB drop relative to the 100% AM case. However, as expected, the uncertainty in the resulting curves is relatively large because the measured response has a lower signal-to-noise ratio than the 100% AM case. Therefore, the second over-modulation case was performed with the total input power equal to the 100% AM case to demonstrate that the technique can produce data with comparable uncertainty, but still using only half of the required input bandwidth. The resulting responses are shown in Fig. 6.6, along with the 100% AM magnitude response shifted by both -7.44 dB (cf. first over-mod. case) and -2.67 dB (cf. second over-mod. case), and its phase response shifted by -90°. Note that these curves have not been corrected for the quasi-steady jet deflection curve, although its effects are small at this flow rate at these frequencies. The magnitude-shifted responses are in good agreement. The magnitude-shift of -2.67 dB is expected for the second over-modulation case with equal input power to the 100% AM case; see (6.17). The phase of the over-modulated data was found by taking the difference between the output phase at $2f_m$ and the input phase at f_m. The observed phase shift is expected because the Fourier series calculations in section 6.4 indicated that if the modulating tone is a sine wave at f_m, the output is a negative cosine at $2f_m$, a phase shift of -90°; see (6.15).

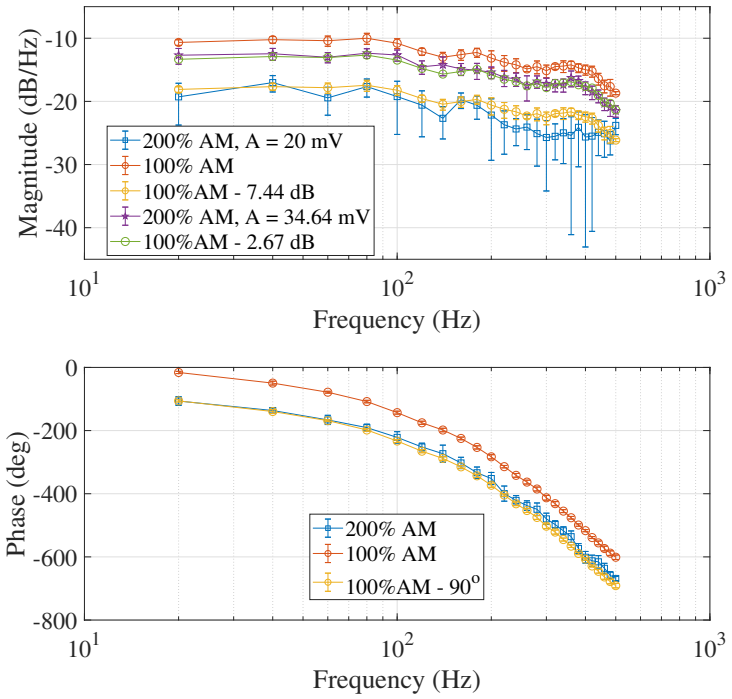

Figure 6.6: Dynamic response at 300 slpm: 200% AM with $A = 20$ mV (blue, squares), 100% AM (red, circles), 100% AM shifted by -7.44 dB and -90° (yellow, stars), 200% AM with $A = 20\sqrt{3} = 34.64$ mV for input power equality (purple, stars, magnitude only), and 100% AM shifted by -2.67 dB (green, circles, magnitude only). No quasi-steady deflection curve correction.

6.6 Nyquist sampling theorem analogy

Following the preceding discussion, the shear layer can be thought of as sampling the carrier tone amplitude, i.e. the modulating signal, time-averaged over the carrier tone period. In the present work, it is assumed that vortices are produced during the negative half period of the carrier tone. This is rather arbitrary and is purely for ease of explanation - the arguments apply if the vortices are produced during any fraction of the carrier tone period. This was the assumption for the calculation of the size of the vortices in the vortex trains in Fig. 6.2. With this assumption, the vortex amplitude is the value of the modulating signal time-averaged over the negative half-period of the carrier signal. Consider, for example, the 100% AM case for the shear layer input $u_{\mathrm{SL}}(t)$, as in Fig. 6.2b. As the modulation frequency is increased, the number of carrier tone periods, or 'samples', per period of the modulation tone decreases. When $f_m = f_c/2$, one vortex will have an amplitude equal to the half-period average of the modulation signal, and the next vortex's amplitude will

average the other half-period of the modulation signal. As such, there will be only two different sizes of vortex produced in the shear layer. If f_m is increased beyond $f_c/2$, the shear layer response now decreases below f_m. The cases of the Nyquist limit, $f_m = f_c/2$, and $f_m = 0.7f_c$, are shown in Fig. 6.7. In the case where $f_m = 0.7f_c$ in Fig. 6.7b, the shear

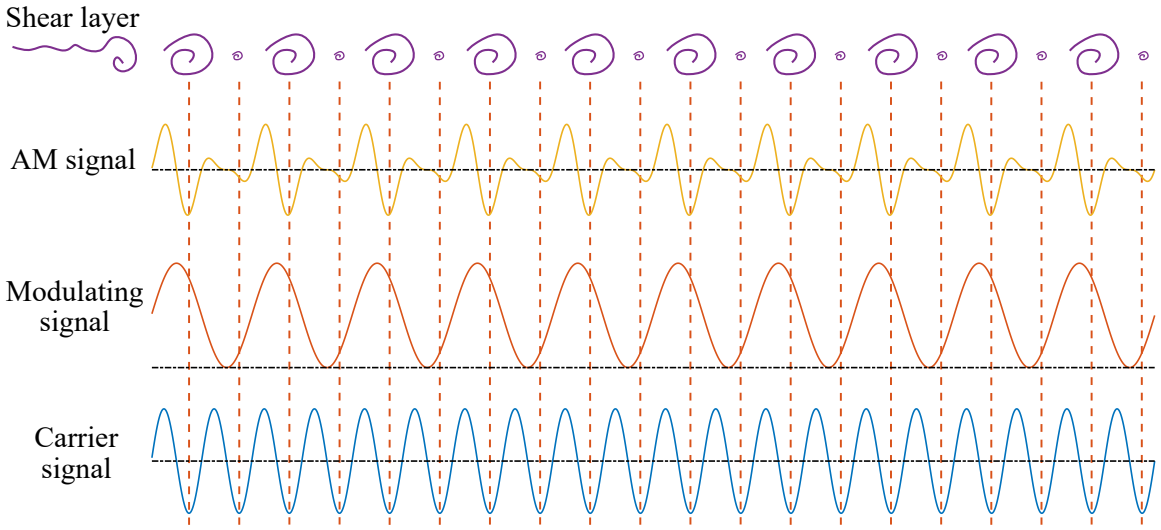

(a) Nyquist limit: $f_m = f_c/2$

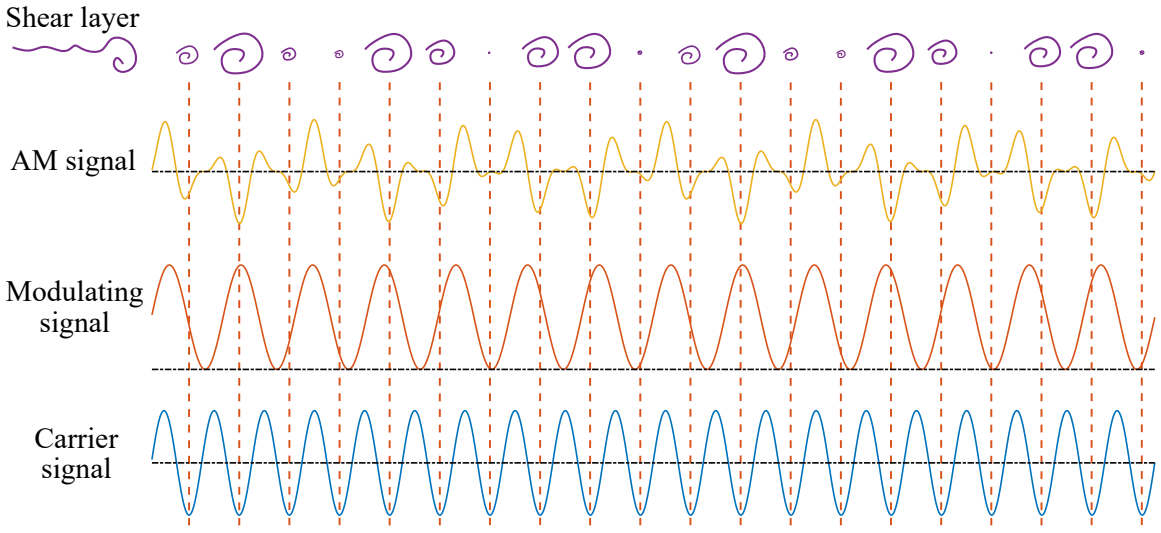

(b) Beyond Nyquist limit: $f_m = 0.7f_c$

Figure 6.7: Shear layer response to 100% AM tones at Nyquist limit and beyond

layer response frequency is clearly lower than the Nyquist limit case in 6.7a. The Nyquist theorem analogue indicates that the shear layer response frequency reduces for $f_m > f_c/2$, because if a sampled signal has a bandwidth above the Nyquist frequency, it is folded down

into the DC to $f_c/2$ band. The maximum frequency of jet spreading response is therefore $f_c/2$.

In consideration of this, the shear layer operations should be updated to include the sampling operation. The order of the operations can be determined by considering a 200% AM input. In this case, the Nyquist theorem still applies to the primary response at $2f_m$ (and all higher harmonics): the shear layer output frequency cannot exceed $f_c/2$. However, if the modulus operation comes after the sampling, then the sampling operation is applied to the input tones at $f_c \pm f_m$. Assuming $f_m < f_c/2$, both lower and upper side bands exceed the Nyquist limit, $f_c/2$. The sampling folds the input tones down to f_m (at base band), so the aliasing effectively demodulates the input signal. However, the modulus operation would then convert the tone at f_m to DC and $2f_m$, $4f_m$... etc. Any of these harmonics above $f_c/2$ would violate the Nyquist theorem, so the modulus operation must come first. The resulting shear layer operations are given by:

Shear layer operations: Nyquist theorem
1. The modulus is applied
2. The signal is sampled at f_c

Without the inclusion of the sampling operation, the aliasing behaviour observed for $f_m > f_c/2$ would be neglected.

In the case of flows where the demodulation mechanism is the merging of vortices, the arguments made in this section still apply. In the limiting case of $f_m = f_c/2$, neighbouring vortices will merge to produce vortices at $f_c/2$. However, if f_m is increased beyond this value, the same arguments apply: it is not possible to produce merged vortices at frequencies greater than $f_c/2$.

An experiment was conducted where the Nyquist condition introduced above was violated to test its validity. A jet dynamic response identification was performed with $f_c = 450$ Hz at 180 slpm using 100% input modulation. At this condition, repeating the calculations in section 6.1 & 6.3 gives the average number of vortices present in the shear layer simulta-

neously to be in the range $0.40 \leq N_v \leq 0.64$, again assuming they exist for a length of $5b$. This indicates that merging events are not possible because there is only a maximum of one vortex present at any given time. The modulating frequency was set to vary in separate experiments from $f_m = 20$ Hz up to $f_m = 380$ Hz in 20 Hz steps. The resulting dynamic response is shown in Fig 6.8. The static deflection curve in this region of frequencies at 180

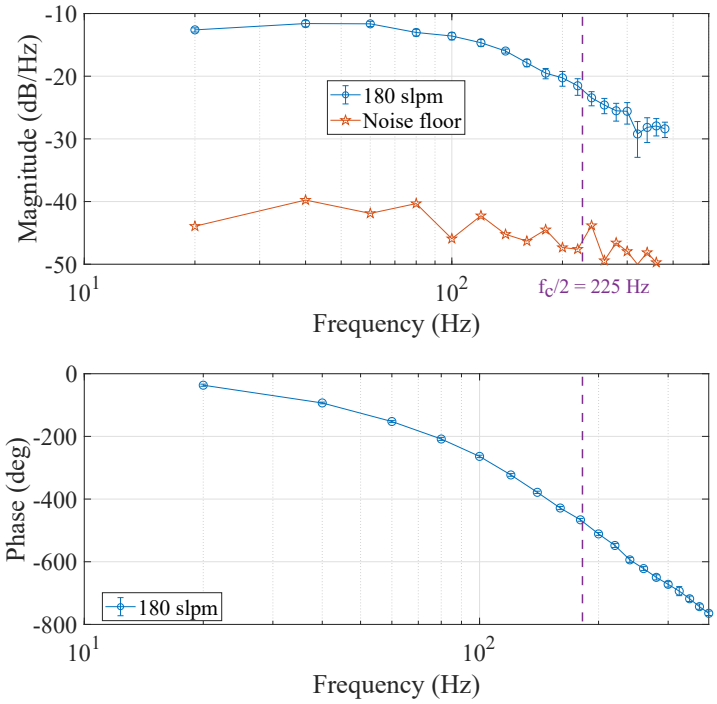

Figure 6.8: Dynamic response at 180 slpm, $f_c = 450$ Hz (blue, circles), and noise floor (red, stars).

slpm in shown in Fig. 6.9. When f_m exceeds $f_c/2$, the tones produced at $f_c - f_m$ are coincident with the expected frequency of the jet response. However, Fig. 6.9 shows that the response appears to continue at f_m for $f_m > f_c/2 = 225$ Hz. This is an unexpected result because it violates the Nyquist analogy, as well as the paradigm of shear layer modulation presented in this chapter. The possible reasons are listed as follows:

- *A tone at f_m is produced by the loudspeaker because of its nonlinearity, which is picked up directly by the pressure transducer and misidentified as the jet response.*

  In chapter 4, the direct pick-up of demodulated input tones was demonstrated to produce a local maximum at 650 Hz in Fig. 4.12. However, a direct magnitude

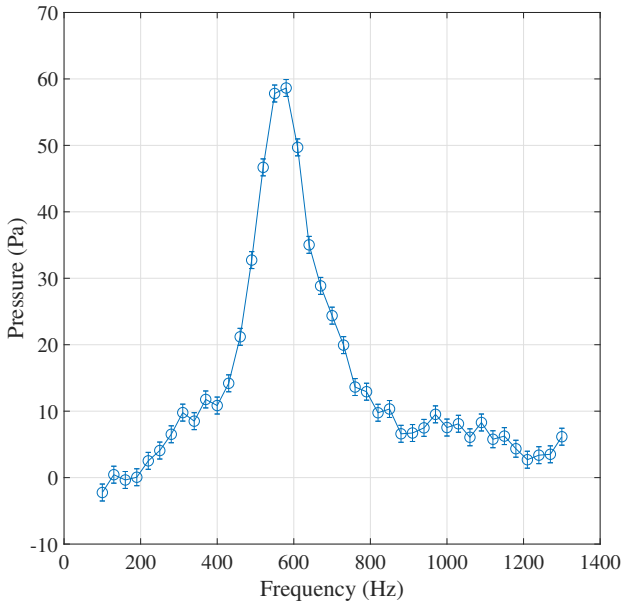

Figure 6.9: Static deflection curve for lower frequencies at 180 slpm

comparison with the no-flow response is not sufficient to rule it out. This is illustrated by the local maximum in the dynamic responses at the higher flow rates in Fig. 4.10. If the no-flow magnitude response was plotted on the same axes as the responses for flow rates ≥ 280 slpm, it would be ~ 10 dB below the observed local maximum at 650 Hz. This shows that the flow has an effect on the acoustic field, and the possibility of direct pick-up cannot eliminated in the experiment presented in the present chapter in Fig. 6.8.

- *The shear layer does not lock onto the carrier frequency, but some other frequency associated with the input.*

  The possibilities for the shear layer lock-on frequency are all of the frequencies between $f_c - f_m$ and $f_c + f_m$ in steps of $f_m/2$. For example, if the sum frequency at $f_c + f_m$ dominates the input to the shear layer, $u_{\mathrm{SL}}(t)$, then the shear layer could lock on to that frequency. In this case, there is still a response at f_m, given by the mean of the inputs at $(f_c + f_m) - f_m = f_c$, the input at the carrier tone, and $(f_c + f_m) + f_m = f_c + 2f_m$, where there is no input. The Nyquist frequency would be $(f_c + f_m)/2$, which is reached when the modulating frequency is set to $f_m = f_c$.

Alternatively, if the difference frequency, $f_c - f_m$, is weak at the input to the shear layer because of the small value of the SDC there (Fig 6.9), the jet could perceive the input tones at f_c and $f_c + f_m$ as the sum and difference frequencies resulting from the 200% AM input given by the product of $\sin(2\pi(f_c + f_m/2)t)\sin(2\pi(f_m/2)t)$, which would also produce a primary response at f_m. In this case, the jet would have had to lock onto $(f_c + f_m/2)$ from the beginning or a step change of 7.4 dB between two consecutive frequencies would be expected, as indicated by the calculations in section 6.4.

It is difficult to rule out these possibilities conclusively.

- *The shear layer does not lock on to any of the input frequencies and the mechanism is different to that described in this chapter.*

  This would indicate that the current thinking for how shear layers respond to modulated signals is incorrect. The vortex lock-on has been shown to occur when exciting the jet at the preferred mode [24] or when the perturbation amplitude is large enough as in Wiltse & Glezer [131]. The mechanism may be different in the present work.

The measurement techniques used in the present work are insufficient to be conclusive about the dynamic jet response in Fig. 6.8. It has not been possible to eliminate certain experiment artefacts as the causes for the violation of the proposed Nyquist analogy, hence further work is required to be definitive.

6.7 Conclusions

This chapter has explained the operations of a jet shear layer in response to a modulated perturbation from a signal processing perspective. The insights gained are important for applications where it is desired to modulate a jet continuously by periodic variation of the Coandă attachment strength by means of shear layer excitation. It was determined that the demodulation process performed by jets is an envelope detector, equivalent to a full-wave rectifier in electronic systems that demodulate AM signals. The over-modulation technique provides insight into the operations of the shear layer, as well as being a tool for extending actuator bandwidth, identifying jet dynamics, and more. The analogy with the

Nyquist sampling theorem defines a limit on the modulating signal frequency, which was violated in the experiment presented. Several possible reasons were given to the explain this, with one being a fundamental misunderstanding of how shear layers response to modulated perturbations. This represents an exciting research avenue that requires more advanced measurement techniques than those presented in this thesis.

Chapter 7

Summary & conclusions

This thesis has tackled the problems of analysing, modelling, and controlling a fluidic device. The starting point was the study of the fluid mechanics of an attached jet, the canonical element of fluidic devices. A novel means of setting the virtual origin of the Görtler profile led to a 'well-behaved' dividing streamline. Following this, a novel unsteady jet curvature equation was derived from first principles, which provided the central element of an analytical model and removed the need for the quasi-steady jet assumption. Several equations, both differential and algebraic, were derived and combined with the jet curvature equation to form the model. This consisted of a set of nonlinear differential equations with associated algebraic constraints. The acoustic input was modelled for the first time as a varying spread factor, and a discussion of the strengths and weaknesses of the model was provided.

Operating points were required to solve for the system equilibrium at each flow rate. To aid with determining these equilibria, an experiment was setup where a jet issued from a nozzle into an expanding interaction region and attached to one of the two setback sidewalls. This setup matched the geometry in the model (which resembled a typical fluidic device). A loudspeaker was used to deflect the jet and pressure measurements were made in order to determine the operating points required for solving the system equilibrium. The jet was then perturbed dynamically by making use of the property discovered by Wiltse & Glezer [131] that jets demodulate perturbations to their shear layers. The dependence of the system response to different carrier tone frequencies, named here as the static deflection

curve, had to be removed by inversion at the output. The nonlinear equations from the attached jet model were linearised at each operating point, producing a set of 4^{th} order state space systems. Frequency responses produced from each of the linearised systems were compared with the experimentally-determined dynamic jet responses and were found to agree reasonably well. The model parameters required to produce these outputs were discussed and justified, and a Monte Carlo analysis was performed to evaluate the model sensitivity to parameter perturbations.

Following the successful modelling of the attached jet, a fluidic amplifier was studied. A new mode of operation was established where, instead of switching the jet in the device fully, it remained attached to one side at all times but was deflected so that part of it exited via the unattached side outlet. This approach reduced the system gain but allowed the operating flow rate to increase significantly, so that the wider bandwidth associated with higher speeds could be harnessed. Experiments were conducted where the jet was perturbed acoustically, this time by a robust piezoelectric buzzer, to determine the dynamic response of the jet. In order to achieve this, the nonlinearity of the jet response with respect to the excitation amplitude, which was found to arise principally from the audio amplifier-piezo system, had to be inverted. The model was adapted to predict the experimentally-determined dynamic responses, which required the adjustment of several parameters. The variation of system damping with flow rate was not predicted by the model. Several explanations for this were given, including additional supporting analysis. A transfer function was fitted to dynamic response at the design flow rate (40 lpm) for control purposes. The effects of the static deflection curves were quantified by both simulations and further experiments, and were shown to be largely invariant to flow rate. The transfer function model was used as the basis of an LQG controller design. The controller had to overcome to challenge of the system noise existing in the same bandwidth as the jet response, leading to a necessarily careful choice of LQR and Kalman filter cost function parameters. The controller was implemented experimentally and its performance was evaluated relative to the conventional, lower speed, full switch mode of operation. The new mode of operation was demonstrated to out-perform its traditional counterpart in all respects tested.

The signal processing operations performed by jet shear layers in response to perturbations were explored. The demodulation process performed by jets was shown to be the result of an envelope detector, equivalent to a full-wave rectifier in electronic systems that demodulate AM signals. This led to the development of the input over-modulation technique, which made use of the shear layer phase insensitivity to double the response frequency. This technique requires half the input bandwidth of 100% AM with only a modest reduction in response power. Finally, it was hypothesised that the jet shear layer performs a sampling operation on the modulation signal at the carrier tone frequency, in addition to the envelope detection. An analogy with the Nyqyist sampling theorem was proposed. Experimental data appeared to violate the Nyquist theorem, although limited measurement techniques made it impossible to be conclusive.

The conclusions of this thesis are

1. The principal conclusion of chapters 3 & 4 was that the frequency responses produced by the model appear to agree well with the experimental data, particularly at lower flow rates. The rate of increasing roll-off frequency with flow rate is reflected in the model frequency responses accurately. A second roll-off was observed in the data that was not capture by the model. It was suggested that this feature is not related to the bulk jet dynamics that are the subject of the model. Possible causes for the second roll-off are the shear layer response and channel filling time.

   The other validation available was the model fit to the experimentally-identified frequency responses from the fluidic device in chapter 5. Several parameter adjustments were required, but the model captured the roll-off frequency well for most flow rates. The increasing resonance with flow rate seen in the experimental data was not reflected in the model responses. Several explanations were offered as to why the experimental data from the fluidic device are unlikely to match the model data precisely. Chief of these was the presence of the outlet channels and splitter, which were calculated to

respond at the frequency of the resonance. However, the model magnitude response roll-off frequencies were in close agreement with the experimental data for all but one case. This supports the notion that the model of the attached jet is the basis for the model of any fluidic device.

2. It is possible to use feedback control in continuously-modulated fluidic devices to provide robustness to disturbances. The control design is hampered by the fact that the jet noise bandwidth is coincident with that of the bulk jet dynamics, leading to a small system gain and a modest closed-loop system bandwidth. The result is that the control system is limited by measurement noise rather than by the input or system dynamics. However, the jet noise is not spatially correlated, so that using spatially distinct measurements could unlock significant improvements in closed-loop bandwidth. Specifically, the pressure difference across the jet could be used as a second measurement, and the known transport delay between this and the outlet channel pitot probe raises some interesting prospects for disturbance identification and rejection.

3. It was determined in chapter 6 that the demodulation property of jet shear layers first observed by Wiltse & Glezer [131] is analagous to an envelope detector. That is to say that the shear layer is insensitive to the phase of the input perturbations, and a modulus operation captures this property as well as the demodulation property. This is equivalent to a full-wave rectifier in electronics.

4. Use was made of this insight in chapter 6 in the formulation of the input over-modulation technique. This novel technique requires half the actuator bandwidth of standard 100% amplitude modulation, and suffers only a 2.7 dB (a factor of 1.4 in amplitude) penalty at the response frequency when the input power is equated to the 100% AM case. Several possible applications were suggested, and it has been used principally in this thesis to gain further insight into shear layer modulation.

5. It was hypothesised that the shear layer also acts as a sampler at the carrier tone frequency. This operation was suggested to occur after the modulus operation described

above. The Nyquist sampling theorem limit therefore applies to the shear layer response and consequently the bulk jet response: if the modulation frequency exceeds half of the carrier frequency, the response is aliased. However, experimental results appeared to contradict this hypothesis, although it was not possible to be conclusive due to limitations of the measurement techniques used.

Future work of interest following this thesis includes

i. Using multiple measurements in the control of a piezo-fluidic device: the pressure difference across the jet could be used as well as the unattached side outlet total pressure, and possibly other pressures, in order to improve signal-to-noise ratio and increase the closed-loop bandwidth.

ii. Extending the model developed in chapter 3 to describe the operation of fluidic oscillators of the type introduced by Spyropoulos [112]. The control port tube dynamics should be straightforward to model, and an experimental correlation may be required to deal with the phases of switching after the jet detaches.

iii. Combining elements from actively- and passively-controlled fluidic amplifiers to create a variable-frequency fluidic oscillator that can phase-lock onto a reference oscillation. This would be a fluidic oscillator of the type introduced by Spyropoulos [112] with the addition of an acoustic source to modify the feedback mechanism and change the oscillation frequency.

iv. Demonstrating the value of the input over-modulation technique developed in chapter 6 through an example application with a narrow-band actuator driven with continuous modulation.

v. Investigating the apparent violation of the Nyquist-Shannon sampling theorem analogy proposed in chapter 6.

Appendix A

Derivation of Görtler velocity profile

The starting point is the definition of the jet momentum flux width, b_m. The jet momentum flux is equated to the momentum flux of a jet with a flat velocity profile but finite width, b_m, as follows

$$J = \rho \int_{\infty}^{\infty} u^2 \, \mathrm{d}y \; = \; \rho \int_{-\frac{b_m}{2}}^{\frac{b_m}{2}} u_c^2 \, \mathrm{d}y \; = \; \rho b_m u_c^2. \tag{A.1}$$

Next, Prandtl's observation that jet width is proportional to downstream distance from the nozzle is applied, giving

$$b_m \; = \; k_1 x. \tag{A.2}$$

Substituting (A.2) into (A.1) gives the centreline velocity as

$$u_c = \sqrt{\frac{J}{\rho k_1 x}}. \tag{A.3}$$

Prandtl's assumption of eddy viscosity proportional to jet width and centreline velocity gives

$$\epsilon_{\mathrm{v}} \; = \; k_2 b_m u_c, \tag{A.4}$$

so that substituting (A.1) and (A.3) into (A.4) results in

$$\epsilon_{\mathrm{v}} \;=\; k_2\sqrt{\frac{Jk_1}{\rho}}\,x^{\frac{1}{2}}, \tag{A.5}$$

where the constants of proportionality, k_1 and k_2, are to be determined by boundary conditions. The expression for eddy viscosity in (A.5) was used by Görtler in his solution of the two-dimensional jet [40]. To derive the velocity profile, the streamwise (x-direction) momentum equation is taken, assuming no pressure gradient and replacing the kinematic viscosity with the eddy viscosity in (A.5), which gives

$$u\frac{\partial u}{\partial x} + v\frac{\partial u}{\partial y} \;=\; k_2\sqrt{\frac{Jk_1}{\rho}}\,x^{\frac{1}{2}}\frac{\partial^2 u}{\partial y^2}. \tag{A.6}$$

A solution with a stream function given by

$$\psi \;=\; C_1 x^p F(\eta) \tag{A.7}$$

$$\eta \;=\; \sigma x^q y, \tag{A.8}$$

is assumed, where σ is an constant. Substitution of (A.7) into the momentum equation (A.6) using the boundary conditions

$$\text{at } y = 0: \;\; v = 0, \;\; \frac{\partial u}{\partial y} = 0 \tag{A.9}$$

$$\text{as } y \to \pm\infty: \;\; u \to 0, \tag{A.10}$$

yields the Görtler velocity profile:

$$u \;=\; \frac{1}{2}\sqrt{\frac{3J\sigma}{\rho x}}\,\mathrm{sech}^2(\eta) \tag{A.11}$$

$$v \;=\; \frac{1}{4}\sqrt{\frac{3J}{\rho\sigma x}}\left[2\eta\,\mathrm{sech}^2(\eta) - \tanh(\eta)\right] \tag{A.12}$$

$$\eta \;=\; \frac{\sigma y}{x}. \tag{A.13}$$

Bibliography

[1] John David Anderson Jr. Introduction to flight (5th international ed.), 2004.

[2] Holger Babinsky. How do wings work? *Physics Education*, 38(6):497–503, November 2003.

[3] S P Banks. *Control Systems Engineering: Modelling and Simulation, Control Theory and Microprocessor Implementation*. Prentice Hall, 1986.

[4] Jean-François Beaudoin, Olivier Cadot, Jean-Luc Aider, and José-Eduardo Wesfreid. Drag reduction of a bluff body using adaptive control methods. *Physics of Fluids*, 18(8):085107, 2006.

[5] Ralf Becker, Rudibert King, Ralf Petz, and Wolfgang Nitsche. Adaptive closed-loop separation control on a high-lift configuration using extremum seeking. *AIAA Journal*, 45(6):1382–1392, 2007.

[6] Thomas Behr. *Control of rotor tip leakage and secondary flow by casing air injection in unshrouded axial turbines*. PhD thesis, ETH Zurich, 2007.

[7] Thomas J Benson and Jonathan A Seidel. Gas turbine engines: Inlets. *Encyclopedia of Aerospace Engineering*, 2010.

[8] Hendrik Wade Bode et al. Network analysis and feedback amplifier design. 1945.

[9] Jeffrey P Bons, Rolf Sondergaard, and Richard B Rivir. The fluid dynamics of LPT blade separation control using pulsed jets. *Journal of Turbomachinery*, 124(1):77–85, February 2002.

[10] TC Booth, PR Dodge, and HK Hepworth. Rotor-tip leakage: part I - basic methodology. 1982.

[11] C Bourque and BG Newman. Reattachment of a two-dimensional, incompressible jet to an adjacent flat plate. *The Aeronautical Quarterly*, 11(3):201–232, 1960.

[12] Steven L. Brunton and Bernd R. Noack. Closed-Loop Turbulence Control: Progress and Challenges. *Applied Mechanics Reviews*, 67(5), 08 2015. 050801.

[13] Andrei Buzica, Julius Bartasevicius, and Christian Breitsamter. Experimental investigation of high-incidence delta-wing flow control. *Experiments in Fluids*, 58(9):131, 2017.

[14] L Cattafesta, III, S Garg, M Choudhari, F Li, L Cattafesta, III, S Garg, M Choudhari, and F Li. Active control of flow-induced cavity resonance. In *28th Fluid Dynamics Conference*, page 1804, 1997.

[15] Louis N Cattafesta III and Mark Sheplak. Actuators for active flow control. *Annual Review of Fluid Mechanics*, 43:247–272, 2011.

[16] Ciro Cerretelli and Kevin Kirtley. Boundary layer separation control with fluidic oscillators. *Journal of Turbomachinery*, 131(4):041001, 2009.

[17] Ciro Cerretelli, Werner Wuerz, and Emad Gharaibah. Unsteady separation control on wind turbine blades using fluidic oscillators. *AIAA Journal*, 48(7):1302–1311, 2010.

[18] Hyo Whan Chang. *Dynamic Analysis of a Monostable Fluid Amplifier*. PhD thesis, Oklahoma State University, 1978.

[19] DR Chapman, DM Kuehn, and HK Larson. Investigation of separated flows in supersonic and subsonic streams with emphasis on the effect of transition. Technical Report 1356, NASA, 1957.

[20] Charlotte Clark and Stephen A Stansfeld. The effect of transportation noise on health and cognitive development: A review of recent evidence. *International Journal of Comparative Psychology*, 20(2), 2007.

[21] Henri Coanda. Device for deflecting a stream of elastic fluid projected into an elastic fluid, September 1 1936. US Patent 2,052,869.

[22] John D Coull, Nicholas R Atkins, and Howard P Hodson. High efficiency cavity winglets for high pressure turbines. In *ASME Turbo Expo 2014: Turbine Technical Conference and Exposition*. American Society of Mechanical Engineers Digital Collection, 2014.

[23] Thomas Crittenden, Ari Glezer, Robert Funk, and David Parekh. Combustion-driven jet actuators for flow control. In *15th AIAA Computational Fluid Dynamics Conference*, page 2768, 2001.

[24] SC Crow and FH Champagne. Orderly structure in jet turbulence. *Journal of Fluid Mechanics*, 48(3):547–591, 1971.

[25] Dennis Culley. Variable frequency diverter actuation for flow control. In *3rd AIAA Flow Control Conference*, page 3034, 2006.

[26] A. de Juniac. Remarks at the HK tourism board global online forum. June 2020.

[27] J. I. Dodds. PhD thesis, Cambridge University, 1960.

[28] John Donovan. Control of shock wave/turbulent boundary layer interactions using tangential injection. In *34th Aerospace Sciences Meeting and Exhibit*, number 96-0443, January 1996.

[29] John Doyle. Guaranteed margins for LQG regulators. *IEEE Transactions on Automatic Control*, 23(4):756–757, 1978.

[30] John Doyle and Guter Stein. Robustness with observers. *IEEE Transactions on Automatic Control*, 24(4):607–611, 1979.

[31] M Epstein. Theoretical investigation of the switching mechanism in a bistable wall attachment fluid amplifier. *Journal of Basic Engineering*, 93(1):55–62, 1971.

[32] Maxime Forte, Jerome Jolibois, J Pons, Eric Moreau, G Touchard, and M Cazalens. Optimization of a dielectric barrier discharge actuator by stationary and non-stationary measurements of the induced flow velocity: application to airflow control. *Experiments in Fluids*, 43(6):917–928, 2007.

[33] E Forthmann. Uber turbulente strahlausbreitung. *Ing. Arch*, 5(1):42–54, 1934.

[34] M Gad-el Hak. *Flow Control*. Cambridge University Press, 2000.

[35] Mohamed Gad-el Hak and Dennis M Bushnell. Separation control. 1991.

[36] Semiu A. Gbadebo, Nicholas A. Cumpsty, and Tom P. Hynes. Control of Three-Dimensional Separations in Axial Compressors by Tailored Boundary Layer Suction. *Journal of Turbomachinery*, 130(1), 12 2007. 011004.

[37] Ari Glezer and Michael Amitay. Synthetic jets. *Annual Review of Fluid Mechanics*, 34(1):503–529, 2002.

[38] Suleyman Gokoglu, Maria Kuczmarski, Dennis Culley, and Surya Raghu. Numerical studies of a fluidic diverter for flow control. In *39th AIAA Fluid Dynamics Conference*, page 4012, 2009.

[39] Fabio Gori, Ivano Petracci, and Matteo Angelino. Influence of the reynolds number on the instant flow evolution of a turbulent rectangular free jet of air. *International Journal of Heat and Fluid Flow*, 50:386–401, 2014.

[40] von H Görtler. Berechnung von aufgaben der freien turbulenz auf grund eines neuen näherungsansatzes. *ZAMM-Journal of Applied Mathematics and Mechanics/Zeitschrift für Angewandte Mathematik und Mechanik*, 22(5):244–254, 1942.

[41] JM Goto and TM Drzewiecki. An analytical model for the response of flueric wall attachment amplifiers. *Harry Diamond Laboratories, HDL-TR-1598*, 1972.

[42] William Richard Graham, Cesare Alan Hall, and M Vera Morales. The potential of future aircraft technology for noise and pollutant emissions reduction. *Transport Policy*, 34:36–51, 2014.

[43] James Gregory, Ebenezer Gnanamanickam, John Sullivan, and Surya Raghu. Variable-frequency fluidic oscillator driven by piezoelectric devices. In *43rd AIAA Aerospace Sciences Meeting and Exhibit*, page 108, 2005.

[44] James Gregory, Joseph Ruotolo, Aaron Byerley, and Thomas McLaughlin. Switching behavior of a plasma-fluidic actuator. In *45th AIAA Aerospace Sciences Meeting and Exhibit*, page 785, 2007.

[45] James Gregory and Mehmet N Tomac. A review of fluidic oscillator development. In *43rd AIAA Fluid Dynamics Conference*, page 2474, 2013.

[46] James W Gregory, Ebenezer P Gnanamanickam, John P Sullivan, and Surya Raghu. Variable-frequency fluidic oscillator driven by a piezoelectric bender. *AIAA Journal*, 47(11):2717–2725, 2009.

[47] James W Gregory, John P Sullivan, and Surya Raghu. Visualization of jet mixing in a fluidic oscillator. *Journal of Visualization*, 8(2):169–176, 2005.

[48] James W Gregory, John P Sullivan, Ganesh Raman, and Surya Raghu. Characterization of the microfluidic oscillator. *AIAA Journal*, 45(3):568–576, 2007.

[49] Martin Hecklau, Olaf Wiederhold, Vincent Zander, Rudibert King, Wolfgang Nitsche, A Huppertz, and M Swoboda. Active separation control with pulsed jets in a critically loaded compressor cascade. *AIAA Journal*, 49(8):1729–1739, 2011.

[50] Lars Henning and Rudibert King. Drag reduction by closed-loop control of a separated flow over a bluff body with a blunt trailing edge. In *44th IEEE Conference on Decision and Control*, pages 494–499. IEEE, 2005.

[51] ZD Husain and AKMF Hussain. Natural instability of free shear layers. *AIAA Journal*, 21(11):1512–1517, 1983.

[52] AKM Fazle Hussain. Coherent structures and turbulence. *Journal of Fluid Mechanics*, 173:303–356, 1986.

[53] IATA Economics. Economic performance of the airline industry: End-of-year report. Technical report, International Air Transport Association, 2019.

[54] P Jiang, YC Guo, CK Chan, and WY Lin. Frequency characteristics of coherent structures and their excitations in small aspect-ratio rectangular jets using large eddy simulation. *Computers & Fluids*, 36(3):611–621, 2007.

[55] James P. Johnston and Michihiro Nishi. Vortex generator jets - means for flow separation control. *AIAA Journal*, 28(6):989–994, 1990.

[56] James W Joyce. Fluidics: basic components and applications. Technical report, Harry Diamond Labs, 1983.

[57] M.C. Keerthi and Abhijit Kushari. Effectiveness of vortex generator jets and wall suction on separated flows in serpentine-duct diffuser. *Aerospace Science and Technology*, 34:12 – 19, 2014.

[58] Michael Kegerise, Randolph Cabell, and Lousi Cattafesta. Real-time adaptive control of flow-induced cavity tones. In *42nd AIAA Aerospace Sciences Meeting and Exhibit*, page 572, 2004.

[59] J. L. Kerrebrock, D. P. Reijnen, W. S. Ziminsky, and L. M. Smilg. Aspirated Compressors. volume Volume 1: Aircraft Engine; Marine; Turbomachinery; Microturbines and Small Turbomachinery of *Turbo Expo: Power for Land, Sea, and Air*, 06 1997. V001T03A108.

[60] JM Kirshner and S Katz. *Design theory of fluidic components*. Academic Press, 2012.

[61] Ching-Wen Kuo, Jordan Cluts, and Mo Samimy. Effects of excitation around jet preferred mode strouhal number in high-speed jets. *Experiments in Fluids*, 58(4):35, 2017.

[62] Joachim Kurzke and Ian Halliwell. *Propulsion and Power: An Exploration of Gas Turbine Performance Modeling*. Springer, 2018.

[63] Scott Lattime and Bruce Steinetz. Turbine engine clearance control systems: current practices and future directions. In *38th AIAA/ASME/SAE/ASEE Joint Propulsion Conference & Exhibit*, page 3790, 2002.

[64] Sheldon G Levin and Francis M Manion. Jet attachment distance as a function of adjacent wall offset and angle. Technical Report 1087, Harry Diamond Labs, 1962.

[65] Der-Cherng Liaw and Eyad H Abed. Active control of compressor stall inception: a bifurcation-theoretic approach. *Automatica*, 32(1):109–115, 1996.

[66] Feng Lin and Jingyi Chen. Oscillatory tip leakage flows and stability enhancement in axial compressors. *International Journal of Rotating Machinery*, 2018, 2018.

[67] PA Lush. Investigation of the switching mechanism in a large scale model of a turbulent reattachment amplifier. In *2nd Cranfield Fluidics Conference, Cambridge, UK*, volume 3, 1967.

[68] PA Lush. A theoretical and experimental investigation of the switching mechanism in a wall attachment fluid amplifier. In *IFAC Symposium on Fluidics*, 1968.

[69] Jan Maciejowski. Asymptotic recovery for discrete-time systems. *IEEE Transactions on Automatic Control*, 30(6):602–605, 1985.

[70] M Mair. *On dynamics of fluidic jet switching and shear layer instabilities*. PhD thesis, University of Oxford, 2019.

[71] M Mair, M Bacic, K Chakravarthy, and B Williams. Jet preferred mode vs shear layer mode. *Physics of Fluids*, 32(6):064106, 2020.

[72] Michael Mair and Marko Bacic. Active fluidic switching at high mach numbers. In *AIAA Aviation 2019 Forum*, page 3683, 2019.

[73] Michael Mair, Marko Bacic, and Peter Ireland. On dynamics of acoustically driven bistable fluidic valves. *Journal of Fluids Engineering*, 141(6):061202, 2019.

[74] Michael Mair, Li-Wei Chen, James Turner, Marko Bacic, and Peter Ireland. Experimental and numerical analysis of a piezo driven fluidic device for active flow control. In *52nd AIAA/SAE/ASEE Joint Propulsion Conference*, page 4860, 2016.

[75] Michael Mair, James Turner, Marko Bacic, and Peter Ireland. Switching dynamics of a fluid diverter valve using ultrasonic excitation for active flow control. In *47th AIAA Fluid Dynamics Conference*, page 4309, 2017.

[76] Nicholas D Martin, Michael Bottomley, and Alan Packwood. Switching of a bistable diverter valve with synthetic jet actuators. *AIAA Journal*, 52(7):1563–1568, 2014.

[77] WV Miller. Experimental feasibility study of an analog electrical-to-fluidic transducer. *IEEE Transactions on Industrial Electronics and Control Instrumentation*, (1):50–58, 1969.

[78] Eric Moreau, Roberto Sosa, and Guillermo Artana. Electric wind produced by surface plasma actuators: a new dielectric barrier discharge based on a three-electrode geometry. *Journal of Physics D: Applied Physics*, 41(11):115204, 2008.

[79] Leong MS and Lim Meng Hee. Blades rubs and looseness detection in gas turbines - operational field experience and laboratory study. *Journal of Vibroengineering*, 15(3):1311–1321, 2013.

[80] HR Muller. A study of the dynamic features of a wall-reattachment fluid amplifier. *Journal of Basic Engineering*, 86(4):819–826, 1964.

[81] HR Muller. Wall reattachment device with pulsed control flow. In *Fluid Amplification Symposium*, page 179, 1964.

[82] Chris Nicholls and Marko Bacic. Closed-loop control of a piezo-fluidic amplifier. In *2018 Flow Control Conference*, page 3695, 2018.

[83] Chris Nicholls and Marko Bacic. Closed-loop control of a piezo-fluidic amplifier. *AIAA Journal*, 58(6):2414–2427, 2020.

[84] Chris Nicholls, Brian Tang, James Turner, and Marko Bacic. Experimental and numerical studies of physical mechanisms in fluidic oscillators. In *AIAA Aviation 2019 Forum*, page 3394, 2019.

[85] B. Nishri and I. Wygnanski. Effects of periodic excitation on turbulent flow separation from a flap. *AIAA Journal*, 36(4):547–556, 1998.

[86] M. R. Ozgu and A. H. Stenning. Switching dynamisc of bistable fluidic devices with low setbacks. *Journal of Dynamic Systems, Measurement, and Control*, 94(1):32–33, 03 1972.

[87] Jeremy T Pinier, Julie M Ausseur, Mark N Glauser, and Hiroshi Higuchi. Proportional closed-loop feedback control of flow separation. *AIAA Journal*, 45(1):181–190, 2007.

[88] Kay O Ploetner, Raoul Rothfeld, Marcia Urban, Mirko Hornung, Gilbert Tay, and Oluwaferanmi Oguntona. Technological and operational scenarios on aircraft fleet-level towards ATAG and IATA 2050 emission targets. In *17th AIAA Aviation Technology, Integration, and Operations Conference*, page 3771, 2017.

[89] Martiqua L Post and Thomas C Corke. Separation control using plasma actuators: Dynamic stall vortex control on oscillating airfoil. *AIAA Journal*, 44(12):3125–3135, 2006.

[90] Surya Raghu. Feedback-free fluidic oscillator and method, July 3 2001. US Patent 6,253,782.

[91] Surya Raghu. Fluidic oscillators for flow control. *Experiments in Fluids*, 54(2):1455, 2013.

[92] Ganesh Raman and Surya Raghu. Cavity resonance suppression using miniature fluidic oscillators. *AIAA Journal*, 42(12):2608–2612, 2004.

[93] Ganesh Raman, Edward J Rice, and David M Cornelius. Evaluation of flip-flop jet nozzles for use as practical excitation devices. 1994.

[94] Danny Rapoport, I Fono, K Cohen, and A Seifert. Closed-loop vectoring control of a turbulent jet using periodic excitation. *Journal of Propulsion and Power*, 19(4):646–654, 2003.

[95] H Reichardt. Gesetzmäßigkeiten der freien turbulenz. *VDI-Forschungsheft*, 1942.

[96] James P Ries. Dynamic modeling of the bistable fluid amplifier. Technical report, Department of Mechanical Engineering and Mechanics, Lehigh Unviersity, Bethlehem, PA, 1972.

[97] JE Rossiter. The effects of cavities on the buffeting of aircraft. *RAE Technical Memorandum No. Aero 754*, 1962.

[98] Mo Samimy, Nathan Webb, and Michael Crawley. Excitation of free shear-layer instabilities for high-speed flow control. *AIAA Journal*, 56(5):1770–1791, 2018.

[99] RA Sawyer. The flow due to a two-dimensional jet issuing parallel to a flat plate. *Journal of Fluid Mechanics*, 9(4):543–559, 1960.

[100] RA Sawyer. Two-dimensional reattaching jet flows including the effects of curvature on entrainment. *Journal of Fluid Mechanics*, 17(4):481–498, 1963.

[101] Zbigniew Schabowski and Howard Hodson. The reduction of over tip leakage loss in unshrouded axial turbines using winglets and squealers. *Journal of Turbomachinery*, 136(4):041001, 2014.

[102] Hermann Schlichting and Klaus Gersten. *Boundary-layer theory*. Springer, 9$^{\text{th}}$ edition, 2016.

[103] A. Seifert, T. Bachar, D. Koss, M. Shepshelovich, and I. Wygnanski. Oscillatory blowing: A tool to delay boundary-layer separation. *AIAA Journal*, 31(11):2052–2060, 1993.

[104] A. Seifert, A. Darabi, and I. Wyganski. Delay of airfoil stall by periodic excitation. *Journal of Aircraft*, 33(4):691–698, 1996.

[105] A. Seifert, A. Daraby, and B. Nishiriand I. Wygnanski. The effects of forced oscillations on the performance of airfoils. In *3rd Shear Flow Conference*, number 93-3264, July 2012.

[106] A Seifert and LG Pack. Oscillatory control of separation at high reynolds numbers. *AIAA Journal*, 37(9):1062–1071, 1999.

[107] U Shaked. Guaranteed stability margins for the discrete-time linear quadratic optimal regulator. *IEEE Transactions on Automatic Control*, 31(2):162–165, 1986.

[108] Achal Singhal, David Castañeda, Nathan Webb, and Mo Samimy. Control of dynamic stall over a NACA 0015 airfoil using plasma actuators. *AIAA Journal*, 56(1):78–89, 2018.

[109] SA Sjolander. Secondary and tip-clearance flows in axial turbines. VKI Lecture Series, 1997.

[110] Barton L. Smith and Ari Glezer. The formation and evolution of synthetic jets. *Physics of Fluids*, 10(9):2281–2297, 1998.

[111] András Sóbester. Tradeoffs in jet inlet design: A historical perspective. *Journal of Aircraft*, 44(3):705–717, 2007.

[112] C. E. Spyropoulos. A sonic oscillator. In *Proceedings of the Fluid Amplification Symposium*, volume III, pages 27–51, Washington D.C., 1964.

[113] Marcel Staats and Wolfgang Nitsche. Active control of the corner separation on a highly loaded compressor cascade with periodic nonsteady boundary conditions by means of fluidic actuators. *Journal of Turbomachinery*, 138(3), 2016.

[114] Edward A Stalker. Axial blower, August 13 1946. US Patent 2,405,768.

[115] Edward A Stalker. Compressor, June 5 1956. US Patent 2,749,027.

[116] Edward A Stalker. Compressors, April 15 1958. US Patent 2,830,754.

[117] Julia Stephens, Thomas Corke, and Scott Morris. Control of a turbine tip leakage vortex using casing vortex generators. In *47th AIAA Aerospace Sciences Meeting including The New Horizons Forum and Aerospace Exposition*, page 299, 2009.

[118] Ronald D Stouffer. Liquid oscillator device, April 2 1985. US Patent 4,508,267.

[119] Kunihiko Taira, Clarence W Rowley, Tim Colonius, and David R Williams. Lift enhancement for low-aspect-ratio wings with periodic excitation. *AIAA Journal*, 48(8):1785–1790, 2010.

[120] Ye Tian, Louis Cattafesta, and Rajat Mittal. Adaptive control of separated flow. In *44th AIAA Aerospace Sciences Meeting and Exhibit*, page 1401, 2006.

[121] Wei Tuo, Yajun Lu, Wei Yuan, Sheng Zhou, and Qiushi Li. Experimental Investigation on the Effects of Unsteady Excitation Frequency of Casing Treatment on Transonic Compressor Performance. *Journal of Turbomachinery*, 133(2), 10 2010. 021014.

[122] Henk Kaarle Versteeg and Weeratunge Malalasekera. *An introduction to computational fluid dynamics: the finite volume method*. Pearson education, 2007.

[123] Hermann Viets. Flip-flop jet nozzle. *AIAA Journal*, 13(10):1375–1379, 1975.

[124] PR Viswanath, G Ramesh, and KT Madhavan. Separation control by tangential blowing inside the bubble. *Experiments in Fluids*, 29(1):96–102, 2000.

[125] Ralph J Volino. Control of tip leakage in a high-pressure turbine cascade using tip blowing. *Journal of Turbomachinery*, 139(6):061008, 2017.

[126] Bojan Vukasinovic, David Lucas, and Ari Glezer. Direct manipulation of small-scale motions in a plane shear layer. In *2nd AIAA Flow Control Conference*, page 2617, 2004.

[127] RA Wallis. The use of air jets for boundary layer control. Technical report, Aeronautical Research Labs, Melbourne, Australia, 1952.

[128] H Wang, SBM Beck, GH Priestman, and RF Boucher. Fluidic pressure pulse transmitting flowmeter. *Chemical Engineering Research and Design*, 75(4):381–391, 1997.

[129] M. E. White, R. E. Lee, M. W. Thompson, A. Carpenter, and W. J. Yanta. Tangential mass addition for shock/boundary-layer interaction control in scramjet inlets. *Journal of Propulsion and Power*, 7(6):1023–1029, 1991.

[130] David R Williams, Daniel Cornelius, and Clarence W Rowley. Supersonic cavity response to open-loop forcing. In *Active Flow Control*, pages 230–243. Springer, 2007.

[131] John M Wiltse and Ari Glezer. Manipulation of free shear flows using piezoelectric actuators. *Journal of Fluid Mechanics*, 249:261–285, 1993.

[132] John M Wiltse and Ari Glezer. Direct excitation of small-scale motions in free shear flows. *Physics of Fluids*, 10(8):2026–2036, 1998.

[133] Gu Xu and Robert Antonia. Effect of different initial conditions on a turbulent round free jet. *Experiments in fluids*, 33(5):677–683, 2002.

[134] KBMQ Zaman and AKMF Hussain. Vortex pairing in a circular jet under controlled excitation. part 1. general jet response. *Journal of Fluid Mechanics*, 101(3):449–491, 1980.

[135] KBMQ Zaman and AKMF Hussain. Turbulence suppression in free shear flows by controlled excitation. In *13th Fluid and Plasma Dynamics Conference*, page 1338, 1981.